Towards Understanding the Mixing Characteristics of Turbulent Buoyant Flows

Thesis by

Phares L. Carroll

In Partial Fulfillment of the Requirements

for the Degree of

Doctor of Philosophy

California Institute of Technology

Pasadena, California

2014

(Defended April 29, 2014)

ii

This work is dedicated in the memory of Harold E. Prewitt, who, through his quiet and steadfast character, taught me what hard work, perseverance, and integrity were. Without such an example, I would never have had the grit to make it.

Abstract

This work proposes a new simulation methodology in which variable density turbulent flows can be studied in the context of a mixing layer with or without the presence of gravity. Specifically, this methodology is developed to probe the nature of non-buoyantly-driven (*i.e.* isotropically-driven) or buoyantly-driven mixing deep inside a mixing layer. Numerical forcing methods are incorporated into both the velocity and scalar fields, which extends the length of time over which mixing physics can be studied. The simulation framework is designed to allow for independent variation of four non-dimensional parameters, including the Reynolds, Richardson, Atwood, and Schmidt numbers. Additionally, the governing equations are integrated in such a way to allow for the relative magnitude of buoyant energy production and non-buoyant energy production to be varied.

The computational requirements needed to implement the proposed configuration are presented. They are justified in terms of grid resolution, order of accuracy, and transport scheme. Canonical features of turbulent buoyant flows are reproduced as validation of the proposed methodology. These features include the recovery of isotropic Kolmogorov scales under buoyant and non-buoyant conditions, the recovery of anisotropic one-dimensional energy spectra under buoyant conditions, and the preservation of known statistical distributions in the scalar field, as found in other DNS studies.

This simulation methodology is used to perform a parametric study of turbulent buoyant flows to discern the effects of varying the Reynolds, Richardson, and Atwood numbers on the resulting state of mixing. The effects of the Reynolds and Atwood numbers are isolated by looking at two energy dissipation rate conditions under non-buoyant (variable density) and constant density conditions. The effects of Richardson number are isolated by varying the ratio of buoyant energy production to total energy production from zero (non-buoyant) to one (entirely buoyant) under constant Atwood number, Schmidt number, and energy dissipation rate conditions. It is found that the major differences between non-buoyant and buoyant turbulent flows are contained in the transfer spectrum and longitudinal structure functions, while all other metrics are largely similar (*e.g.* energy spectra, alignment characteristics of the strain-rate tensor). Also, despite the differences noted between fully buoyant and non-buoyant turbulent fields, the scalar field, in all cases, is unchanged by these. The mixing dynamics in the scalar field are found to be insensitive to the source of turbulent kinetic energy production (non-buoyant *vs.* buoyant).

Contents

List of Figures

List of Tables

Chapter 1

Introduction

1.1 Background and Motivation

The first treatment of the effects of buoyancy on mixing was conducted back in 1857 by Professor Jevons, who was interested in understanding why certain cloud formations, specifically the cirrous cloud, looked as they did [45, 88]. A cirrous cloud is composed of long, string-like regions that run almost perfectly parallel to each other over extended tracts of space. Jevons wanted to understand how and why this parallelism was able to persist. Existing explanations at the time were hand-waving at best, and Jevons wanted a more rigorous explanation. He had long hypothesized that this parallelism was due to density differences in stratified regions of atmosphere. He conducted an experimental investigation to test this theory, and the results bore out his suspicions [45]. Coming out of this work was the understanding that different portions of fluids, due to slight differences in density, may be made to mix and pass into one another. If this mixing process is rendered visible, such as by condensation in the atmosphere, then this could explain the parallel and fibrous structure observed in these cloud formations.

Years later in 1883, Lord Rayleigh placed the observations made by Jevons on a more firm theoretical basis [88]. By applying perturbation theory, Lord Rayleigh was able to show that buoyancy-induced mixing was attributable to the stability or instability of growing or decaying harmonic oscillations [88]. Further, Lord Rayleigh developed a criterion to calculate the stability characteristics of any stratified fluid system. Specifically, if the density of the upper fluid in a stratified fluid system is greater than that beneath it, these harmonic oscillations are going to grow in time, resulting in interpenetration and mixing. This is known as an unstable stratification. But, if the upper fluid is less dense than the lower, then these harmonic oscillations will decay in time, there is no interpenetration or mixing, and this is known as a stable stratification.

This is a brief overview of the history of buoyancy in mixing, but it was these initial studies that established the importance of buoyancy in mixing. Since those days, buoyancy-driven mixing processes have been identified in a broad swath of naturally occuring and engineering-oriented prob-

lems. A few examples include sedimentation and plumes in oceanographic flows [51], the dynamics of deflagration waves in atmospheric and astrophysical flows [71, 92], and fusion processes in energy systems. These are just a few examples, but they serve to underscore the ubiquity of buoyancy in mixing.

Despite the presence of these buoyancy-induced mixing processes in a broad range of physical contexts, little is known about the turbulent structure located inside of such buoyant mixing layers. This lack of understanding is not a result of a lack of interest; this is an important issue, and it has received attention from both experimental and computational perspectives [11, 18, 28, 31, 55, 56, 84, 88, 90, 106]. However, due to the disparity in scales involved, extracting small-scale physical features can be too computationally expensive and beyond current experimentally attainable resolution [28, 31, 84, 106]. Thus, this thesis proposes a new, alternative simulation methodology which focuses on these small-scale physics with the intent of interrogating the nature of turbulent structure inside these buoyantly-driven mixing layers. This buoyant structure is then compared against the structure found in canonical isotropic turbulent mixing layers.

This thesis proposes a new mathematical framework for the conduct of buoyant mixing studies. In the literature, there are two existing simulation frameworks that are designed to study buoyant mixing, but neither of these are ideal for the study of the smaller scales of mixing. This non-ideality is rooted in the problems of space and time, which are now presented. The first existing simulation framework relies on a shear layer configuration (Fig. 1.1). In the shear layer geometry, there are two stably stratified fluids of differing densities ($\rho_1 \neq \rho_2$) with a relative velocity (U) between them [11, 15, 28, 31, 34, 84, 88, 90, 106]. As the faster moving fluid travels over the slower moving one, the slower moving fluid is entrained. This entrainment leads to the development of a mixing layer, which then convects downstream. As it convects, it grows both spatially and temporally. This leads to the first problem of space. As the mixing layer grows spatially, it requires an increasingly high resolution to resolve the smallest scale aspects of mixing. This, in general, is not possible, making the data collected from these types of studies more reflective of the larger scale aspects of mixing. This configuration also suffers from the problem of time. As the mixing layer develops, eventually the fluid contained in the layer completely mixes, or homogenizes. This results in a finite time period over which mixing data can be collected, after which the fluids involved have completely mixed together.

The second simulation framework relies on the Rayleigh-Taylor unstable configuration (Fig. 1.2, Fig. 1.3, and Fig. 1.4). In the Rayleigh-Taylor geometry, there are two unstably stratified fluids separated by a partition. At time equal to zero, the partition is removed and a non-zero gravity vector is applied across the unstably stratified layer [11, 19, 54, 55, 56]. This results in the interpenetration of the higher density fluid into the lower density fluid, forming the characteristic spikes and bubbles common to these type of flows. As the two fluids mix, a mixing layer develops. This mixing layer

(a) $t = t_0$ (b) $t = t_1$ (c) $t = t_2$

(d) $t = t_3$ (e) $t = t_4$
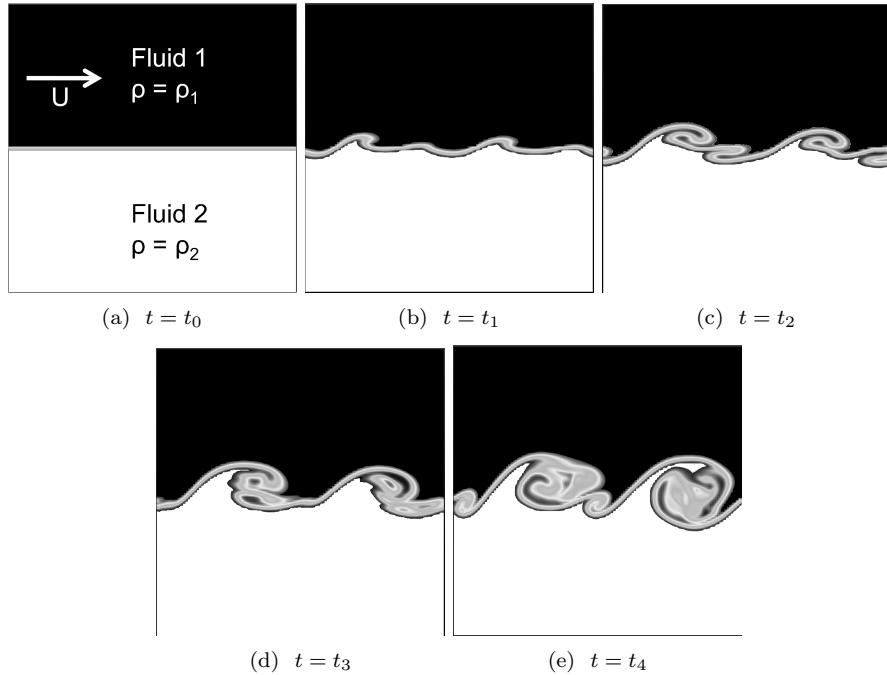
Figure 1.1: Time evolution of a shear layer induced by mean shear flow (momentum-driven). The fluids have differing densities ($\rho_1 \neq \rho_2$), and they are mixed via the mean relative shear velocity (U) acting parallel to the initial fluid interface. These results obtained using in-house code NGA [26], which is detailed in Appendix 8.3, Appendix 8.4, Appendix 8.5, and Appendix 8.6.

grows in space and in time, and, as a result, suffers from the same two problems found in the shear layer configuration. Accordingly, there is a need for a new simulation methodology with which to study the small scale aspects of buoyant mixing.

Further, the existing methods of simulating variable density mixing suffer an additional limitation. These methods cannot independently vary the four non-dimenionsional parameters of importance in mixing studies, which are the Reynolds number (Re), the Richardson number (Ri), the Schmidt number (Sc), and the Atwood Number (A). The Reynolds number informs the relative importance of inertial and viscous forces present in the fluid system itself. The Richardson number indicates the relative strength of buoyancy versus fluid inertia. The Schmidt number is reflective of the ratio of fluid viscosity to scalar diffusivity. The Atwood number describes the extent of density variation in the fluids being mixed. In the Rayleigh-Taylor unstable geometry, buoyancy forces lead to mixing in two initially stationary fluids. As a result, any velocity imparted to the fluid parcels as they mix is due to buoyant effects, which couples the Reynolds and Richardson numbers intrinsically. Current efforts focus on increasing the overall numerical resolution, and, hence, the Reynolds number, in order to get insight into the character of small scale mixing [11, 56, 19]. Unfortunately, the high computational cost limits the parameter space that can be spanned using these conventional simulation geometries, and several open questions about the physics, specifically at the small scales,
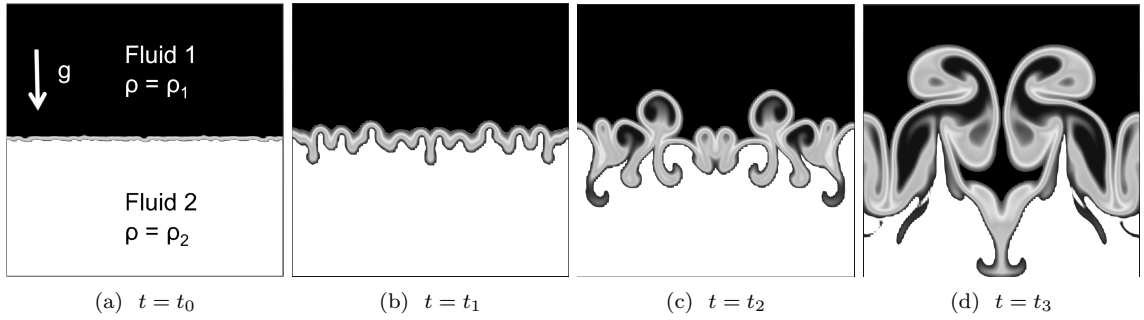
Figure 1.2: Time evolution of a shear layer induced by Rayleigh-Taylor instability (buoyancy-driven). The denser fluid (ρ_1) is atop the lighter fluid (ρ_2). Gravity acts normal to the fluid interface. These results obtained using in-house code NGA [26], which is detailed in Appendix 8.3, Appendix 8.4, Appendix 8.5, and Appendix 8.6.
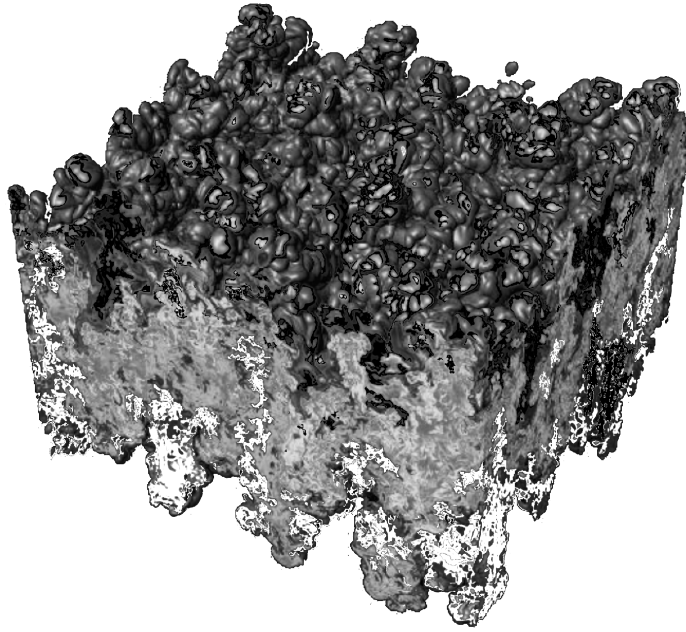
Figure 1.3: Rayleigh-Taylor instability in the fully turbulent regime. Light (white) fluid is light (density = 1) and dark (black) fluid is heavy (density = 3). The gray colors represent mixed fluid of various compositions. The pure fluids above and below the mixing region are not shown. Gravity is directed downwards. This figure and the caption description are taken from Fig. 1 in reference [11]. The computational grid on which these simulations were performed was $N^3 = 3072^3$.

(a) Initial density field	(b) Density field at maximum kinetic energy	(c) Homogenized density field (late time)
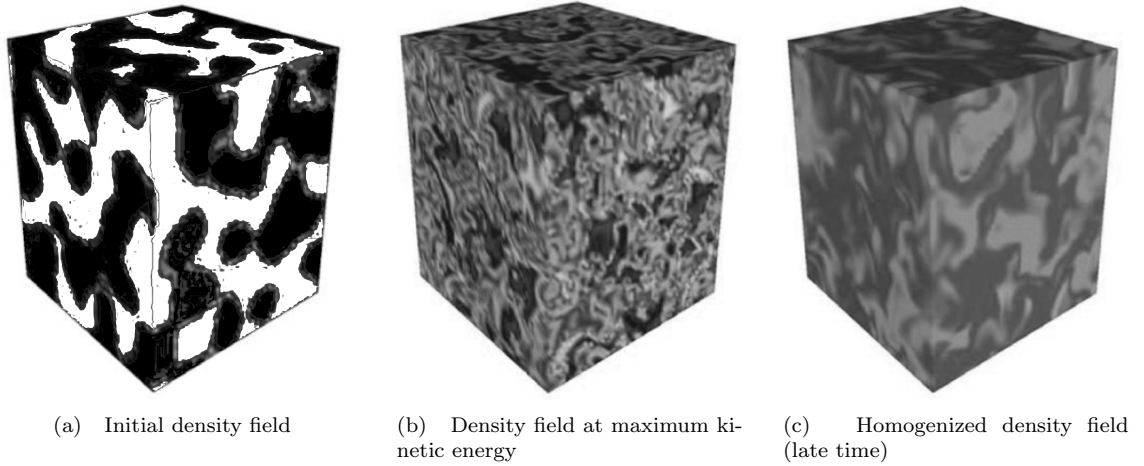
Figure 1.4: Buoyant mixing using a variant of the Rayleigh-Taylor configuration. This geometry does not include reservoirs of pure fluid, but instead buoyancy forces act on variations in the initial density field (a), and these lead to turbulent mixing. These show the initial density field (a) and its evolution toward a fully homogenized state (b and c). Black and white denote high and low fluid densities, and gray denotes a state of complete fluid mixing. Figures and caption descriptions are taken from Fig. 1 and Fig. 2 in reference [54].

remain unanswered.

Thus, there is a need for an alternative means of performing variable density turbulence simulations that can effectively and efficiently span the needed parameter space (Re, Ri, Sc, A) at a lower computational cost. This work proposes such a new simulation methodology to study variable density turbulent mixing. Based on the discussion of the existing simulation methods, the requirements in the development of this new method are fourfold. First, to ensure that the driving force behind mixing is sustained in time, the velocity field needs to be numerically forced. The role of forcing is to provide turbulent kinetic energy to the velocity field via either isotropic or buoyant energy production sources. This ensures that the turbulent fluctuations do not decay, and are perpetuated in time. Second, the scalar field needs to be numerically forced also. Implementing a scalar field forcing term ensures that the variance of the scalar quantity being mixed does not decay. As long as the variance of the scalar field is held constant, the scalar quantity never completely mixes, perpetuating in time the relevant mixing physics. Third, the density field must be prevented from homogenizing. If the density field homogenizes, gravitational effects cease to be important. These three requirements address the time problem mentioned earlier. The fourth requirement addresses the space problem. The geometry of interest must be specifically chosen such that small scale mixing physics are accurately captured. Since the focus of this work is on the small scales, and this aspect of mixing physics is confined to the inner region of the mixing layer, then only this region is included in the computational domain. This has the effect of reducing significantly the computational burden required in these types of simulations and, consequently, addresses the problem of space discussed
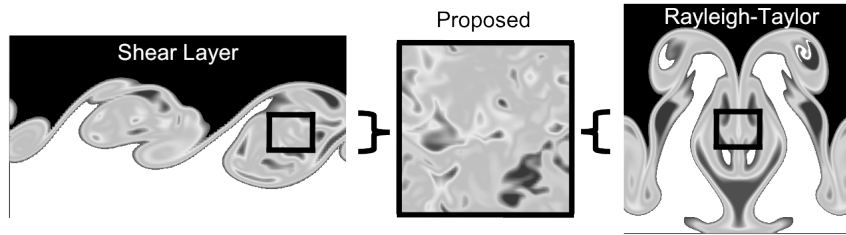
Figure 1.5: Region in which the proposed simulation methodology is applicable.

previously. This also allows for a simplifying assumption to be made. As the region of interest is located in the inner region of the mixing layer, it can be assumed that the boundary conditions are infinitely far away such that the mixing dynamics are independent of them. This enables the use of a box of turbulence containing a variable density fluid subject to periodic boundary conditions. This simplication removes much of the complexity of the problem being studied, and results in the computational domain depicted in Fig. 1.5.

1.2   Literature Review

This work develops the needed simulation tools and computational framework to examine the differences between buoyantly-driven turbulent mixing and isotropically-driven turbulent mixing. However, there has been considerable work carried out towards understanding buoyantly-driven turbulent flows from a non-equilibrium, or decaying, perspective. In the current work, "non-equilibrium flows" refer to transient, non-stationary flows. These are now briefly described. Generally, these experimental and numerical studies have been performed in the context of a shear (mixing) layer. The resulting analyses and conclusions derived have been focused primarily on the time rate of growth of the thickness of the mixing layer and the calculation of various mixing metrics to quantify the efficiency of buoyancy-induced fluid and scalar mixing [88, 90, 84, 28, 31, 106, 11]. An overview of what is known about the structure of buoyant flows is now provided.

The large body of research available on variable density mixing follows the work of Sandoval [83], who simulated the mixing of two incompressible fluids of differing densities under both buoyant and non-buoyant conditions. Sandoval's investigation into the fundamental differences between buoyantly-driven flows, isotropically-driven variable density flows, and Boussinesq flows has since been extended and augmented by others (*e.g.* [11, 18, 19, 28, 54, 55, 56, 57, 70]). The currently known features of buoyant mixing are here summarized. Note that almost all of these studies, both simulation and experimental, address variable density mixing from a non-equilibrium perspective.

It is known that the mixing between different density fluids is starkly different from the mixing between fluids of commensurate densities, for which the Boussinesq approximation is valid [57]. Under a Rayleigh-Taylor unstable simulation configuration, it has been found that the probability

density function (PDF) of the density field becomes skewed towards the less dense fluid as the mixing process occurs. This asymmetric mixing rate suggests that the more dense fluid mixes at a slower rate than the less dense fluid [55, 56, 57]. As a consequence of this, the penetration depth of larger density fluids exceeds that of lower density fluids [28, 55]. This behavior has been found over a significant range of Atwood numbers, which range from those within the Boussinesq limit to those significantly outside of it. Thus, it is accepted that this mixing asymmetry is a robust feature of variable density buoyant mixing, and it becomes more pronounced as the Atwood number is increased [55, 57]. Further, the effects of Schmidt number have been probed. It has been reported that the Schmidt number (diffusion) has a pronounced effect on the energy dissipation rate. Specifically, diffusion plays a prominent role in the rate at which the fluids being mixed transition from true variable density mixing to a Boussinesq-type mixing state [54].

Distinct stages in the Rayleigh-Taylor unstable mixing process have been identified [19]. First, there is a period of transient modal growth. Second, there is a transition to a weakly turbulent state. Third, there is a mixing transition. Lastly, there is the transition and sustenance of strong turbulence. The fourth and final stage has not been studied in detail, and primary focus has been placed on understanding stages one through three. Based on this focus, much is known about the transient mixing process leading up to the development of turbulence. Specifically, it has been found that in these early stages, the dynamics are non-linear. The mixing rate of the two constituent fluids being mixed experience a monotonically increasing mixing rate as the strength of gravity (buoyancy) is increased [70]. But, there is not a monotonic increase in mixing rate when the shear rate is increased. These findings are justified via a stability analysis, and it is determined that shear-induced mixing and buoyant-induced variable density mixing are markedly different in nature [70]. By employing various mixing metrics, buoyancy has been identified as a more efficient mixing agent than shear, and shear has been identified as being an agent to reduce the mixing rate [70]. This surprising finding is justified by the argument, based on an analysis of Kelvin-Helmholtz and Rayleigh-Taylor instabilities, that shear reduces the amount of energy transferred into vertical mixing [70].

It is also known that buoyant flows are anisotropic, and these flows are sustained by the conversion of potential energy into kinetic energy via a mass flux [54]. The extent of anisotropy has been probed using various metrics, but the most common metric is the Favre Reynolds stress anisotropy tensor, b_{ij}. This tensor describes the relative amount of kinetic energy contained in the three velocity component directions. Results over a broad range of Atwood numbers suggest that the normal stress components of the velocity field are consistently anisotropic in the presence of buoyancy [57]. From these types of analyses, it has been found that the extent of anisotropy is the most pronounced at the smallest and largest flows scales, while the intermediate flow scales are subject to less anisotropy [56, 57]. This persistent anisotropy at the small scales has been argued by some to be a direct consequence

of the cancellation between non-linear convective energy transfer and viscous dissipation, which results in the presence of anisotropy due to the (unbalanced) buoyant energy production term [55, 56]. But, based on an analysis of only energy spectra and calculated length-scales, conflicting results have been reported. Although calculated energy spectra confirm the anisotropy of buoyant turbulence, some have found that the smallest scales of turbulence retain isotropic character despite the presence of buoyancy [11]. These results have been used to argue that the anisotropic body force induced by gravity is felt at the intermediate scales (the Taylor micro-scales), but that these effects are lost at the smallest scales (the Kolmogorov scales) [11]. Also based on energy spectra, it has been found that the energy spectrum component in the direction of gravity leads the evolution of the energy spectra in the other two ordinate directions [19]. This is sensible, as, in buoyant flows, all energy is injected via the gravity vector, which is only non-zero in a single direction. This results in a time lag before which the energy injected can be distributed to the directions of the other two velocity components.

Also, information about the alignment of the strain-rate tensor eigenframe and the density gradient is available. It is established in the literature that the gradient of a passive scalar aligns itself in the direction of the most compressive eigenvector of the strain-rate tensor. As the scalar field and the density field are related, it is not unsurprising that this alignment tendency holds for the density gradient. However, it has been noted that, as the Atwood number increases, the alignment of the gradient of the higher density fluid with the strain-rate eigenframe becomes different than the alignment of the gradient of the lower density fluid with the strain-rate eigenframe [57]. Arguments to explain this have been based on the higher inertia found in the more dense fluid compared to the less dense fluid; it is believed that the alignment of the gradient of the larger density fluid with the most compressive eigenvector weakens (relative to the alignment of the gradient of the lower density fluid) owing to the larger fluid inertia [57]. The heavier fluid, it is suggested, is more resistive of deformation due to local strain. This results in a local turbulent structure that changes in response to the local inertia of fluids being mixed [57]. Further, it is thought that this increase in fluid inertia results in a reduction in the rate at which the heavier fluid is mixed [57].

Moreover, the self-similarity of buoyant mixing has been the subject of considerable study [11, 19, 56]. Studies have indicated that Rayleigh-Taylor unstable flows evolve towards a state of self-similar mixing rather quickly (within only a few eddy turn-over times) after the mixing process begins [56]. Further, in this self-similar mixing regime, the growth rate of the mixing layer slows down [19]. It has been found, also, that this state of self-similar mixing only manifests if the memory of initial flow conditions are lost, the boundary conditions of the flow exert no effect on the mixing dynamics, and the Reynolds number and diffusivity are sufficiently high to render viscous effects negligible [19].

Based on the overview provided above, significant insight into buoyant and variable density mixing has been obtained from studies utilizing a non-equilibrium perspective. However, less attention

has been directed towards the equilibrium, or statistically steady, problem. Specifically, only one study addresses the equilibrium problem [18], and, accordingly, there is a gap in the current literature concerning the structure of buoyantly-generated turbulence versus the well-known structure of isotropic turbulence, and the resulting mixing processes. This work is aimed towards closing this gap by investigating key turbulent characteristics obtained under statistically stationary non-buoyant, partially buoyant, and fully buoyant conditions. The characteristics of interest in the current work include the extent of isotropy or anisotropy at the large, intermediate, and small scales, the location (or distribution) of energy and scalar variance, the transfer mechanisms responsible for the energy and scalar variance cascade, the way in which energy and scalar variance are dissipated, and the location (or distribution) at which this occurs. In the literature, there are open questions as to the extent that buoyancy-induced anisotropy is able to permeate into the smaller, more viscous flow scales [11, 18, 56, 55]; the supply of turbulent kinetic energy from only one flow direction (the direction of gravity) does induce deviations from purely isotropic physics, but the severity of these and the depths to which they are able to penetrate are unknown. Following this, the validity of the Kolmogorov hypotheses (*i.e.* local flow isotropy or the presence of an inertial subrange) when density is variable [18, 56, 11] has not been proven. It is unknown how (and if) turbulent mixing varies based on the source of turbulent kinetic energy (*i.e.* isotropic energy production *vs.* buoyant energy production *vs.* shear-induced energy production). Moreover, structural features of interest include the alignments of specific turbulent field variables (*e.g.*, vorticity, strain rate eigenvectors, scalar field gradients) and how such alignment characteristics may or may not be associated with the mechanism of turbulent kinetic energy generation.

1.3 Outline

There are two primary objectives for this thesis work. The first objective is to present an efficient computational methodology for the study of variable density turbulence. To accomplish this, it is necessary to develop the needed simulation tools. Specifically, the forcing methods to sustain statistical stationarity in the velocity and scalar fields must be designed, validated, analyzed, and integrated. The second objective is to use the developed approach to study the differences between buoyantly- and (isotropic) non-buoyantly-driven turbulent mixing via controlled parametric studies.

Per the first objective, the required velocity and scalar field forcing methods are addressed. As this study is concerned with the differences between buoyant and non-buoyant turbulence, the means by which the velocity field is kept at statistical stationarity are crucially important. Hence, the velocity forcing methods used to generate stationary conditions must be highly accurate. A buoyantly-forced velocity field simply requires a non-zero gravity vector and a variation in fluid density; this is easily accomplished, and the results are physically meaningful. Forcing the velocity

field non-buoyantly is not as straightforward. To produce a non-buoyant (isotropic) turbulent field, an isotropic forcing method is required. There are many velocity field forcing methods available that can generate isotropic turbulence [1, 59, 81, 96, 33, 87, 89, 17, 46, 108], but a detailed study of these has not yet been performed in the literature. In order to ensure that the physics generated under the action of velocity field forcing are as physically realistic as possible, such an analysis is required. This allows for an informed choice of method to implement. This study is performed and reported (Chapter 2). Following this, Lundgren's linear forcing method is chosen, and slightly modified for practical simulation purposes, to generate the desired non-buoyant (isotropic) velocity field physics (Chapter 3).

The scalar field also must be forced. In the literature, there are two dominant scalar forcing methods [105, 96]. These are the mean scalar gradient method and a low waveband spectral method. The mean scalar gradient method is known to induce significant anisotropy in the scalar field in the direction of the imposed mean gradient. As the ultimate goal of this work is to study buoyant mixing, which is driven by a physically meaningful density gradient, having a purely (artificial) numerical gradient influencing the scalar field dynamics is not ideal. Spectral forcing schemes are not subject to this anisotropy, but they are less representative of physically attainable turbulent flows. Further, the type of scalar field physics of concern when considering this type of buoyant mixing is more analogous to one-time scalar variance injection or (isotropic) self-similar scalar variance decay. A scalar field forcing method for this self-similar type of physics did not exist in the literature, so it had to be developed. The newly created scalar field forcing method, linear scalar forcing, has been tested and validated, and it generates the needed scalar field physics (Chapter 4).

Following the second objective, the numerical framework to study turbulence under buoyant and isotropic (non-buoyant) conditions is integrated (Chapter 5). A chief advantage of this framework is its ability to vary independently important non-dimensional parameters, including the Reynolds, Schmidt, Richardson, and Atwood numbers, which other available frameworks cannot do. Following its validation, the proposed geometry is applied to the study of variable density turbulent mixing with and without the presence of gravity (Chapter 6).

Chapter 2

Turbulent Mixing in the Velocity Field [13]

Without an energy source, a turbulent velocity field will decay. In Direct Numerical Simulation (DNS) studies of incompressible homogeneous, isotropic turbulence (HIT), turbulent fields are maintained at a state of statistical stationarity by using various velocity field forcing methods. Velocity forcing entails appending a source term to the governing momentum equations. There are several different forcing methods in the literature for preventing energy decay [1, 33, 87, 89, 17, 58, 81]. By investigating the specifics of a forcing method (and its associated momentum source term), the impacts that it has on the produced turbulence can be understood.

A turbulent velocity field can be forced either spectrally in wave-space or in real-space. Historically, simulation studies of forced isotropic turbulence have relied on spectral forcing methods, which provide energy to the low wavenumber regions of the flow field by various means. Low wavenumber energy injection is thought to be consistent with the concept of Richardson's cascade of energy to the progressively smaller scales. There are many variations on low waveband forcing, including those that are purely random in nature (Alvelius' method) [1], those that make use of stochastic processes to promote isotropy [33], those that freeze the value of the Fourier coefficients of the velocity field within a low waveshell band [87, 89], and others that artificially fix the energy content between different low wavenumber shells to produce the desired spectral trends in the resulting energy spectrum [17]. However, as a practical matter, spectral methods can be difficult to implement, as they require periodic boundary conditions, which are not always admitted in engineering problems. Additionally, spectral schemes tend to be best suited for simulation studies concerning homogeneous, isotropic turbulence with constant density flow fields. Recently, Lundgren [58, 81] proposed a physical-space velocity field forcing method that can be integrated into non-spectral codes and can accomodate non-periodic boundary conditions. This method was tested by Rosales and Meneveau [81], and it was found to produce comparable turbulent metrics (*e.g.* energy spectra, temporal statistics) when compared to existing spectral methods.

This chapter is based on the publication [13]: P.L. Carroll and G. Blanquart. "The effect of velocity field forcing techniques on the Karman-Howarth equation." *Journal of Turbulence*. 15(7):429-448, 2014.

Although these methods are applied routinely in simulation studies to generate the same type of turbulent physics (*i.e.* isotropic turbulence), the methods themselves are quite disparate. They are derived from starkly differing assumptions and constraints. An in-depth analysis of the effect of these assumptions on the predicted turbulent physics has yet to be performed. The objective of this chapter is to perform such an analysis.

The effect of implementing a velocity field forcing method can be understood by examination of the Karman-Howarth (KH) equation. As originally derived, the KH equation governs the decay of an isotropic turbulent field [25]. As it is derived from the Navier-Stokes equations, to which velocity field forcing methods append a source term, it will have correspondingly a source term appended to it. In this study, the source terms appended to the Karman-Howarth equation by Lundgren's physical-space method and Alvelius' stochastic spectral method are calculated and investigated. From these source terms, the differences observed in the turbulent fields that the two velocity forcing methods predict are justified.

It should be noted that the subject of this chapter finds context in existing experimental and simulation studies [62, 2, 35] of decaying turbulence. These studies have focused on a corresponding unforced expression of the Karman-Howarth equation, and primary attention has been paid to the significance of the so-called non-stationary term; this term represents non-stationary effects on the turbulent field as caused by the temporal decay of the longitudinal second-order structure function (B_{ll}). It has been noted [2] that the presence of the non-stationary term precludes the calculated third-order structure function (B_{lll}) from ever exceeding the asymptotic limit of $-\frac{4}{5}\epsilon r$, as Kolmogorov's 4/5 law indicates [77], as the sign of the time derivative of B_{ll} is negative [35].

When the results obtained from such studies [62, 2, 35] were compared to structure function data calculated from numerically-forced (via low waveband spectral and linear methods) DNS, which correspond to a forced Karman-Howarth equation, three observations were made. First, the structure functions calculated from linearly-forced data sets more closely matched experimental data (decaying grid turbulence) than the low waveband, spectrally-forced structure function data [62, 2, 35]. Second, for a given Taylor-Reynolds number, Re_λ, the spectrally-forced structure function data displayed a larger B_{lll} magnitude across intermediate scales relative to the linearly-forced and experimentally-obtained data. Third, the compensated, spectrally-forced third-order structure function, $B_{lll}/(\epsilon r)$, was found to approach more rapidly (at lower Re_λ) the asymptotic limit of 4/5 than both experimentally-determined and linearly-forced data [2]. The disparities noted between the three sets of structure function data are generally attributed to the differences between the non-stationary term and the term corresponding to the forcing method-imposed source term. In the case of forced turbulence, the non-stationary effects are non-existent, as the presence of the momentum (and Karman-Howarth) source term eliminates any temporal decay of B_{ll}. These previous studies did not provide causes for the differences observed between the sets of third-order structure

function data. The present work seeks to provide this explanation in way of selecting an appropriate isotropic velocity field forcing method for implementation into the simulation framework to be presented in Chapter 5.

The structure of this chapter is as follows. Section 2.1 introduces the momentum source terms that Alvelius' and Lundgren's velocity forcing methods impose on the velocity field. The assumptions and restrictions on which these methods are based are explained, and their context relative to other existing forcing schemes is defined. Section 2.2 states the turbulent structure that should be expected under conditions of homogeneity and isotropy, and, then, compares this to the turbulent physics obtained from implementing the two forcing methods. Section 2.3 details the derivation of the (forced) Karman-Howarth equation when the two chosen velocity forcing methods are applied. Section 2.4 discusses the qualitative and quantitative behavior of the imposed Karman-Howarth source terms for large, intermediate, and small flow scales for both forcing methods. Lastly, Section 2.5 discusses the significance of the forcing method-imposed energy production spectrum in determining the behavior of the Karman-Howarth source term. Note that the simulation code used to perform the work contained in this chapter is detailed in Appendix 8.3, Appendix 8.4, Appendix 8.5, and Appendix 8.6 at the end of this document.

2.1 The Role of Velocity Forcing Methods

2.1.1 Preventing Turbulence Decay and Sustaining Stationarity

In terms of Richardson's energy cascade, energy is transfered from the large (inertial) scales to the small (viscous) scales. Without a source of turbulent kinetic energy, the velocity field fluctuations will decay, leading to the growth of the viscous scales and the loss of turbulent physics. In order to sustain turbulent physics and to drive the velocity field to a state of statistical stationarity, source (forcing) terms are applied to the momentum equations to serve as such turbulent kinetic energy sources. These forced momentum equations take the form,

$$\frac{\partial u_i}{\partial t} + u_j \frac{\partial u_i}{\partial x_j} = -\frac{1}{\rho}\frac{\partial P}{\partial x_i} + \nu \frac{\partial}{\partial x_j}\left(\frac{\partial u_i}{\partial x_j}\right) + f_i, \tag{2.1}$$

where f_i is the appended source term. Two available method classes for preventing turbulent velocity field decay are narrow-band spectral forcing in wave-space and forcing in physical-space. The analysis included in this chapter is concerned with two representative forcing methods, namely Alvelius' low waveband (spectral) forcing [1] and Lundgren's linear (physical) forcing [58, 81].

A forcing method sustains a turbulent state by compensating for temporal losses in turbulent kinetic energy, k. Multiplying Eq. 2.1 by u_i, assuming incompressibility and homogeneity, and

ensemble averaging (denoted by $\langle \cdot \rangle$) yields the turbulent kinetic energy equation,

$$\frac{dk}{dt} = -\epsilon + \langle u_i f_i \rangle \longrightarrow \frac{d\langle u^2 \rangle}{dt} = -\frac{2}{3}\epsilon + \frac{2}{3}\langle u_i f_i \rangle, \tag{2.2}$$

where $\epsilon = \langle \nu \frac{\partial u_i}{\partial x_j} \frac{\partial u_i}{\partial x_j} \rangle$, $\langle u^2 \rangle = \frac{1}{3}\langle u_i u_i \rangle$, and $k = \langle \frac{1}{2} u_i u_i \rangle$. From Eq. 2.2, the impact of the momentum source term is clear. At steady state, the momentum source term contribution, $\langle u_i f_i \rangle$, compensates for losses from viscous dissipation ($\epsilon = \langle u_i f_i \rangle$).

2.1.2 The Alvelius (Spectral) Velocity Field Forcing Method

Spectral velocity forcing techniques are attractive, as they allow for precise control over the location of energy injection. This injection can be concentrated within a small number of modes lying within a specified range of waveshells with magnitudes $\kappa_{low} \leq |\underline{\kappa}| \leq \kappa_{high}$; modes lying outside these waveshells are not impacted by the forcing term. Alvelius' spectral forcing scheme results in a momentum equation with a form similar to Eq. 2.1. The forcing term, $\hat{f}_i(\underline{\kappa})$, is solenoidal with a Gaussian distribution about a forcing wavenumber $\kappa_f = 3$,

$$\hat{f}_i(\underline{\kappa}) = \sqrt{\frac{P_1}{2\pi\kappa^2\sqrt{c\pi}\,\Delta t}}\ \exp\left(-\frac{(|\underline{\kappa}| - \kappa_f)^2}{2c}\right) g(\phi, \theta, \psi). \tag{2.3}$$

Here, the cubic computational domain has length 2π, $g(\phi, \theta, \psi)$ is a function of random variables ϕ, θ, and ψ used to promote a state of contrived isotropy, and $\kappa = |\underline{\kappa}|$ is the wavenumber corresponding the wavevector $\underline{\kappa}$. P_1 controls the amplitude of the overall momentum source term, while c determines the width of the Gaussian forcing spectrum. From the turbulent kinetic energy equation, it can be shown that $\epsilon = P_1$ at stationarity [1]. Alvelius' forcing method is discrete in nature, as indicated by the presence of the time-step, Δt, in the momentum source term. Note that the magnitude of the time-step is determined by the numerical stability conditions of the Navier-Stokes solver employed, which come primarily from the CFL (Courant-Friedrichs-Lewy) condition imposed. This momentum forcing term is active only within a narrow band of waveshells with magnitudes $2 \leq \kappa \leq 4$, and it is defined to be locally mutually orthogonal to the wavevector and to the velocity Fourier vector.

Alvelius' spectral forcing imposes strict constraints on the range of scales over which its momentum source term is active and the magnitude it can take. It was derived from a discrete, statistical perspective, and it is random in nature to promote isotropy. Additionally, the source term is designed to have a negligible effect on the convective, diffusive, and pressure terms in the Navier-Stokes equations when time-integrated. The time-scale imposed by the forcing term is separated from all flow time-scales [1]. It, therefore, neither imposes a time-scale nor alters the ones present.

2.1.3 The Lundgren (Linear) Velocity Field Forcing Method

More attractive from an implementation perspective is a physical-space forcing technique. Physical-space techniques can be integrated into non-spectral codes and can support non-periodic boundary conditions. Lundgren's linear forcing method [58] injects energy into the velocity field in proportion to the magnitude of the velocity field fluctuations, u_i, and it is active over all flow scales. When implemented, the source term appended to the momentum equation (Eq. 2.1) is $f_i = Qu_i$, where Q is a constant related to the velocity field eddy turn-over time, $\tau = (2Q)^{-1}$.

Lundgren's linear forcing term, Qu_i, imposes few constraints on the turbulent field it sustains. It is a broadband forcing method, and the magnitude of the momentum source term is modulated by the velocity field itself; hence, the power inserted into the turbulent kinetic energy equation will vary with each time-step. The only feature that it imposes on the flow [58, 81] is a time-scale via the constant coefficient $Q = (2\tau)^{-1}$, where $\tau = k/\epsilon$.

2.1.4 "Spectrum" of Other Velocity Field Forcing Methods

Lundgren's linear [58] and Alvelius' spectral [1] forcing methods are representative of the other available velocity field forcing methods used to generate isotropic turbulence. The most commonly-used method in simulation studies of stationary, isotropic turbulence is that developed by Eswaran and Pope [33], which imposes a momentum source term of the form,

$$\hat{f}_i(\underline{\kappa}, t) = \left(\delta_{ij} - \frac{\kappa_i \kappa_j}{\kappa^2}\right) w_j(\underline{\kappa}, t). \tag{2.4}$$

This forcing method relies on the summation of independent realizations of Uhlenbeck-Ornstein stochastic diffusion processes, $w_j(\underline{\kappa}, t)$, to create sufficient randomness for the development of an isotropic field. This source term is correlated in time with an imposed time-scale, T_L, which induces a correlation between the velocity field and forcing term [33]. Siggia and Patterson [87] developed a method in which the Fourier coefficients of the velocity field within the forcing waveband, $1 \leq \kappa \leq 2$, were frozen. This prevented the decay of the large scale physics and supported the development of an energy cascade. Alternatively, Sullivan *et al.* [89] deterministically froze the kinetic energy within the forcing waveshells at a constant value. This is accomplished by, at each time-step, scaling the Fourier coefficients of the forcing term, $\hat{a}_f(\underline{\kappa}, t)$, by a scalar multiple, c, of the Fourier coefficients of the velocity field, $\hat{u}(\underline{\kappa}, t)$, to compensate for deviations from the prior time-step [89],

$$\hat{a}_f(\underline{\kappa}, t) = c\hat{u}(\underline{\kappa}, t). \tag{2.5}$$

Other forcing methods are tuned to ensure that the energy spectrum has a nominal dependence on wavenumber, *i.e.* $E(\kappa) \propto \kappa^{-5/3}$ [17]. Generally, this is accomplished by fixing the ratio of energy

content in the different low wavenumber waveshells to be consistent with the $\kappa^{-5/3}$ dependence [17].

In summary, the parameter space spanned by existing forcing methodologies is multi-dimensional; parameters between which forcing methods can vary include the flow variable with which the momentum forcing term is aligned (if any), the temporal correlation of the forcing term (if any), and the span of wavespace over which it is active. The alternative spectral methods briefly highlighted and Alvelius' method all revolve around low wavenumber energy injection. The chief distinguishing characteristic between them lies in the correlation of their respective forcing terms with differing simulation parameters. Alternatively, Lundgren's method is broadband, and it corresponds to a distinctly different class of forcing approach. Thus, the behaviors that other velocity forcing methods would impose on the Karman-Howarth equation can be, at the very least, qualitatively represented by those imposed by Alvelius' spectral and Lundgren's linear forcing techniques.

2.2 Canonical Isotropic Turbulence *vs.* Forcing-predicted Turbulence

Under high Reynolds number conditions, there is scale separation between the energy containing and dissipating scales. This separation creates an inertial subrange, across which the dynamics are inviscid. Under such conditions, isotropic turbulence displays characteristic scalings. Within the inertial subrange, these behaviors include an energy spectrum scaling, $E(\kappa) \propto \kappa^{-5/3}$; a vanishing transfer spectrum, $T(\kappa) = 0$; and second- and third-order structure function scalings, $B_{ll}(r) = C_K (\epsilon r)^{2/3}$ and $B_{lll}(r) = -\frac{4}{5}\epsilon r$. These metrics are calculated for both forcing methods and compared to the canonical behaviors stated. The theoretical bases of these scaling arguments are provided in Appendix 8.1.

2.2.1 Configuration Setup

To compare the turbulent fields predicted under Lundgren's and Alvelius' forcing methods, a simulation study was conducted. The turbulence is maintained at $Re_\lambda = \langle u^2 \rangle^{1/2}\lambda/\nu = 140$ with a spatial resolution of $\kappa_{max}\eta \geq 1.5$ on a $N^3 = 512^3$ grid within a triply periodic cubic domain of length 2π. The non-dimensional kinematic viscosity was 0.0075 and 0.0028 for linear and Alvelius forcing, respectively. This Taylor-Reynolds number is of comparable magnitude to those that have been experimentally attained (*e.g.* the experiments of Gagne [36] and Mydlarski [65]).

The code package used is NGA [26], which is a physical-space (non-spectral) code suitable for low Mach number flows and uses a standard staggered grid. The staggering of the velocity components results in superior effective wavenumber behavior under second-order discretization [26, 64]. The velocity field is solved implicitly via a second-order finite-difference scheme that is discretely energy

conserving in the velocity field. The combination of staggered variables and discrete energy conservation renders the advantages of a higher order velocity solver negligible. The time advancement is by a semi-implicit Crank-Nicolson method [26]. Further details on the simulation code can be found is Appendix 8.3 - Appendix 8.6. In the results to be presented, data is averaged over no less than five eddy turn-over times, τ. In Section 2.4, the Karman-Howarth equation source terms for the two forcings will be compared directly and used to explain partially the results that follow.

2.2.2   Energy Spectra

First, the energy spectra for the turbulent fields produced by both forcing methods are calculated. The results are displayed in Fig. 2.1 and Fig. 2.2, along with a slightly modified version of the model spectrum put forth by Pope [77]. This model spectrum is,

$$E(\kappa) = C\epsilon^{2/3}\kappa^{-n}f_L(\kappa L)f_\eta(\kappa\eta),$$
$$f_\eta(\kappa\eta) = \exp\left(-\beta\{\left((\kappa\eta)^4 + c_\eta^4\right)^{1/4} - c_\eta\}\right),$$
$$f_L(\kappa L) = \left(\frac{\kappa L}{\left((\kappa L)^2 + c_L\right)^{1/2}}\right)^{11/3}, \tag{2.6}$$

where C is a constant, L is a length-scale defined as $L = k^{3/2}/\epsilon$, and $c_\eta = 0.2$, $\beta = 4.7$, and $c_L = 6.78$ are constants determined by Re_λ [77]. This model spectrum is used to determine the power-law scaling of the energy spectrum, n, across the intermediate wavenumber region by performing a least squares fit. The power-law scaling is a free parameter. The quality of the fit is confirmed by computing the L_2 norm of the fit (denoted by E_{model}) relative to the calculated energy spectrum. This norm is calculated by,

$$L_2 = ||r||_2 = \left(\sum_{i=1}^{n} |E_{model}(\kappa) - E(\kappa)|^2\right)^{1/2}.$$

Following this, the average square of the error is found to be less than 1% of the value of the total turbulent kinetic energy in both cases.

Upon (least squares) curve-fitting the dissipative region of the DNS-obtained energy spectra, it was determined that the Alvelius-produced spectrum displays very nearly a $E(\kappa) \propto \kappa^{-5/3}$ scaling across this region ($n = 5/3$ in Eq. 2.6), while the linearly-forced spectrum displays the weaker scaling of $E(\kappa) \propto \kappa^{-1.42}$ ($n = 1.42$ in Eq. 2.6). These power-law scalings are confirmed by compensating the respective spectra, as depicted in Fig. 2.2; these compensated spectra both contain an approximately horizontal (flat) region, which verifies the appropriateness of the determined energy spectrum scalings. In the case of the linearly-forced data, the weaker wavenumber scaling found relative to $-5/3$ is

consistent with experimentally-inferred spectrum scalings attained at comparable Re_λ [65, 36, 62]. Specifically, following the work of Mydlarski and Warhaft [65], a power-law scaling of approximately $E(\kappa) \propto \kappa^{-1.5}$ is expected for a $Re_\lambda \approx 140$.

To aid in interpretation of Fig. 2.1, two length-scales are included. Here, l_{EI} is a characteristic length for the energy-containing scales and l_{DI} represents the characteristic length for dissipation processes. Following Pope [77], these scales are determined as follows. The spherical waveshell at which 90% of the total (cumulative) turbulent kinetic energy has been attained defines l_{EI}^{-1}. Similarly, the spherical waveshell in wavespace at which 10% of the total (cumulative) energy dissipation has occurred defines l_{DI}^{-1}. In theory, these scales bookend the region of the flow, l, over which an inertial subrange may manifest (i.e. $l_{DI} < l < l_{EI}$). Per Fig. 2.1, there is no scale separation at this moderate Re_λ in either data set, as $l_{EI} < l_{DI}$.

As the Alvelius-generated spectrum exhibits a desired power-law trending ($E(\kappa) \propto \kappa^{-5/3}$), as do most spectral forcing methods, spectral methods are generally the preferred methods in numerical studies of turbulent physics. However, this tends to conflict with the lack of scale separation indicated by the calculated l_{DI} and l_{EI}.

2.2.3 Transfer Spectra

The transfer spectra for the two forcing methods were calculated, and these spectra are depicted in Fig. 2.3 and Fig. 2.4 with their dissipation spectra, $D(\kappa) = 2\nu\kappa^2 E(\kappa)$. The scales l_{DI} and l_{EI} are provided to suggest the vicinity in wavespace where an inertial subrange (if any) may be located. The transfer spectra were calculated as,

$$T(\kappa,t) = -\hat{u}_i^* \mathscr{F}\left(u_j \frac{\partial u_i}{\partial x_j}\right). \tag{2.7}$$

Under inviscid conditions, the transfer spectrum, $T(\kappa,t)$, should have a value of zero within the inertial subrange [79]. The implications of $T(\kappa) = 0$ can be understood by considering the spectral-space version of the energy equation,

$$\frac{dE(\kappa)}{dt} = P(\kappa) + T(\kappa) - D(\kappa), \tag{2.8}$$

where $E(\kappa)$, $P(\kappa)$, and $D(\kappa)$ are the energy, production, and dissipation spectra, respectively. For statistically stationary forced turbulence, $dE(\kappa)/dt = 0$. In that case, $T(\kappa) = 0$ only if there is no overlap between $P(\kappa)$ and $D(\kappa)$ across the inviscid scales. This observation, although obvious, has implications for where a velocity forcing method should deposit energy in wavespace.

At this moderate $Re_\lambda = 140$, finite Reynolds number effects are significant, and the behaviors stated in the introduction to this section should not be obtained. From Fig. 2.3, inviscid scales are
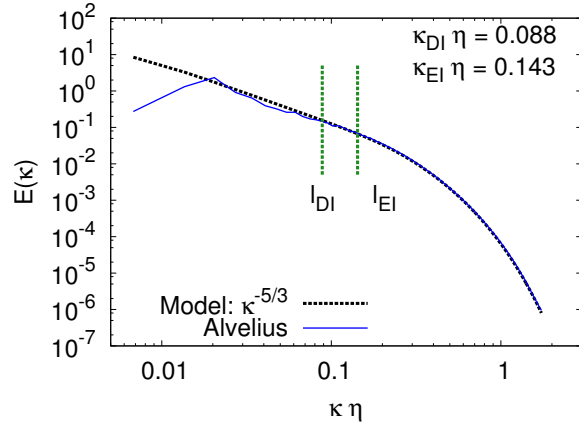
(a) Alvelius *vs.* model spectrum
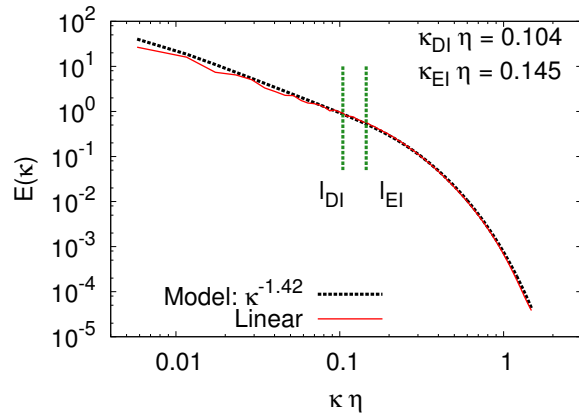
(b) Linear *vs.* model spectrum

Figure 2.1: Comparison of forcing-generated energy spectra with a modified form of Pope's model spectrum [77] (Eq. 2.6). l_{EI} and l_{DI} represent the length-scales demarking the end (beginning) of the energy-containing (dissipative) flow scales.
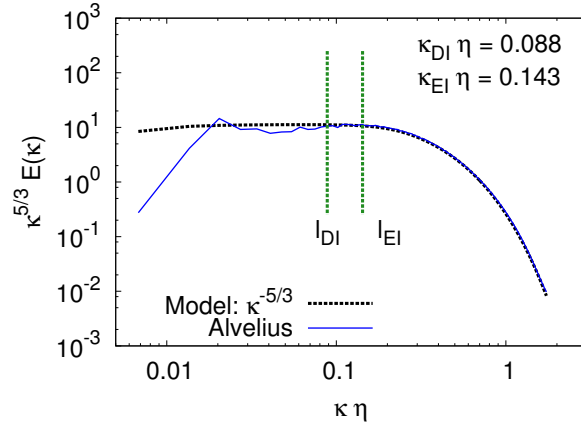
(a) Alvelius *vs.* model spectrum
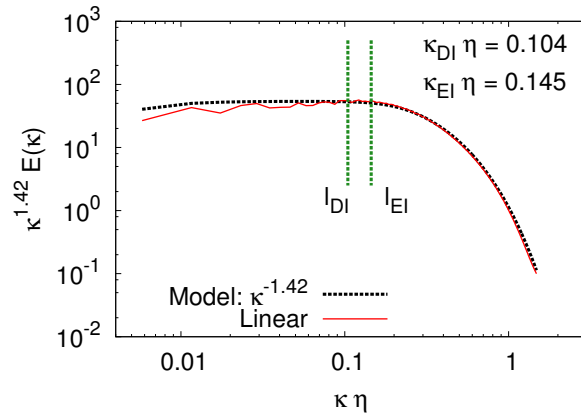
(b) Linear *vs.* model spectrum

Figure 2.2: Comparison of compensated forcing-generated energy spectra with a modified form of Pope's model spectrum [77] (Eq. 2.6). l_{EI} and l_{DI} represent the length-scales demarking the end (beginning) of the energy-containing (dissipative) flow scales.
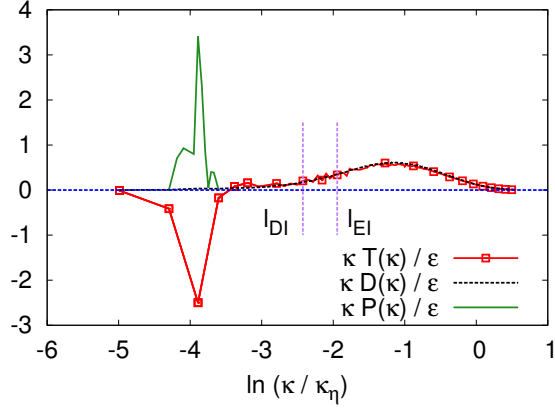
(a) Alvelius forcing
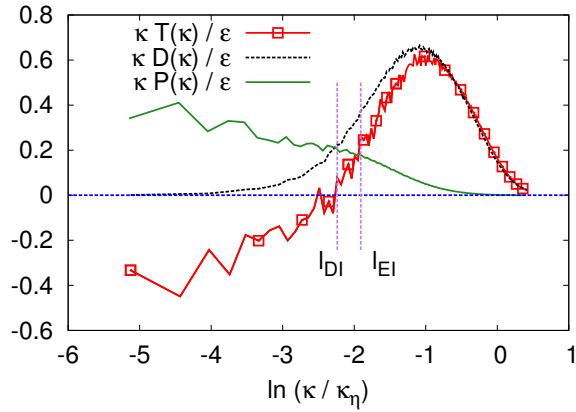
(b) Linear forcing

Figure 2.3: Transfer spectra normalized by wavenumber and inverse dissipation rate. l_{EI} and l_{DI} represent the length-scales demarking the end (beginning) of the energy-containing (dissipative) flow scales. Note that the Kolmogorov scales for the linearly- and Alvelius-forced data sets are $\eta = \left(\nu^3/\epsilon\right)^{1/4} = 0.0058$ and $\eta = 0.0068$, respectively.

not present under the linear forcing method, as the production and dissipation spectra overlap. This is shown more clearly in Fig. 2.4. Alternatively, Fig. 2.3(a) (and Fig. 2.4(a)) suggests an apparent scale separation between the production and dissipation spectra under Alvelius' forcing method, where the transfer spectrum is constant at almost zero $(-3.5 < \ln(\kappa/\kappa_\eta) < -2.5)$. This is roughly the same range of scales over which the energy spectrum shows a $\kappa^{-5/3}$ scaling (Fig. 2.1(a) and Fig. 2.2(a)). This question as to where energy is injected is investigated further in Sections 2.4 and 2.5.
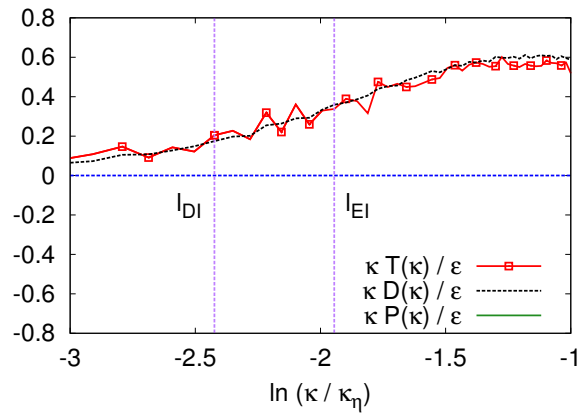
(a)   Alvelius forcing
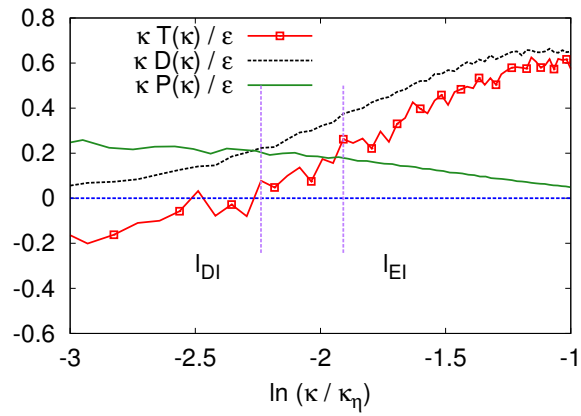
(b)   Linear forcing

Figure 2.4: Enlarged view of the region bounded by l_{DI} and l_{EI} in the compensated transfer spectra shown in Fig. 2.3.

2.2.4 Structure Functions

The second- and third-order longitudinal structure functions are evaluated for both data sets according to the definition,

$$B_{ll}(r,t) = \langle (u_l(x+r\underline{l},t) - u_l(x,t))^2 \rangle,$$
$$B_{lll}(r,t) = \langle (u_l(x+r\underline{l},t) - u_l(x,t))^3 \rangle, \tag{2.9}$$

where u_l is the velocity component aligned in the direction of unit vector, $\underline{l}$. The compensated versions for the two cases are provided in Fig. 2.5. The similarity between linear and Alvelius forcing method-produced B_{ll} and B_{lll} at the small scales ($r < 20\eta$) and the considerable divergence elsewhere is clear. Following Fig. 2.3, there is no inviscid subrange at the moderate Reynolds number considered in this study. Consistently, Fig 2.5(b) clearly shows that there is no 4/5 plateau in B_{lll}. Both forcing methods produce turbulent fields with compensated $B_{lll}(r)$ that are well below 4/5, although the curve corresponding to Alvelius' forcing method is of a greater magnitude.

The normalized second-order longitudinal structure functions should be interpreted based on the presence (or lack) of a plateau across the intermediate scales ($B_{ll}/(\epsilon r)^{2/3} = C_K$) and the absolute value at which this plateau occurs. Experiments [82] have reported an approximate value of $C_K = 2.0$, with some arguing [77] that this value can vary by $\pm 15\%$. If there is a $C_K = 2.0 \pm 15\%$ region in the second-order structure function data, then, Kolmogorov's 4/5 law should be present in the third-order structure function. As a result, observation of Fig 2.5(a) raises concern. The compensated B_{ll} for linear forcing lacks a plateau near the $C_K = 2.0$ benchmark, consistent with its lack of a 4/5 plateau in its compensated B_{lll}. Alternatively, the compensated B_{ll} for Alvelius forcing has a region that falls within the $C_K = 2.0 \pm 15\%$ window over a short range of intermediate scales. As B_{ll} is related to $E(\kappa)$[77], this result is consistent with the observed $-5/3$ energy spectrum scaling. However, these results are inconsistent with the absence of a 4/5 plateau for $B_{lll}(r)$. It should be here noted that, irrespective of the forcing method employed, the Reynolds number is too low in these cases to attain a physically meaningful self-similar energy spectrum scaling of $\kappa^{-5/3}$ [79, 80]. Hence, the compensated structure functions should not be exhibiting their inviscid scaling behaviors. It follows that the Alvelius spectral forcing method needs to be further investigated.

2.2.5 Summary of Observations

In summary, when analyzing the linearly-forced turbulent field, all turbulent metrics are self-consistent and in qualitative agreement with experimentally-measured data [65] of decaying grid turbulence under the same Re_λ conditions. However, the turbulent statistics extracted from the Alvelius-forced fields may be inconsistent. The third-order structure function, $B_{lll}(r)$, and the over-
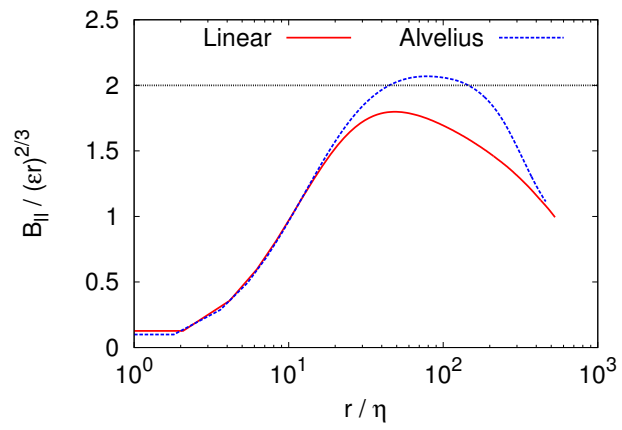
(a)   Second-order structure function
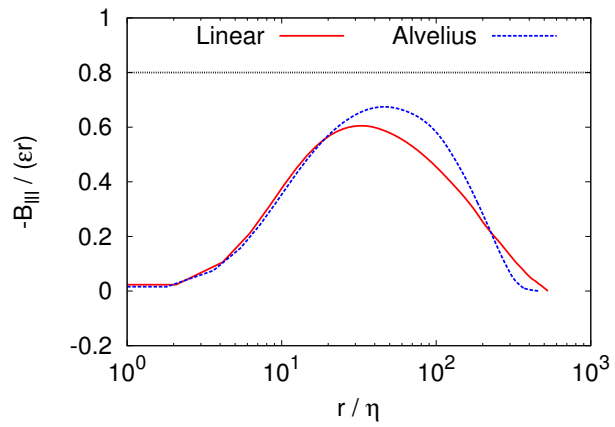
(b)   Third-order structure function

Figure 2.5: Normalized structure functions.

lap of the energy-containing and dissipative scales, l_{EI} and l_{DI}, suggest a lack of an inertial range, while the transfer spectrum, $T(\kappa)$, and second-order structure function, $B_{ll}(r)$, suggest its presence. Following these observations, in the next sections, the specific forms of the Karman-Howarth source terms, $S(r)$, imposed by these two representative methods are expressed, and the behaviors of these source terms are investigated.

2.3 Derivation of the Forced Karman-Howarth Equation

2.3.1 Overview of the Original (Unforced) Karman-Howarth Equation

The Karman-Howarth equation, published by Karman and Howarth in 1938 [25], describes the evolution of the longitudinal velocity correlation function, $f(r,t)$, under conditions of decaying, isotropic turbulence. It is derived from the momentum and continuity equations using assumptions of incompressibility, isotropy, and homogeneity. It can be expressed as,

$$\frac{\partial \left(\langle u^2 \rangle f \right)}{\partial t} = \langle u^2 \rangle^{3/2} \left(\frac{\partial h}{\partial r} + \frac{4}{r} h \right) + 2\nu \langle u^2 \rangle \left(\frac{\partial^2 f}{\partial r^2} + \frac{4}{r} \frac{\partial f}{\partial r} \right), \tag{2.10}$$

where $\langle u^2 \rangle$ is the velocity field variance and h is a scalar function of the two-point separation distance, r, that is related to the longitudinal triple velocity correlation function, $S_{111} = \langle u^3 \rangle (t) h(r,t)$; its full derivation is provided in Appendix 8.2.

This expression was recast by Monin and Yaglom [63] in terms of the second- and third-order longitudinal structure functions per Eq. 2.9. Structure functions describe the correlation of the velocity differences between two different fluid points separated by a distance of magnitude r. Note that the velocity component, u_l, is in the direction of the unit vector, $\underline{l}$. By applying the identity,

$$\frac{1}{2} B_{ll}(r,t) = \langle u^2 \rangle \left(f(0,t) - f(r,t) \right) = \langle u^2 \rangle \left(1 - f(r,t) \right), \tag{2.11}$$

Monin and Yaglom obtained a structure function-based representation of the decay of turbulence under isotropic conditions, which is given by,

$$\frac{d\langle u^2 \rangle}{dt} - \frac{1}{2} \frac{\partial B_{ll}(r,t)}{\partial t} = \frac{1}{6r^4} \frac{\partial \left(r^4 B_{lll}(r,t) \right)}{\partial r} - \frac{\nu}{r^4} \frac{\partial}{\partial r} \left(r^4 \frac{\partial B_{ll}(r,t)}{\partial r} \right). \tag{2.12}$$

This is the original version of the Karman-Howarth equation in structure function form.

2.3.2 General Form of the Forced Karman-Howarth Equation

In the context of forced turbulence, where energy decay is prevented, the Karman-Howarth (KH) equation is altered by the presence of a momentum source term, leading to an augmented (forced)

Karman-Howarth equation. Equation 2.1 can be written in symbolic form as,

$$\frac{\partial u_i}{\partial t} = T_i + f_i, \tag{2.13}$$

where all convective, viscous, and pressure terms are contained in T_i. The time derivative of the correlation function can be calculated as,

$$\frac{\partial R_{ii}(\underline{r}, t)}{\partial t} = \langle u_i(\underline{x}, t) T_i(\underline{x}', t) + u_i(\underline{x}', t) T_i(\underline{x}, t) \rangle + \langle u_i(\underline{x}, t) f_i(\underline{x}', t) + u_i(\underline{x}', t) f_i(\underline{x}, t) \rangle, \tag{2.14}$$

from which the time derivative of the longitudinal correlation function, $\frac{\partial \langle u^2 \rangle f(r,t)}{\partial t}$, can be evaluated. Recall the relation between these two derivatives,

$$\frac{\partial R_{ii}(\underline{r}, t)}{\partial t} = 3 \frac{\partial \left(\langle u^2 \rangle f(r, t) \right)}{\partial t} + r \frac{\partial}{\partial r} \left(\frac{\partial \left(\langle u^2 \rangle f(r, t) \right)}{\partial t} \right). \tag{2.15}$$

Lundgren [58] solved Eq. 2.15 for the needed time derivative via an integration-by-parts procedure, yielding

$$\frac{\partial \left(\langle u^2 \rangle f(r, t) \right)}{\partial t} = \frac{1}{r^3} \int_0^r r^2 \frac{\partial R_{ii}(\underline{r}, t)}{\partial t} \, dr. \tag{2.16}$$

Using Eq. 2.16, the first and second terms on the right hand-side of Eq. 2.14 lead to the unforced KH equation (Eq. 2.10). The third and fourth terms on the right hand-side of Eq. 2.14, which will be referred to as $\partial R_{ii}^*(\underline{r}, t) / \partial t$, contain the contribution from the momentum source term, and result in a source term addition to the KH equation. Under the condition of statistical stationarity, the new, forced Karman-Howarth equation can be expressed as,

$$0 = \frac{1}{6r^4} \frac{\partial \left(r^4 B_{lll}(r) \right)}{\partial r} - \frac{\nu}{r^4} \frac{\partial}{\partial r} \left(r^4 \frac{\partial B_{ll}(r)}{\partial r} \right) + S(r), \tag{2.17}$$

with $S(r)$ evaluated as,

$$S(r) = \frac{1}{r^3} \int_0^r r^2 \frac{\partial R_{ii}^*(\underline{r}, t)}{\partial t} dr. \tag{2.18}$$

Depending on the velocity field forcing method (momentum source term) implemented, different turbulent physics may be produced, as the KH source term may vary. It is important, therefore, to understand how different methods affect $S(r)$. It is interesting to note the value of $S(r = 0)$. Using Eq. 2.2, it is found that $S(r = 0) = \frac{2}{3}\epsilon$ regardless of the forcing method implemented.

2.3.3   The Linear Forcing and the Resulting Karman-Howarth Equation

Following a process outlined by Lundgren [58] and the above discussion, $S(r)$ is evaluated as,

$$S(r) = \frac{1}{r^3} \int r^2 \langle u_i f_i' + u_i' f_i \rangle dr = \frac{2Q}{r^3} \int_0^r r^2 \langle u_i u_i' \rangle dr = \frac{2Q}{r^3} \int_0^r r^2 R_{ii}(\underline{r}) dr, \tag{2.19}$$

with $f_i = Q u_i$ and $r = |\underline{r}|$. Further, $R_{ii}(\underline{r})$ can be written as [58, 77],

$$R_{ii}(\underline{r}) = 3\langle u^2 \rangle - \frac{1}{2r^2} \frac{\partial}{\partial r} \left(r^3 B_{ll}(r) \right). \tag{2.20}$$

Inserting Eq. 2.20 into Eq. 2.19 results in an expression which can be integrated to,

$$S(r) = 2Q\langle u^2 \rangle - Q B_{ll}(r). \tag{2.21}$$

Using $2Q\langle u^2 \rangle = \frac{2}{3}\epsilon$ and Eq. 2.21, the forced Karman-Howarth equation under the linear forcing method is obtained,

$$0 = \frac{1}{6r^4} \frac{\partial \left(r^4 B_{lll}(r) \right)}{\partial r} - \frac{\nu}{r^4} \frac{\partial}{\partial r} \left(r^4 \frac{\partial B_{ll}(r)}{\partial r} \right) + \frac{2}{3}\epsilon - Q B_{ll}(r). \tag{2.22}$$

2.3.4   The Alvelius Forcing and the Resulting Karman-Howarth Equation

The forced Karman-Howarth equation under Alvelius' forcing method is obtained in a slightly different way due to its discretized implementation [1]. As a consequence of its stochastic and discrete implementation, the velocity field is not differentiable in time. However, the expectation values of the velocity field (used here) still remain differentiable in time.

The source term is derived from the following procedure. Following Alvelius [1], the Navier-Stokes equations at two different fluid points can be discretized according to,

$$u_i(\underline{x})^{n+1} = u_i(\underline{x})^n + \Delta t \left(T_i(\underline{x})^n + f_i(\underline{x})^n \right),$$
$$u_j(\underline{x}')^{n+1} = u_j(\underline{x}')^n + \Delta t \left(T_j(\underline{x}')^n + f_j(\underline{x}')^n \right), \tag{2.23}$$

where $T(\underline{x})^n$ represents the transport terms (convective, diffusive, and pressure gradient). The time derivative of the two-point velocity correlation tensor can be written discretely in time at successive timesteps n and $n+1$,

$$\begin{aligned}
\frac{\partial R_{ij}(\underline{r}, t)}{\partial t} = \frac{\partial \langle u_i(\underline{x}, t) u_j'(\underline{x}', t) \rangle}{\partial t} &= \lim_{\Delta t \to 0} \frac{\Delta R_{ij}(\underline{r}, t)}{\Delta t} \\
&= \lim_{\Delta t \to 0} \frac{1}{\Delta t} \left(\langle u_i(\underline{x}, t) u_j(\underline{x}', t) \rangle^{n+1} - \langle u_i(\underline{x}, t) u_j(\underline{x}', t) \rangle^n \right).
\end{aligned} \tag{2.24}$$

Upon substitution of Eq. 2.23 into Eq. 2.24, a discrete equation for $\partial R_{ii}(\underline{r},t)/\partial t$ is obtained (Eq. 2.25), which can be thought of as the discretized version of the (not yet volume integrated) forced Karman-Howarth equation.

$$\frac{\Delta R_{ii}(\underline{r},t)}{\Delta t} = \langle u_i(\underline{x})T_i(\underline{x}') + u_i(\underline{x}')T_i(\underline{x})\rangle^n + \Delta t\langle T_i(\underline{x})T_i(\underline{x}')\rangle^n + \Delta t\langle f_i(\underline{x})f_i(\underline{x}')\rangle^n$$
$$+ \langle u_i(\underline{x})f_i(\underline{x}') + u_i(\underline{x}')f_i(\underline{x})\rangle^n + \Delta t\langle T_i(\underline{x})f_i(\underline{x}') + T_i(\underline{x}')f_i(\underline{x})\rangle^n \quad (2.25)$$

Accordingly, the left hand-side of Eq. 2.12 is related to $\Delta R_{ii}(\underline{r},t)/\Delta t$. Since this is forced (stationary turbulence), this term will be necessarily zero.

As with the continuous case, the right hand-side of Eq. 2.12 corresponds to the first terms of the right-hand side of Eq. 2.25 ($\langle u_i(\underline{x})T_i(\underline{x}') + u_i(\underline{x}')T_i(\underline{x})\rangle^n$). Thus, the Karman-Howarth source term is contained in the remaining five terms. In the limit of $\Delta t \to 0$, the second and fifth terms ($\Delta t\langle T_i(\underline{x})T_i(\underline{x}')\rangle^n$ and $\Delta t\langle T_i(\underline{x})f_i(\underline{x}') + T_i(\underline{x}')f_i(\underline{x})\rangle^n$) vanish. Further, Alvelius' forcing method imposes mutual orthogonality between the velocity vector and the forcing term. Thus, the fourth term ($\langle u_i(\underline{x})f_i(\underline{x}') + u_i(\underline{x}')f_i(\underline{x})\rangle^n$) vanishes. With these observations and the relation that $f_i \propto \Delta t^{-1/2}$ [1], it can be concluded that the imposed Karman-Howarth source term is given by,

$$S(r) = \frac{1}{r^3}\int_0^r r^2 \lim_{\Delta t\to 0}\ \Delta t\langle f_i(\underline{x})f_i(\underline{x}')\rangle^n\ dr. \quad (2.26)$$

The analysis to this point has relied on the real-space version, $f_i(\underline{x})$, of the momentum source term's spectral form, $\hat{f}_i(\underline{\kappa})$. When Fourier-transformed, $f_i(\underline{x})$ and $f_i(\underline{x}')$ from Eq. 2.3 admit the same Fourier vector, $\hat{f}_i(\underline{\kappa})$, as the shift between $\underline{x}$ and $\underline{x}'$ corresponds to multiplication by $\exp(i\underline{\kappa}\cdot\underline{r})$. The momentum source terms are, then, related by,

$$f_i(\underline{x})^n = \sum_{\underline{\kappa}} \hat{f}_i(\underline{\kappa})^n \exp(i\underline{\kappa}\cdot(\underline{x}'-\underline{r})) \qquad f_i(\underline{x}')^n = \sum_{\underline{\kappa}} \hat{f}_i^*(\underline{\kappa})^n \exp(-i\underline{\kappa}\cdot\underline{x}'). \quad (2.27)$$

After ensemble averaging and using spatial homogeneity, it is obtained,

$$\langle f_i(\underline{x})^n f_i(\underline{x}')^n\rangle = \sum_{\underline{\kappa}} \hat{f}_i(\underline{\kappa})^n \hat{f}_i^*(\underline{\kappa})^n \exp(-i\underline{\kappa}\cdot\underline{r}) = \sum_{\underline{\kappa}} |f_i(\underline{\kappa})^n|^2 \exp(-i\underline{\kappa}\cdot\underline{r}). \quad (2.28)$$

By performing a summation in wavespace over all forcing mode wavevectors and inverse Fourier-transforming this waveshell-averaged source term, the discrete-space equivalent of Eq. 2.18 is attained,

$$S(r) = \frac{1}{r^3}\int_0^r r^2 \left(\langle \mathscr{F}^{-1}\left(\sum_{\underline{\kappa}} |f_i(\underline{\kappa})^n|^2\right)\rangle\Delta t\right) dr, \quad (2.29)$$

and this is the source term appended to Eq. 2.17.

2.4 Behavior of the Karman-Howarth (KH) Source Terms

Calculated structure function data suggests that the velocity fields produced by these two forcing methods are similar at the small, viscous scales and different at the intermediate and large scales. In this section, analysis is conducted into their Karman-Howarth equation source terms to explain this observation.

2.4.1 Source Terms

The source terms, $S(r)$, that the two forcing methods append to the Karman-Howarth equation are evaluated using Eq. 2.21 and Eq. 2.29, and the results are provided in Fig. 2.6. A discussion of the source term behavior at small and large scales is contained in the following sub-sections. However, a few macroscopic comments are made first. Figure 2.6 suggests that the two forcing methods affect the turbulent field similarly at small scales ($r/\eta < 5$), but have significantly different effects at intermediate and large scales ($r/\eta > 5$). A key feature of Fig. 2.6 is that, as $r \to 0$, the source terms assume a value of $\frac{2}{3}\epsilon$.

Outside of the small-scale region, the source terms deviate from $\frac{2}{3}\epsilon$. This is a direct result of their form; both presented source terms take the form of autocorrelation functions, as stated in Eq. 2.21 and Eq. 2.29. The autocorrelation is between velocity components in the case of linear forcing and between the momentum source terms in the case of Alvelius' forcing. It is expected that there is high velocity correlation at small displacements, which becomes weaker as separation increases. This explains the decline of the linear forcing KH source term. With Alvelius' forcing, there is a similar initial decrease in magnitude, which is expected due to the finite bandwidth over which forcing is active. The increase in correlation at large separation ($r > 2$) is due to the injection of energy at these large scales.

Further insight can be obtained by considering the different terms of the statistically steady, forced Karman-Howarth equation derived for each forcing (Eq. 2.17). Here, a balance exists between the inertial, viscous, and source terms. Figure 2.7 displays each term as a function of separation distance, r. From this perspective, three distinct regions can be identified. First, there is a small-scale region ($0 < r < 10\eta$) that is dominated by viscosity and affected primarily by $B_{ll}(r)$. Second, there is an intermediate region ($10\eta < r < 0.5l_0$) that is influenced by both $B_{ll}(r)$ and $B_{lll}(r)$; here, $l_0 = \langle u^2 \rangle^{3/2}/\epsilon$ is the integral length-scale of the velocity field, which, in the case of Lundgren's linear forcing at this Re_λ is approximately 20% of the computational domain, and in the case of Alvelius' forcing is approximately 25% of the computational domain. Third, there is a large-scale region ($r > 0.5l_0$) dominated by inertial processes and affected primarily by $B_{lll}(r)$. The role of $B_{ll}(r)$ and
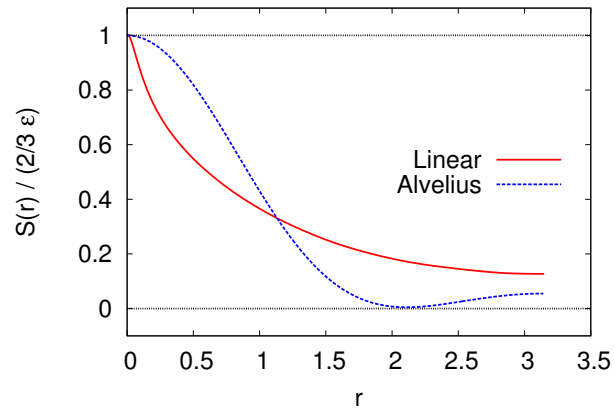
(a)   Large-scale behavior
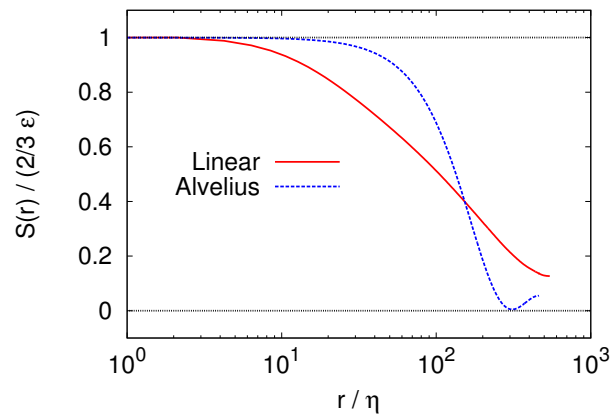
(b)   Small-scale behavior

Figure 2.6: Behavior of forcing method-imposed source terms. One half of the computational domain is plotted, $r = [0, \pi]$.
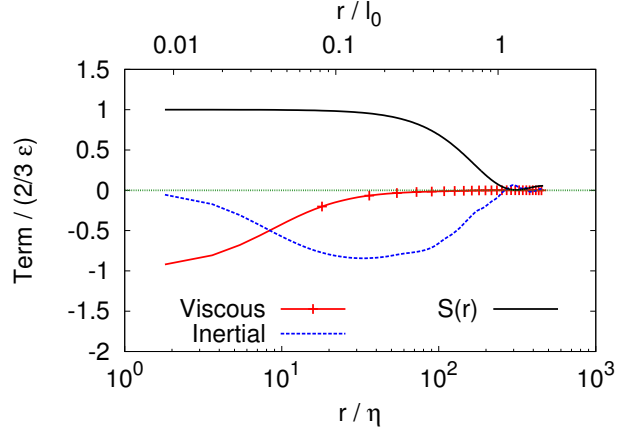
(a)   Alvelius forcing method
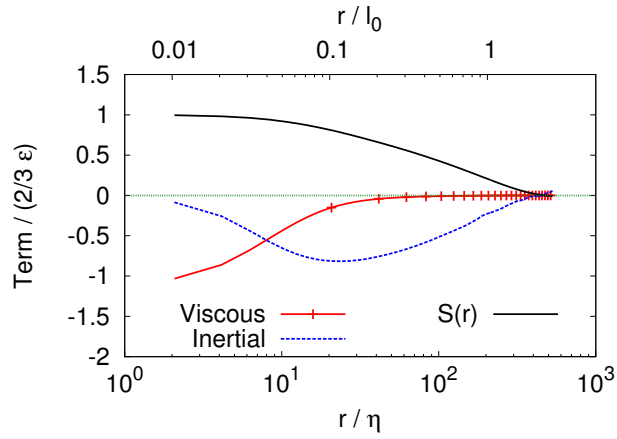
(b)   Linear forcing method

Figure 2.7: Behavior of the three terms in the stationary forced Karman-Howarth equation (Eq. 2.17). One half of the computational domain is plotted, $r = [0, \pi]$.

$B_{lll}(r)$ over these three regions is to compensate for $S(r)$. This suggests that the structure functions adjust to the dictates of the imposed source term. From a global perspective, $S(r)$ impacts B_{ll} and B_{lll}, which, in turn, influence $E(\kappa)$ and $T(\kappa)$.

2.4.2   Behavior in the Small (Viscous) Scales

At the small scales, the forced Karman-Howarth equation can be examined with a series expansion. Assuming a generic velocity forcing method, the structure functions and KH source term can be

Taylor-expanded for small arguments, r, as

$$B_{ll}(r) = \sum_{n=1}^{\infty} a_n r^{2n} = a_1 r^2 + a_2 r^4 + ...$$

$$B_{lll}(r) = \sum_{n=1}^{\infty} b_n r^{2n+1} = b_1 r^3 + b_2 r^5 + ...$$

$$S(r) = \sum_{n=0}^{\infty} s_n r^{2n} = s_1 + s_2 r^2 + s_3 r^4 + ... \tag{2.30}$$

where the even or odd nature of the expressions is used. By definition (Eq. 2.9), expansions of $B_{ll}(r)$ and $B_{lll}(r)$ are parabolic and cubic to leading order, respectively.

For both forcing methods, the initial term in the series expansion of the KH source term, s_1, can be specified from Eq. 2.2 and Eq. 2.21 as $s_1 = \frac{2}{3}\epsilon$. Substituting this relation and the other expansions into the stationary Karman-Howarth equation results, to leading order, in a balance between the viscous and source terms; the inertial term, as expected, does not play a role. Upon matching the leading order terms, the first coefficient for $B_{ll}(r)$ can be evaluated as $a_1 = \frac{1}{15}\epsilon/\nu$. This result is valid for both the linear and the Alvelius forcing methods, as the a_1 term corresponds to the s_1 term.

Under isotropic conditions, the dissipation rate is defined as $\epsilon = 15\nu\langle u^2\rangle/\lambda_g^2$, where λ_g is the transverse Taylor micro-scale. With this, the significance of a_1 becomes clear. In terms of these parameters, it can be written $a_1 = \epsilon/15\nu = \langle u^2\rangle\lambda_g^{-2}$, which is the inverse time-scale (squared) appropriate for small-scale physics. Further, the scaling for $B_{ll}(r)$ becomes,

$$B_{ll}(r) = \langle u^2\rangle\frac{r^2}{\lambda_g^2}. \tag{2.31}$$

This is sufficient to capture the behavior of $B_{ll}(r)$ in this small-scale limit (Fig. 2.8(a)). This finding suggests that the small turbulent length-scales are not affected detrimentally by either forcing technique. Instead, they only enforce the physically appropriate length- and time-scales.

2.4.3 Behavior at Intermediate (Pseudo-Inviscid) and Large (Inertial) Scales

Across the intermediate and large flow scales, the source term behaviors differ starkly. To explain this, the asymptotic trends of the source terms are examined.

2.4.3.1 Linearly-Forced Turbulent Field Results

When the series expansion of $B_{ll}(r)$ is inserted into $S(r)$ (Eq. 2.21), and the appropriate polynomial powers matched, it can be shown that $s_2 = -\left(\frac{1}{3}\epsilon/\langle u^2\rangle\right)a_1 = -\epsilon^2/(45\nu\langle u^2\rangle)$. At small scales, then,
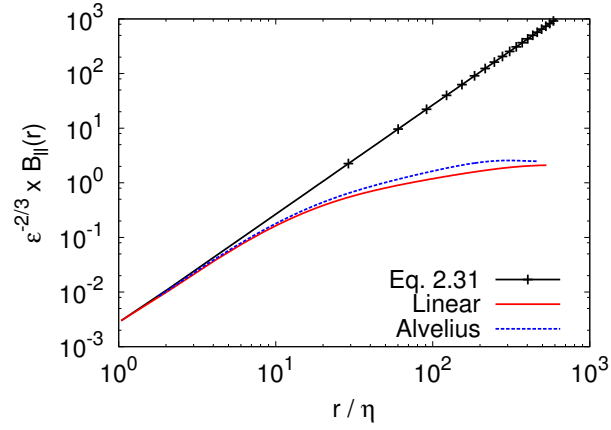
(a) Small scale behavior of $B_{ll}(r)$
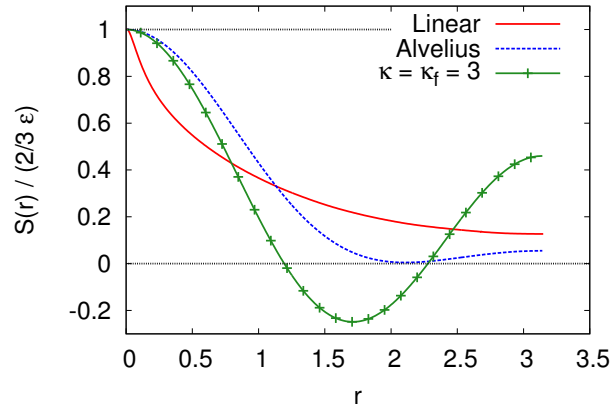
(b) Role of forcing location in $S(r)$ behavior

Figure 2.8: Behavior of second-order longitudinal structure function at small viscous scales and the Karman-Howarth source term at intermediate scales. One half of the computational domain ($0 \le r \le \pi$) is plotted. The legend entry termed $\kappa = \kappa_f = 3$ corresponds to the simulation with injection at a single wavenumber.

the source term can be expressed as,

$$S(r) = \frac{2}{3}\epsilon - \frac{\epsilon^2}{45\nu\langle u^2 \rangle}r^2 + O(r^4) = \frac{2}{3}\epsilon \left(1 - \frac{1}{2}\frac{r^2}{\lambda_g^2}\right) + O(r^4). \tag{2.32}$$

The Karman-Howarth source term, $S(r)$, begins to decay at the transverse Taylor micro-scale, λ_g, as indicated in Eq. 2.32. Then, in the limiting case of $r \to \infty$ (at infinite separation), the Karman-Howarth source term vanishes, as suggested in Fig. 2.6 and Fig. 2.7(b). At large separation, the velocities at $\underline{u}(\underline{x} + \underline{r}, t)$ and $\underline{u}(\underline{x}, t)$ become de-correlated from each other, which consequently sends $B_{ll}(r)$ to a value of $2\langle u^2 \rangle$ and implies $S(r \to \infty) = 2Q\langle u^2 \rangle - QB_{ll}(r \to \infty) = 0$.

2.4.3.2 Alvelius-Forced Turbulent Field Results

As presented in the original paper [1], this low waveshell forcing method assumes a forcing wavenumber of $\kappa_f = 3$ with forcing bound of $\kappa_{low} = 2 \leq \kappa \leq \kappa_{high} = 4$. To better understand the effects of this narrow waveband forcing, a limiting case is considered. The forcing waveband is contracted to include only a single forcing wavenumber, $\kappa_{low} = 3 \leq |\underline{\kappa}| \leq \kappa_{high} = 3$, reducing the number of forcing wavevectors, $\underline{\kappa}$, to seventeen, and the resulting KH source term is calculated.

The KH source term for this contracted case is compared to the one obtained for the original forcing band in Fig. 2.8(b), along with the linear forcing results. Clearly, changing the forcing band has a strong effect on $S(r)$. The main differences between the two spectral forcing curves are the larger magnitude at the largest scales and the region that assumes negative values. This limiting case underscores the dependence of the imposed Karman-Howarth source term on the chosen forcing band outside of the viscosity-dominated, small scales. Additionally, it suggests that the decay of $S(r)$ is determined by κ_f.

Returning to the forced Karman-Howarth equation (Eq. 2.17), the impact of $S(r)$ on B_{ll} and B_{lll} can be discussed (Fig. 2.7). The viscous term is negligible across the intermediate and large scales; the dominant terms are the inertial and source terms. As the inertial term compensates for the source term contribution to Eq. 2.17, it must assume a virtually constant value solely because of the nature of $S(r)$. This constancy of the inertial term, which contains $B_{lll}(r)$, is similar to the behavior suggested by Kolmogorov's 4/5-law. The KH source term compels the inertial term to assume a constant value, which is generally indicative of inviscid dynamics. The inertial term, then, influences the development of the structure functions, and imparts in them behaviors that appear to be inviscid. Although these behavioral traits may be consistent with typical measures of inviscid character, in this instance, they are solely an artifact of the source term. This is a partial justification for the observations made in previous studies [2, 35] of isotropic turbulence; in such studies, the spectrally-forced DNS data consistently produced third-order structure functions of larger magnitude than linearly-forced data at a given Re_λ.

There are two conclusions to be reached from this. First, where energy is injected (in wave- or physical-space) matters, as it affects the form of the Karman-Howarth source term. If the Reynolds number is sufficiently high to support physically meaningful separation between the production and dissipation scales, then the forcing bounds imposed by spectral forcing methods may be consistent with those experienced by real turbulent flows. However, if the Reynolds number is not high enough, which is the case in many simulation studies of turbulence, the imposed spectral forcing bounds may be inconsistent with those found in experimentally-attainable flows, which suggests that, in such instances, the physical structures derived may not be independent of the forcing bounds imposed. Second, the behavior of the source term in the intermediate region is responsible for the pseudo-inviscid characterstics produced by Alvelius' forcing method. Tendencies that are associated generally with inviscid behavior are imposed by Alvelius' method on its resulting structure functions.

2.5   The KH Source Term and the Production Spectrum

Although the previous analysis has focused on only one low waveband spectral method, there are two key traits that can be generalized to all methods. First, a distinction should be made between energy-producing and energy-containing scales. In low waveband forcing methods [33, 87, 89, 17], energy is only injected into a narrow band of waveshells; these waveshells do not correspond necessarily to the scales in which energy is contained. A comparison of the production spectra and the associated energy spectra for each forcing method is provided in Fig. 2.9. The production spectrum is defined as the region in wavespace over which a spectral forcing term is active. In the case of Alvelius' forcing method, this corresponds to $2 \leq \kappa \leq 4$ where the energy injected has a Gaussian distribution (Eq. 2.3). Alvelius showed [1] that the production spectrum for this method could be expressed as,

$$P(\kappa) = \frac{1}{2}\Delta t \, \langle f(\kappa)_i^n f(\kappa)_i^n \rangle, \tag{2.33}$$

while the production spectrum for linear forcing is given by,

$$P(\kappa) = 2QE(\kappa). \tag{2.34}$$

With Alvelius' forcing method (Fig. 2.9(a)), the energy-containing scales in $E(\kappa)$ are of greater spectral extent than the energy-producing scales in $P(\kappa)$. This creates a separation between energy-producing scales and dissipative scales, but not between energy-containing scales and dissipative scales (Fig. 2.3(a)). Alternatively, with linear forcing, where the momentum source term is active over all flow scales, energy-containing and energy-production scales are coincident (Fig. 2.9(b)).

These results imply that Alvelius' method imposes a pseudo-scale separation within the turbulent field, which is a consequence of the nature of low waveband energy injection. This is reflected in
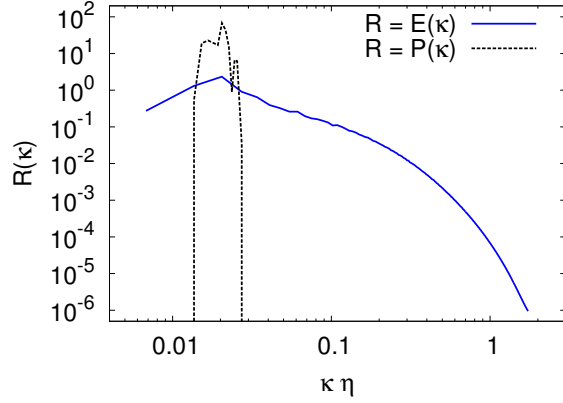
(a)   Spectral (Alvelius) forcing
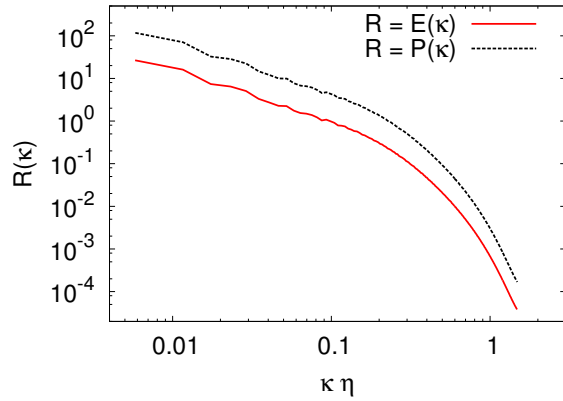
(b)   Linear (Lundgren) forcing

Figure 2.9: Comparison of energy and production spectra.

the production scale it imposes. The production scale, $l_{PI} \propto \kappa_{PI}^{-1}$, is defined as the length-scale corresponding to the waveshell in wavespace, κ_{PI}, at which 90% of total energy production by the forcing method has been deposited. For Alvelius' forcing method, $\kappa_{PI} \approx 3.3$; this corresponds to $ln\left(\kappa/\kappa_\eta\right) \approx -3.8$ in Fig. 2.3(a). For linear forcing, $l_{EI} = l_{PI}$, whilst for Alvelius' forcing, $l_{EI} \neq l_{PI}$. Also, for Alvelius' forcing, there is separation between the scales over which energy is injected and those over which energy is dissipated, but not between those in which energy is contained versus dissipated. Under insufficiently high Re_λ conditions, this can create inconsistencies, as noted by the different behaviors observed across the intermediate scales in the calculated transfer spectra (Fig. 2.3). However, if the Re_λ is high enough to induce actual scale separation between energy-containing and dissipating scales, then the effects that such a low waveband forcing method may have would be negligible.

Second, spectral schemes assume an energy production spectrum that is strictly zero outside of a defined low wavenumber range (Fig. 2.9(a)). This artificial partition between the production

and dissipation scales is responsible for the differences between the Karman-Howarth source terms for linear (physical-space) and Alvelius (spectral-space) forcing methods (Fig. 2.6). In support of this, the Alvelius spectral method was modified slightly, and two additional tests were performed under the same turbulent conditions ($Re_\lambda = 140$, $\nu = 0.0028$). In these two cases, the production spectrum was changed from the Gaussian forcing spectrum (Eq. 2.28 and Eq. 2.33) implemented by Alvelius [1] to an energy spectrum model (Eq. 2.6) that was fit to the energy spectrum obtained from the linearly-forced data. This accomplishes two tasks. First, it extends the region of overlap between energy-producing and energy-containing scales. Second, it requires that the magnitude of energy injected at a point in wavespace is in proportion to the energy said point contains.

In these additional cases, the largest forcing waveshell, κ_{high}, is progressively increased to include more of the energy-containing wavenumbers, while the lowest forcing waveshell is held at $\kappa_{low} = 1$. These cases have forcing wavenumbers of $1 \leq \kappa \leq 25$ and $1 \leq \kappa \leq 35$, which correspond to the locations by which 90% and 95% of total energy produced has been deposited, respectively. Note that these wavenumber ranges constitute less than 1% of the total number of wavevectors supported by the computational grid. The KH source terms are calculated for these two cases, and they are compared to those found from the linear and the unmodified Alvelius forcing methods. The comparison is provided in Fig. 2.10.

When the Alvelius spectral forcing scheme is modified such that the production scales (those containing at least 90% of total energy produced) are made to match more closely the energy containing scales, the differences between the source terms noted in Fig. 2.6 vanish. These results confirm that it is the artifically-imposed separation between the energy-producing and dissipating scales found in the spectral (Alvelius) forcing method that is responsible for the disparities betweeen the Karman-Howarth source terms shown in Fig. 2.6.

The conclusion to be obtained from these observations is that where energy is produced in wavespace, relative to where it is contained, matters, at least at moderate Re_λ such as these. The nature of forcing (*i.e.* spectral- *v.s.* physical-space) and the variables to (from) which the momentum source terms are correlated (de-correlated) are largely unimportant. The critical feature is where the energy is deposited in spectral space.

2.6   Summary and Conclusions

In summary, two representative velocity forcing methods, Lundgren's linear and Alvelius' spectral forcing methods, were analyzed. The effects of implementing these two methods on the resulting turbulent fields have been investigated in the context of the Karman-Howarth (KH) equation. The source terms the methods append to the KH equation have been derived, and the character they impose on structure function behavior has been discussed. Through the second-order structure
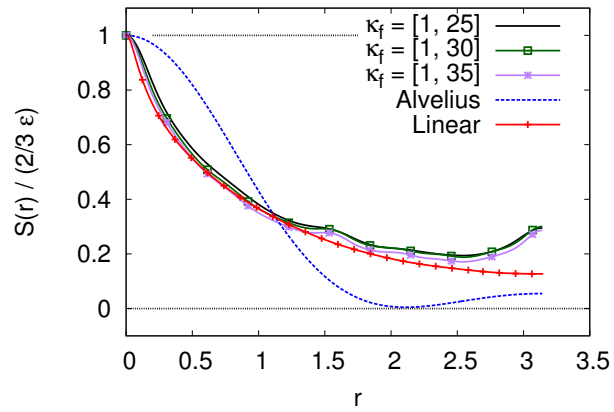
(a)   Large-scale behavior
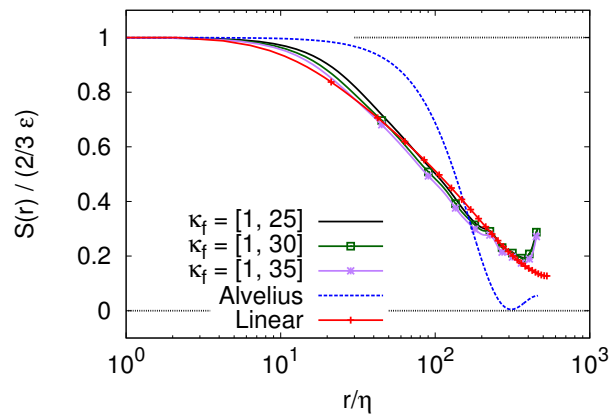
(b)   Small-scale behavior

Figure 2.10: Comparison of the Karman-Howarth source terms obtained when the production spectrum is expanded. One half of the computational domain is plotted, $r = [0, \pi]$.

function, their role in determining the energy spectrum was presented. Additionally, explanations for the small-scale similarity of major turbulent statistics, including structure functions and source terms, were offered. Outside of the small-scale region, the disparity in turbulent metrics predicted by the two representative methods is attributed to their differing KH source terms, which are ultimately dictated by their respective energy production spectra.

In conclusion, there are three findings of this work. First, at the small dissipative scales (*i.e.* $r/\eta < 10$), forcing methods generate comparable turbulent fields, as evidenced by the coincidence of linearly-forced and spectrally-forced $B_{ll}(r)$, $B_{lll}(r)$, and $S(r)$. This result is due to the dominance of viscosity in this range, which renders the specifics of any forcing method irrelevant and the value of the method-imposed KH source term, $S(r = 0)$, equal to $\frac{2}{3}\epsilon$.

Second, across the intermediate scales (*i.e.* $10 < r/\eta < 0.5l_0/\eta$), the differences noted between the two forcing methods can be attributed to their KH source terms, as $S(r)$ governs the behavior of B_{ll} and B_{lll} via the inertial and viscous terms in the forced KH equation. Note that the upper bound on this intermediate range of scales, $r/\eta < 0.5l_0/\eta$, is dependent on the Re_λ of the flow. Further, B_{ll} and B_{lll} are related to $E(\kappa)$ and $T(\kappa)$; thus, $S(r)$ is responsible for the turbulent structures that develop under the action of these (or any) velocity field forcing methods. Consequently, for Alvelius' spectral forcing, B_{ll} and B_{lll} are larger in magnitude when compared to their linear forcing-predicted versions. The resulting structure functions may suggest the presence of inviscid dynamics when there are none. This explains the inconsistencies noted in the Alvelius-forced data, specifically the spectral slope of the energy spectrum.

Third, of chief importance is the energy production spectrum, $P(\kappa)$, assumed by the forcing method implemented. This determines where in wavespace a forcing method injects its energy relative to the energy-containing scales. In regards to low waveband spectral forcing, the scales over which energy is deposited relative to the energy-containing scales may be different. This creates an artificial partition between the dissipating and production scales, despite overlap between the dissipating and energy-containing scales. When a production spectrum similar to Lundgren's imposed spectrum is applied within the context of the Alvelius forcing method, the source terms (physical *vs.* spectral) become consistent.

The implications of these findings are threefold. First, when implementing spectral methods, care must be taken when defining the waveshells over which power will be injected to minimize the effects of the numerical forcing technique. Second, the primary factor used in determining the merit of a forcing method ought not be its recovery of an energy spectrum scaling (*e.g.* $E(\kappa) \propto \kappa^{-5/3}$), but should be the character of its imposed energy production spectrum. This is not a physical-space *vs.* wave-space issue, but an energy-producing *vs.* energy-containing scale issue. Lastly, in fairness, if the Re_λ is high enough, then these issues may not manifest strongly, as the region of meaningful scale separation present would reduce the impact of the mismatch in the energy-containing and

energy-producing scales.

In regards to choosing an isotropic velocity field forcing method for application in the new simulation framework with which to study variable density flows, based on this chapter's work, Lundgren's linear, physical-space method is selected in favor of the other available spectral schemes. This is done for two reasons. First, Lundgren's method can more easily handle the challenges associated with a variable density fluid. Second, for the Reynolds numbers with which the later variable density and buoyant work is to be concerned, the linear method is more consistent with available experimental data. Thus, the physics generated will be more accurate and the conclusions drawn from them will be more precise.

Chapter 3

Forcing the Velocity Field: A Practical Modification [12]

Following Chapter 2, Lundgren's linear forcing method is deemed more representative of real turbulent flows than the other available spectral methods. Accordingly, it is this forcing method that is to be used in the simulation framework to be presented in Chapter 5 and applied in Chapter 6. However, Lundgren's method can produce highly oscillatory turbulent statistics, necessitating extended simulation run times to ensure time invariant statistical metrics [59]. This is now addressed.

This problem of statistical oscillation is not specific to Lundgren's method. It has been well documented that most velocity field forcing methods produce turbulent quantities (*i.e.* turbulent kinetic energy, dissipation rate) that can be subject to significant statistical variation [74]. The literature provides several examples of forcing methods that have been designed to reduce such temporal fluctuations. These efforts are varied and include artificially freezing the energy content in the largest flow scales [87], fixing the ratio of energy content between subsequent waveshells [17, 108], and imposing a model energy spectrum to which forcing is done in proportion [74]. This chapter contains a proposed modification to Lundgren's method that reduces the extent of oscillation in relevant turbulent statistics and significantly reduces the length of simulation time needed to attain statistical stationarity. These improvements result in more efficient simulations.

3.1 Justification for Proposed Modification

When implemented as proposed by Lundgren, the linearly-forced (incompressible) momentum equations take the form,

$$\frac{\partial u_i}{\partial t} + u_j \frac{\partial u_i}{\partial x_j} = -\frac{1}{\rho}\frac{\partial p}{\partial x_i} + \nu \frac{\partial}{\partial x_j}\left(\frac{\partial u_i}{\partial x_j}\right) + Qu_i. \tag{3.1}$$

The forcing parameter, Q, controls the magnitude of the energy added to the velocity field. This parameter is controlled by the user, and it is sufficient (with the viscosity, ν, and a defined length-scale, l) to completely prescribe all pertinent physical parameters [81], including the Reynolds number, Re_λ, the turbulent kinetic energy, k, the dissipation rate, ϵ, and the eddy turn-over time, τ. To understand how this method is able to control the resulting turbulent field, consider the turbulent kinetic energy equation derived from Eq. 3.1,

$$\frac{dk}{dt} = -\epsilon + 2Qk, \tag{3.2}$$

where, during the spatial (volume) averaging step, denoted as $\langle \, \cdot \, \rangle$, incompressibility ($\partial u_i / \partial x_i = 0$) and homogeneity ($\langle \nabla \cdot (\,) \rangle = 0$) have been assumed, and the definitions $k = \langle \frac{1}{2} u_i u_i \rangle$ and $\epsilon = \langle 2\nu \, s_{ij} s_{ij} \rangle$ were used for turbulent kinetic energy and dissipation rate, respectively. Applying the condition of statistical stationarity, Eq. 3.2 reduces to simply a balance between the dissipation rate and a scalar multiple of the turbulent kinetic energy,

$$0 = -\epsilon + 2Qk. \tag{3.3}$$

From Eq. 3.3, the physical significance of the forcing parameter, Q, becomes clear; Q is simply the inverse of twice the eddy turn-over time, τ, or $Q = (2\tau)^{-1}$, with $\tau = k/\epsilon$. Thus, the forcing parameter provided by the user imposes the time-scale over which energy is injected into the turbulent velocity field.

Rosales and Meneveau [81] found that this linear forcing technique generates a turbulent velocity field that asymptotically approaches a unique solution. This asymptotic state is characterized by an integral length-scale, which is approximately 20% of the computational domain. The integral length-scale, l, can be expressed in terms of physical parameters as $l = \langle u^2 \rangle^{3/2}/\epsilon$, where $\langle u^2 \rangle$ is the variance of the velocity field (i.e. $k = \frac{3}{2}\langle u^2 \rangle$). If such an asymptotic state exists, as defined by Eq. 3.3, then, together with the definitions of the integral length-scale and the turbulent kinetic energy provided, the asymptotic values for key turbulent metrics can be evaluated. For example, the turbulent Reynolds number, Re, and its Taylor micro-scale counterpart, Re_λ, can be written as,

$$Re = \frac{l \, u}{\nu} = \frac{3Q \, l^2}{\nu} \qquad Re_\lambda = \frac{\lambda_g u}{\nu} = \left(\frac{45 \, Q \, l^2}{\nu} \right)^{1/2}, \tag{3.4}$$

and the characteristic velocity, u, mean turbulent kinetic energy, k_0, and mean dissipation rate, ϵ_0, can be written as,

$$u = 3Al, \qquad k_0 = \frac{27}{2} Q^2 l^2, \qquad \epsilon_0 = 27 \, l^2 Q^3. \tag{3.5}$$

Note that to obtain the Taylor micro-scale, λ_g, the relation for the dissipation rate under isotropic conditions [77] was used, $\epsilon = 15 \, \nu \langle u^2 \rangle / \lambda_g^2$. Note further that there are two degrees of freedom available to the user, namely the forcing parameter, Q, and the viscosity, ν.

However, it was noted by Rosales and Meneveau [81], as well as by Lundgren in the original work [58], that the turbulent statistics generated under this method were sometimes subject to large oscillations around the above average values. Additionally, these oscillations were found to increase with increasing Re_λ. To reduce the amplitude of these oscillations, this work proposes a slight modification to Lundgren's original momentum source term. This modification changes the original source term from $Q u_i$ to $Q \left(\frac{k_0}{k} \right) u_i$, resulting in forced (incompressible) momentum equations of the form,

$$\frac{\partial u_i}{\partial t} + u_j \frac{\partial u_i}{\partial x_j} = -\frac{1}{\rho} \frac{\partial p}{\partial x_i} + \nu \frac{\partial}{\partial x_j} \left(\frac{\partial u_i}{\partial x_j} \right) + Q \left(\frac{k_0}{k} \right) u_i, \tag{3.6}$$

where k is the instantaneously calculated turbulent kinetic energy and k_0 is the desired steady-state turbulent kinetic energy (Eq. 3.5). Changing the source term in this manner is conceptually consistent with implementing a relaxation term or a damping coefficient as implemented by Overholt and Pope [74]. The velocity field is driven towards the desired turbulent kinetic energy value in a more constrained fashion, thereby reducing the amplitude of its oscillations. Note that in the (long-time) limit of $k = k_0$, this term is equivalent to the original source term. Also, the turbulent parameters under this modification are controlled in the same fashion. After specifying Re_λ, the value for Q required for a given ν can be calculated straightforwardly from Eq. 3.4, and the long-time kinetic energy and dissipation rate can be determined from Eq. 3.5. The modification proposed does mitigate the "localness" of Lundgren's original method, as a globally-averaged quantity, k, is added to the source term. However, the stability resulting from this modification, which is discussed later, justifies this mitigation.

It is found that this modified source term does not significantly or detrimentally impact the generated turbulent fields; its sole effect is to reduce the oscillatory behavior of the turbulent statistics. This can be verified both analytically and graphically via a comparison between the turbulent fields produced under the action of the original and modified source terms. The analytical justification for this claim is addressed first.

The turbulent kinetic energy equation corresponding to Eq. 3.6 is,

$$\frac{dk}{dt} = -\epsilon + Q \frac{k_0}{k} \langle u_i^2 \rangle = -\epsilon + 2Q k_0, \tag{3.7}$$

where incompressibility and homogeneity are assumed. At stationarity, it is obtained,

$$0 = -\epsilon + 2Q k_0. \tag{3.8}$$

Note that the only difference between this equation and that of the original source term (Eq. 3.2 and Eq. 3.3) is that now, instead of the instantaneous turbulent kinetic energy being of importance, only the long-time asymptotic (stationary) turbulent kinetic energy is important. This has the effect of reducing the variation in the resulting dissipation rate, ϵ. Further, the physical meaning of the forcing parameter Q is preserved under this proposed modification. It is still related to the eddy turn-over time via $Q = (2\tau_0)^{-1}$, where $\tau_0 = k_0/\epsilon$. This eddy turn-over time is equivalent to the τ from the original source term once stationarity sets in, as $k = k_0$ and $\epsilon = \epsilon_0$.

It is of note that using this modified source term is more consistent with spectrally-based forcing schemes. Spectral schemes generally inject a fixed, constant amount of energy into the computational domain during each timestep. As the modified source term results in a term in the turbulent kinetic energy equation that depends only on k_0 and Q, both of which have constant, temporally unchanging values, it is conceptually similar to the more widely-used spectral forcing schemes.

3.2 Simulation Study

In addition to analytical support for the claim that the modified source term has only the intended effects of reducing unwanted oscillations in the calculated turbulent statistics, simulation-based (practical/empirical) verification is now provided. A comparison between turbulent physics produced by the modified and original source terms is performed for two Re_λ cases: $Re_\lambda = 110$ and $Re_\lambda = 140$ on an $N^3 = 384^3$ grid and an $N^3 = 512^3$ grid, respectively. For the $Re_\lambda = 110$ cases, the forcing parameters are $Q = 0.96$ and $\nu = 0.005$. For the $Re_\lambda = 140$ cases, the forcing parameters are $Q = 1.40$ and $\nu = 0.005$. In all cases, the grid resolution is kept at $\kappa_{max}\eta \geq 1.5$.

The initial velocity fields were Gaussianly distributed following the initialization procedure in Eswaran and Pope [33]. In the plots to be referenced, the legend entries "Original" and "Modified" denote the results obtained when implementing the original and modified source terms, respectively. The "Original" and "Modified 1" data were subject to initial conditions of $k(t = 0) = 0.014$ and $\epsilon(t = 0) = 7.3 \times 10^{-4}$ for both Re_λ; "Modified 2" data had initial conditions of $k(t = 0) = k_0 = 17$ and $\epsilon(t = 0) = 0.87$ for $Re_\lambda = 110$ and $k(t = 0) = k_0 = 36$ and $\epsilon(t = 0) = 1.83$ for $Re_\lambda = 140$. As will be shown in Figs. 3.1-3.6, the results appear to be independent of the initial conditions implemented. The code package used to perform these simulations is NGA [26]. The code is physical (non-spectral), suitable for low Mach number flows, and uses a standard staggered grid. The velocity field is solved implicitly via a second-order accurate finite-difference scheme, and this scheme is discretely energy conserving. The time advancement is accomplished by a semi-implicit Crank-Nicolson method. Further details on the simulation code employed can be found in Appendix 8.3, Appendix 8.4, and Appendix 8.6.

The first two statistics of interest are the time evolution of the turbulent kinetic energy and the

dissipation rate, which are depicted in Fig. 3.1 and Fig. 3.2. As is apparent from the statistics for the original source term, there is considerable variation in turbulent kinetic energy and dissipation rate even after stationary conditions have set in (approximately $t/\tau \geq 15$ for $Re_\lambda = 110$ and $Re_\lambda = 140$). As shown in Fig. 3.1(a) and Fig. 3.2(a), large jumps in calculated turbulent statistics are possible when the original source term is used (*e.g.* $t/\tau \geq 30$), and these cannot be modulated. The modified source term, as evidenced by both the $Re_\lambda = 110$ and $Re_\lambda = 140$ cases, produces markedly smoother statistics, free from significant deviations from the asymptotic stationary values. It is important to note, also, that statistical stationarity is obtained much more rapidly with the modified source term ($t/\tau \geq 4$ for both Re_λ) than with the original source term ($t/\tau \geq 15$ for both Re_λ). Regardless, however, both the original and the modified source terms produce equivalent eddy turn-over times, as depicted in Fig. 3.3. This is significant, as it supports the earlier claim that only the variations are being damped by the modified source term; the underlying physics are largely unchanged.

Since all relevant turbulent fields (*e.g.,* the energy spectrum, $E(\kappa)$, the dissipation spectrum, $D(\kappa)$, and the transfer spectrum, $T(\kappa)$) are related directly to the dissipation rate and turbulent kinetic energy, the variation in these metrics correspondingly decreases. The practical ramifications of this is quite significant, as fewer datasets are now required to obtain statistically stationary, time invariant statistics. This translates into shorter simulations and a reduced computational burden.

As the key turbulent statistics indicate that the modified source term is having the intended effect of reducing large amplitude oscillations without significantly altering any asymptotic behavior, the spectra generated are presented now to verify that the spectral distribution of energy has not been affected. The energy, dissipation, and transfer spectra for the six cases are provided in Fig. 3.4, Fig. 3.5, and Fig. 3.6. In these three sets of spectra, the distribution in wavespace is unchanged; the magnitudes of the curves, however, do vary slightly (as expected) between the turbulent fields obtained with the original and modified source terms. This slight variation is most pronounced in the dissipation spectra (Fig. 3.5), and these differences in magnitude can be attributed to the oscillatory behavior of the turbulent fields obtained with the original source term. The critical feature of Fig. 3.4, Fig. 3.5, and Fig. 3.6 is that the respective spectrum shapes are preserved when implementing the modified source term.

3.3   Linear Perturbation (Stability) Analysis

The objective of applying a velocity field forcing method is to prevent the decay of the turbulent fluctuations. While it is difficult (if not impossible) to prove convergence towards a unique statistically stationary state irrespective of initial conditions, all numerical tests performed tend to suggest that this is the case. However, it has been shown that the original form of the source term induces significant oscillation in the long-time behavior of its produced turbulent statistics, while the modified
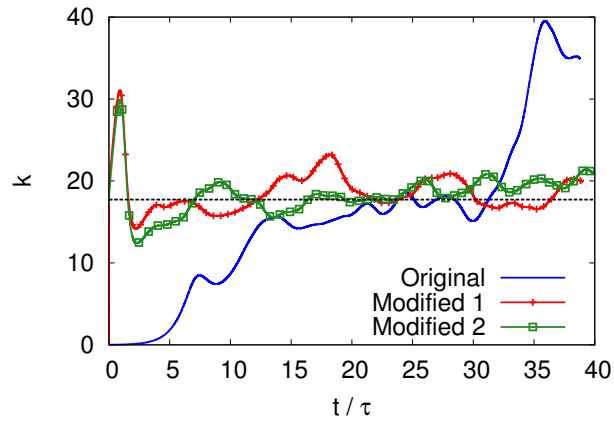
(a) $Re_\lambda = 110$
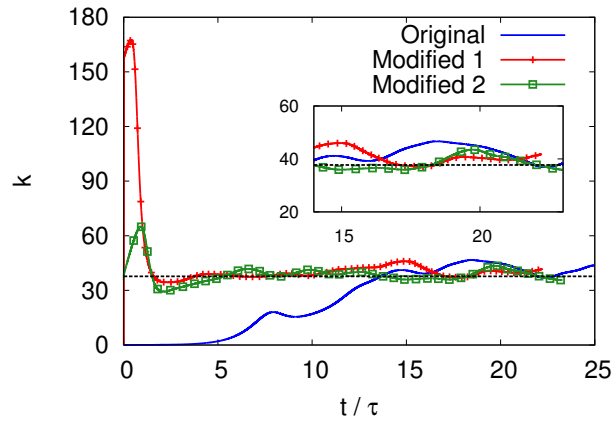
(b) $Re_\lambda = 140$

Figure 3.1: Time evolution of turbulent kinetic energy. The (black) dashed line denotes the expected stationary value, k_0, calculated from Eq. 3.5.
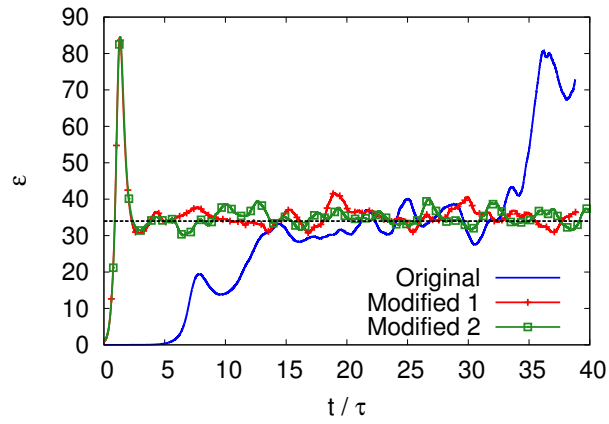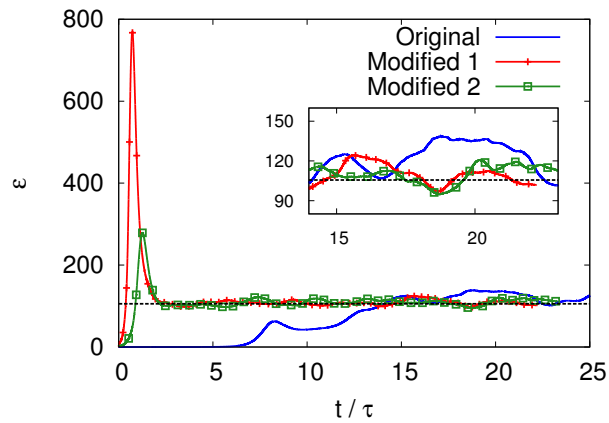
(a) $Re_\lambda = 110$

(b) $Re_\lambda = 140$

Figure 3.2: Time evolution of dissipation rate. The (black) dashed line denotes the expected stationary value, ϵ_0, calculated from Eq. 3.5.
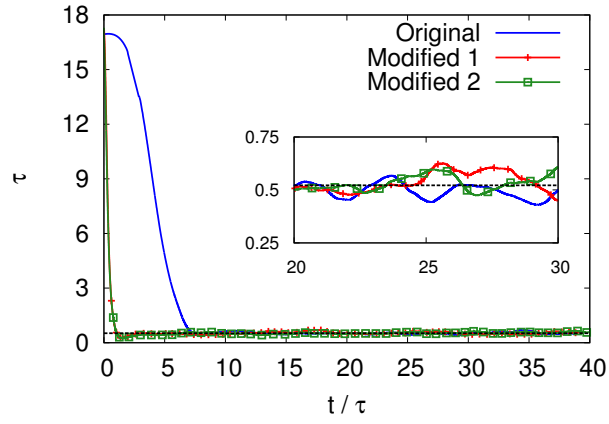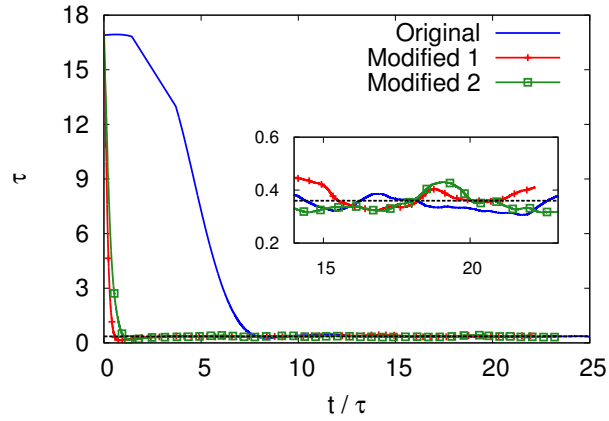
(a) $Re_\lambda = 110$

(b) $Re_\lambda = 140$

Figure 3.3: Time evolution of eddy turn-over time. The (black) dashed line denotes the expected stationary value, τ_0, calculated from $\tau_0 = (2Q)^{-1} = k_0/\epsilon_0$.
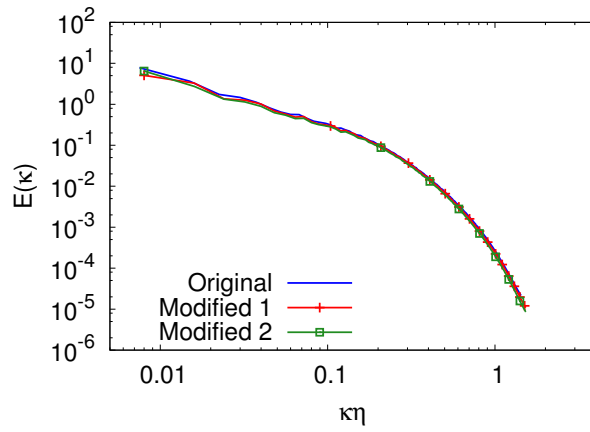
(a) $Re_\lambda = 110$
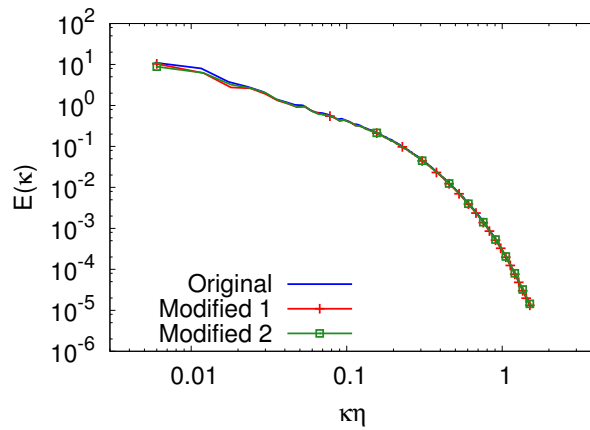
(b) $Re_\lambda = 140$

Figure 3.4: Energy spectra at statistical stationarity (averaged over a minimum of 10 τ). Here, η is the Kolmogorov length-scale, defined as $\eta = (\nu^3/\epsilon)^{1/4}$.
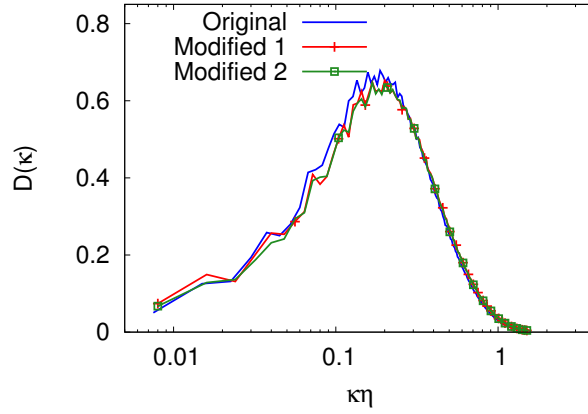
(a) $Re_\lambda = 110$
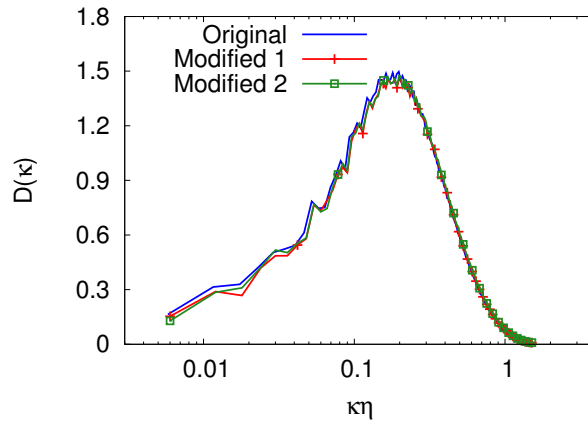
(b) $Re_\lambda = 140$

Figure 3.5: Dissipation spectra at statistical stationarity (averaged over a minimum of 10 τ). The dissipation spectrum is defined as $D(\kappa) = 2\nu\kappa^2 E(\kappa)$.
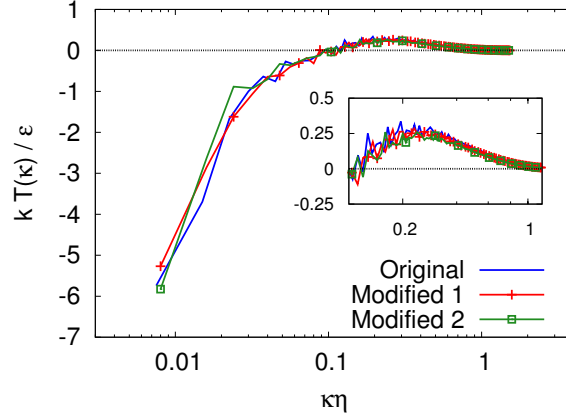
(a) $Re_\lambda = 110$
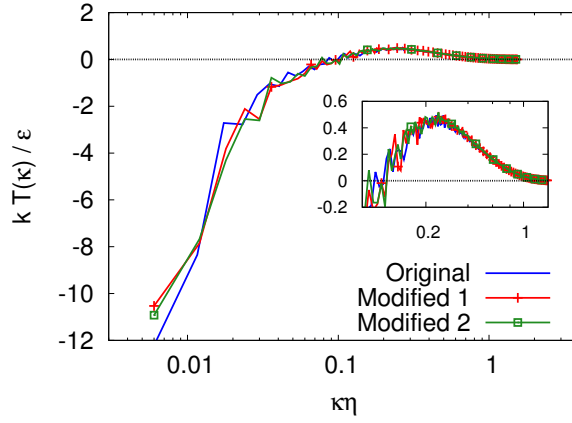
(b) $Re_\lambda = 140$

Figure 3.6: Transfer spectra at statistical stationarity (averaged over a minimum of 10 τ). The transfer spectrum is defined as $T(\kappa) = \langle -\hat{u}_i \mathscr{F} \left(u_j \frac{\partial u_i}{\partial x_j} \right) \rangle$, a scalar function of the wavenumber. Here, $\mathscr{F}(\cdot)$ denotes the Fourier transform and $\hat{u}$ denotes the Fourier-transformed velocity field.

source term does not. To better understand the reasons behind these oscillations, a straightforward, perturbation-based analysis of the two relevant governing equations for the turbulent kinetic energy and dissipation rate around the asymptotic values of k_0 and ϵ_0 is conducted. The pertinent turbulent kinetic energy equations are Eq. 3.2 for the original source term and Eq. 3.7 for the modified source term. These expressions involve the dissipation rate directly, necessitating an evolution equation for this parameter also. Although an analytical transport equation for the dissipation rate is attainable by manipulation of the momentum equations (Eq. 3.1 and Eq. 3.6), the resulting expressions are not closed, a commonly-encountered problem in the study of turbulence. As an approximation, a $k - \epsilon$ model evolution equation [99] is assumed, which can be written in a general form as,

$$\frac{\partial \epsilon}{\partial t} + U_j \frac{\partial \epsilon}{\partial x_j} = C_{\epsilon 1} \frac{\epsilon}{k} \tau_{ij} \frac{\partial U_i}{\partial x_j} - C_{\epsilon 2} \frac{\epsilon^2}{k} + \frac{\partial}{\partial x_j} \left((\nu + \nu_T/\sigma_\epsilon) \frac{\partial \epsilon}{\partial x_j} \right) + f, \quad (3.9)$$

where U_j and ν_T denote mean velocity and turbulent eddy-viscosity; σ_ϵ, $C_{\epsilon 1}$, and $C_{\epsilon 2}$ are positive constants resulting from closure approximations; and f is a source term resulting from the velocity field forcing method implemented. Under the present configuration (isotropic, triply periodic box turbulence) and using the conditions of homogeneity and a zero mean velocity, this reduces to,

$$\frac{\partial \epsilon}{\partial t} = -C_{\epsilon 2} \frac{\epsilon^2}{k} + f, \quad (3.10)$$

where $f = 2Q\epsilon$ under the action of the original momentum source term and $f = 2Q\epsilon (k_0/k)$ under the action of the proposed modified source term. This form of f (and Eq. 3.9) is obtained by taking the following moment of the proper momentum equation (Eq. 3.1 or Eq. 3.6),

$$2\nu \left\langle \frac{\partial u_i}{\partial x_j} \frac{\partial}{\partial x_j} \left[\mathcal{N}(u_i) \right] \right\rangle = 0. \quad (3.11)$$

Here, $\mathcal{N}(u_i)$ represents the appropriate momentum equation (Eq. 3.1 or Eq. 3.6). It is important to note that the above expression (Eq. 3.9) is only a model and may not describe adequately the evolution of ϵ under all conditions.

The turbulent kinetic energy and dissipation rate are perturbed about their asymptotic (time-invariant) mean values, k_0 and ϵ_0, according to $k = k_0 + k'$ and $\epsilon = \epsilon_0 + \epsilon'$. These perturbed expressions are inserted into Eq. 3.2, Eq. 3.7, and Eq. 3.10. For the original source term, the results are,

$$(a) \ \ 0 = -\epsilon_0 + 2Qk_0 \qquad\qquad (b) \ \ \frac{dk'}{dt} = -\epsilon' + 2Qk'$$

$$(c) \ \ 0 = -C_{\epsilon 2} \frac{\epsilon_0}{\tau_0} + 2Q\epsilon_0 \qquad (d) \ \ \frac{d\epsilon'}{dt} = \frac{C_{\epsilon 2}}{\tau_0^2} k' + \epsilon' \left(2Q - 2\frac{C_{\epsilon 2}}{\tau_0} \right), \quad (3.12)$$

where only terms that are at most first-order (linear) in the perturbed quantity have been kept. For

the modified source term, the results are,

$$(a) \ \ 0 = -\epsilon_0 + 2Qk_0 \qquad\qquad\qquad (b) \ \ \frac{dk'}{dt} = -\epsilon'$$

$$(c) \ \ 0 = -C_{\epsilon 2}\frac{\epsilon_0}{\tau_0} + 2Q\epsilon_0 \qquad (d) \ \ \frac{d\epsilon'}{dt} = \left(\frac{C_{\epsilon 2}}{\tau_0^2} - \frac{2Q}{\tau_0}\right)k' + \left(2Q - 2\frac{C_{\epsilon 2}}{\tau_0}\right)\epsilon'. \qquad (3.13)$$

To obtain these linearized perturbation equations, the denominators of the dissipation rate equations (Eq. 3.12 and Eq. 3.13) were Taylor-expanded for small k'. Under statistically stationary conditions and, irrespective of the source term used (original or modified), it is recovered $Q = \epsilon_0/(2\ k_0) = 1/(2\ \tau_0)$. Additionally, it is found that a necessary (but not sufficient) condition for the existence of an asymptotic state is that $C_{\epsilon 2} = 1$. (This result is independent of the form of the source term.) This value for $C_{\epsilon 2}$ differs from that of a standard $k - \epsilon$ model [50, 102], as it now corresponds to a stationary, forced turbulent field, not a decaying one. As such, Eq. 3.10 with $C_{\epsilon 2} = 1$ may not be used to describe the initial stages of the forced velocity field (prior to reaching statistical stationarity), and it may not be used to prove convergence independent of the initial conditions (*i.e.* k_0 and ϵ_0).

Using Eq. 3.12 and Eq. 3.13, the needed coupled turbulent kinetic energy-dissipation rate system can be specified. For the original source term, this system takes the form in Eq. 3.14(a). For the modified source term, this system takes the form in Eq. 3.14(b). For the modified forcing method proposed to be stable, a necessary condition is that perturbations about the asymptotic values of k_0 and ϵ_0 should temporally decrease; such behavior is indicated by the eigenvalues of the coupled equation system.

$$(a) \ \ \frac{d}{dt}\begin{bmatrix} k' \\ \epsilon' \end{bmatrix} = \frac{1}{\tau_0}\begin{bmatrix} 1 & -\tau_0 \\ \frac{1}{\tau_0} & -1 \end{bmatrix}\begin{bmatrix} k' \\ \epsilon' \end{bmatrix} \qquad\qquad (b) \ \ \frac{d}{dt}\begin{bmatrix} k' \\ \epsilon' \end{bmatrix} = \frac{1}{\tau_0}\begin{bmatrix} 0 & -\tau_0 \\ 0 & -1 \end{bmatrix}\begin{bmatrix} k' \\ \epsilon' \end{bmatrix} \qquad (3.14)$$

For the original momentum source term, the eigenvalues are found to be zero, $\lambda_1 = \lambda_2 = 0$. Eigenvalues of zero are associated with marginal stability, implying that oscillations will neither be compelled to grow nor to decay in time. There is no mechanism to dampen or reduce the amplitudes of the fluctuating turbulent quantities. It is believed that this is the cause for the sensitivity and oscillatory nature of the turbulent kinetic energy and dissipation rate statistics depicted in Fig. 3.1 and Fig. 3.2.

Alternatively, when the eigenvalues corresponding to the system for the modified source term are calculated, one eigenvalue is found to be negative, $\lambda_1 = -1/\tau_0$, and the other is found to be zero, $\lambda_2 = 0$. The negative eigenvalue suggests that variations in calculated turbulent quantities will be driven towards progressively smaller amplitudes. This negative eigenvalue is responsible for the improved long-time behavior of the pertinent turbulent field statistics, and justifies the proposed

modification to Lundgren's original source term.

3.4 Summary and Conclusions

In summary, although Lundgren's original velocity field forcing technique can successfully drive a turbulent field to and sustain it at the desired Re_λ, the turbulent statistics are subject to considerable and large oscillations in their long-time behavior. A practical implication of these large amplitude fluctuations is that simulations must be conducted for a significantly longer period of time in order to obtain time-invariant quantities. Through a linear perturbation analysis, the cause for this undulating statistical behavior has been connected to the form of the momentum source term appended to the Navier-Stokes equations and to the resulting stability characteristics of the forced-turbulent kinetic energy-dissipation rate equation system. A modification to Lundgren's momentum source term has been proposed, which is more consistent with existing spectral forcing methods. Upon application of this modified source term, the temporal behavior of the turbulent statistics was found to be improved, while the spectral characteristics of the velocity field produced were preserved. Moreover, statistical stationarity was reached much earlier in the simulation when the proposed modification was implemented. As DNS studies are computationally intensive from the outset, this reduction in the time necessary to attain temporally-invariant turbulent physics when using the proposed modified source term is of practical significance.

Chapter 4

Turbulent Mixing in the Scalar Field [14]

Turbulent mixing in the velocity field is not the only type of mixing of concern in the current work. The numerical framework to be proposed also endeavors to represent accurately turbulent mixing in the scalar field. Accordingly, a new scalar field forcing method has been developed to simulate the relevant scalar field physics in preparation for the later study of mixing in turbulent buoyant mixing layers.

A passive scalar is a quantity in a flow that will convect and diffuse without impacting the evolution of the velocity field. The mixing of these types of scalars in turbulent flow environments are found in a broad range of fields, including combustion, atmospheric flow dynamics, and oceanography. Direct Numerical Simulation (DNS) studies of scalar mixing often use numerically-forced velocity and scalar fields to prevent the turbulent fluctuations from decaying. To ensure that results obtained in such DNS studies are representative of the physics of scalar mixing, and not an artifact of the numerical schemes, the forcing methods used must not alter the physics of the flow configuration to be studied. The most commonly used method for sustaining turbulent fluctuations in a scalar field is to supply scalar variance continuously via a spatially-uniform mean scalar gradient [105, 30]. Spectral schemes utilizing low waveband forcing [46] have been used also, and these supply scalar variance over a narrow band of waveshells within the turbulent scalar field. These methods are both equivalent to holding the scalar variance constant via continuous variance injection. This chapter presents a new scalar forcing technique that instead uses one-time variance injection to prevent variance decay. It is shown that this new scalar forcing methodology corresponds to a distinctly different physics than the other two commonly used methods, and that it is more representative of the mixing regime of ultimate interest.

There are many applications in which forcing proportional to a scalar gradient is physically meaningful. In many oceanographic and atmospheric flows, there are gradients in species concentration or temperature. In these instances, as long as the gradient of the scalar quantity of interest

---

is uniform over distances longer than the largest characteristic length-scale of the turbulent flow, implementing such a numerical forcing technique is entirely consistent with the physics of the flow configuration [20, 21]. Applying a spatially uniform scalar gradient across the scalar field allows this field to remain homogeneous and to reach a state of statistical stationarity [41, 29, 21]. Nevertheless, the imposed mean scalar gradient introduces robust anisotropy into the scalar field, which can be problematic for studies of scalar mixing under isotropic conditions. Low waveshell spectral forcing techniques [46, 96, 16] eliminate this problem by implementing a perfectly isotropic forcing term. However, these schemes are less physically representative of experimentally attainable flows.

The goal of this work is to develop and validate a new scalar field forcing technique that can capture the physics of self-similar scalar field decay, which is an inherently different physics than that captured by the two existing scalar forcing methods. As decay processes are isotropic, the statistics of isotropy need to be respected. Further, such a self-similar scalar mixing state is the regime that is most appropriate for turbulent buoyant mixing, the study of which is the ultimate aim of this work. Accordingly, the objectives for this forcing are two-fold. First, the forcing must be able to reproduce scalar mixing under the desired turbulent conditions. Second, the forcing must preserve the statistics of isotropic turbulence across all scales of the flow. These requirements will be considered in light of existing velocity forcing methods, which have been proven to be effective means of preventing turbulent kinetic energy from decaying [58, 81].

Central to this work is the observation that turbulent mixing of scalars may not always occur in an environment where the scalar field is subject to continuous energy injection; these scalars may undergo turbulent mixing where there is only an initial source of scalar energy, followed by scalar variance decay. This new proposed scheme aims to create a scalar field constrained to constant scalar energy (or scalar variance), and it will be shown to be equivalent to creating a state of "normalized decay." Examples of situations for which this forcing would be appropriate can be found in engineering applications, such as in heated grid turbulence experiments, and in natural phenomena, such as sedimentation processes found in oceanographic flows. Note that these types of flows are subject to buoyancy effects. This proposed forcing scheme, referred to as the linear scalar forcing method throughout the remainder of this work, is validated against its ability to predict the statistical characteristics and energy spectrum of a scalar field subject to temporal decay. The forcing method is examined over a range of relatively low Taylor-Reynolds numbers and low to moderately high Schmidt numbers.

The structure of this chapter is as follows. Section 4.1 provides a brief overview of passive scalar transport. Section 4.2 presents the two most commonly implemented scalar forcing methods (mean gradient and low waveband spectral) and introduces the linear scalar forcing method. The derivation and motivation for the linear scalar forcing method is provided. Section 4.3 describes the connection between the physics captured by scalar field forcing methods to those measured in experimentally

attainable geometries. Section 4.4 details the procedure and test cases used to validate the linear scalar forcing method. Additionally, key single- and two-point scalar field metrics are shown and used to support the physical fidelity of the proposed method. Section 4.5 investigates high Schmidt number physics as generated by the mean gradient and the linear scalar forcing method. This is done to highlight the distinctly different physics (continuous *vs.* one-time scalar variance injection) to which the two methods correspond. Lastly, Section 4.6 provides a justification as to why the proposed method is appropriate for turbulent and turbulent buoyant mixing studies. It is noted here that the code implemented in the presented simulations is described in Appendices 8.3, Appendix 8.4, and 8.6, and the scalar transport schemes implemented (HOUC5 and QUICK) are described in Appendix 8.5.

4.1 Turbulent Scalar Transport and Yaglom's Equation

4.1.1 Scaling Regions in the Scalar Energy Spectrum

Prior to delving into the specifics of scalar field forcing, an overview of a few of the most salient features involved in passive scalar transport is given. Following Chapters 2 and 3, the spectral content of a scalar field is analogous to that discussed for the velocity field. The kinetic energy in the velocity field is distributed spectrally, and this spectral distribution is described by the energy spectrum, $E(\kappa)$. The integral of $E(\kappa)$ in wavespace provides the turbulent kinetic energy, $k = \frac{1}{2}\langle u_i u_i \rangle = \int_0^\kappa E(\kappa)\ d\kappa$. If the Reynolds number is high enough to support complete separation between the energy producing and the energy dissipating scales, then there manifests a (self-similar) inertial subrange across the so-called inviscid scales, $1/l_0 \ll \kappa \ll 1/\eta$. Here, l_0 and η remain the integral length-scale for the velocity field and the Kolmogorov scale ($\eta = \left(\nu^3/\epsilon\right)^{1/4}$). Within this range, under suitably high Reynolds number conditions, the classic energy spectrum scaling is obtained,

$$E(\kappa) \propto \epsilon^{2/3}\kappa^{-5/3}. \tag{4.1}$$

Such spectrum scaling approaches to turbulence revolve around characterizing the dependence of flow statistics on the range of scales present, while also incorporating the effects of multiple physical processes acting over different scales in space and time [77]. A similar approach can be applied to the scalar field to develop scalar energy spectrum scalings [91]. In the scalar field, the scalar energy spectrum, $E_Z(\kappa)$, has a form that is dependent on the relative comparison of the size of the smallest viscous scale (η) to the smallest diffusive scale (the Batchelor scale, $\eta_B = \eta Sc^{-1/2}$). Note that this still assumes that the Reynolds number is sufficiently high for an inertial subrange to form in the velocity field. Thus, depending on the Schmidt number, Sc, of the flow, the behavior of the scalar

energy spectrum across these inviscid scales varies.

Kolmogorov's phenomenological theory of turbulence was first applied to passive scalar transport by Obukhov [69] and Corrsin [21] for $Sc \sim O(1)$. This was accomplished by relating the time-scale, $\tau_\kappa = \kappa E_Z(\kappa)/\chi$, of the scalar energy spectrum at a particular scale, $1/\kappa$, to that of the velocity field, $\tau_v = \left(\epsilon^{1/3}\kappa^{2/3}\right)^{-1}$, at the same scale. If $Sc \sim O(1)$, then the range of scales present in the scalar and velocity fields ought to be similar. Here, and throughout the remainder of this thesis, $\chi = \langle 2\mathcal{D}|\nabla Z|^2\rangle$ is the scalar dissipation rate. When τ_κ is equated with τ_v, the energy spectrum obtained is,

$$E_Z(\kappa) = C_{OC}\chi\epsilon^{-1/3}\kappa^{-5/3}. \tag{4.2}$$

This is valid for the range of scales $1/L \ll \kappa \ll 1/\eta_B$, and C_{OC} is the Obukhov-Corrsin constant. This range of scales, across which neither viscosity nor diffusivity is important, is termed the inertial-convective subrange.

Similar efforts have also been applied to derive scaling laws for the scalar energy spectrum under high $(Sc \gg 1)$ and low $(Sc \ll 1)$ Schmidt number conditions. Under high Schmidt number conditions, the Batchelor scale, η_B, is smaller than the Kolmogorov scale, η. In this instance, a viscous-convective subrange may develop. In the viscous-convective subrange, $\kappa\eta \gg 1$ and $\kappa\eta_B \ll 1$. This implies that viscosity is important, but diffusivity is not yet important. Batchelor [7] derived an expression for the scaling across such a region of the scalar energy spectrum by arguing that the scalar field at these scales were subject to a strain-rate of $\tau_\eta^{-1} = (\nu/\epsilon)^{-1/2}$. If this is equated with the scalar energy time-scale $\tau_\kappa = \kappa E_Z(\kappa)/\chi$, then Batchelor's classic energy spectrum scaling is obtained,

$$E_Z(\kappa) = C_B\chi\left(\nu/\epsilon\right)^{1/2}\kappa^{-1}. \tag{4.3}$$

This is valid for the range of scales $1/\eta \ll \kappa \ll 1/\eta_B$ and C_B is the so-called Batchelor constant. A slight correction to this was later added by Kraichnan [49]; this correction allowed for the strain-rate to fluctuate instead of being a constant, as assumed by Batchelor $(\tau_\eta^{-1} = (\nu/\epsilon)^{-1/2})$. This scaling will be revisited in Section 4.5, and the assumptions on which it is based are more thoroughly discussed.

Under low Schmidt number conditions, an inertial-diffusive region of the scalar energy spectrum may emerge. This region is described by $\kappa\eta_B \gg 1$ and $\kappa\eta \ll 1$. Batchelor provided an energy spectrum scaling for this span of diffusion dominated scales based on a balance between convection and diffusion [42],

$$E_Z(\kappa) = \frac{1}{3}C_K\chi\epsilon^{2/3}\mathcal{D}^{-3}\kappa^{-17/3}. \tag{4.4}$$
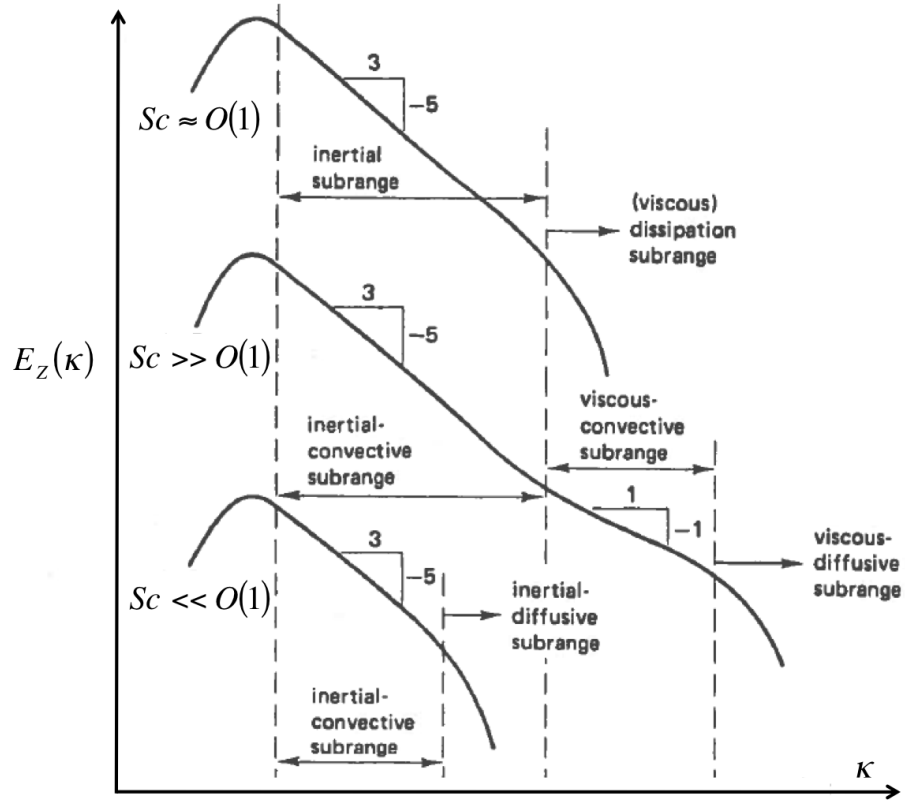
Figure 4.1: Figure modified from *A First Course in Turbulence* [91] (Fig. 8.11).

Gibson [42, 39] also offered a scaling argument for this class of scalar field physics based on considerations focused around zones of weak or vanishing scalar gradients,

$$E_Z(\kappa) = C_G \chi \mathcal{D}^{-1} \kappa^{-3}. \tag{4.5}$$

As this regime of scalar field physics, $Sc \ll 1$, has not been subject to rigorous examination by Direct Numerical Simulation (DNS) studies and it is difficult to experimentally probe, these two scaling expressions are largely untested.

A sketch of these regions of the scalar energy spectrum is provided in Fig. 4.1. This sketch serves to highlight the role of Sc in determining the span of scales present in the scalar field. This work focuses only on the inertial-convective and viscous-diffusive subranges of the scalar energy spectrum, as low Sc conditions are not considered. However, the included description of the inertial-diffusive subrange is included for the sake of completeness.

4.1.2   Yaglom's Equation

In Chapter 2, the Karman-Howarth (KH) equation was derived. The KH equation described the evolution of velocity correlation, $f(r)$, in terms of structure functions $B_{ll}(r)$ and $B_{lll}(r)$. Recall that r corresponded to the magnitude of the two-point separation between fluid points. Thus, $r = |\underline{r}|$. These structure functions were defined in terms of correlations of moments of velocity field differences (Eq. 2.9). A similar type of evolution equation for the scalar field was derived by Yaglom [4, 63, 101] in terms of the second-order moment of the scalar increment, $\langle (\Delta Z)^2 \rangle$, and the third-order mixed moment of the scalar increment with the longitudinal component of the velocity increment, $\langle \Delta u_l \, (\Delta Z)^2 \rangle$. Here, $\Delta Z = Z(\underline{x} + \underline{r}, t) - Z(\underline{x}, t)$ and $\Delta u_l = u_l(\underline{x} + \underline{r}, t) - u_l(\underline{x}, t)$.

Note that the averaging procedure, $\langle \cdot \rangle$, as intially performed by Yaglom denoted time averaging. In the current work, time averages can be replaced with volume averages. The current work is concerned only with turbulent fields that reach a state of statistical stationarity. Under this condition, ensemble averages are equivalent to averages over an infinite time. Similarly, since the configuration in all presented data sets is homogeneous in space, ensemble averages are equivalent to averages over an infinite volume. Thus, ensemble averages can be represented as volume averages over the triply periodic domain.

Following the same procedure as outlined in Chapter 2 to derive the KH equation, Yaglom's equation can be obtained by manipulating the (incompressible) advection-diffusion equation at two different fluid points. Using the notation $Z = Z(\underline{x}, t)$, $Z' = Z(\underline{x} + \underline{r}, t) = Z(\underline{x}', t)$, $u_i = u_i(\underline{x}, t)$, and $u_i' = u_i(\underline{x} + \underline{r}, t) = u_i(\underline{x}', t)$, the relevant equations become,

$$\frac{\partial Z}{\partial t} + u_i \frac{\partial Z}{\partial x_i} = \frac{\partial}{\partial x_i} \left(\mathcal{D} \frac{\partial Z}{\partial x_i} \right) \tag{4.6}$$

$$\frac{\partial Z'}{\partial t} + u_i' \frac{\partial Z'}{\partial x_i'} = \frac{\partial}{\partial x_i'} \left(\mathcal{D} \frac{\partial Z'}{\partial x_i'} \right). \tag{4.7}$$

By multiplying Eq. 4.6 by Z' and Eq. 4.7 by Z, and then adding the two resulting expressions, Yaglom's equation is found [4, 22, 23, 72, 101, 63]. Note that in Eq. 4.6 and Eq. 4.7, Z is the fluctuating scalar quantity, u_i is the velocity component, and $\mathcal{D}$ is the molecular diffusivity. When these two resulting expressions are summed, (ensemble) averaged, have the assumptions of homogeneity and isotropy applied (such that $\Delta u_l(r) = \Delta u_i(\underline{r}) r_i / r$), and volume-integrated, it is obtained,

$$-\frac{2}{3} \chi r - \frac{1}{r^2} \int_0^r y^2 \frac{\partial}{\partial t} \langle (\Delta Z)^2 \rangle \, dy = \langle \Delta u_l \, (\Delta Z)^2 \rangle - 2 \mathcal{D} \frac{d}{dr} \langle (\Delta Z)^2 \rangle. \tag{4.8}$$

This equation has four terms each of which is now a function of the magnitude of the two-point separation distance between fluid points, $r = |\underline{r}|$. Beginning on the left-hand side, there are two terms. The first term on the left-hand side is associated with the transfer of scalar variance at scale

r. The second term on the left-hand side is a so-called non-stationary term. In the cases to be considered in this study, this term is necessarily zero, as all scalar fields to be presented are forced to a state of statistical stationarity. The right-hand side also has two terms. The first term on the right-hand side is a turbulent advection term that is associated with the transfer of scalar variance at scale r. The term on the far right is a diffusive term, which describes the transport of scalar variance by diffusion [22, 23, 72, 42].

In Yaglom's original derivation, the non-stationary term was neglected. Thus, Yaglom's equation describes the transfer of scalar variance (left-hand side) as having contributions from turbulent advection and molecular diffusion (right-hand side),

$$-\frac{2}{3}\chi r = \langle \Delta u_l \left(\Delta Z \right)^2 \rangle - 2\mathcal{D}\frac{d}{dr}\langle (\Delta Z)^2 \rangle. \tag{4.9}$$

Under conditions where the diffusivity of the scalar is not of importance, such as across $\eta_B \ll r \ll l_Z$, where l_Z is the integral scale of the passive scalar [42], Yaglom's relation, or the two-thirds law, is obtained,

$$\langle \Delta u_l \left(\Delta Z \right)^2 \rangle = -\frac{2}{3}\chi r. \tag{4.10}$$

It should be here noted that one of the necessary conditions for the realization of the two-thirds law is the neglect of the diffusion term, and this is valid in both the inertial-convective and viscous-convective subranges of the scalar field. One of these ranges will manifest if either the Reynolds number is sufficiently high ($Re \sim O(10^4)$) [79, 80] or the Schmidt number is large ($Sc \gg O(1)$).

It is not uncommon to calculate the mixed third-order correlation term, $\langle \Delta u_l \left(\Delta Z \right)^2 \rangle$, and χ, and then to compensate their ratio by the separation distance, r, to determine how closely a given scalar field approaches the two-thirds law [4]. However, it is not entirely agreed upon as to the rate at which such an asymptotic behavior is approached ($\langle \Delta u_l \left(\Delta Z \right)^2 \rangle / \left(\chi r \right) = -2/3$), nor how the explicit and implicit assumptions in Yaglom's derivation affect its realization in real flow fields. It follows from this that, for the current work, the asymptotic behaviors of the terms in Yaglom's equation are not investigated for any of the scalar field data to be presented. This is done for four reasons. First, the Reynolds and Schmidt numbers included in this thesis are relatively low or moderate ($Re_\lambda \leq 140$ and $1 < Sc < 256$). For intermediate Reynolds numbers ($100 < Re_\lambda < 500$) and moderate Schmidt numbers, Yaglom's (and Kolmogorov's) equation are known to not be satisfied, as both assume a sufficiently high Re_λ to ensure scale separation and an inviscid subrange in the scalar (and velocity) field [23, 65, 66]. Second, a span of Sc are examined. It has been suggested that the asymptotic behavior of these mixed third-order and second-order moments has a Schmidt number dependence [72]. These two points create uncertainty as to the asymptotic behaviors that ought to be obtained for the terms in Yaglom's equation. Third, the objective of this chapter is to

develop, discuss, and validate a new scalar field forcing technique. Calculating the behavior of the turbulent transport term and the diffusive transport term in Eq. 4.9 does not advance this objective. However, an introduction and brief discussion of Yaglom's equation is included here for completeness and to draw a corollary with the work presented for the velocity field in Chapter 2. Lastly, although the scalar forcing methods derived in this chapter focus on passive scalar quantities, an ultimate end of this work is to study variable density scalar mixing. In this instance, the scalar is active. As such, it is not known how (or if) Yaglom's relation holds under these circumstances.

4.2 Scalar Field Forcing Methods

4.2.1 Mean Scalar Gradient Method

In simulation studies of turbulent passive scalar mixing, the mean scalar gradient forcing technique superimposes a uniform mean gradient across the scalar field,

$$z = Z + \mathcal{G}_i x_i, \tag{4.11}$$

where the total scalar quantity, z, is broken down into a fluctuating part, Z, and a spatially-varying mean part, $\mathcal{G}_i x_i$. All simulations discussed in this chapter impose the mean gradient in a single direction, $\mathcal{G} = [-1, 0, 0]$. Such a forcing technique captures the formation of ramp-cliff structures in, and the intermittency of, the scalar field, consistent with the findings of experimental studies of passive scalar mixing, by virtue of the anisotropy it induces [94, 97]. This scalar forcing technique is quite effective, and it was created to capture the scalar field behavior present in grid turbulence experiments [21].

The transport equation for the fluctuating scalar in the presence of a mean gradient, assuming incompressibility ($\partial u_i / \partial x_i = 0$), is given by,

$$\frac{\partial Z}{\partial t} + u_i \frac{\partial Z}{\partial x_i} = \frac{\partial}{\partial x_i} \left(\mathcal{D} \frac{\partial Z}{\partial x_i} \right) - \mathcal{G}_i u_i, \tag{4.12}$$

where $\mathcal{D}$ is the molecular diffusivity. The imposed mean scalar gradient term, $\mathcal{G}$, acts as an infinite reservoir for the scalar field. Whenever there are losses due to dissipation, the presence of a gradient term will immediately "inject" into the scalar field a scalar quantity magnitude sufficient to compensate. Thus, it provides for continuous scalar energy injection, sustaining the scalar field at a statistically stationary state. Beginning with the forced advection-diffusion equation, Eq. 4.12, and multiplying by the scalar fluctuation, Z, results in,

$$\frac{\partial Z^2}{\partial t} + \frac{\partial \left(u_i Z^2 \right)}{\partial x_i} = \frac{\partial}{\partial x_i} \left(\mathcal{D} \frac{\partial Z^2}{\partial x_i} \right) - 2\mathcal{D} \frac{\partial Z}{\partial x_i} \frac{\partial Z}{\partial x_i} - 2\, Z \left(\mathcal{G}_i u_i \right), \tag{4.13}$$

where incompressibility has been assumed. When Eq. 4.13 is averaged over a triply periodic, homogeneous domain (in which all work to be presented is conducted), only the time derivative, scalar dissipation rate ($\chi = \langle 2\mathcal{D} \mid \nabla Z \mid^2 \rangle$), and the forcing term retain non-zero values. This leaves,

$$\frac{\partial \langle Z^2 \rangle}{\partial t} = -\chi - 2\,\mathcal{G}_i \langle u_i Z \rangle = -\chi + 2\,\langle u_x Z \rangle. \tag{4.14}$$

The angled brackets, $\langle \, \cdot \, \rangle$, refer to volumetric averages. Equation 4.14 implies that if the scalar field were to attain perfect isotropy (*i.e.* $\langle u_i Z \rangle = 0$), then the time-rate of change of scalar variance would always be negative and equal to the scalar dissipation rate (χ), causing continuous scalar field decay. It is the anisotropy, evident from the skewed probability density function (PDF) of the scalar fluxes in Fig. 4.2, that prevents the variance of the scalar field from decaying.

Further, due to the anisotropy inherent in this forcing mechanism, it is used primarily for passive scalars; the velocity field affects the scalar field, but the scalar field does not couple back to effect the velocity field. With an active scalar, the coupling is two-way, with information being passed between the turbulent velocity and scalar fields. The anisotropy that is methodically maintained in the scalar field would have the opportunity to permeate into the velocity field. There may be physical configurations in which such a coupling is consistent with the physics governing the problem, but this may not always be the case.

4.2.2   Low Waveband (Spectral) Method

Spectral forcing techniques continuously provide energy into the scalar field over a range of tightly constrained, low wavenumber shells ($\kappa_{lower} \leq \kappa \leq \kappa_{upper}$) [16, 96, 46]. The advection-diffusion equation resulting from such a forcing scheme is given by,

$$\frac{\partial Z}{\partial t} + u_i \frac{\partial Z}{\partial x_i} = \frac{\partial}{\partial x_i}\left(\mathcal{D}\frac{\partial Z}{\partial x_i}\right) + \mathscr{F}_{\underline{x}}^{-1}\{\hat{f}_Z(\kappa)\}, \tag{4.15}$$

where $\mathscr{F}_{\underline{x}}^{-1}\{\cdot\}$ denotes the inverse Fourier-transform of the forcing term in spectral space. The spectral forcing implemented in this work has a forcing term with a Gaussian distribution centered about a wavenumber of $\kappa = 3$ that is active only between the upper and lower bounds of $\kappa_{upper} = 4$ and $\kappa_{lower} = 2$. With such a forcing scheme, as with the mean gradient method, the scalar variance is held fixed in time because losses from scalar dissipation are balanced by continuous injection of scalar variance into the scalar field by the forcing term, $\langle Z\mathscr{F}_{\underline{x}}^{-1}\{\hat{f}_Z(\kappa)\}\rangle$.

The primary, and only significant, difference between the mean gradient and spectral scalar forcing methods is that a random spectral forcing is capable of producing perfectly isotropic scalar fluxes, as illustrated in Fig. 4.3(a). The character of the scalar field produced under the action of the two forcings are consistent. Both produce a scalar quantity that is approximately normally distributed
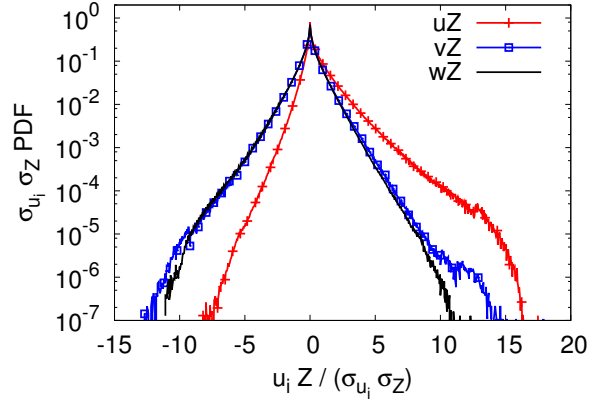
(a) Spectral velocity forcing [1]
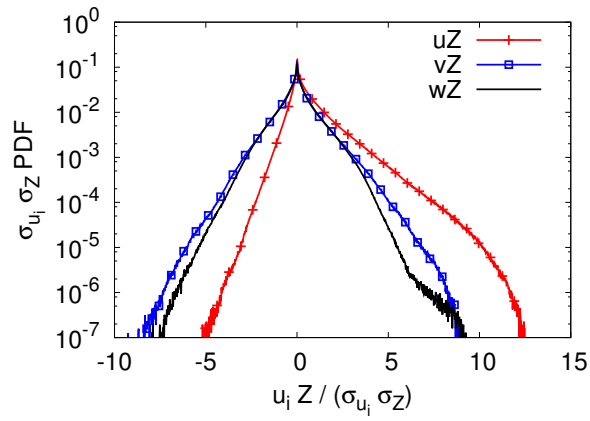
(b) Linear velocity forcing [81]

Figure 4.2: PDF of scalar fluxes obtained using a mean scalar gradient forcing and two different velocity forcing techniques [1, 81]. The σ variables refer to standard deviations. The simulation code implemented is described in Appendix 8.3 and Appendix 8.4, and the HOUC5 scalar transport scheme implemented is described in Appendix 8.5. The simulation parameters are $N = 512^3$, $Re_\lambda = 140$, $Sc = 1$, and $\kappa_{max}\eta_B = 1.5$.
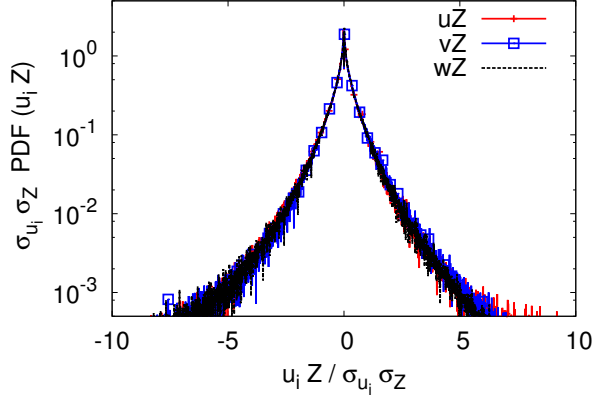
(a) Scalar fluxes, $u_i Z$
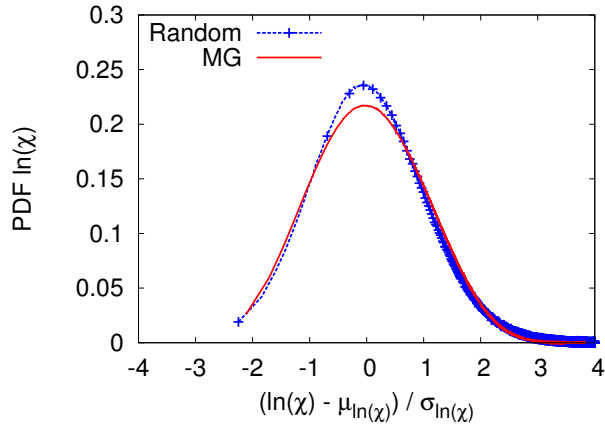
(b) Scalar dissipation rate, χ

Figure 4.3: Statistical metrics of the scalar field produced via low waveband spectral (random) forcing versus mean gradient forcing (MG) ($N = 256^3, Re_\lambda = 55, Sc = 1, \kappa_{max}\eta_B = 3.0$). The simulation code implemented is described in Appendix 8.3 and Appendix 8.4, and the HOUC5 scalar transport scheme implemented is described in Appendix 8.5.

about a mean of zero and a log-normally distributed scalar dissipation rate. Representative results are provided in Fig. 4.3(b). Furthermore, as depicted in Fig. 4.4, a low waveband spectral forcing scheme and the mean scalar gradient scheme give comparable scalar spectra over a range of Schmidt numbers, $Sc = \nu/\mathcal{D}$. Here, ν represents the kinematic viscosity of the fluid. Representative low and high Sc cases are included in support of this claim.

As the only chief difference in these two methods is the issue of isotropy in the scalar fluxes, the rest of this chapter focuses primarily on the direct comparison of the proposed linear scalar forcing method to the mean scalar gradient forcing method. This comparison is preferred, as the mean scalar gradient is more widely applied in simulation studies of mixing, and the configuration it represents is more readily attainable experimentally.
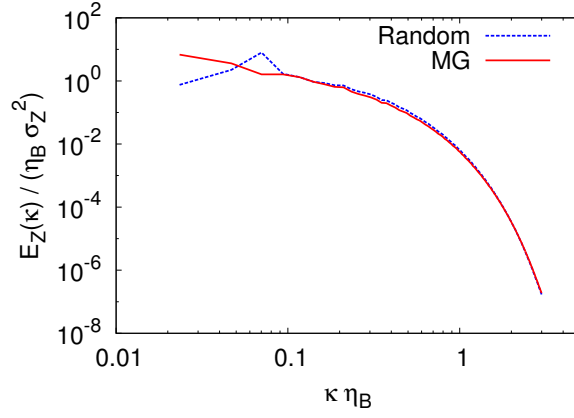
(a) $N = 256^3, Re_\lambda = 55, Sc = 1, \kappa_{max}\eta_B = 3.0$ (linear velocity forcing [81])
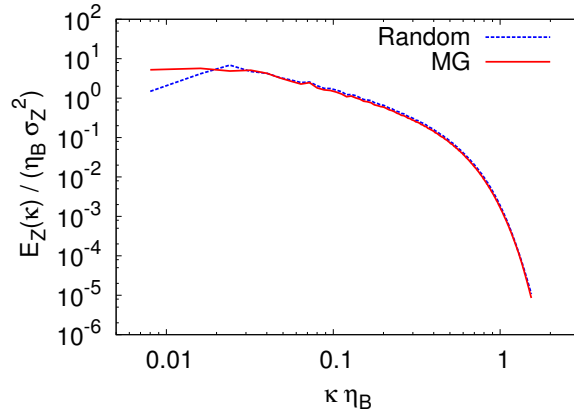
(b) $N = 384^3, Re_\lambda = 8, Sc = 256, \kappa_{max}\eta_B = 1.5$ (spectral velocity forcing [1])

Figure 4.4: Comparison of scalar energy spectra obtained using the mean gradient (MG) and random spectral forcing.

4.2.3 Linear Scalar Method

As discussed in Chapter 2, there are two broadly-accepted ways of forcing the velocity field in numerical studies, linearly [58, 81] and spectrally [1]. The present work draws on Lundgren's linear forcing scheme [81] as inspiration for the development of the linear scalar forcing technique. According to the linear forcing scheme, momentum is injected into the velocity field proportional to the magnitude of the velocity fluctuations, and it assumes the form,

$$\frac{\partial u_i}{\partial t} + u_j \frac{\partial u_i}{\partial x_j} = -\frac{1}{\rho}\frac{\partial p}{\partial x_i} + \nu \frac{\partial}{\partial x_j}\left(\frac{\partial u_i}{\partial x_j}\right) + Qu_i, \tag{4.16}$$

where Q is a constant related to the energy dissipation rate and eddy turn-over time, τ, and incompressibility is assumed.

Forcing linearly is equivalent to injecting energy at all scales of the flow, from the integral scales to the dissipative scales. But, as the fluctuations are the largest at the integral scales, the energy injection is biased preferentially towards these larger scales. The linear forcing scheme is found to produce characteristics consistent with the requirements of homogeneous, isotropic turbulence, namely equal-averaged Reynolds stresses and symmetrically distributed scalar fluxes with reflectional symmetry [81]. More relevant to the present work, Lundgren's linear forcing method can be connected directly to the self-similar nature of decaying turbulence [58]. In this method, energy injection can be thought of as a rescaling of the kinetic energy to a constant value. By performing a change of variables in space, time, and velocity on the forced and unforced (freely-decaying) momentum equations, Lundgren found that the transformed, freely-decaying momentum equation admitted terms that were similar in form to those present in the linearly-forced momentum equation. From this finding, he concluded that the effect of the linear forcing technique is similar to that of energy decay, which is inherently isotropic and self-similar. Thus, the self-similar decay of energy in the velocity field is suggested to be analogous to the imposed isotropic forcing term, Qu_i [58].

4.2.3.1 Self-Similarity of Scalar Mixing

Following Lundgren's work on linear velocity forcing, the objective of this work is to develop a new forcing scheme that reproduces the physics of the self-similar decay of a scalar field. The self-similar regime of scalar mixing manifests itself whenever there is one-time energy injection into a scalar field. Following this energy injection, there is a short-lived transient period of decay which eventually gives way to a self-similar flow regime. Self-similarity, in the context of a decaying scalar field, is characterized by the collapse of freely decaying scalar spectra onto a single spectrum shape after appropriate normalization. To demonstrate this aspect of self-similarity, a scalar field is forced to statistical stationarity and then allowed to decay. Referring to Fig. 4.5(a), forcing in the scalar field is removed at $t/\tau = 0$, and the variance is allowed to decay. Here, τ is the eddy turn-over time,
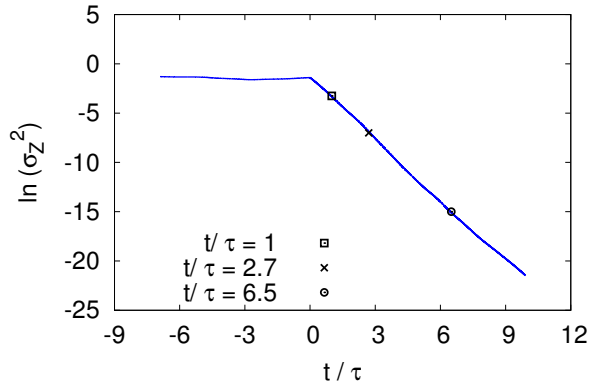
(a) Scalar variance
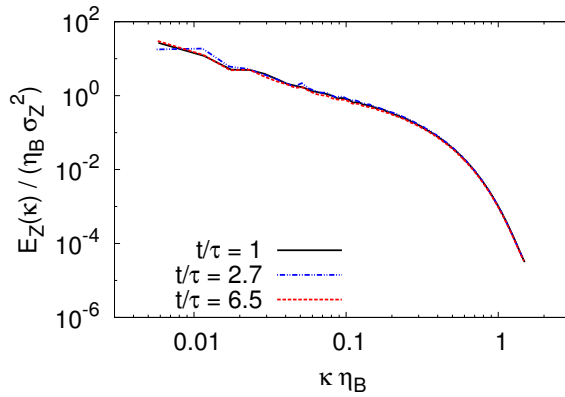
(b) Normalized scalar spectra

Figure 4.5: Decay of scalar variance and collapse of scalar energy spectra in the self-similar regime ($N = 512^3$, $Re_\lambda = 140$, $Sc = 1$, $\kappa_{max}\eta_B = 1.5$).

which is equal to the ratio of turbulent kinetic energy to the energy dissipation rate. It is clear from Fig. 4.5(a) that the scalar field is losing variance without the forcing term active. Figure 4.5(b) illustrates the behavior of the self-similar field; the three normalized scalar spectra in Fig. 4.5(b) correspond to the three data points in Fig. 4.5(a) at 1, 2.7, and 6.5 τ after the scalar forcing was removed. The coincidence of the spectra to one unchanging shape when normalized by their variances indicates that this scalar field has entered the self-similar regime.

Considering the nature of self-similar decay, it can be argued that to model this type of scalar mixing, a scalar forcing method based on scalar variance normalization is needed. These concepts of variance normalization and self-similarity, in addition to Lundgren's insight that an isotropic forcing can be thought of in terms of sustained, normalized energy decay, serve as the foundation for the development of the proposed linear scalar forcing method.

4.2.3.2 Derivation of the Proposed Linear Scalar Forcing Term

As mentioned previously, the development of this new scalar forcing is motivated by the successful implementation [81] of the linear velocity forcing of Lundgren [58] and the concepts of normalization and self-similarity. Note that in the derivation to follow that, although the same variables are used to denote scalar quantities (Z and z), these quantities do not have the same definitions that were used in Sections 4.2.1 and 4.2.2. Following Lundgren's linear velocity forcing, a normalization method is needed to drive the scalar field (z) towards a constant energy, or variance, $\sigma_z^2 = \langle z^2 \rangle - \langle z \rangle^2$. After initialization, all turbulent quantities begin to decay as they are convected and diffused through the simulation domain. The proposed scalar forcing technique seeks to generate self-similar conditions by implementing two steps. First, there is a rescaling step. Second, there is a step to drive the scalar field to a specified, imposed variance value, α^2. The absolute value of the rescaled scalar field variance, α^2, is inconsequential; the significant factor is solely that the scalar field variance is constant in time.

Beginning with the rescaling step, the scalar field is rescaled according to,

$$Z = z\sqrt{\frac{\alpha^2}{\sigma_z^2}}, \tag{4.17}$$

where Z is the normalized, forced scalar quantity, z is the unforced (non-normalized) scalar quantity, and σ_z^2 is the variance of the non-normalized scalar field. Using the normalization defined, the required form of the linearly-forced advection-diffusion equation can be determined readily by consideration of the spatially-averaged variance equation (Eq. 4.14 without the mean gradient term),

$$\frac{\partial \sigma_z^2}{\partial t} = -\chi, \tag{4.18}$$

where it has been assumed that the mean of the decaying scalar quantity is zero, $\langle z \rangle = 0$. By differentiating Eq. 4.17 and substituting Eq. 4.18, the rate of change of the rescaled scalar quantity, Z, can be written as,

$$\frac{\partial Z}{\partial t} = \sqrt{\frac{\alpha^2}{\sigma_z^2}}\frac{\partial z}{\partial t} + \frac{1}{2}\frac{\chi(z)}{\sigma_z^2}Z, \tag{4.19}$$

where $\chi(z)$ and σ_z^2 are functions of the decaying scalar (z), not the rescaled scalar (Z). Recall that the advection-diffusion equation for any scalar quantity under incompressible conditions can be expressed as,

$$\frac{\partial z}{\partial t} = \frac{\partial}{\partial x_i}\left(\mathcal{D}\frac{\partial z}{\partial x_i}\right) - u_i\frac{\partial z}{\partial x_i}. \tag{4.20}$$

Using this expression for $\frac{\partial z}{\partial t}$, Eq. 4.19 becomes,

$$\frac{\partial Z}{\partial t} = \frac{1}{2}\frac{\chi(z)}{\sigma_z^2}Z + \frac{\alpha}{\sigma_z}\left(\frac{\partial}{\partial x_i}\left(\mathcal{D}\frac{\partial z}{\partial x_i}\right) - u_i\frac{\partial z}{\partial x_i}\right). \qquad (4.21)$$

Note that α^2 and σ_z^2 are volume-averaged quantities and, therefore, are constant with respect to any spatial derivative. In other words,

$$\nabla Z = \frac{\alpha}{\sigma_z}\nabla z, \qquad (4.22)$$

and, further,

$$\chi(Z) = \chi(z)\frac{\alpha^2}{\sigma_z^2}. \qquad (4.23)$$

Substituting these expressions into Eq. 4.21 results in an expression for the time-rate of change of the rescaled scalar quantity (Z) in terms of Z only,

$$\frac{\partial Z}{\partial t} = \frac{\partial}{\partial x_i}\left(\mathcal{D}\frac{\partial Z}{\partial x_i}\right) - u_i\frac{\partial Z}{\partial x_i} + \frac{1}{2}\frac{\chi(Z)}{\alpha^2}Z. \qquad (4.24)$$

Although the above expression is mathematically consistent with the rescaling step, it was found that the scalar field could become divergent, depending on its initial variance. It is the presence of α^2 in the denominator that is responsible for this behavior. This behavior can be understood by examining the variance equation corresponding to Eq. 4.24. Upon volume-averaging, applying the condition of homogeneity, and recalling the definition of χ, Eq. 4.25 is obtained,

$$\frac{\partial\langle Z^2\rangle}{\partial t} = \frac{\partial\sigma_Z^2}{\partial t} = \chi(Z)\left(\frac{\sigma_Z^2}{\alpha^2} - 1\right). \qquad (4.25)$$

By inspection of Eq. 4.25, if the variance value (σ_Z^2) is less than (greater than) α^2, then the time derivative of scalar variance will attain a negative (positive) value, and the scalar variance will decay away towards zero (grow indefinitely).

To avoid this problem, an approximation is made. As it is the long-time (statistically stationary) scalar field behavior with which this study is interested, not the initial transient behavior, α^2 was replaced with the variance of the rescaled scalar field, σ_Z^2. This is a justifiable approximation, as at stationarity, the rescaled scalar field variance will approach α^2. This is not the case in the initial transient period, but it is true in the long-time limit $(\alpha^2 = \sigma_Z^2)$. Thus, Eq. 4.24 can be written as,

$$\frac{\partial Z}{\partial t} = \frac{\partial}{\partial x_i}\left(\mathcal{D}\frac{\partial Z}{\partial x_i}\right) - u_i\frac{\partial Z}{\partial x_i} + \frac{1}{2}\frac{\chi(Z)}{\sigma_Z^2}Z, \qquad (4.26)$$

where the last term on the right hand-side is a scalar production term. With such an expression, the

right hand-side of Eq. 4.25 now becomes zero, enabling the scalar field to attain a state of constant variance.

If energy were discretely conserved in the scalar field, then the solution of the above equation analytically would lead to a statistically stationary scalar field with a constant variance, as the newly added production term would balance exactly all molecular dissipation. Assuming the scalar transport scheme implemented in the numerical solver is perfectly energy conserving, this production term is sufficient to produce a scalar field with a constant time-averaged variance. However, if the transport scheme implemented is not energy conserving (*e.g.* a Weighted-Essentially Non-Oscillatory (WENO) scheme [53], a High-Order Upstream Central (HOUC) scheme [68], or Quadratic Upstream Interpolation for Convective Kinematics (QUICK) scheme [52]), then there are losses in scalar variance due to numerical diffusion. These losses can be easily compensated for via the addition of a second term, which is active only when the effects of numerical diffusion manifest in the scalar field. Note that the simulation code implemented in this work is discretely energy conserving in the velocity field, but it is not discretely energy conserving in the scalar field [26].

The constraints in constructing this second term are threefold. First, it should take the form of a relaxation term, being active only when the variance of the rescaled scalar field is not equal to α^2. This will have the effect of driving the variance to α^2 and sustaining it at α^2. Second, it needs to be dimensionally consistent with Eq. 4.24 (or, equivalently, Eq. 4.26). Lastly, the additional term should be linear with respect to the rescaled scalar quantity, such that it preserves the linearity of the rescaled and unforced advection-diffusion equations. In light of these requirements, this additional relaxation term is of the form,

$$\frac{1}{\tau_R}\left(\sqrt{\frac{\alpha^2}{\sigma_Z^2}}-1\right)Z, \tag{4.27}$$

where τ_R is a relaxation time-scale. If $\sigma_Z^2 = \alpha^2$, then the term is inactive, as the variance of the rescaled field is at its desired value; if $\sigma_Z^2 \neq \alpha^2$, then more (or less) variance is added to (or subtracted from) the rescaled scalar field. The role of the relaxation time-scale is to prevent the relaxation term from adjusting too strongly to changes in scalar variance. Using a time-scale associated with the larger scale flow structures instead of a smaller time-scale on the order of viscous processes (where losses in scalar variance actually occur) ensures that the scalar variance is adjusted sufficiently slowly and smoothly to prevent transient behaviors from being introduced in the scalar field.

The final form of the scalar transport equation with the proposed linear scalar forcing technique is obtained by combining Eq. 4.26 and Eq. 4.27,

$$\frac{\partial Z}{\partial t}+u_i\frac{\partial Z}{\partial x_i}=\frac{\partial}{\partial x_i}\left(\mathcal{D}\frac{\partial Z}{\partial x_i}\right)+\left[\frac{1}{\tau_R}\left(\sqrt{\frac{\alpha^2}{\sigma_Z^2}}-1\right)+\frac{1}{2}\frac{\chi(Z)}{\sigma_Z^2}\right]Z. \tag{4.28}$$

To reiterate, the proposed forcing function is composed of two terms. The relaxation term allows the scalar field to evolve towards a specified variance, or average scalar energy, while the production term balances exactly any losses from scalar dissipation. Note, however, that the relaxation term is required only if the scalar transport scheme used is not energy conserving. If it is energy conserving, then the relaxation term will be effectively inactive. This proposed linear scalar forcing scheme has the advantage of being truly mathematically isotropic, imposing no preferred direction. It is interesting to note that the production term is similar to the linear velocity field forcing term, Qu_i. Analogous to Q, the linear factor, $\frac{1}{2}\chi(Z)/\sigma_Z^2$, is the inverse of a time-scale. However, in this case, it is the inverse of the scalar time-scale, $\tau_Z = \sigma_Z^2/\chi(Z)$.

4.3 Consistency of Mean Scalar Gradient and Linear Scalar Forcing Methods with Physical Geometries

To place the concept of scalar field forcing on a more physical footing, the physical conditions to which forcing proportional to a mean scalar gradient (Section 4.2.1) and forcing according to the linear scalar method (Section 4.2.3) correspond are discussed. The mean scalar gradient method is addressed first.

The physical situation for which forcing proportional to a mean scalar gradient stands as a proxy in simulation studies (*e.g.*, [41, 73, 97, 98, 105]) is commonly found in decaying grid turbulence experiments (*e.g.*, [5, 44, 66, 94]). In these experimental studies, scalar field metrics (*e.g.*, one-dimensional spectra, scalar flux, scalar structure functions, scalar field statitics, *etc.*) are extracted. Generally, the wind tunnel in which these studies are performed has a mean temperature gradient placed across it, and the scalar of interest is the temperature. The mean temperature gradient is usually small such that temperature can be treated still as a passive scalar quantity [5]. The presence of the mean temperature gradient is sustained by heating the front and the back of the wind tunnel differentially. This perpetuates the gradient throughout the experiment and supports temperature fluctuations in the scalar field being convected. The mean scalar gradient forcing method was originally developed to capture this kind of physical scenario [21].

The physical situation for which forcing according to the linear scalar method is appropriate is slightly different. As discussed previously, when the linear scalar method is applied, it sustains the physics of self-similar scalar field decay. This class of physics is attained experimentally by making use of heated grids [3, 5, 24, 44, 95, 94, 107]. This involves differentially heating mandoline wires to a specified temperature to serve as a source of scalar (temperature) variance. Instead of heating the front and back ends of the wind tunnel, only the grid itself is heated. Then, as the fluid of interest is forced through the heated grid, an initial "injection" of temperature (scalar) variance is applied to the flow. After this, the scalar field is convected downstream, and it enters into a self-similar

regime of (isotropic) scalar field decay, as the temperature fluctuations are not replenished. This is the class of physics that the developed linear scalar forcing method is meant to capture [14].

4.4 Validation of the Linear Scalar Forcing Method

The validation of the proposed linear scalar forcing takes the following form. First, the temporal behavior of the forcing is investigated to ensure the average scalar variance asymptotes indeed to a constant value, independent of the initial conditions imposed. Second, the impact of varying the magnitude of the relaxation time-scale is studied. Third, the relevant single-point metrics for isotropy, such as variance and the three scalar fluxes, are calculated to ensure appropriate behavior. Additionally, the distributions of scalar quantities with accepted analytical forms, such as the distribution of the scalar dissipation rate (log-normal), are calculated and verified to be predicted correctly. Lastly, two-point statistics (*e.g.,* spectra) are considered. For each (Re_λ, Sc) combination included in this study, the spectra generated from the linear scalar forcing are compared to spectra from the decay of a scalar field in the self-similar regime.

4.4.1 Simulation Study

The primary objective of this study is to evaluate the characteristics of the proposed linear scalar forcing technique in homogeneous, isotropic turbulent flow over a range of Schmidt numbers. The velocity field is linearly-forced [81] in cases 1-3 and cases 6-11 (Table 4.1), as discussed in Section 4.2.3, and spectrally-forced [1] in cases 4-5 to maintain a suitable Re_λ. The scalar field is forced with both the proposed method (referred to as LS) and the mean scalar gradient method (referred to as MG) to allow for comparison.

The specific simulation parameters and fluid properties (kinematic viscosity, ν, and molecular diffusivity, $\mathcal{D}$), are summarized in Table 4.1. The columns entitled $\kappa_{max}\eta$ and $\kappa_{max}\eta_B$ quantify the simulation resolution, where κ_{max} corresponds to the maximum wavenumber accessible in the simulation, η is the Kolmogorov length-scale, and η_B is the Batchelor length-scale defined as $\eta_B = \eta Sc^{-\frac{1}{2}}$. The Kolmogorov and Batchelor length-scales indicate the smallest characteristic length-scales for the velocity and scalar fields, respectively. Convention mandates highly restrictive resolution requirements for both the velocity and scalar fields when performing DNS studies, or the physics of the dynamically important small scales will not be captured fully. The accepted resolution limits for the velocity and scalar fields are $\kappa_{max}\eta \geq 1.5$ and $\kappa_{max}\eta_B \geq 1.5$, respectively [104], for spectral codes. As the code package implemented in this work is non-spectral, the limits $\kappa_{max}\eta \geq 3.0$ and $\kappa_{max}\eta_B \geq 3.0$ are used to ensure accuracy in the presented test cases. One unfortunate result of these resolution criteria is that simulation studies are restricted to moderate Schmidt numbers, as high-Schmidt number simulations can become too computationally expensive to perform.

To illustrate the robustness and validity of the proposed scalar forcing, a parametric study is performed. The parameters methodically varied include the relaxation time-scale, τ_R, the scalar transport scheme, the nature of the initial conditions, and the Schmidt number, Sc. As will become evident in the following sections, the proposed linear scalar forcing is quite robust.

The simulations to be presented were conducted in a configuration of 3-D periodic turbulence of size $(2\pi)^3$. They were performed with the NGA code package [26]. The code is physical (non-spectral) and uses a standard staggered grid. The velocity field is solved implicitly via a second-order accurate finite-difference scheme, and this scheme is energy conserving. The scalar field is solved implicitly via either the QUICK scalar transport scheme, which is a third-order upwinded finite-volume scheme [52], or a fifth-order accurate upwinded scheme (HOUC5) [68]. The time advancement is accomplished by a semi-implicit Crank-Nicolson method [26]. Further details are provided in Appendices 8.3 - 8.6.

Table 4.1: Simulation parameters for the DNS study conducted. N is the number of grid points, and $\mathcal{D}$ is the molecular diffusivity of the scalar quantity. The following is of note. For cases 3 and 4, $\tau_R = 0.1$. This is done to reduce computational burden for this (Re_λ, Sc) combination. For cases 4 and 5, the velocity field is spectrally-forced [1]; all others are linearly-forced. For case 4, the QUICK scalar transport scheme is used.

Variation of Schmidt Number with HOUC5 scheme (except case 4) and $\tau_R = 1$ fixed						
Case ID	N^3	Re_λ	$\kappa_{max}\eta$	$\kappa_{max}\eta_B$	Sc	$\mathcal{D}$
1	256^3	55	3.0	3.0	1	7.50×10^{-3}
2	256^3	55	2.4	3.4	0.5	1.50×10^{-2}
3	1024^3	55	11.8	2.95	16	4.69×10^{-4}
4	1024^3	140	3.4	3.4	1	2.80×10^{-3}
5	768^3	8	49	3.06	256	6.20×10^{-4}
Variation of Scalar Transport Scheme with $\tau_R = 1$, $Sc = 1$, and $Re_\lambda = 55$ fixed						
Case ID	N^3	Re_λ	$\mathcal{D}$	$\kappa_{max}\eta_B$	Scalar Scheme	
1	256^3	55	7.50×10^{-3}	3.0	HOUC5	
6	256^3	55	7.50×10^{-3}	3.0	QUICK	
Variation of Relaxation Timescale with HOUC5 scheme, $Sc = 1$, and $Re_\lambda = 55$ fixed						
Case ID	N^3	Re_λ	$\mathcal{D}$	$\kappa_{max}\eta_B$	τ_R	
1	256^3	55	7.50×10^{-3}	3.0	1	
7	256^3	55	7.50×10^{-3}	3.0	0.1	
8	256^3	55	7.50×10^{-3}	3.0	0.5	
Variation of Initial Condition with HOUC5 scheme, $\tau_R = 1$, $Sc = 1$, and $Re_\lambda = 55$ fixed						
Case ID	N^3	Re_λ	$\mathcal{D}$	$\kappa_{max}\eta_B$	Initial Condition	
9	256^3	55	7.50×10^{-3}	3.0	Gaussian	
10	256^3	55	7.50×10^{-3}	3.0	Random	
11	256^3	55	7.50×10^{-3}	3.0	Mean Scalar Gradient-Forced	

4.4.2 Time Evolution

To illustrate the effectiveness of the proposed scalar forcing at driving the scalar field towards a state of constant variance, consider Fig. 4.6(a), which contains the evolution of variance of the scalar field as a function of time for cases 1-3 in Table 4.1. Initially, the energy content of the scalar field is negligible. As the forcing is applied, the field assumes a constant scalar variance value, as determined by the value of α^2 specified. For all simulations performed, α^2 was set to unity. As can be verified from Fig. 4.6(a), the energy content of the scalar field does relax towards the imposed constant value.

However, depending on the quality of the scalar transport scheme used, the scalar variance may not assume a value of precisely unity. This is illustrated in Fig. 4.6(b). The disparity can be explained as follows. The third-order accurate QUICK scheme suffers from comparatively greater numerical diffusion than the fifth-order accurate HOUC5 scheme. Both curves shown in Fig. 4.6(b) are obtained using the same value of τ_R, which is not sufficient to overcome the effects of numerical diffusion when the QUICK scheme is used for scalar transport. Upon decreasing the value of τ_R, the steady state scalar variance obtained with the QUICK scheme increases towards the desired value. Note that the highest $Re_\lambda = 140$ case included in this study is run with the QUICK transport scheme instead of the less dissipative HOUC5 scheme due to numerical stability issues. To compensate for any losses from utilizing the QUICK scheme, this $Re_\lambda = 140$ case is run at increased resolution, $\kappa\eta_B = 3.4$.

These observations verify that both the production and relaxation terms are necessary for the success of the proposed scalar forcing technique. The production term compensates for losses in scalar variance from physical diffusion, and the relaxation term accomodates for errors in the scalar transport scheme and determines the final, steady state variance value. Further evidence of the need to compensate for discretization errors can be obtained by examining Fig. 4.7, which depicts the temporal variance data obtained when the proposed linear scalar forcing is run with and without the relaxation term active. Initially ($t/\tau \leq 23$), the relaxation term is active and the scalar variance is driven to and sustained at the specified $\alpha^2 = 1$ value. Then, the relaxation term is removed from the forcing ($t/\tau \geq 23$). The scalar variance is observed to remain constant for approximately 5 τ before losses due to the imperfect nature of the HOUC5 scheme begin to manifest as a reduction in variance. Assuming perfect energy conservation in the scalar transport scheme, the production term would be sufficient to sustain the scalar field at the desired variance value. Unfortunately, no scalar transport scheme is truly energy conserving; physical schemes induce discretization errors and spectral schemes may induce dealiasing errors. As a result, the relaxation term is necessary, and once at statistical stationarity, it is only needed to compensate for numerical errors.

Recall that the relaxation parameter, τ_R, is a free parameter that controls the overall stiffness
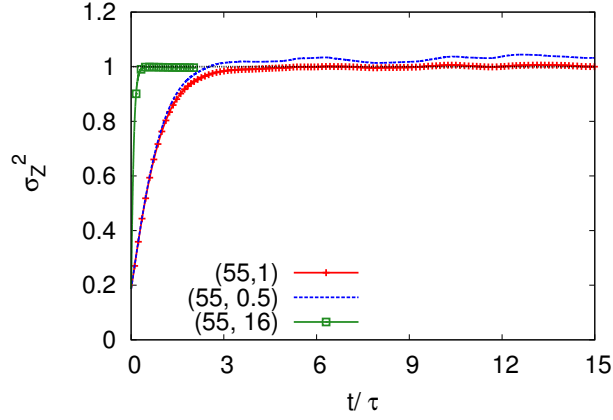
(a) Time evolution of scalar field variance. $Re_\lambda = 55, Sc = 16$ plateaus more quickly as $\tau_R = 0.1$. The legend refers to (Re_λ, Sc).
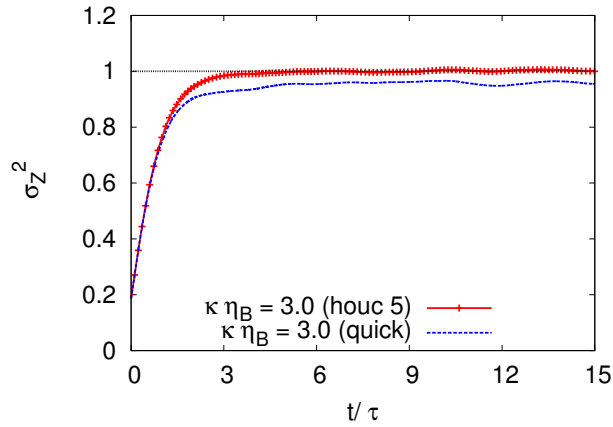
(b) Effect of reducing numerical error via improving the scalar scheme (cases 1 and 6, $Re_\lambda = 55$, $Sc = 1$).

Figure 4.6: Time evolution of scalar field statistics for $\alpha^2 = 1$.
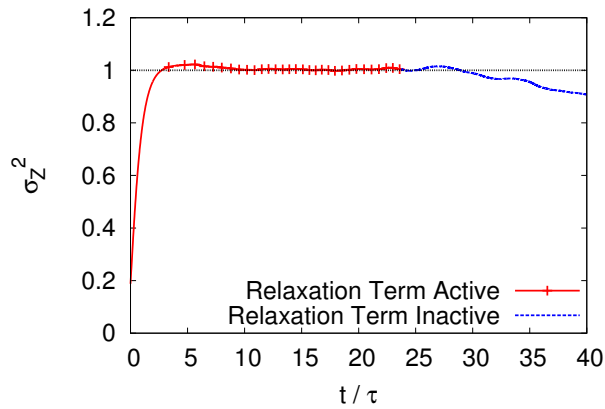
Figure 4.7: Effect of relaxation term on scalar field variance $Re_\lambda = 55$, $Sc = 1$, $\kappa\eta_B = 3.0$. Note that the scalar field variance is unchanged from that of the initial scalar field when the relaxation term is zeroed.

of the forced scalar transport equation, Eq. 4.28. To show the effectiveness of the proposed scheme at driving the scalar field towards stationarity, τ_R is varied, as indicated in cases 1, 7, and 8. Figure 4.8(a) indicates the impact of the relaxation parameter on the performance of the proposed forcing. A smaller value, $\tau_R = 0.1$, results in a faster initial rise to the specified variance and serves to weight the relaxation term preferentially in comparison to the production term.

Additionally, the behavior of this linear scalar forcing is independent of initial conditions. The effect of the initial conditions is qualified by making use of three different initialization methods. First, the initial scalar field is generated as Gaussian in space (case 9), following the scalar field initialization technique of Eswaran and Pope [33]. Second, a completely random field is used to seed the simulation, consisting of random numbers bounded from -1 to 1 (case 10). Lastly, the initial scalar field is taken to be a statistically stationary field obtained from implementing the mean scalar gradient forcing (case 11). The impact of these three different initial conditions on the behavior of the proposed forcing technique is depicted in Fig. 4.8(b). The proposed forcing technique successfully drives the scalar field to a constant variance regardless of its initial state.

In summary, the (potential) impact of the addition of the relaxation term in Eq. 4.28 on the long-term behavior of the scalar field has been investigated by considering different relaxation time-scales (Fig. 4.8(a)), different initial conditions (Fig. 4.8(b)), and different times (*e.g.* $t/\tau = 2$ and $t/\tau = 35$ in Fig. 4.7). The statistics are found to be unchanged. As a result, it is believed that it is appropriate to conclude that the relaxation term included in Eq. 4.28 only drives the scalar variance to its desired value. It has no adverse effect on the long-term statistics of the scalar field.

The statistical character of the scalar field under the action of the linear scalar forcing is found, also, to be favorable and approximately Gaussian, consistent with experimental findings. The skewness and flatness were calculated for each case included in the study. The skewness data indicated that the scalar field was symmetric about its mean (equally probable to have positive and negative scalar values), a requirement for homogeneous, isotropic turbulence. Additionally, the flatness of the scalar field was found to have a value of approximately three, consistent with that of a Gaussian distribution.

4.4.3 Single Point Scalar Field Statistics

To remain consistent with the physics of scalar mixing in a decaying turbulent field, the scalar statistics must be isotropic and symmetric. To determine if the proposed forcing is able to reproduce these requirements, the probability density functions of the three scalar fluxes for each simulation are calculated for cases 1-4. These cases correspond to moderate $Re_\lambda = 55$ conditions over a range of low to moderate Schmidt numbers ($Sc = 0.5$, 1, and 16), and one high $Re_\lambda = 140$ condition at $Sc = 1$. These scalar fluxes are averaged over multiple τ (eddy turn-over times) and two representative PDFs are depicted in Fig. 4.9. As is apparent in Fig. 4.9, the scalar fluxes are symmetrically distributed
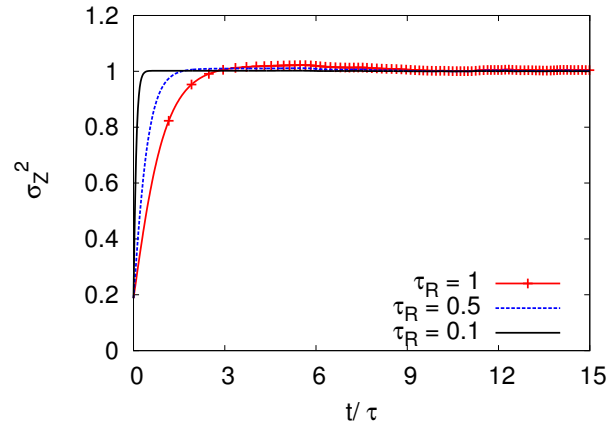
(a) Effect of the relaxation time-scale ($\kappa_{max}\eta_B = 3.0$, cases 1, 7, 8)
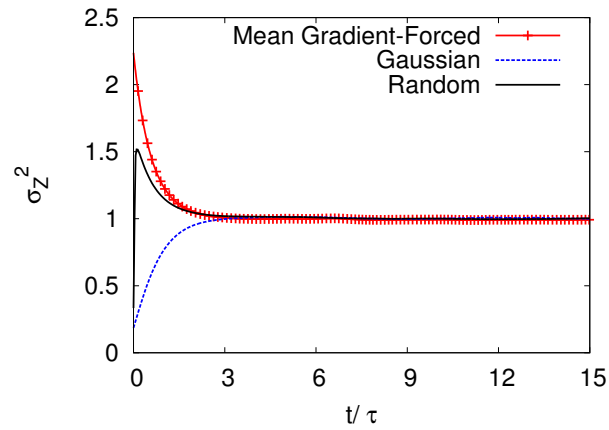
(b) Effect of scalar field initial conditions ($\kappa_{max}\eta_B = 3.0$, cases 9, 10, 11)

Figure 4.8: Effect of relaxation time-scale and initial conditions on the performance of the proposed linear scalar forcing ($Re_\lambda = 55$, $Sc = 1$).
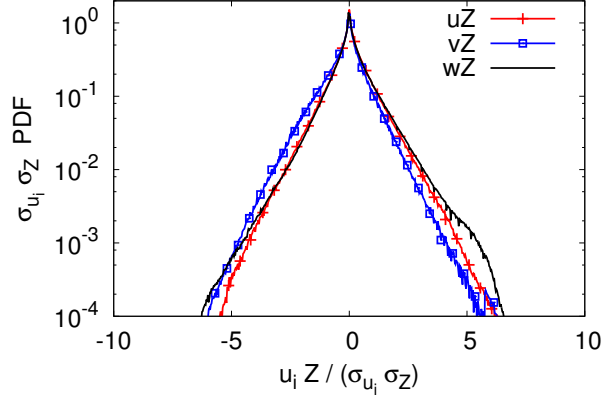
(a) $Sc = 1, Re_\lambda = 55$
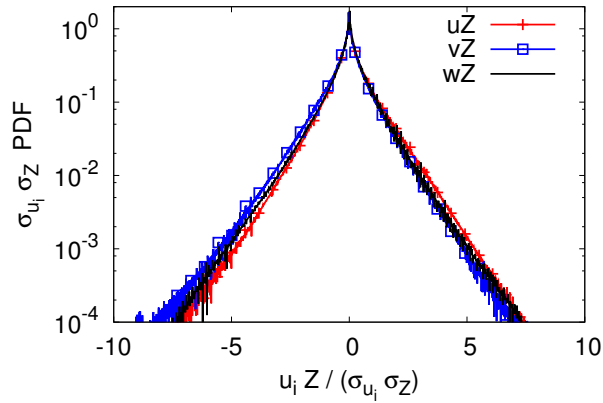
(b) $Sc = 16, Re_\lambda = 55$

Figure 4.9: PDF of scalar flux with the proposed linear scalar forcing for cases 1 and 3.

about a value of zero. Comparable distributions were found for all Re_λ and Sc examined in this study. This is in contrast to the strong anisotropy in the scalar fluxes obtained with the mean scalar gradient forcing (Fig. 4.2).

The distribution of the scalar and scalar dissipation rate are calculated also. Under conditions of isotropy and homogeneity, the distribution of a scalar quantity is expected to be close to Gaussian, while that of the scalar dissipation rate is close to log-normal. The PDFs for these two quantities are included in Fig. 4.10. As shown in Fig. 4.10(a), the approximately Gaussian distribution of the scalar quantity, Z, is preserved with the proposed forcing. Additionally, Fig. 4.10(b) indicates that the commonly-accepted log-normal distribution for the scalar dissipation rate, χ, is preserved under the action of the linear scalar forcing.
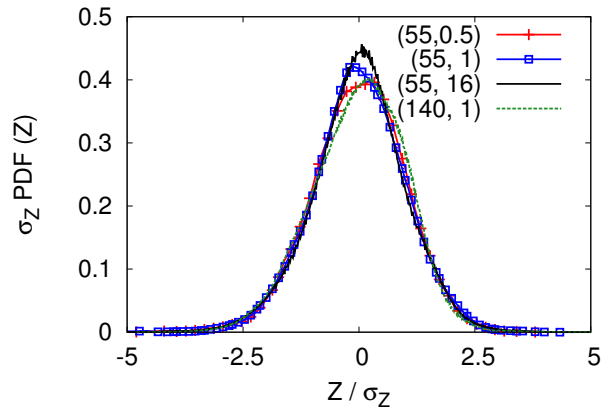
(a) Scalar field quantity, Z
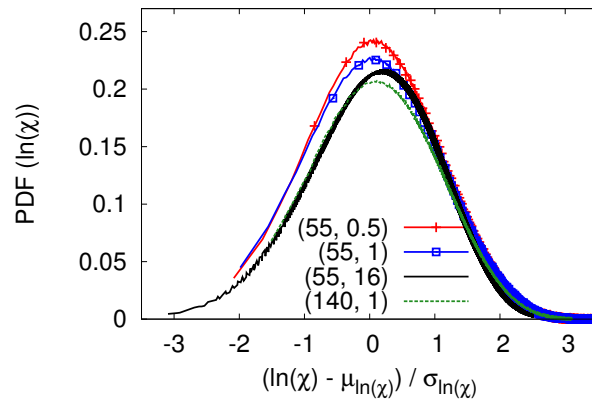
(b) Scalar dissipation rate, χ

Figure 4.10: PDF of scalar quantity, Z, and scalar dissipation rate, χ, with the proposed linear scalar forcing for cases 1-4. The legends refer to the (Re_λ, Sc) combination implemented.

4.4.4   Two-Point Scalar Field Statistics

The final test is to ensure that the proposed scalar forcing reproduces adequately the scalar energy spectrum in the self-similar regime (Fig. 4.11). Towards that end, a scalar field is forced via the mean gradient forcing from $t/\tau = -15$ until $t/\tau = 0$, after which it is allowed to decay. It is clear from Fig. 4.11(a) that after $t/\tau = 0$, the scalar variance decays in the absence of any external forcing. The analysis that follows focuses on the three data points depicted in Fig. 4.11(a), obtained 1, 4, and 7 eddy turn-over times (τ) after the beginning of decay, with the mean scalar gradient forcing term zeroed. The scalar spectra for these three data points are presented in Fig. 4.11(b), along with the spectrum obtained when the field is forced with a mean gradient, just prior to decay ($t/\tau = 0$). These spectra are not normalized, and they clearly indicate that the energy content of the scalar field is decreasing. However, the shape of the spectra are largely unchanged, suggesting a possible self-similar behavior.

To verify that the scalar field had entered a self-similar state, the spectra at 1, 4, and 7 τ after the onset of variance decay are suitably normalized by their variances, σ_Z^2. The results are displayed in Fig. 4.11(c). The collapse of the spectra to one consistent curve for two of the three data points ($t/\tau = 4$ and 7) confirms that the scalar field has entered into a self-similar regime. The scalar dissipation spectra, defined as $D(\kappa) = \mathcal{D}\kappa^2 E(\kappa)$, are presented in the inset to highlight this collapse. As shown in the dissipation spectra comparison, the data at $t/\tau = 1$ does not collapse on to the same spectrum as the other two, indicating that this data point is located in the transient period between statistical stationarity and self-similar behavior. The number of eddy turn-over times (τ) of decay needed for the scalar field to enter into the self-similar regime varies with Re_λ and Sc; in all cases included in this study, it was verified that sufficient time had passed to allow for the self-similar regime to develop fully.

To prove that the linear scalar forcing produces the physics of self-similar decay, the decaying spectra that have entered the self-similar regime, such as those in Fig. 4.11(c), are compared to the scalar spectrum obtained when a scalar field is forced via the linear scalar forcing method. Representative results are depicted in Fig. 4.11(d). Collapse of the normalized decaying spectra onto the spectrum predicted by the linear scalar forcing confirms that the proposed forcing does reproduce accurately the physics of scalar mixing in the self-similar regime. For clarity, only one of the three decaying spectra, at $t/\tau = 7$, is used for the comparison to the linearly-forced scalar spectrum. It should be stated, however, that the spectra at $t/\tau = 4$ and 7 exhibit the same behavior.

The preceeding analysis focused on case 1 in Table 4.1, where the Schmidt number was unity. To confirm that this behavior persisted for non-unity Sc and other Re_λ, the same analysis was conducted using cases 2-5. In all cases, the freely decaying spectra assumed the spectrum shape predicted by the linear scalar forcing method. Taking as examples the two extreme Sc included

in this study ($Sc = 0.5$ and $Sc = 256$), Fig. 4.12 details the self-similar collapse of freely-decaying spectra onto the spectrum shape predicted by the linear scalar forcing. The extent of agreement between the decaying and linearly-forced scalar spectra is highlighted in Fig. 4.12 (c) and (d), which display the dissipation spectra for the two cases. As is apparent, the linear scalar forcing predicts the appropriate spectrum of a decaying scalar. This behavior was observed for all cases included in this study and persisted irrespective of the initial conditions implemented.

4.5 High Schmidt Number Characteristics

The mean gradient and linear scalar forcings are intended to capture two distinctly different scalar field physics. This difference manifests in the structure of the scalar spectra that the two methods predict. The stationary scalar spectra generated by the two techniques are provided in Fig. 4.12 for the lowest and highest Schmidt numbers investigated ($Sc = 0.5$ and 256). Comparing these spectra, it is clear that continuous energy injection (mean gradient forcing) and one-time energy injection (linear scalar forcing) can predict different scalar field structures under certain conditions.

The simulation results for small Sc are considered first (Figs. 4.12 (a) and (c)). At $Sc < 1$, the spectra predicted by the two forcing methods are comparable. However, at $Sc \gg 1$ (Fig. 4.12 (b) and (d)), there are distinct differences in shape (the distribution of scalar variance in wavespace) observable between the scalar spectra generated under mean gradient and linear scalar forcing. These differences are more pronounced at larger Sc and can be considered in terms of Batchelor's theory [7] and experimentally-observed high-Schmidt number scalar behavior [61, 38, 48, 60].

Batchelor's theory predicts that the scalar energy spectrum presents distinct regions in wavenumber space with distinct scalings. The emergence of these regions is dependent on the Schmidt number of the scalar [7]. For high-Schmidt number scalars ($Sc \gg 1$), there are two characteristic regions. The first is the inertial-convective subrange, which manifests at scales larger than the Kolmogorov scale. The second is the viscous-convective subrange, which is present for scales, l, bounded between the Kolmogorov and Batchelor scales, $\eta \ll l \ll \eta_B$. The scalar energy spectrum, $E_Z(\kappa)$, in the inertial-convective and viscous-convective subranges is predicted, further, to scale according to $\kappa^{-5/3}$ for sufficiently high Reynolds numbers [21] and κ^{-1} irrespective of the Reynolds number, respectively, where κ is the wavenumber [7]. It is the scaling in the viscous-convective region with which the present analysis is concerned. In contradiction to Batchelor's prediction, several experimental studies of high-Schmidt number turbulent scalars have not observed the κ^{-1} scaling behavior [61, 38, 48, 60]. Some observed that a weaker scaling, possibly a log-normal scaling, across the viscous-convective subrange may be more representative of experimental data [61].

Case 5 has a sufficiently high Schmidt number ($Sc = 256$) to allow for a comparison of the scalar spectra produced by the linear scalar and mean gradient forcing methods to both Batchelor's

predictions and the summarized experimental results. As the Reynolds number is low ($Re_\lambda \approx 8$), it is not expected to capture the $\kappa^{-5/3}$ scaling across the inertial-convective subrange as predicted by Obukhov [69] and Corrsin [21], but it is expected that the Schmidt number is high enough to capture the correct behavior across the viscous-convective subrange. To compare the data presented to Batchelor's scaling prediction, the Kraichnan model spectrum (K-form) will be used. The Kraichnan spectrum introduces into Batchelor's proposed spectrum form a correction allowing for fluctuations in strain-rate [49]. This model form is obtained strictly theoretically, and it is given by,

$$E_Z(\kappa) = q\langle \chi \rangle \left(\frac{\nu}{\epsilon}\right)^{-1/2} \kappa^{-1} \left(1 + \kappa\eta_B\sqrt{6q}\right) \exp\left(-\kappa\eta_B\sqrt{6q}\right), \qquad (4.29)$$

where q was determined by Qian to have a value of $2\sqrt{5}$ for homogeneous, isotropic turbulence [78]. One of the assumptions made by both Batchelor and Kraichnan is that the scalar field is subject to continuous scalar variance injection (infinite scalar reservoir). The presence of an infinite reservoir of variance produces a scalar energy distribution that is distinct, and this is the distribution that the mean scalar gradient forcing is meant to capture.

To emphasize the differences between the mean gradient and linear scalar forcing techniques, they are compared to the K-form model spectrum. This model fit is obtained by calculating the scalar dissipation rate, χ, in the two data sets, calculating the viscosity, ν, and the energy dissipation rate, ϵ, present in the velocity field, which is the same for the two data sets, and then applying the constant value $q = 2\sqrt{5}$ obtained by Qian. Figure 4.13(a) compares the statistically stationary scalar spectrum predicted by the mean gradient forcing to Kraichnan's model. As is apparent in Fig. 4.13(a), the mean gradient spectrum agrees quite well with the K-form spectrum. Alternatively, the linear forcing assumes one-time scalar variance injection, contrary to the explicit assumptions of the K-form spectrum. Unsurprisingly, Fig. 4.13(b), which compares Kraichnan's model to the spectrum predicted by the linear scalar forcing, finds virtually no agreement. These results are made more clear when the scalar energy spectra are compensated by the Batchelor scaling, $\kappa E_Z(\kappa)$; these compensated spectra are depicted in Fig. 4.13(c) and Fig. 4.13(d). The disagreement between the mean gradient generated spectrum and the K-form spectrum in the viscous-diffusive subrange is likely caused numerical losses, which has minimal effect on the viscous-convective subrange.

From Fig. 4.13, the scalar spectra from the two different scalar forcing techniques have different scaling behaviors in the viscous-convective subrange. The mean scalar gradient forcing obeys the κ^{-1} scaling, while the proposed scalar forcing does not. In fact, the linear scalar forcing implies a scaling with wavenumber that is weaker than κ^{-1}, possibly consistent with experimental findings. The difference between the physics corresponding to the two scalar forcing techniques could provide insight into the apparent disagreement between experimental results and theoretical analysis. The presence of a constant, uniform mean scalar gradient is more consistent with the assumptions used in

the derivation of Batchelor's theoretical scaling, namely the assumption of an infinite scalar reservoir. Alternatively, the self-similar nature of scalar mixing in decaying turbulence might be more consistent with experimental observations, as they both are limited to having only a finite, initial scalar variance distribution. Thus, the apparent disagreement between experiments and theory could be due only to the conditions under which scalar mixing is considered, whether that be in a decaying, self-similar (appropriate for experiments) or forced (appropriate for Batchelor's predictions) scalar field.

4.6 Appropriateness of Linear Scalar Forcing Method for Mixing Studies

It has been stated at various points throughout this chapter that the class of scalar field physics which is more appropriate for the proposed buoyant mixing study is consistent with that of sustained self-similar decay. This rather strong statement is now supported with two arguments.

First, although Batchelor theory [7] rigorously shows that within the viscous-convective subrange there should be a scaling region behaving as $E_Z(\kappa) \propto \kappa^{-1}$, experimental data has not always found such a spectral scaling [61, 85, 43, 37, 40, 100]. In fact, data collected in turbulent jet experiments, tidal current experiments, grid turbulence experiments, and atmospheric boundary layer experiments all find the presence of a weaker wavenumber dependence across the viscous-convective subrange, consistent with the scalar field behavior generated under the presented linear scalar forcing method. It might be stated that the reason the presented simulation data does not capture a κ^{-1} region is that the Schmidt number is not high enough. And, this is a fair point. However, the experiments referenced here were performed with Schmidt numbers of $O(10^3)$; this is certainly high enough to see the presence of a κ^{-1} scaling range. From this, it can be stated that the physics produced under the action of the mean scalar gradient forcing method may not be the most representative. Recall that the mean gradient method generated scalar energy spectra with the Batchelor scaling, κ^{-1}. The proposed linear scalar forcing method, alternatively, predicts scalar energy spectra that qualitatively agree with the analysis of experimental data obtained from a broad range of turbulent flow configurations.

Second, the self-similar regime of scalar mixing manifests itself whenever there is one-time energy injection into a scalar field. Single-shot scalar variance injection corresponds to there being an initial scalar quantity distribution of some kind. This could be a distribution of species concentration or temperature fluctuations, for example. What this work ultimately endeavors to examine is how that buoyancy (and turbulence) are able to mix that specific scalar field distribution, Z. Therefore, that distribution (*i.e.* the PDF(Z)) must be preserved in time. The distribution of any quantity is described by its variance and its mean. The linear scalar forcing method lets both parameters be controlled and held fixed. Hence, in the forced sense, the proposed linear scalar forcing method's

renormalization of scalar field variance at each time-step allows for precisely this type of scalar mixing to be perpetuated.

4.7 Summary of Conclusions

The primary objective of this work was to develop a methodology for numerically simulating the self-similar decay of a turbulent scalar field. The linear scalar forcing technique has been presented and the statistics produced by its implementation have been shown to reproduce the characteristics of homogeneous, isotropic turbulence. For the range of Schmidt numbers considered in this study, the spectra predicted by the proposed scalar forcing are consistent with the sustained decay of a turbulent scalar field. The proposed forcing is robust, performing well irrespective of the initial conditions of the flow field.

The proposed scalar forcing is both novel and attractive relative to the most commonly-used scalar forcings (mean scalar gradient and spectral). Spectral schemes require periodic boundaries, are, in general, memory and computationally intensive, and impose constraints that are not easily realizable in experiments. In comparison, the linear scalar forcing can accomodate non-periodic boundary conditions, which are almost always needed when modeling engineering problems, and it can be integrated easily into non-spectral (physical) codes. Compared to the mean gradient forcing, the proposed linear scalar forcing will be slightly more memory intensive, as it requires storage and calculation of the scalar field variance and scalar dissipation rate at each timestep. However, this is not a significant increase.

Lastly, it has been suggested that the proposed linear scalar forcing may provide insight into the nature of high-Schmidt number flows. Specifically, the disparity observed between the scalar energy spectra generated by the well-established mean scalar gradient and the proposed linear scalar forcing are reminiscent of the observed differences between theoretical predictions and experimental results. These differences may be simply a consequence of the conditions under which scalar mixing is studied. The implementation of a mean scalar gradient corresponds to a scalar field with continuous energy injection, while the proposed linear scalar forcing simulates a sustained decay. Thus, as presented, this methodology can be implemented to perform simulation studies of turbulent scalar mixing.

(a) Decay of scalar variance. Points correspond to scalar variance 1, 4, and 7 τ after forcing removed.

(b) Scalar spectra in self-similar regime.
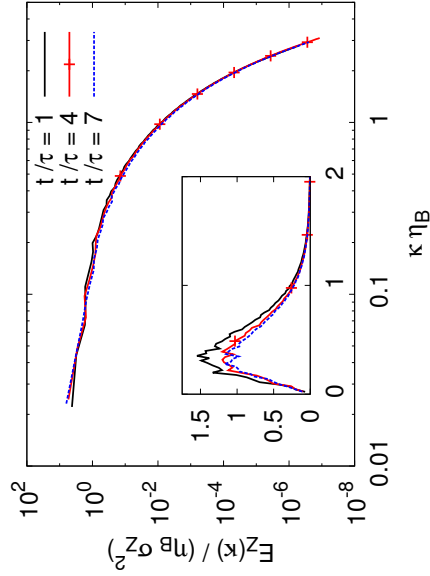
(c) Collapse of normalized scalar spectra. The inset is the dissipation spectrum, $10^2 \times D(\kappa)$.

(d) Collapse of normalized scalar spectra in the self-similar regime.

Figure 4.11: Evolution of a purely decaying scalar spectrum into the shape predicted by the proposed linear scalar forcing method ($Re_\lambda = 55$, $Sc = 1$, case 1).
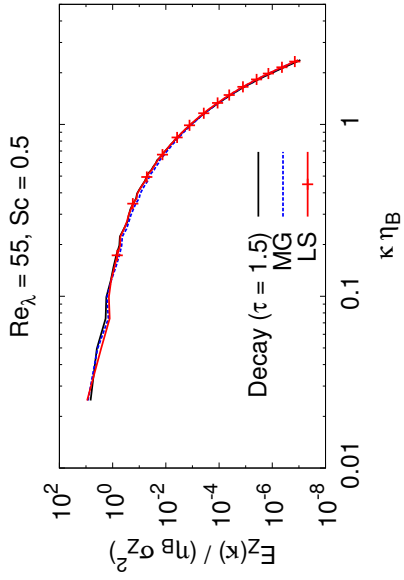
(a) Collapse of decaying spectra onto linear scalar forcing-predicted shape
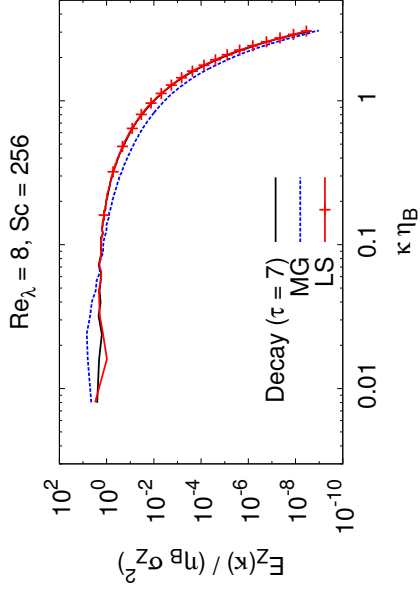
(b) Collapse of decaying spectra onto linear scalar forcing-predicted shape
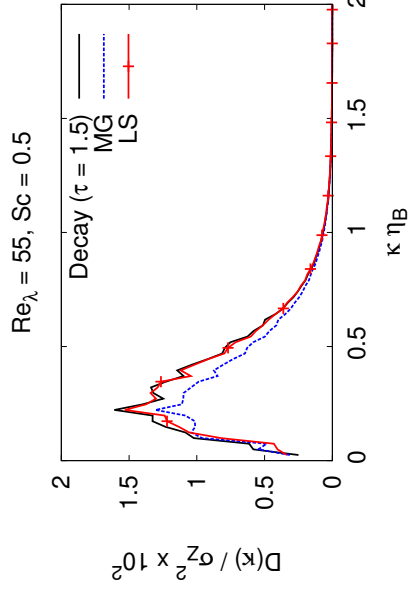
(c) Comparison of freely decaying and linear scalar forcing-predicted dissipation spectra
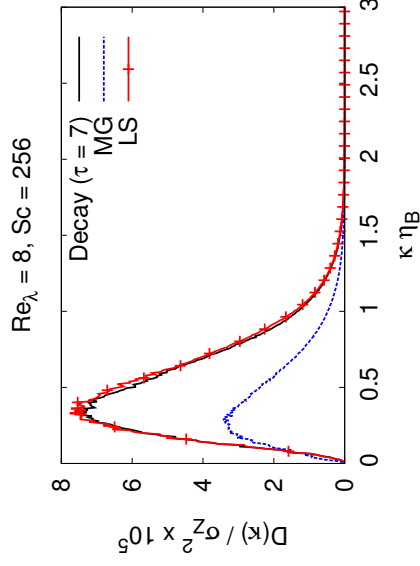
(d) Comparison of freely decaying and linear scalar forcing-predicted dissipation spectra

Figure 4.12: Evolution of a purely decaying scalar spectrum into the shape predicted by the proposed linear scalar forcing method. Linear scalar and mean gradient forcing are denoted as LS and MG.
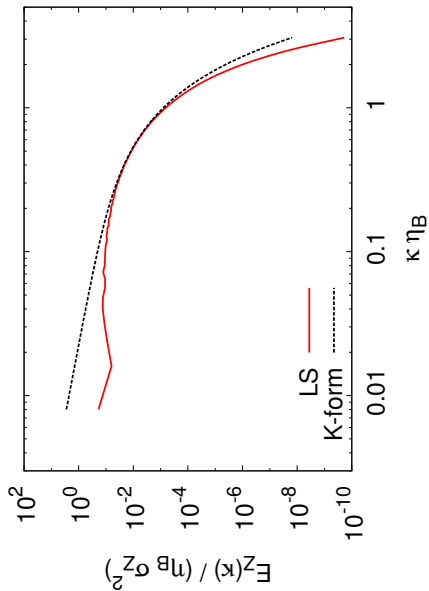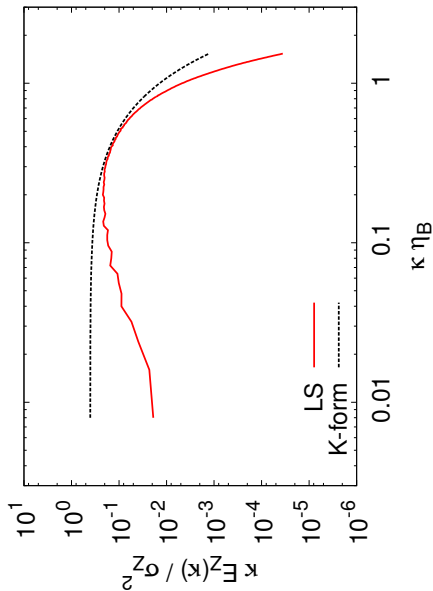
(a) Mean gradient-forced spectra
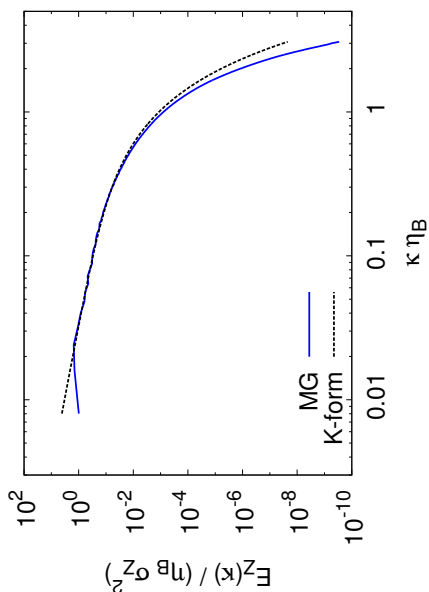
(b) Linear scalar-forced spectra

(c) Mean gradient-forced spectra compensated by Batchelor's scaling, $\kappa E_Z(\kappa)$
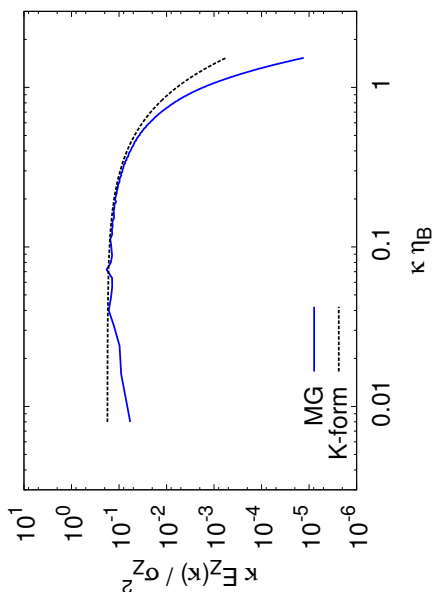
(d) Linear scalar-forced spectra compensated by Batchelor's scaling, $\kappa E_Z(\kappa)$

Figure 4.13: Comparison of predicted scalar spectra to Kraichnan-predicted form ($Re_\lambda = 8$, $Sc = 256$). Batchelor and Kraichnan predicted scaling of $E_Z(\kappa) \propto \kappa^{-1}$ is represented by the Kraichnan model spectrum (black). Note the Kraichnan spectra have been shifted slightly vertically to highlight consistency (or inconsistency) with the MG and LS spectra.

Chapter 5

Turbulent Buoyant Flows: A Simulation Framework

Chapters 2-4 have involved the development, validation, and testing of the components needed to create the simulation framework described in Chapter 1. This chapter integrates these separate pieces into one cohesive unit. This new framework, in which variable density turbulent mixing can be studied, and the process through which it is validated are presented.

This chapter is organized as follows. Section 5.1 and Section 5.2 describe the numerical framework developed, including the governing equations and the required restraints on the implemented forcing methods. Section 5.3 discusses the means by which the relevant non-dimensional parameters can be adjusted independently to provide desired Reynolds number (Re), Richardson number (Ri), Schmidt number (Sc), and Atwood number (A) combinations. Section 5.4 discusses the resolution requirements, transport schemes, and order of accuracy needed to satisfy the physical and numerical constraints referenced in Section 5.2. Section 5.5 examines the results from three test cases generated under the proposed simulation methodology. The three test cases correspond to forced simulations of purely isotropic variable density turbulence, of purely buoyant variable density turbulence, and of a variable density turbulent case subject to both isotropic and buoyant forcing. Canonical flow features are calculated for the three cases as a means of validation. Lastly, Sections 5.6 and 5.7 provide top-level analysis of the data garnered under the proposed simulation framework within the velocity (Section 5.6) and scalar fields (Section 5.7). This analysis is performed to confirm the quality of the physics predicted by this simulation methodology under buoyant and non-buoyant conditions.

5.1 Proposed Configuration

Chapter 1 provided an overview of the two existing simulation methods currently published in the literature, namely the Rayleigh-Taylor unstable method and the shear layer method. A nuance of

---

This chapter is based on the publication: P.L. Carroll and G. Blanquart. "A new framework for simulating forced variable density and buoyant turbulent flows." *Journal of Computational Physics*. Submitted (2014).

the shear layer configuration is now addressed prior to describing the configuration chosen for the current work. In the shear layer geometry, the two fluids involved are stably stratified, and there is a mean relative (shear) velocity between them. For such geometries, with both a mean shear and non-zero gravity vector, there is a dynamical competition between the gravitational stability of the density stratification and the mean shear [10, 27, 93]. This competition is expressed in terms of a gradient Richardson number,

$$Ri_g = N^2 / \left(\frac{\partial u_h}{\partial z} \right)^2. \tag{5.1}$$

In the gradient Richardson number definition, $N^2 = -(g/\rho_0)(\partial\rho/\partial z)$ is related to the buoyant frequency of the density stratification, ρ_0 is the mean density of the stratified fluid system, g is the magnitude of the gravity vector, u_h are the components of the velocity field perpendicular to the action of gravity (horizontal components), and z is the coordinate direction in the direction of the gravity vector. When studying sheared, stably stratified buoyant flows, there is an important length-scale that must be considered. This is the Ozmidov length-scale, L_O, and it is defined as,

$$L_O = \sqrt{\frac{\epsilon}{N^3}}, \tag{5.2}$$

where ϵ is the energy dissipation rate and N is the buoyant frequency [10, 27].

In (decaying) stably stratified fluid systems, the flow field evolves in three stages. Initially, the fluid is stably stratified in the horizontal plane ($x - y$ plane), which is perpendicular to the action of gravity (z-direction), and there is no mean shear velocity. Then, a mean shear velocity is applied, turbulence is generated, and is then modified by the density stratification. The buoyancy momentum flux (in z) is minimal, having been generated by the mixing induced by the mean shear. This is the initial stage. The second stage is marked by the formation of internal (gravity) waves, which travel away from the mixing plane in the $\pm z$ directions. This leads to the creation of horizontal layers (in the $x - y$ plane) that expand into the non-turbulent regions of the stratified flow. The vertical size (in z) of these layers when they first emerge is termed the Ozmidov length-scale. The physical significance of the Ozmidov length-scale is that it indicates the vertical height below which vertical overturning is possible and above which vertical overturning is inhibited by the strength of the (stable) fluid stratification [10, 27, 93]. For $l < L_O$, overturning is not strongly inhibited, but, for $l > L_O$, it is. The growth of these vertical layers to their maximum vertical height concludes the second stage. Lastly, in the third stage, these layers collapse until they approach the (growing) Kolmogorov scale, $\eta = (\nu^3/\epsilon)^{1/4}$. The final result of this process is that any generated internal waves have left the turbulent region, the turbulence self-organizes into anisotropic vortices, and the vertical velocity component virtually vanishes relative to the magnitude of the horizontal velocity

components; the stably density gradient is able to return the flow to a stably stratified state. Thus, overall, the mean shear is destabilizing, and drives the mixing process, while the density gradient serves to try to stabilize and suppress the induced buoyancy effects [10, 27, 93].

The Ozmidov length-scale can also be interpreted as denoting the transition between stratified and Kolmogorovian turbulence [10, 27, 93] in sheared, stably stratified flows; below this length-scale, Kolmogorovian turbulence is found [10], despite the presence of a mean shear and a globally stabilizing density gradient. This small-scale region of flow ($l < L_O$) corresponds to the region with which the current work is concerned, as the effects of the boundary conditions (*i.e.*, the mean density gradient) are no longer dynamically important. However, there are two important distinctions to be made. First, the current work removes the effect of a shear velocity entirely from the problem, as there is no non-zero applied mean shear, and mixing is driven only by isotropic turbulence or a buoyancy-induced momentum flux. Second, buoyancy is made to be a source of energy production, which is destabilizing.

Following the above discussion, the objective of this work is to develop a means by which the mixing physics occuring in the inner region of a turbulent mixing layer can be interrograted, whether it be stably or unstably stratified. Within this region, the small scale mixing features are of primary concern. As this is the inner region of the mixing layer, it is believed that the boundary conditions of the flow are unable to impact the small scale mixing dynamics [18]. Whether the flow be globally stably stratified (sheared) or globally unstably (RTI) stratified, the proposed simulation geometry is appropriate to study the smallest scales of turbulent mixing subject to density variations and buoyancy forces.

Deep in the mixing layer, the small scale mixing features are quite fine, and, accordingly, are not always accurately captured in large simulations or experiments of buoyancy- or shear-induced mixing. To probe the nature of variable density mixing at these scales and in this mixing layer region, statistically stationary conditions must be induced. This perpetuates the relevant mixing physics such that detailed flow data can be collected. To study variable density mixing under statistically stationary conditions, there are two approaches that could be taken. The first approach entails the sustenance of a mean density gradient via a perpetually present unstable density stratification; this approach was successfully accomplished by Chung and Pullin [18]. The second would require using forcing methods; this latter approach has not be done, and it is the subject of this thesis work.

The first approach successfully sustains the process of variable density fluid mixing. The method advanced by Chung [18], maintains an unstable stratification of a dense fluid atop a less dense fluid by imposing a fringe method [8, 67]. Two fringe regions are located at the top and bottom faces (separated by a vertical distance L_z) of a rectangular, periodic computational domain. The fringe region on the upper face continuously adds high density fluid at the same rate as fluid is removed via the fringe at the lower face, which is mass conservative and promotes the development of a

stationary state of mixing.

Chung's fringe-based method was used to study the characteristics of turbulence during the mixing of an active scalar by two incompressible fluids under two high Atwood number conditions ($A = 0.25$ and 0.75 as defined in Eq. 5.26) in the presence of gravity; no energy production mechanism other than gravity acting on a persistent mean density gradient was present. The findings from this study were threefold. First, the appropriate scales for small scale buoyant mixing remain the Kolmogorov (viscous) scales. When the energy spectra for these non-Boussinesq buoyantly-driven cases were calcuated, they collapsed to a single curve once normalized by their Kolmogorov scales ($\kappa\eta$ vs. $\epsilon^{-1/4}\nu^{-5/4}E(\kappa)$). Second, the asymmetrical nature of variable density mixing in high Atwood number flows was confirmed. When the probability density functions (PDF) of the density field were calculated, they were found to be slightly skewed towards the lighter fluid side. This suggested that the lower density fluid mixed at a faster rate than the denser fluid, which is consistent with other studies [28, 55, 56, 57]. Third, the large and small scales are suggested to be anisotropic, while the intermediate scales tend to be more isotropic when compared. This was supported by the calculation of one-dimensional energy spectra, which indicated that, at the large and small scales, significantly more energy was concentrated in the direction in which gravity was applied.

The other approach, which is the one taken by this work, adopts a forced configuration to sustain the mixing process. Although it is designed to capture the same region of mixing as Chung's method, that located deep inside of a turbulent mixing layer, the proposed method has the added capability of being able to vary independently the four non-dimensional parameters of importance in (buoyant) variable density mixing processes. Chung's method imposes a link between the Reynolds number and the Richardson number; one determines the other. The methodology presented in this chapter offers a means by which these two can be decoupled.

Accordingly, this chapter proposes a new simulation method for the study of variable density turbulent mixing which relies on numerical forcing. Focus is still placed on the small scales, and the region probed is still that located in the inner region of a turbulent mixing layer. This region is sufficiently far from the boundary conditions of the flow (regions of pure fluid density or pure scalar) such that its dynamics can be considered to be independent of them. Two simplifications follow from this. First, there is no mean density gradient acting across the region of interest, making the physics in this volume independent of the physical boundary conditions of the mixing layer. Second, if the effects of the physical boundaries cannot be felt, then mixing can be represented by triply periodic, homogeneous (box) turbulence containing a variable density fluid.

5.2 Governing Equations

5.2.1 Mathematical and Numerical Framework

To create stationary, variable density box turbulence with a constant turbulent kinetic energy and scalar variance, the turbulent fluctuations must not decay. This is accomplished by using velocity field forcing methods (Chapters 2 and 3) to generate variable density isotropic turbulence and scalar field (Chapter 4) forcing methods. Forcing methods add a source term to the governing momentum and scalar transport equations. The (forced) governing equations needed to describe variable density mixing are the mass conservation (Eq. 5.3), momentum (Eq. 5.4), and scalar transport (Eq. 5.5) equations, which can be written as,

$$\frac{\partial \rho}{\partial t} + \frac{\partial \rho u_j}{\partial x_j} = 0, \tag{5.3}$$

$$\frac{\partial \rho u_i}{\partial t} + \frac{\partial \rho u_i u_j}{\partial x_j} = -\frac{\partial p}{\partial x_i} + \frac{\partial \tau_{ij}}{\partial x_j} + (\rho - \langle \rho \rangle) g_i + f_{u_i}, \tag{5.4}$$

$$\frac{\partial \rho Z}{\partial t} + \frac{\partial \rho Z u_j}{\partial x_j} = \frac{\partial}{\partial x_j} \left(\rho \mathcal{D} \frac{\partial Z}{\partial x_j} \right) + f_Z. \tag{5.5}$$

Here, ρ represents the density, u_i represents the i-component of velocity, Z is the scalar parameter, $\mathcal{D}$ is the molecular diffusivity, ν is the kinematic viscosity, $\mu = \nu \rho$ is the dynamic viscosity, g_i is the i-component of the gravity vector, p is pressure, and τ_{ij} is the deviatoric contribution to the stress tensor. The kinematic viscosity, ν, is always held fixed; any changes in the density correspond to a change in the dynamic viscosity. The momentum and scalar transport equations are forced via the addition of source terms, demarked by f_{u_i} and f_z, respectively, to prevent the decay of both turbulent kinetic energy and scalar variance. At this point, the specific form of the source terms is not relevant. The different forcing methods are discussed in Section 5.2.3. Irrespective of the forcing scheme implemented, they serve to drive the velocity and scalar fields to statistically steady conditions, after which all the physical parameters will assume fixed distributions that are preserved in time.

A constitutive relation (equation of state) is introduced between the scalar field, Z, and the density field, ρ, such that the density is defined at every point in the domain based on the corresponding fluctuating scalar value (Z) at that point. This constitutive relation takes the form,

$$\rho = \frac{1}{aZ + b}, \tag{5.6}$$

where a and b are constants that determine the variability of the density field that is calculated. This expression can be thought of as representing the mixing of two fluids with either different temperatures or different molecular weights. Note that in the implementation of this equation of state, it is infrequently required to "clip" the scalar values before calculating the density. This is necessary for rare events in which the scalar is large and negative in value ($Z \ll 0$). These extremely rare events can lead to negative density values if not so addressed. The scalar field, Z, is initialized following the procedure developed by Eswaran [33] and, then, sustained under the action of the applied forcing term.

5.2.2 Necessary Restrictions on Forcing Methods

Without assuming a specific velocity or scalar field forcing, the five key constraints required in the proposed configuration can be derived. These constraints can be obtained by considering the implications of statistically stationary turbulent velocity and scalar fields. Following a Reynolds decomposition approach, all variables are decomposed into the sum of a mean ensemble average, $\langle \, \cdot \, \rangle$, and a fluctuating component, $(\cdot)'$, according to $\rho = \langle \rho \rangle + \rho'$, $u_i = \langle u_i \rangle + u_i'$, and $Z = \langle Z \rangle + Z'$.

The distinction between ensemble averaging and volume-averaging should be made here. The proposed configuration reaches a state of statistical stationarity. Under this condition, ensemble averages are (theoretically) equivalent to averages over an infinite time. Similarly, since the configuration is homogeneous in space, ensemble averages are equivalent also to averages over an infinite volume. Thus, ensemble averages can be represented as volume averages over the triply periodic domain.

Statistical stationarity implies,

$$\frac{\partial \langle \rho \rangle}{\partial t} = 0,$$
$$\frac{\partial \langle \rho u_i \rangle}{\partial t} = 0,$$
$$\frac{\partial \langle \rho Z \rangle}{\partial t} = 0. \tag{5.7}$$

Physically, these correspond to a constancy in ensemble-averaged density, $\langle \rho \rangle$, momentum, $\langle \rho u_i \rangle$, and scalar concentration, $\langle \rho Z \rangle$. Returning to the forced-momentum and forced-scalar transport equations (Eq. 5.4 and Eq. 5.5), when ensemble-averaged, these equations reduce to,

$$(a) \;\; \frac{\partial \langle \rho u_i \rangle}{\partial t} = \langle f_{u_i} \rangle + \langle \rho' g_i \rangle \qquad (b) \;\; \frac{\partial \langle \rho Z \rangle}{\partial t} = \langle f_Z \rangle. \tag{5.8}$$

Here, the condition of homogeneity, under which the ensemble average of terms written as divergences vanish, has been applied. The requirement of constant momentum and scalar concentration (Eq. 5.7)

implies three further constraints on the governing equations. First, from Eq. 5.8(a),

$$\langle f_{u_i} \rangle = 0, \tag{5.9}$$

$$\langle \rho' g \rangle = 0, \tag{5.10}$$

are obtained. A net zero buoyant force and a zero-averaged momentum source term prevent the linear growth of $\langle \rho u_i \rangle$ in time. Second, from Eq. 5.8(b),

$$\langle f_Z \rangle = 0, \tag{5.11}$$

is obtained; this is necessary to respect the constancy of the scalar concentration, $\langle \rho Z \rangle$. Lastly, and without loss of generality, the constant average values of momentum and scalar concentration are chosen to be zero for the sake of simplicity,

$$\langle \rho u_i \rangle = 0, \tag{5.12}$$

$$\langle \rho Z \rangle = \langle \rho Z \rangle_{t=0} = 0. \tag{5.13}$$

Accordingly, Eq. 5.9 - Eq. 5.13 constitute the applied contraints on the system of (forced) governing equations.

5.2.3 Forcing Methodologies and Proposed Source Terms

The forcing techniques implemented in this work are the linear velocity forcing method discussed in Chapters 2 and 3, the mean scalar gradient forcing method described in Chapter 4, and the linear scalar forcing method derived in Chapter 4.

5.2.3.1 Velocity Field Forcing

The linear velocity field forcing method imposes a momentum source term of the form,

$$f_{u_i} = Q \frac{k_0}{k} \rho u_i, \tag{5.14}$$

where Q is a constant forcing coefficient related to the time-scale of the large-scale turbulent structures, and k_0 and $k = \langle \frac{1}{2} \rho u_i u_i \rangle$ are the (desired) long-time steady-state and instantaneous turbulent kinetic energy values, respectively. With the above momentum source term, Eq. 5.9 is verified due to Eq. 5.12. It follows that the forced momentum equations become,

$$\frac{\partial \rho u_i}{\partial t} + \frac{\partial \rho u_i u_j}{\partial x_j} = -\frac{\partial p}{\partial x_i} + \frac{\partial \tau_{ij}}{\partial x_j} + Q \frac{k_0}{k} \rho u_i + \rho' g_i. \tag{5.15}$$

This is the momentum equation that must be implemented under the proposed geometry to study variable density turbulence.

5.2.3.2 Scalar Field Forcing

The most commonly-used scalar field forcing method involves applying a constant, mean spatial gradient across the scalar field. Under such a mean gradient forcing method, the scalar forcing term becomes,

$$f_Z = \mathcal{G}_i \rho u_i, \tag{5.16}$$

where $\mathcal{G}$ is generally taken to have one non-zero component; $\mathcal{G}$ is defined here as $[-1, 0, 0]$. For the current work, the mean momentum is selected to be zero (Eq. 5.12), such that the needed form of the forced scalar transport equation is,

$$\frac{\partial \rho Z}{\partial t} + \frac{\partial \rho Z u_j}{\partial x_j} = \frac{\partial}{\partial x_j} \left(\rho \mathcal{D} \frac{\partial Z}{\partial x_j} \right) + \mathcal{G}_i \rho u_i. \tag{5.17}$$

This is the advection-diffusion equation that must be implemented under the proposed geometry if forcing is done in proportion to a mean scalar gradient and the density is variable.

Although the mean scalar gradient forcing method is quite robust and reliable as discussed in Chapter 4, it is anisotropic due to its imposed scalar gradient. As one of the motivating interests for the development of this new framework is to study buoyant flows, this may not be an ideal forcing method. The imposition of an arbitrary (*i.e.* not physically-relevant) mean gradient may not be desirable. This is illustrated in Fig. 5.1, where forced variable density (non-buoyant) turbulence is considered. The averages of the velocity field components conditioned on the density field are plotted. The velocity field is maintained at stationarity via the isotropic linear velocity forcing method discussed in Section 5.2.3.1 and initially presented in Chapters 2 and 3. As shown in Fig. 5.1(a), the imposition of a mean gradient when considering an active scalar (variable density) can alter detrimentally the velocity field dynamics by imposing a non-negligible correlation between the u velocity component and $\mathcal{G}$ (recall $\mathcal{G}$ is in the x-direction). Under purely isotropic conditions, whether the scalar is passive or active, the velocity field components ought to have zero-averaged conditional means, which is not the case when the mean gradient method is used.

In light of this, an alternate scalar field forcing method is selected. The linear scalar forcing method [14], which is an isotropic forcing method, suggests a scalar source term of the form,

$$f_Z = \left(\frac{1}{\tau_I} \left(\frac{\alpha}{\sigma_Z} - 1 \right) + \frac{\chi}{2\sigma_Z^2} \right) \rho Z, \tag{5.18}$$

where τ_I is an inertial timescale, α^2 is the long-time steady-state variance to which the scalar field
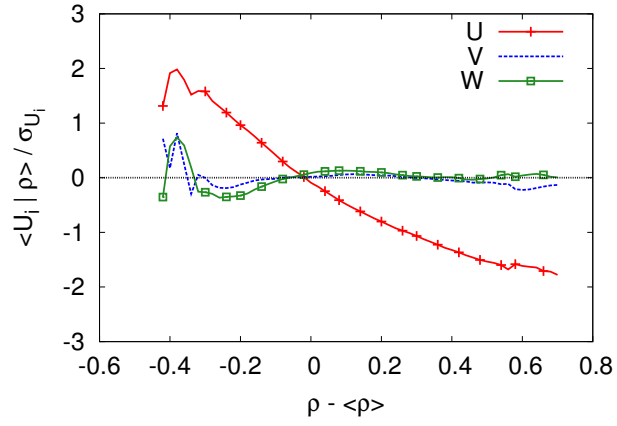
(a) MSG forcing method.
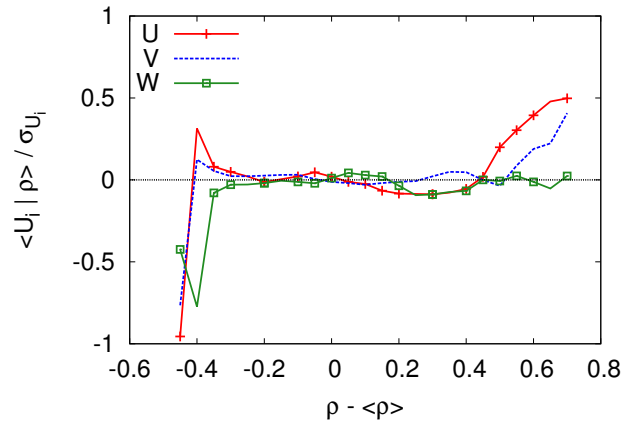
(b) LSF forcing method.

Figure 5.1: Conditional average of the three velocity field components on the density field when the velocity field is forced isotropically and the scalar field is forced by either the mean scalar gradient method (MSG) or the linear scalar forcing method (LSF). Simulation parameters are $N^3 = 256^3$, $Sc = 1$, $\epsilon \approx 2$, and $\sigma_Z^2 \approx 1$.

evolves (specified *a priori* by the user), $\sigma_Z^2 = \langle \rho Z^2 \rangle - \langle \sqrt{\rho} Z \rangle^2$ is the variance of the density-weighted scalar field, and $\chi = \langle 2\rho \mathcal{D} |\nabla Z|^2 \rangle$ is the scalar dissipation rate. Following from Eq. 5.13, this is the source term that must be applied to the advection-diffusion equation (Eq. 5.5),

$$\frac{\partial \rho Z}{\partial t} + \frac{\partial \rho Z u_j}{\partial x_j} = \frac{\partial}{\partial x_j} \left(\rho \mathcal{D} \frac{\partial Z}{\partial x_j} \right) + \left(\frac{1}{\tau_I} \left(\frac{\alpha}{\sigma_Z} - 1 \right) + \frac{\chi}{2\sigma_Z^2} \right) \rho Z. \tag{5.19}$$

This ensures that the ensemble-averaged scalar field source term is zero, and it prevents the decay of the scalar field variance. Further, from examination of Fig. 5.1(b), the linear scalar forcing does not suffer the unphysical coupling between the velocity and (active) scalar field. Under an isotropically-forced velocity field, the conditional means of the three velocity components and the density fields are, indeed, of zero average. Note that the non-zero conditional average values for the lowest and highest density deviations shown in Fig. 5.1(b) can be attributed to the (low) frequency at which these large deviations occur. As these large deviations are infrequent, the statistics there are not meaningful.

5.2.4 Effect of Forcing Methods on Global Quantities

Until now, it has only been asserted that appending such forcing terms induces a statistically stationary turbulent field. This is now supported more rigorously. The turbulent kinetic energy equation can be obtained by multiplying Eq. 5.15 by u_i. After some manipulation and using mass conservation (Eq. 5.3), it is obtained,

$$\frac{\partial \frac{1}{2} \rho u_i^2}{\partial t} + \frac{\partial \frac{1}{2} \rho u_i^2 u_j}{\partial x_j} = -\frac{\partial p u_i}{\partial x_i} + p \frac{\partial u_i}{\partial x_i} + \frac{\partial \tau_{ij} u_i}{\partial x_j} - \tau_{ij} \frac{\partial u_i}{\partial x_j} + Q \frac{k_0}{k} \rho u_i^2 + \rho' g_i u_i. \tag{5.20}$$

After (ensemble) domain-averaging, applying the definitions of kinetic energy, $k = \langle \frac{1}{2} \rho u_i u_i \rangle$, and dissipation, $\epsilon = \langle 2\nu S_{ij} S_{ij} \rangle = \langle 2\nu S_{ij} \frac{\partial u_i}{\partial x_j} \rangle$, and imposing a Newtonian-form for the deviatoric stress tensor, $\tau_{ij} = 2\mu S_{ij}$, the following emerges,

$$\frac{\partial k}{\partial t} + \langle \frac{\partial \frac{1}{2} \rho u_i^2 u_j}{\partial x_j} \rangle = \langle -\frac{\partial p u_i}{\partial x_i} \rangle + \langle p \frac{\partial u_i}{\partial x_i} \rangle + \langle \frac{\partial \tau_{ij} u_i}{\partial x_j} \rangle - \tilde{\epsilon} + 2Q k_0 + \langle \rho' g_i u_i \rangle, \tag{5.21}$$

where $\tilde{\epsilon} = \langle 2\mu S_{ij} \frac{\partial u_i}{\partial x_j} \rangle$. For the present purposes, it can be written $\tilde{\epsilon} \approx \epsilon$. When homogeneity is applied ($\langle \nabla (\cdot) \rangle = 0$), the energy equation reduces further to,

$$\frac{\partial k}{\partial t} = \langle p \frac{\partial u_i}{\partial x_i} \rangle - \epsilon + 2Q k_0 + \langle \rho' g_i u_i \rangle. \tag{5.22}$$

This expression states that the time rate of change of kinetic energy is a balance between the pressure dilatation, energy dissipation, and energy production from isotropic and anisotropic (buoyant) sources. A steady state manifests when dissipation grows sufficiently to counter the other three

contributing terms. In all numerical tests performed, the pressure dilatation term was found to be small. Therefore, at steady state, it can be written,

$$\epsilon = 2Qk_0 + \langle \rho' g_i u_i \rangle. \tag{5.23}$$

By adjusting the values of Q and g, the proposed equations can model all flows from fully isotropic ($g = 0$) to purely buoyant ($Q = 0$) turbulent conditions.

The scalar transport equation can be analyzed similarly. Recall Eq. 5.5, the scalar transport equation for the fluctuating scalar quantity, Z, where the source terms assume the form of Eq. 5.16 for mean scalar gradient forcing and Eq. 5.18 for linear scalar forcing. When Eq. 5.5 is multiplied by the fluctuating scalar quantity, Z, and (ensemble) spatially-averaged, evolution equations for the density-weighted scalar field variance, σ_Z^2, emerge,

$$(a)\ \frac{\partial \sigma_Z^2}{\partial t} = -\chi - 2\langle \mathcal{G}_i \rho u_i Z \rangle, \qquad (b)\ \frac{\partial \sigma_Z^2}{\partial t} = 2\frac{\sigma_Z^2}{\tau_I}\left(\frac{\alpha}{\sigma_Z} - 1\right). \tag{5.24}$$

Note that it is assumed for the purposes of this discussion that $\langle \sqrt{\rho} Z \rangle^2 = 0$ in Eq. 5.24. Equation 5.24(a) corresponds to the mean scalar gradient forcing and Eq. 5.24(b) corresponds to the linear scalar forcing. In the case of mean scalar gradient forcing, the mean gradient serves to produce scalar variance by its interaction with the scalar flux. This production is sufficient to compensate for the scalar dissipation rate, χ. This leads to the creation of a scalar field with a temporally constant variance. A similar compensation occurs when imposing the linear scalar forcing method; the linear scalar forcing will drive the scalar field to a specified variance value. When the standard deviation of the scalar field reaches this value ($\alpha = \sigma_Z$), the right hand-side of Eq. 5.24(b) vanishes, and the scalar field is held at a fixed variance value, inducing a statistically stationary state.

5.3 Relevant Non-Dimensional Parameters

5.3.1 Definitions

In studies of variable density mixing of incompressible fluids, the three dimensionless groups of primary importance are the Reynolds, Atwood, and Richardson numbers. The Reynolds number, Re, is informative of the relative importance of viscosity and inertia in the flow, and it is defined as,

$$Re = \frac{ul_v}{\nu}, \tag{5.25}$$

where l_v and u are taken to be representative length-scales and velocity scales, respectively. The Atwood number, A, is informative of the extent of density variation present in the mixing fluids,

and it is defined traditionally as,

$$A = \frac{\rho_2 - \rho_1}{\rho_2 + \rho_1}, \tag{5.26}$$

where ρ_1 and ρ_2 are the densities of the two incompressible (pure) fluids being mixed. The larger the difference in the densities of the pure fluids, the larger the Atwood number. The Richardson number, Ri, indicates the relative strength of buoyancy and momentum forces. It can be defined as,

$$Ri = \frac{A g l_\rho}{u^2}, \tag{5.27}$$

where g is gravity, l_ρ is a representative length-scale of the distance over which density varies. If $Ri = 0$, then the mixing is momentum-driven; if $Ri \neq 0$, the mixing is subject to buoyancy effects. In the present work, an alternative definition of the Atwood number is used,

$$A = \frac{\sigma_\rho}{\langle \rho \rangle}, \tag{5.28}$$

where σ_ρ is the standard deviation of the density field and $\langle \rho \rangle$ is the mean density. The standard deviation of the density is informative of the spread in density values throughout the domain, as there are not any regions of pure fluid at ρ_1 or ρ_2 in the proposed geometry. This definition is adopted in place of using the minimum and maximum density values in the domain, as is done in Eq. 5.26. There is also an important dimensionless group used to describe scalar field dynamics. This final non-dimensional group is the Schmidt number,

$$Sc = \frac{\nu}{\mathcal{D}}, \tag{5.29}$$

which is indicative the relative strength of viscous diffusion versus that from the molecular diffusivity of the scalar quantity itself (*i.e.* temperature or species concentration).

5.3.2 Non-Dimensional Governing Equations

The dominance of the different physical processes occurring within a turbulent velocity and scalar field can be understood by non-dimensionalizing the momentum (Eq. 5.15) and scalar transport (Eq. 5.19) equations. The characteristic scales to be used to non-dimensionalize the pertinent variables are defined to be,

$$\hat{\rho} = \rho/\rho_c \qquad \hat{u}_i = u_i/u_{ic} \qquad \hat{p} = p/p_c \qquad \hat{x}_i = x_i/l_{ic} \qquad \hat{g}_i = g_i/g_{ic}$$
$$\hat{t} = t/\tau_c = t u_{ic}/l_{ic} \quad \hat{\mu} = \mu/\mu_0 \quad \hat{\mathcal{D}} = \mathcal{D}/\mathcal{D}_0 \quad \hat{Z} = Z/\phi \tag{5.30}$$

where $(\hat{\cdot})$ variables are unitless and of order one and $(\cdot)_c$ or $(\cdot)_0$ variables are characteristic scales. When applied to the (forced) momentum equation, it is obtained,

$$\frac{\partial \hat{\rho}\hat{u}_i}{\partial \hat{t}} + \frac{\partial \hat{\rho}\hat{u}_i\hat{u}_j}{\partial \hat{x}_j} = -\frac{\partial \hat{p}}{\partial \hat{x}_i} + \frac{1}{Re}\frac{\partial}{\partial \hat{x}_j}\left\{\hat{\mu}\left(\frac{\partial \hat{u}_i}{\partial \hat{x}_j} + \frac{\partial \hat{u}_j}{\partial \hat{x}_i}\right)\right\} + \frac{\tau_c}{2\tau_v}\frac{k_0}{k}\hat{\rho}\hat{u}_i + \frac{Ri}{A}\left(\hat{\rho}\hat{g}_i - \langle\hat{\rho}\rangle\hat{g}_i\right), \quad (5.31)$$

where the definitions provided in Section 5.3.1 have been used. To get this expression, three things have been assumed. First, it is assumed that the correct pressure scaling is an inertial one such that $p_c \sim \rho_c u_c^2$. Second, it has been assumed that the characteristic scales for the u, v, and w components of velocity are equivalent such that $u_{ic} = u_c$ in all cases. Following this, it assumed that $l_{ic} = l_c$. While this is not generally true, for the purposes of scaling, the approximations are reasonable. Third, the magnitude of the linear forcing term, Q, has been written in terms of the eddy turn-over time of the velocity field, $Q = (2\tau_v)^{-1}$. Here, $\tau_v = k/\epsilon$ represents the eddy-turnover time. Note that the time-scale ratio on the right-hand side, τ_c/τ_v, is of order one.

The left-hand side of Eq. 5.31 is of order one, and the right-hand side clarifies the effect of varying any of the three non-dimensional parameters. If the Reynolds is increased, the viscous diffusion term is reduced in magnitude, and the inertial terms become increasingly dominant. If the ratio of the Richardson number to the Atwood number is increased, the magnitude of the buoyant term becomes larger; whereas, if the ratio is decreased, the Boussinesq limit is obtained, where the importance of gravity on the velocity field dynamics becomes negligibly small.

The same procedure can be applied to the scalar transport equation. By using the defined characteristic scales, the advection-diffusion equation under the linear scalar forcing method becomes,

$$\frac{\partial \hat{\rho}\hat{Z}}{\partial \hat{t}} + \frac{\partial \hat{\rho}\hat{u}_j\hat{Z}}{\partial \hat{x}_j} = \frac{1}{ReSc}\frac{\partial}{\partial \hat{x}_j}\left(\hat{\rho}\hat{\mathcal{D}}\frac{\partial \hat{Z}}{\partial \hat{x}_j}\right) + \frac{\tau_c}{2\tau_Z}\hat{\rho}\hat{Z}, \quad (5.32)$$

where the final term, the forcing term, has been written in terms of a scalar time scale $(\tau_Z = \sigma_Z^2/\chi)$. As before, it is assumed here that $l_{ic} = l_c$ and $u_{ic} = u_c$. From this expression, increasing either the Reynolds or Schmidt numbers has the effect of reducing the relative importance of scalar diffusion; conversely, decreasing either parameter increases the importance of scalar diffusion. As with the momentum equation, the effect of the scalar forcing term is to impose a time scale on the problem, which will vary in value depending on the Schmidt number. The time-scale ratio, τ_c/τ_Z, in the scalar field is of order one, as was seen in the velocity field in the momentum equation (Eq. 5.31).

5.3.3 Range of Attainable Atwood Numbers

A representative table of Atwood numbers attainable by implementing the equation of state discussed in Section 5.2.1 (Eq. 5.6) under the new definition proposed (Eq. 5.28) is provided in Table 5.1. From dimensional analysis, the Atwood number is proportional to the ratio of the parameters a and b and

Table 5.1: The effect of varying equation of state parameters on the Atwood number. These are representative values with $Re_\lambda = 30$ and $Sc = 1$. The integral length-scale of the density field, l_ρ, is defined in Section 5.3.4, and it should be compared to the simulation box size (2π in this case).

No.	a	b	A	l_ρ
1	0.050	1.000	0.068	1.80
2	0.075	1.000	0.115	1.62
3	0.100	1.000	0.140	1.50
4	0.125	1.000	0.161	1.42
5	0.150	1.000	0.250	1.22

the standard deviation of the scalar field. Thus, it can be written,

$$A \propto \frac{a}{b^2}\sigma_Z. \tag{5.33}$$

From the numerical tests performed, it is found that the proportionality constant is slightly larger than unity. The variance of the stationary scalar field (σ_Z^2) can be set by altering α in the case of linear scalar forcing (Eq. 5.18) or by changing the magnitude of the imposed scalar gradient, $\mathcal{G}_i$, when using the mean scalar gradient forcing method (Eq. 5.16). For simplicity, and without losss of generality, the coefficient b is set to unity for all simulations. Under this condition, and using the fact that the mixture fraction is reasonably well represented by a Gaussian (see Section 5.5.2), the average density in the domain is approximately equal to unity, $\langle \rho \rangle \sim 1$.

As the present definition of the Atwood number relies on local density values, and not those of the two fluid reservoirs significantly removed from the mixing region, the span of attainable Atwood numbers should not be compared to those reported in other studies (*e.g.,* [54, 55, 56]). Some of these studies report Atwood numbers as high as 0.75 (as calculated according to Eq. 5.26). In fact, the lower magnitude Atwood numbers calculated in the current work (from Eq. 5.28) are indicative of larger density differences in the mixing region, as they are based only on local values. Flows with comparably large variations in density in the mixing region are found in physically meaningful atmospheric and oceanographic flows. An advantage of this method of incorporating variations in density is that the present framework can support Atwood numbers that are larger than the Boussinesq limit ($A < 0.05$ per the definition in Eq. 5.26). The presence of these large attainable density ratios (Table 5.1) suggests that strongly buoyant flows can be interrogated.

5.3.4 Relevant Characteristic Length and Velocity Scales

The length-scale chosen for the Richardson number is the integral scale for the density field, l_ρ, which is defined via the two-point correlation function to be,

$$l_\rho = \frac{1}{\sigma_\rho^2} \int_0^\infty \langle \rho'(y)\rho'(y + \hat{e}_y r) \rangle \, dr, \qquad (5.34)$$

where σ_ρ^2 is the variance of the density field, r is the separation distance between two fluid points along the direction $\hat{e}_y$, and y is the coordinate direction aligned with the direction of gravity. As gravity acts on density differences, the distance over which the density fluctuations are correlated with one another along its direction of action is the physically relevant dimension. This length-scale is taken to be representative, and it is a reasonable metric to use to quantify the strength of buoyant forces in the numerator of Ri.

The length-scale for the Reynolds number is the integral length-scale for the velocity field. For the current purposes, the only physically representative velocity component to use in the determination of the integral length-scale is the velocity component in the direction of the gravity vector. In a purely buoyant flow (*i.e.* $Q = 0$), all energy production is concentrated into the velocity component aligned with gravity (Eq. 5.22). There is no energy injected into velocity components that are orthogonal to the gravity vector, making them necessarily and perpetually smaller in magnitude. Thus, the integral length-scale of the v velocity component is more suggestive of the strength of buoyancy-induced turbulent kinetic energy. In the other extreme of isotropic energy production (*i.e.* $g = 0$), the magnitude and the nature of all three velocity components ought to be statistically equivalent. Thus, using the velocity component in the direction that would be aligned with the gravity vector, if it were non-zero, to calculate the integral length-scale in this scenario is still physically appropriate. In summary, the characteristic velocity length-scale is defined as,

$$l_v = \frac{1}{\sigma_V^2} \int_0^\infty \langle v'(y)v'(y + \hat{e}_y r) \rangle \, dr, \qquad (5.35)$$

where σ_V^2 is variance of the v component of velocity, the gravity vector is in the y-direction, and $v' = v - \langle v \rangle$.

A velocity scale is needed also to quantify the Ri and Re numbers. For the current purpose, and for the same reasons discussed above, the standard deviation of the v component of velocity is used, $u^2 = \sigma_V^2 = \langle v^2 \rangle - \langle v \rangle^2$. Under these conditions, the Richardson number can be expressed as,

$$Ri = \frac{Agl_\rho}{\sigma_V^2}. \qquad (5.36)$$

The same velocity scale is used to define the Reynolds number,

$$Re = \frac{\sigma_V l_v}{\nu}. \tag{5.37}$$

5.3.5 Controlling the Reynolds and Richardson Numbers

One of the most attractive features of the proposed simulation configuration is the ability to vary independently the Ri and Re numbers. This allows for the influences of convective mixing (Re) and buoyancy (Ri) to be isolated and examined systematically. All four dimensionless parameters ($Sc = \nu/\mathcal{D}$, A, Ri, and Re) can be manipulated to give a desired combination in parameter space. The Atwood number, which is the parameter that should generally be held fixed at a specified value to study variable density flows, is determined by adjusting a, b, and the scalar field variance. The Schmidt number can be changed to any desired value by changing the diffusion coefficient ($\mathcal{D}$) or the kinematic viscosity. Specifying Q in the momentum equation (Eq. 5.14) with ν from the Sc number fixes the Reynolds number (Eq. 5.37). Then, any change in the desired of Ri induced by changing Re can be offset by adjusting g in Eq. 5.36.

Scaling arguments are useful also in illustrating how the Re and Ri numbers can be varied independent of each other. A length-scale for the large (energy production) scales can be defined as $L = k^{2/3}/\epsilon$. Using this definition, the turbulent kinetic energy can be expressed as $k = (L\epsilon)^{2/3}$. Scaling arguments for the Re and Ri numbers follow,

$$Re = \frac{\sigma_V l_v}{\nu} \propto \frac{\sqrt{k}L}{\nu} \propto \frac{L^{4/3}\epsilon^{1/3}}{\nu}, \tag{5.38}$$

$$Ri = \frac{Agl_\rho}{\sigma_V^2} \propto \frac{AgL}{k} \propto \frac{AgL^{1/3}}{\epsilon^{2/3}}. \tag{5.39}$$

Here, it has been assumed that the relevant length-scales for velocity (l_v) and density (l_ρ) are proportional to L. This assumption has been confirmed by the numerical tests performed, but the proportionality constant is different for l_v and l_ρ. For the present purposes, this is inconsequential. Equations 5.38 and 5.39 depict that Re and Ri are linked by the dissipation rate and the length scale. The amount of energy present in the computational domain fixes ϵ, which, together with the Schmidt number (ν), determines the Reynolds number. The Richardson number is similarly influenced by ϵ and L, but there is one additional free parameter, the magnitude of gravity (g), that can be adjusted to yield the desired Ri value.

5.4 Resolution Requirements and Numerical Schemes

To validate the proposed framework, it is necessary to identify the operating parameters required to generate accurate physics under the proposed simulation methodology. To ensure that the five

constraints discussed in Section 5.2.2 are satisfied when simulations are performed in the proposed configuration, certain numerical and resolution requirements must be specified. A simulation study is performed in which the grid resolution, order of accuracy in the velocity solver, and scalar transport scheme are varied to identify these constraints. This study includes test cases subject to isotropic forcing only (cases 1, 3, 5, and 7) and for those that are subject to buoyant forcing only (cases 2, 4, 6, and 8). For the purposes of plotting, the purely isotropically-forced data sets are denoted as "case A" and the purely buoyantly-forced data sets are denoted as "case B." Tables 5.2-5.4 contain all the pertinent simulation details.

The code package used in this study is NGA [26]. The code is physical (non-spectral), suitable for low Mach number flows, and uses a standard staggered grid. The velocity field is solved implicitly via a second- or fourth-order accurate finite-difference scheme, and this scheme is discretely energy conserving. The scalar field is solved implicitly via either the QUICK scalar transport scheme, which is a third-order upwinded finite-volume scheme [52], or a fifth-order accurate upwinded scheme (HOUC5)[68]. The time advancement is by a semi-implicit Crank-Nicolson method [26]. Additional details on the simulation code are provided in Appendix 8.3, Appendix 8.4, Appendix 8.5, and Appendix 8.6 at the end of this document.

5.4.1 Grid Resolution Requirements

In order to capture the dynamically important scales and to prevent drift in the momentum, $\langle \rho u_i \rangle$, and scalar concentration, $\langle \rho Z \rangle$, values, the computational grid must be sufficiently resolved. To quantify the resolution needed, the results from the cases in Table 5.2 are examined. The results are contained in Fig. 5.2(a) and Fig. 5.2(b). Two of the crucial constraints for this configuration are the prevention of drift in scalar concentration, $\langle \rho Z \rangle \approx \langle \rho Z \rangle_{t=0}$, and of drift in momentum, $\langle \rho u_i \rangle = 0$. Beginning with the isotropically-driven turbulent field, the scalar concentration is held at its initial value with a resolution of $\kappa \eta \geq 1.5$. The grid resolution requirement in the velocity field is similar, with sufficiently minimal momentum drift attained with $\kappa \eta = 1.5$. The story is similar with the buoyant cases examined. Thus, the preferrable overall grid resolution is $\kappa \eta \geq 1.5$.

5.4.2 Order of Accuracy Requirements

The NGA package implemented allows for velocity solvers of arbitrarily high order. To determine the order of accuracy needed to satisfy the constraint for momentum, the velocity solver is run with second- and fourth-order accuracy for the cases in Table 5.3. The results are shown in Fig. 5.3(a) and Fig. 5.3(b). Clearly, increasing the order of accuracy employed has minimal effect on the resulting scalar concentration and momentum drift. Thus, second-order accuracy in the velocity solver is sufficient for the proposed configuration.

Table 5.2: Grid resolution effects for isotropically- and buoyantly-driven turbulent flows ($\nu = 0.005$, $A = 0.13$, $Sc = 1$). The HOUC 5 scalar transport scheme is used.

No.	ϵ	Re (Eq. 5.37)	g	Ri (Eq. 5.36)	N^3	$\kappa_{max}\eta$	$\kappa_{max}\eta_B$	Order
1	1.88	780	0	0	192^3	1.5	1.5	2nd
2	1.94	2070	12	0.61	192^3	1.5	1.5	2nd
3	2.15	480	0	0	384^3	3.0	3.0	2nd
4	2.82	2860	12	0.54	384^3	2.7	2.7	2nd

Table 5.3: Order of accuracy effects in the velocity solver for isotropically- and buoyantly-driven turbulent flows ($\nu = 0.005$, $A = 0.13$, $Sc = 1$). The HOUC 5 scalar transport scheme is used.

No.	ϵ	Re (Eq. 5.37)	g	Ri (Eq. 5.36)	N^3	$\kappa_{max}\eta$	$\kappa_{max}\eta_B$	Order
1	1.88	780	0	0	192^3	1.5	1.5	2nd
2	1.94	2070	12	0.61	192^3	1.5	1.5	2nd
5	1.96	600	0	0	256^3	2.0	2.0	4th
6	1.91	1700	12	0.64	256^3	2.0	2.0	4th

5.4.3 Transport Scheme Requirements

Scalar transport schemes can be dissipative, resulting in the smoothing of fine scalar field features and the loss of important scalar field physics during advection. To determine the sensitivity of the proposed simulation configuration to the scalar transport scheme used, the scalar field is advected with two upwinded schemes. A fifth-order scheme (HOUC) is used and compared to a third-order finite-volume scheme (QUICK). The results of this comparison (Table 5.4) are depicted in Fig. 5.4(a) and Fig. 5.4(b). It is clear that either scheme produces acceptably small variation in the domain-averaged scalar concentration. Hence, either method is allowable. The details pertinent to these two transport schemes are included in Appendix 8.5.

5.5 Characteristics of Turbulent Buoyant Flows

The previous sections have defined the simulation geometry, presented the governing equations and associated constraints on the forcing methods applied, and defined the pertinent non-dimensional

Table 5.4: Effects of varying the scalar transport scheme for isotropically- and buoyantly-driven turbulent flows ($\nu = 0.005$, $A = 0.13$, $Sc = 1$). The velocity solver is second-order.

No.	ϵ	Re (Eq. 5.37)	g	Ri (Eq. 5.36)	N^3	κ_{max}	$\kappa_{max}\eta_B$	Scheme
1	1.88	780	0	0	192^3	1.5	1.5	HOUC 5
2	1.94	2070	12	0.61	192^3	1.5	1.5	HOUC 5
7	2.06	390	0	0	256^3	2.0	2.0	QUICK
8	2.25	2790	12	0.64	256^3	2.0	2.0	QUICK

(a) Temporal drift of scalar concentration, $\langle \rho Z \rangle$.

(b) Temporal drift of momentum, $\langle \rho u \rangle$.
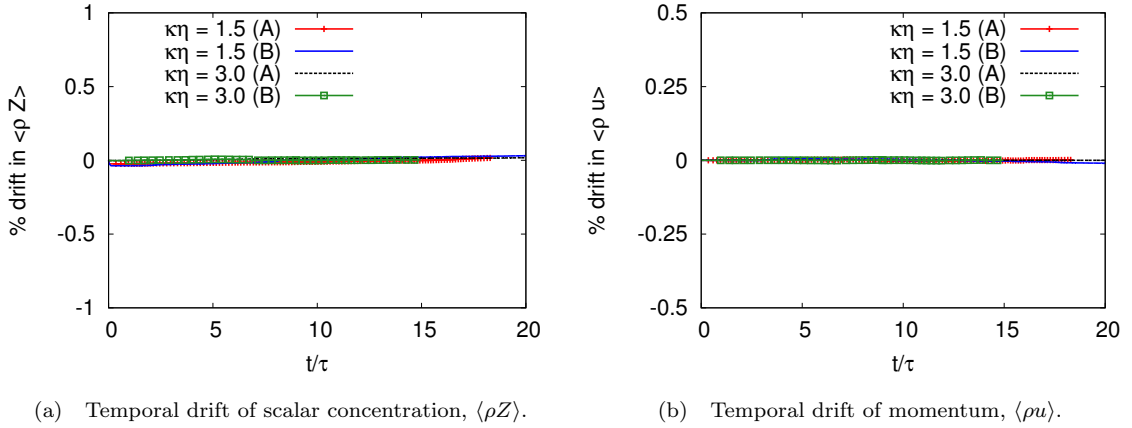
Figure 5.2: Grid resolution requirements under purely isotropic (A) and purely buoyant (B) conditions. Percent (%) drift is defined as $(\langle \rho Z \rangle - \langle \rho Z \rangle_{t=0})/\langle \rho Z \rangle_{t=0} * 100$.

(a) Temporal drift of scalar concentration, $\langle \rho Z \rangle$.

(b) Temporal drift of momentum, $\langle \rho u \rangle$.
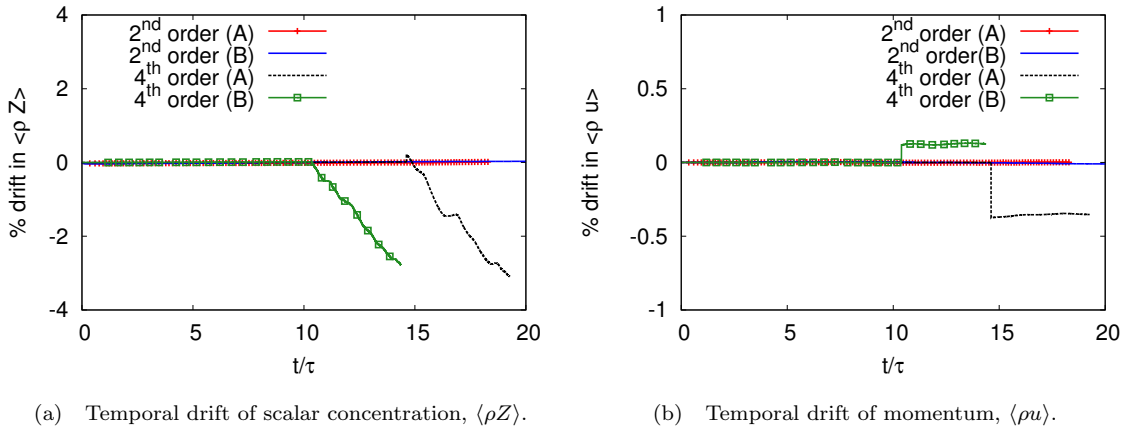
Figure 5.3: Order of accuracy requirements under purely isotropic (A) and purely buoyant (B) conditions. Percent (%) drift is defined as $(\langle \rho Z \rangle - \langle \rho Z \rangle_{t=0})/\langle \rho Z \rangle_{t=0} * 100$.

(a) Isotropic turbulence.

(b) Buoyant turbulence.
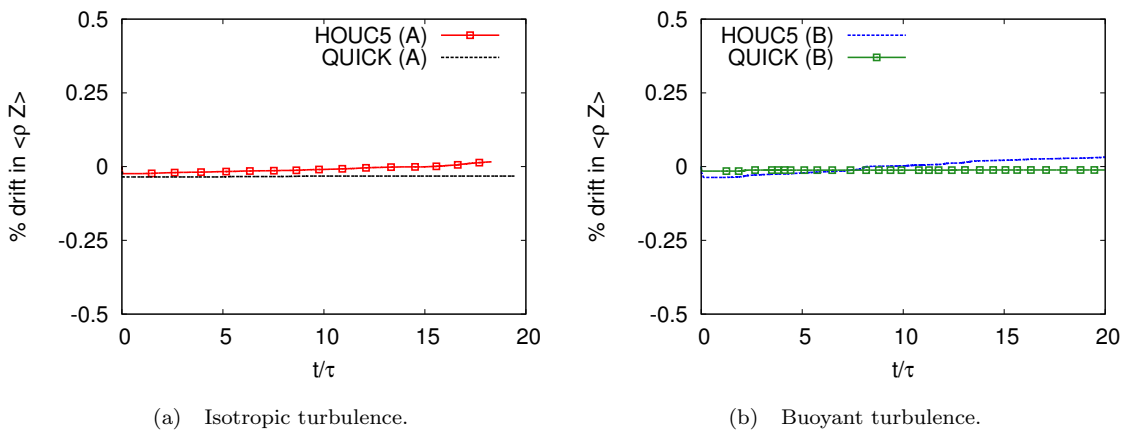
Figure 5.4: Impact of scalar transport scheme on the temporal drift of scalar concentration, $\langle \rho Z \rangle$. Percent (%) drift is defined as $(\langle \rho Z \rangle - \langle \rho Z \rangle_{t=0})/\langle \rho Z \rangle_{t=0} * 100$.

Table 5.5: Isotropically- and buoyantly-driven turbulent flows under the proposed configuration for unity Schmidt number conditions. The scalar transport scheme is HOUC5.

No.	ϵ	Re (Eq. 5.37)	$|g|$	Ri (Eq. 5.36)	N^3	$\kappa_{max}\eta$	$\kappa_{max}\eta_B$	Order
A	2.02	480	0	0	256^3	2.0	2.0	2nd
B	2.03	2290	12	0.48	256^3	2.0	2.0	2nd
C	1.95	1205	9	0.50	256^3	2.0	2.0	2nd

numbers needed to characterize turbulent buoyant flows. In Sections 5.5.1 - 5.5.3, the test cases (shown in Table 5.5) used to evaluate the proposed simulation method are presented, and some results provided. From the data garnered, statistical metrics are calculated in way of validation of the presented framework. Specifically, the results are compared to canonical turbulent or accepted buoyant behaviors, and consistency between them is verified.

5.5.1 Presentation of Numerical Tests

The results obtained from the proposed numerical framework are examined and discussed for three cases; case A is subject to purely isotropic forcing ($g = [0, 0, 0]$ and $Q = 0.382$ in Eq. 5.15), case B is subject to only buoyant forcing ($g = [0, -12, 0]$ and $Q = 0$ in Eq. 5.15), and case C is subject to both isotropic and buoyant energy production ($g = [0, -9, 0]$ and $Q = 0.287$ in Eq. 5.15). Cases A, B, and C have an Atwood number of 0.13. This relatively high Atwood number was chosen such that the differences between isotropically-driven and buoyantly-driven flow, if any, would be maximized and more clearly identifiable. The scalar forcing method used in all three cases is the linear scalar method with $\alpha = 1$ and $\tau_I = 0.1$. These three cases are described in Table 5.5. Note that the total energy dissipation rate, ϵ, is held approximately fixed across cases A, B, and C. This constancy is useful for comparison purposes, as it ensures that the Kolmogorov length-scales are uniform across the three cases.

This validation process includes reproducing a few canonical features of isotropic turbulence for the purely isotropically-forced case (case A). For the sake of comparison, and to highlight any disparities, these features are calculated also for fully buoyant conditions (case B) and partially buoyant conditions (case C).

In the case of isotropic (non-buoyant) turbulence, the turbulent kinetic energy is produced from the momentum source term, f_{u_i}. When this is multiplied by u_i and appropriately averaged as done in Eq. 5.22, a constant magnitude of power is injected into the computational domain, $2Qk_0$. When written in terms of a spectral-space representation, an energy production spectrum of the form $P(\kappa) = 2QE(\kappa)$ arises, where $E(\kappa)$ is the three-dimensional energy spectrum. This energy production spectrum is shown in Fig. 5.5. Alternatively, buoyant flows provide power in proportion to the density difference and the strength of gravity according to $P(\kappa) = -\hat{v}^* \mathscr{F}_{\underline{\kappa}}\left(\frac{\rho'}{\rho}g\right)$; here $\mathscr{F}_{\underline{\kappa}}(\cdot)$
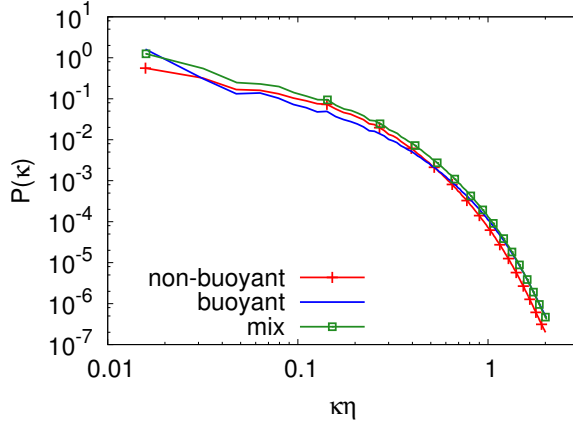
Figure 5.5: Energy production spectra for the isotropically- and buoyantly-driven turbulent flows in Table 5.5 ($\epsilon \approx 2$, $Sc = 1$, $\kappa\eta = 2.0$).

denotes the Fourier transform, and $\hat{u}_i^*$ denotes the complex conjugate of the Fourier coefficient for the i-th component of velocity, u. It should be noted that in case C, approximately half of the energy production comes from buoyancy and the other half is from isotropic forcing, such that $P(\kappa) = 2QE(\kappa) - \hat{v}^* \mathscr{F}_{\underline{\kappa}} \left(\frac{\rho'}{\rho} g \right)$. The energy production spectra for cases B and C are shown also in Fig. 5.5.

5.5.2 Scalar and Density Field Distributions

The current methodology links the scalar field and the density field through the use of an equation of state (Eq. 5.6). To ensure that this coupling is not adversely affecting the evolution of the two fields, the steady state distributions they assume are calculated and briefly discussed.

It is generally accepted that a scalar field subject to isotropic turbulent conditions (mixing) has a nearly Gaussian probability density function (PDF) [41, 96, 103, 18]. To confirm that this distribution is preserved in the implemented framework, the PDFs of the scalar fields in cases A, B, and C are calculated (Fig. 5.6(a)). As indicated in Fig. 5.6(a), the scalar fields in all three cases are approximately Gaussian in distribution.

The density field can be discussed also. As the Gaussianly-distributed scalar field is used to determine the density field (per Eq. 5.6), a theoretical PDF for the density can be obtained in terms of the PDF of the scalar field. This theoretical density field distribution is compared to the density field PDFs calculated for cases A, B, and C; the results are shown in Fig. 5.6(b). As with the scalar fields, the density fields are approximately Gaussian.
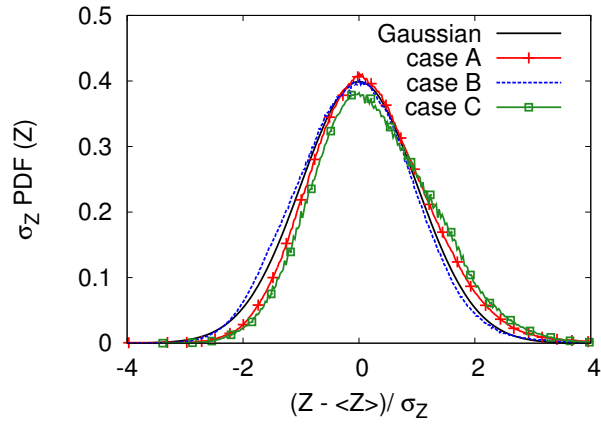
(a) Scalar field distribution.
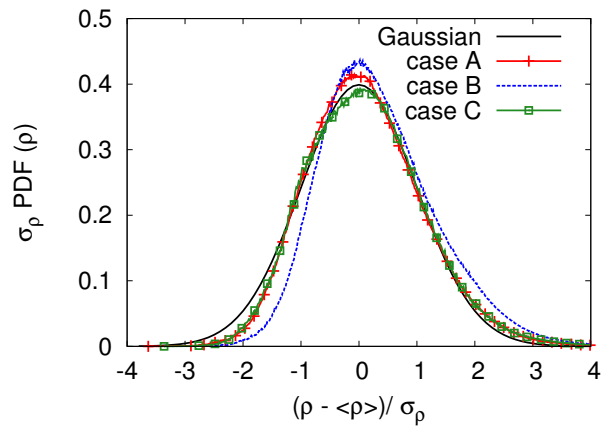
(b) Density field distribution.

Figure 5.6: Probability density functions of the scalar, Z, and density, ρ, fields for the cases in Table 5.5.

5.5.3 Universality and (An)isotropy: Characteristic Length-scales

There is some conflict in the literature as to the isotropic, or anisotropic, nature of buoyant flows. There are studies which find evidence that the intermediate scales are more isotropic than the smallest viscous scales [18, 56], and there are others which find evidence for the inverse [11]. In light of this, the isotropic nature of the flows generated under the proposed numerical framework is investigated for cases A, B, and C. The presence of isotropy in these turbulent fields can be qualified via a calculation of the characteristic length-scales of the flow and a calculation of energy content in the three ordinate directions.

Two characteristic length-scales of importance in turbulent flows are the Kolmogorov scale and the Taylor micro-scale. The Kolmogorov scale, η, is the smallest dynamically significant flow scale, and it is representative of the length-scale at which viscous dissipation of kinetic energy in the fluid becomes important. The Taylor micro-scale, λ, is the smallest of the flow scales associated with large-scale energy production; it can be used to represent the intermediate flow scales. In order to quantify the extent of isotropy or anisotropy at the different flow scales, directional Taylor micro-scales and Kolmogorov scales are calculated according to,

$$\eta_i = \left(\nu^3/\epsilon_i\right)^{1/4} \qquad \epsilon_i = 15\nu\langle\,(\partial u_i/\partial x_i)^2\rangle, \tag{5.40}$$

and

$$\lambda_i = \left(\frac{\sigma_i^2}{\langle(\partial u_i/\partial x_i)^2\rangle}\right)^{1/2}, \tag{5.41}$$

where ϵ_i is the energy dissipation rate in each of the three ordinate directions (no implicit summation on repeated indices). These are the same definitions used in similar studies, such as those by Cabot and Cook [11]. In way of providing context, ϵ_i so defined is related to the three diagonal elements in the (un-averaged) energy dissipation rate tensor, $\epsilon = \nu \frac{\partial u_i}{\partial x_j}\left(\frac{\partial u_i}{\partial x_j} + \frac{\partial u_j}{\partial x_i}\right)$. Other metrics that indicate the extent of isotropy at the largest flow scales are the variances of the three components of the velocity field, u, v, and w, and these are defined as,

$$\sigma_i^2 = \langle u_i^2 \rangle - \langle u_i \rangle^2. \tag{5.42}$$

If the variances of these are approximately the same, it indicates that the largest flow scales are relatively isotropic.

To answer the question as to the extent of scale isotropy under buoyant versus non-buoyant (isotropic) conditions, the three directional Kolmogorov and Taylor micro-scales and the three velocity component variances are calculated. The results for cases A, B, and C are provided in

Table 5.6: Directional Kolmogorov and Taylor micro-scales (Eq. 5.40 and Eq. 5.41) and velocity field variances (Eq. 5.42).

case A isotropic			case B buoyant			case C mix		
η_x	η_y	η_z	η_x	η_y	η_z	η_x	η_y	η_z
0.013	0.013	0.016	0.014	0.013	0.015	0.014	0.013	0.014
λ_x	λ_y	λ_z	λ_x	λ_y	λ_z	λ_x	λ_y	λ_z
0.032	0.030	0.036	0.034	0.101	0.036	0.037	0.063	0.036
σ_u^2	σ_v^2	σ_w^2	σ_u^2	σ_v^2	σ_w^2	σ_u^2	σ_v^2	σ_w^2
1.75	1.63	1.98	1.76	6.81	1.85	1.69	3.26	1.62

Table 5.6. The Kolmogorov scales for the non-buoyant data indicate that the scale at which dissipation becomes important is the same for the three velocity component directions. Additionally, the variances suggest an approximately equal distribution of energy at the largest scales, and the intermediate scales indicate isotropy ($\lambda_x \approx \lambda_y \approx \lambda_z$).

The fully and partially buoyant data (cases B and C) agree, to an extent, with this non-buoyant data; the Kolmogorov scales suggest that dissipation becomes important at equivalent points despite the presence of anisotropic buoyancy effects. This finding of isotropic Kolmogorov scales is consistent with previous studies [11] and with energy cascade concept, which states that, as energy is transferred downwards towards increasingly smaller scales, it loses dependence on large scale flow features. The Taylor micro-scales and the velocity field variances for cases B and C are clearly anisotropic, as expected from Eq. 5.42 where $\sigma_U^2 \approx \sigma_W^2 \neq \sigma_V^2$. With buoyant energy production being inherently anisotropic, this is not an unexpected result.

In summary, the results obtained under the proposed framework are consistent with previous DNS studies [19, 18, 11]. The current framework preserves appropriate quantity distributions and recovers expected (an)isotropic behaviors. Additionally, it allows for the relative magnitude of buoyant and isotropic (non-buoyant) energy production to be varied to facilitate effective parametric studies of physically meaningful flows. Further, the computational cost incurred when using the presented framework is significantly less than that required by other simulation configurations. Thus, as presented, it can be used to perform efficient simulation studies of turbulent buoyant flows and the associated mixing.

5.6 Velocity Field Physics

Section 5.5 established that the framework, as implemented, produces low-order turbulent metrics that are consistent with other studies. Although this is an important step in showing the validity of the proposed simulation framework, it is not enough to prove its utility. Thus, the physics that are predicted under the proposed framework for the three test cases listed in Table 5.5 are now briefly

discussed. This is done in way of showing that the simulation framework produces accurate data. Attention is directed towards identifying the location of any anisotropy in the generated turbulent fields and the extent to which such anisotropy is able to permeate into said turbulent fields.

5.6.1 Single Point Statistics

The largest physical scales, or the smallest wavenumber scales, are first examined. For the present purposes, attention is restricted to only cases A and B, as they represent the two extremes of turbulent buoyant flows. Beginning with purely buoyant energy production (case B), all energy is injected in a single direction (the direction of non-zero gravity), which, in this case, is the y-direction. Accordingly, there is an increased amount of energy associated with that direction (the v velocity component direction) relative to the other two (the u and w velocity component directions). To identify the extent to which this anisotropy is able to permeate into the intermediate scales, the conditional average of each of the three velocity components on the density field is calculated. This is done, then, also, with the isotropically-produced turbulent data to serve as a baseline for comparison. The results of this conditional averaging are provided in Fig. 5.7.

Under perfectly isotropic conditions, the velocity field should have no dependence on the value of the density, resulting in a conditional average that is zero for all values of density. In the case of the isotropic forcing (case A), this is what is found in Fig. 5.7(a), with the conditional average of the velocity fields virtually vanishing. The behaviors for $\rho - \langle\rho\rangle \leq -0.4$ and $\rho - \langle\rho\rangle \geq 0.5$ can be attributed to the limited frequency of such large deviations from the mean density; thus, the averages that are obtained are not truly significant. Irrespective of this, the data suggest that the three components of velocity are isotropic and have no significant dependence on the value of the density field when subject to isotropic forcing.

Alternatively, under only buoyant conditions (case B), this is clearly not the case. Figure 5.7(b) suggests that the fluid parcels with a density less than the mean ($\rho - \langle\rho\rangle \leq 0$) rise and those with one larger than the mean ($\rho - \langle\rho\rangle \geq 0$) fall, as expected. Note that the conditional averages of the u and w components on density are unaffected and appear to behave similarly to the isotropic case shown in Fig. 5.7(a). To identify how far these anisotropic effects are able to penetrate into the velocity field, the v component of velocity is filtered. The v component is split into two parts, one which contains the contributions to v from the smallest wavenumbers ($\kappa L < 40$) and one which contains the contributions from the larger wavenumbers ($\kappa L > 40$). Here, $L = k^{3/2}/\epsilon$ is the characteristic length for large-scale motion, with k and ϵ being the turbulent kinetic energy and energy dissipation rate, respectively; L is found to be approximately 80% of the domain. For the current work, this corresponds to removing the lowest eight modes, which are responsible for approximately 85% of the total energy produced (Fig. 5.5). After this filtering operation, the conditional averaging is performed again. As is clear from Fig. 5.7(c), the anisotropy seen in Fig. 5.7(b) is confined to the

smallest wavenumber contributions. When these low wavenumber contributions are removed, the velocity field assumes an isotropic nature, similar to that calculated for the isotropically-forced case (case A).

From these observations, it can be stated that there is no significant permeation of anisotropy into the velocity field; when the lowest wavenumber contributions are removed, the pronounced anisotropic behavior vanishes. From a structural sense, once these low wavenumber features are removed from the entirety of the velocity field data, the buoyantly-driven data and the isotropically-driven turbulent data become quite similar.

5.6.2 Two-Point Statistics

One of the motivating objectives of this work is to study the extent of scale isotropy in turbulent buoyant flows. Specifically, it is of interest to identify where in the turbulent fields anisotropy manifests. The conditional averages of the velocity field components indicate that the anisotropy is confined to only the largest flow scales. A more systematic metric that can be used to examine scale isotropy is the energy spectrum. Consequently, the energy spectra for the limiting cases in Table 5.5 are calculated (Fig. 5.8(a) and Fig. 5.9(a)), and these energy spectra are averaged over nine eddy turn-over times. The three-dimensional energy spectra are compared, then, against a model fit [77], which takes the form,

$$E(\kappa) = C\epsilon^{2/3}\kappa^{-n}f_L(\kappa L)f_\eta(\kappa\eta)$$

$$f_\eta(\kappa\eta) = \exp\left(-\beta\{\left((\kappa\eta)^4 + c_\eta^4\right)^{1/4} - c_\eta\}\right)$$

$$f_L(\kappa L) = \left(\frac{\kappa L}{\left((\kappa L)^2 + c_L\right)^{1/2}}\right)^{11/3}, \tag{5.43}$$

where C is a constant, L is the integral length-scale defined as $L = k^{3/2}/\epsilon$, and c_η, β, and c_L are constants determined by the Reynolds number. This model spectrum is fit to the presented DNS data via a least squares method. Again, as in Chapter 2, the quality of the fit is confirmed by calculating the L_2 norm of the error according to,

$$L_2 = ||r||_2 = \left(\sum_{i=1}^{n}|E_{model}(\kappa) - E(\kappa)|^2\right)^{1/2}.$$

E_{model} is the spectrum obtained from the fit and $E(\kappa)$ is the DNS data. It is found that the average square of the error is found to be less than 1% of the value of the total turbulent kinetic energy in both cases. This spectrum can be used also to quantify the spectral scaling present in the energy spectrum. Although not pivotal for the current work, the model fits to the present data correspond
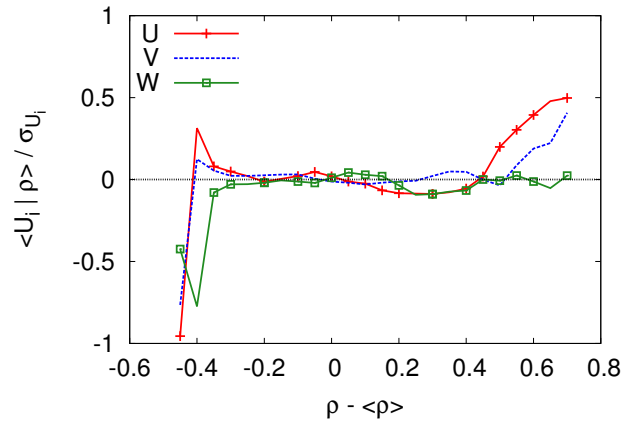
(a)   Isotropic conditions.
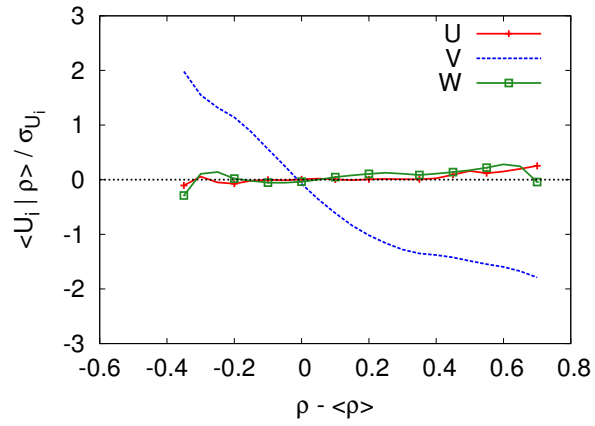
(b)   Buoyant conditions.
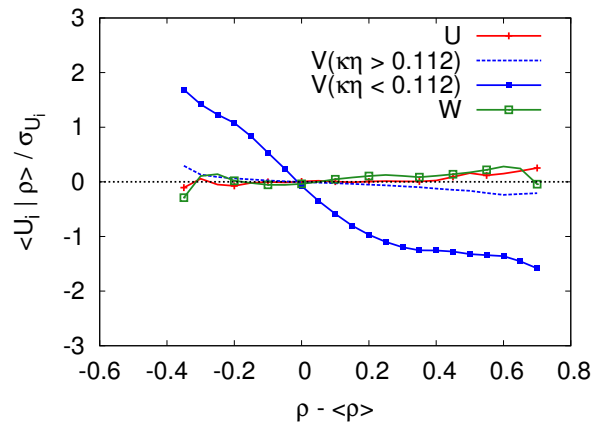
(c)   Buoyant conditions after low wavenumber filtering is applied.

Figure 5.7: Conditional average of the velocity components on the density field for cases A and B.

to $E(\kappa) \propto \kappa^{-1.4}$.

As Pope's model spectrum is derived to match isotropic turbulent data (only case A in the present study), the agreement between the model fit and the buoyant (case B) data is surprisingly good; in both cases, the model spectrum is able to match the contours of the three-dimensional energy spectrum within the dissipation region and some region outside of it. From this perspective, there is no apparent presence of anisotropy. But, as the three-dimensional energy spectrum is the average of the contribution of nine different components, it is possible that any anisotropies are being masked. To determine if this is the case, the one-dimensional energy spectra are calculated.

The one-dimensional energy spectra are indicative of the distribution of turbulent kinetic energy among the three velocity components, and they are calculated according to,

$$E_{ij}(\kappa_m) = \frac{1}{\pi} \int_{-\infty}^{\infty} R_{ij}(\hat{e}_m r_m) \exp\left(-i\kappa_m r_m\right) \, dr_m, \tag{5.44}$$

where $R_{ij} = \langle u_i(\underline{x})u_j(\underline{x}+\underline{r})\rangle$ is the velocity correlation tensor. The one-dimensional energy spectra for the limiting cases are provided in Fig. 5.8(b) and Fig. 5.9(b), and they represent the average over nine eddy turn-over times. To emphasize the anisotropies in energy content that may (or may not) be present, and following Chung and Pullin [18], the one-dimensional spectra are normalized further by the total amount of energy present in all three directions according to,

$$E_{ii}(\kappa_i)^{\dagger} = \frac{E_{ii}(\kappa_i)}{\sum_{i=1}^{i=3} E_{ii}(\kappa_i)} - \frac{1}{3}. \tag{5.45}$$

These normalized one-dimensional energy spectra are depicted in Fig. 5.8(c) and Fig. 5.9(c). The normalized quantities are used, as they emphasize the differences between the spectra in the three ordinate directions. Under isotropic conditions, $E_{ii}(\kappa_i)^{\dagger}$ ought to be zero across all wavenumbers, indicating that energy is evenly distributed in the u, v, and w component directions.

Beginning with the non-buoyant case in Fig. 5.8(b) and Fig. 5.8(c), true isotropy is suggested for all flow scales, κ. As Fig. 5.8(c) indicates, the normalized values are approximately zero across all wavenumbers, suggesting an almost perfectly even distribution of energy at all scales of the flow. Thus, the isotropically-forced turbulent case under the proposed simulation framework does have an isotropic distribution of energy.

The purely buoyant case, however, behaves differently. Figure 5.9(b) and Fig. 5.9(c) display the one-dimensional energy spectra under buoyant conditions. As is clear from Fig. 5.9(c), the low wavenumber region ($\kappa\eta \leq 0.05$) has a significantly anisotropic distribution of energy, consistent with the conditional averages calculated in the preceeding section. The intermediate scales suggest only a weakly anisotropic distribution of kinetic energy, while the small scales suggest a significantly anisotropic energy distribution. Note that these findings are consistent with other published data [11,

19, 55, 56, 57].

5.6.3 Physical-Space Behaviors

To provide a more physically-intuitive explanation of the differences in buoyant (case B in Table 5.5) and non-buoyant (case A in Table 5.5) flows, countour plots of the velocity, density, and vorticity fields are provided. These depictions contain instantaneous realizations of the relevant quantity at one instant in time. The presented realizations are representative of the overall, time-averaged nature of the flow fields.

5.6.3.1 Velocity Contours

The velocity contours of the u and w velocity components are first considered. In the case of non-buoyant (isotropic) turbulence (case A), all three components of velocity are subject to energy injection. Further, there is no difference between the x-, y-, and z-directions under isotropic conditions. Hence, the u and w component field ought to be statistically similar, with no distinguishingly different behaviors between them. This is precisely what is suggested by Fig. 5.10. The dispersion of large positive (white), intermediate (gray), and large negative (black) velocity magnitudes indicate a lack of coherent structure, and an effective uniformity or equivalence between these two components of the velocity field.

The buoyant results are largely similar. In this study, the gravity vector is aligned in the direction of the v velocity component. Energy production is, therefore, concentrated into the v component direction, while the u and w component directions have energy transferred into them. As the u and w components appear identical from the perspective of the v component, the energy transfer into u and w is statistically the same. Accordingly, the u and w fields are statistically equivalent, as shown in Fig. 5.11, and there is a lack of any coherent structure.

5.6.3.2 Density Contours

Based on the conditional averaging of the velocity field components and the density field, it was stated that the v component and the density field, ρ, are correlated under buoyant conditions and decorrelated under non-buoyant conditions (Fig. 5.7). The basis of this was the strong dependence of the sign of the v velocity component on the value of the density. If the density assumed a value less than the mean ($\rho < \bar{\rho}$), then the fluid rose ($v > 0$); if the density ($\rho > \bar{\rho}$) exceeded that of the mean, it fell ($v < 0$). However, irrespective of the density field value, the u and w components were unaffected; their orientation (sign) was independent of the value of the density field. This independence of velocity field orientation is the mark of decorrelation. These tendencies are best reflected in contour plots of the v and ρ fields under non-buoyant and buoyant conditions.
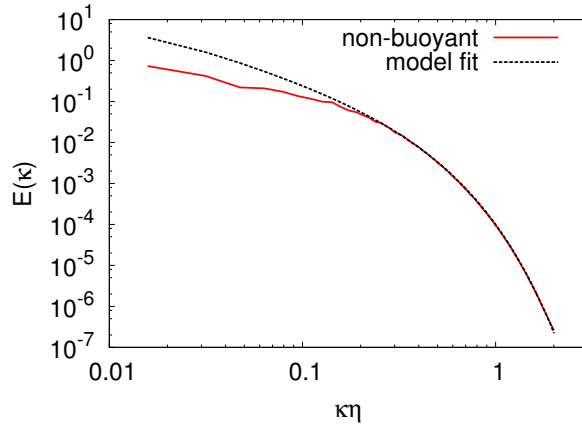
(a) 3D spectra for case A.
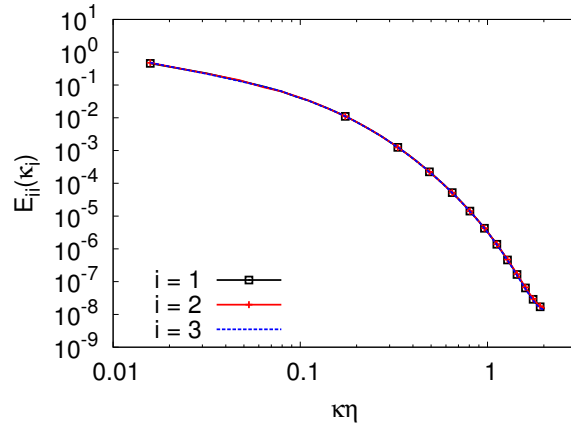
(b) 1D spectra for case A.
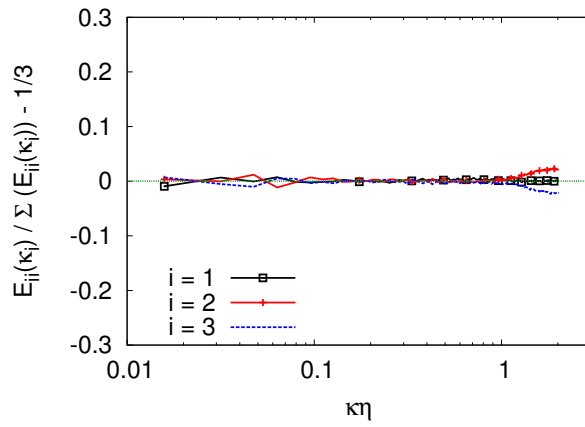
(c) Compensated 1D spectra for case A.

Figure 5.8: Normalized three-dimensional (Eq. 5.43) and one-dimensional energy spectra (Eq. 5.44 and Eq. 5.45) under purely isotropic conditions (Table 5.5).
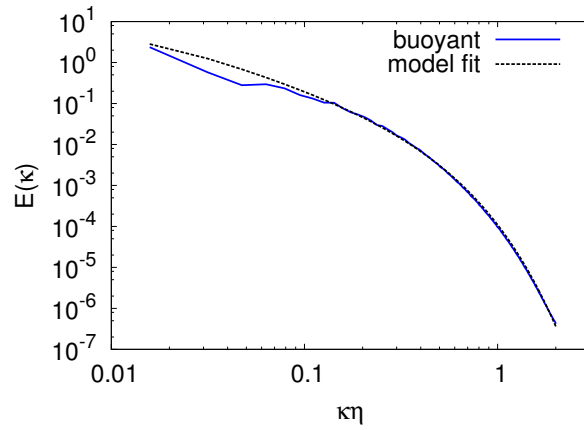
(a) 3D spectra for case B.
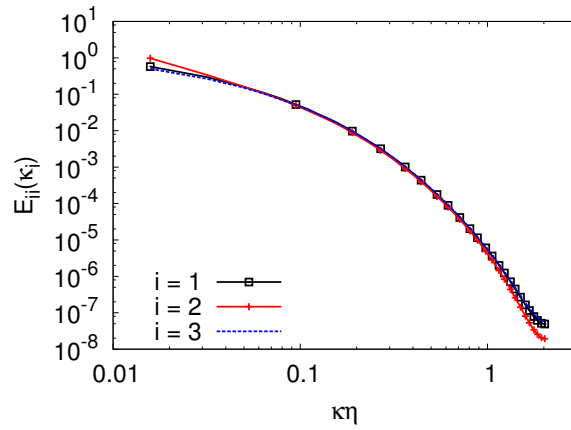
(b) 1D spectra for case B.
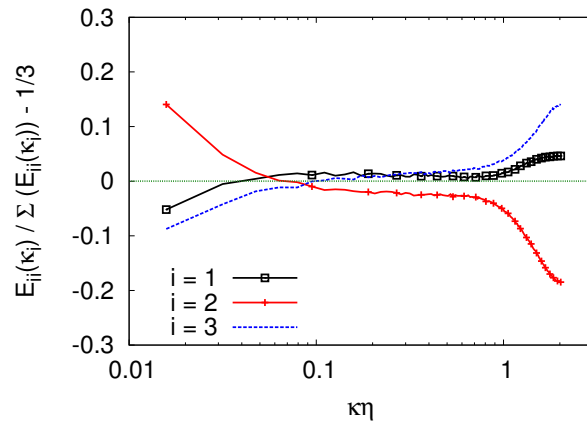
(c) Compensated 1D spectra for case B.

Figure 5.9: Normalized three-dimensional (Eq. 5.43) and one-dimensional energy spectra (Eq. 5.44 and Eq. 5.45) under purely buoyant conditions (Table 5.5).

(a) u velocity component.

(b) w velocity component.
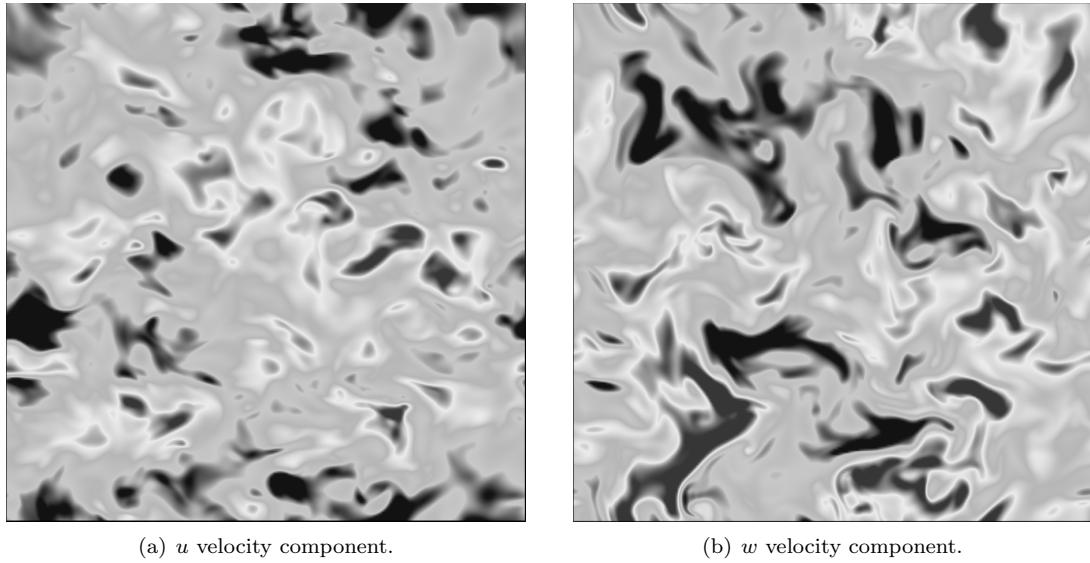
Figure 5.10: Contour plots of the u and w velocity components under non-buoyant conditions (Table 5.5). The velocity magnitudes are colored with values between -2.5 (black), 0.00 (gray), and +2.5 (white).

(a) u velocity component.

(b) w velocity component.
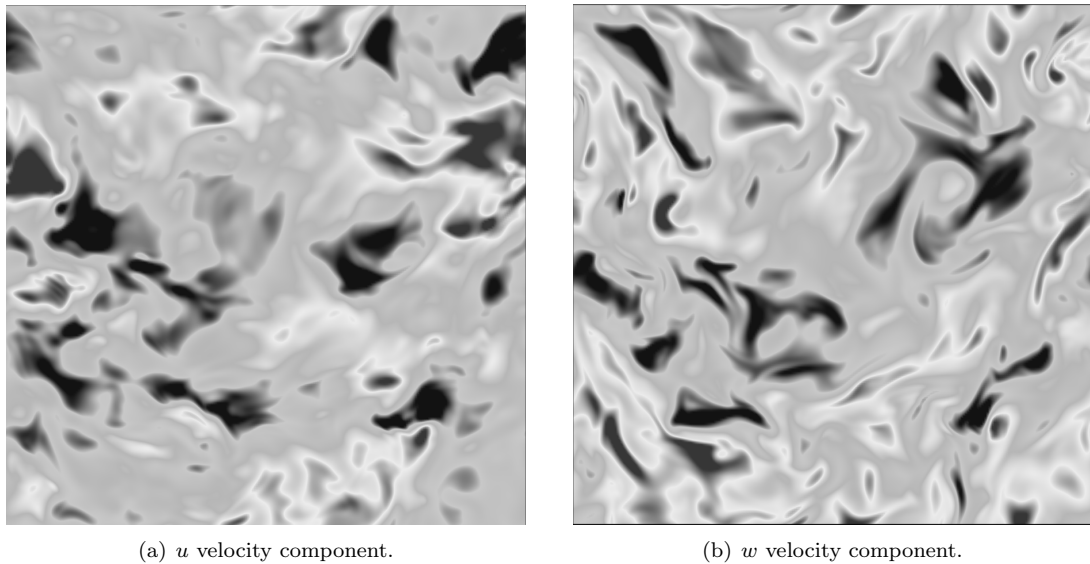
Figure 5.11: Contour plots of the u and w velocity components under buoyant conditions (Table 5.5). The velocity magnitudes are colored with values between -2.5 (black), 0.00 (gray), and +2.5 (white).

(a) v velocity component.

(b) ρ field.
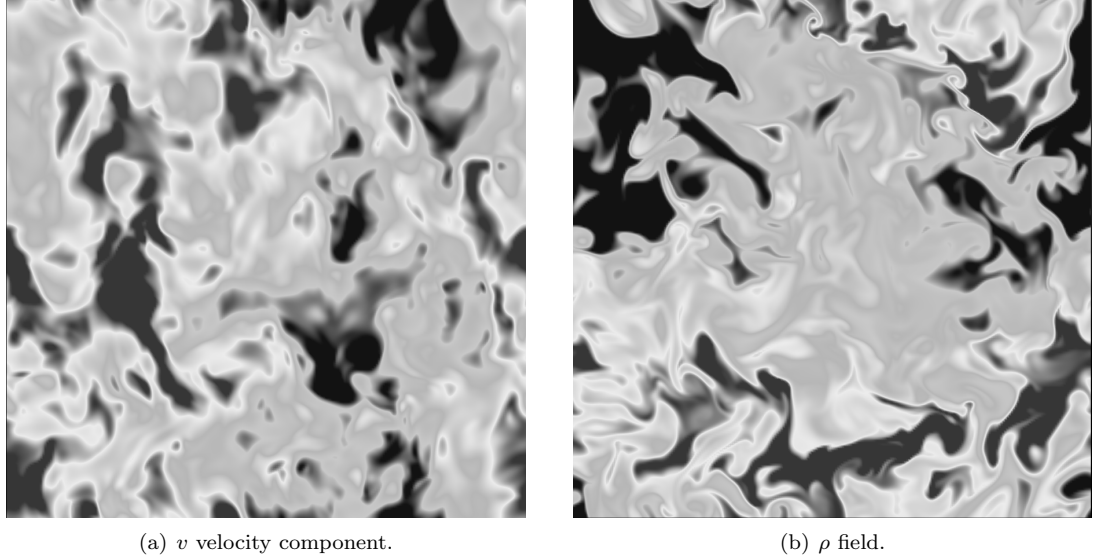
Figure 5.12: Contour plots of the v velocity component and ρ field under non-buoyant conditions (Table 5.5). The velocity magnitudes are colored with values between -2.5 (black), 0.00 (gray), and $+2.5$ (white). The density field values are colored by 0.8 (black), 1.0 (gray), and 1.2 (white).

Beginning with the non-buoyant data, the form of energy production is isotropic. This imparts an equivalence between the u, v, and w components, which is reflected in Fig. 5.12(a). Further, the independence of the velocity component orientation (*i.e.*, $v > 0$ *vs.* $v < 0$) is reflected in the density contour (Fig. 5.12(b)).

A distinctly different behavior is noted in the buoyant data. The sense of the v component of the velocity field is dependent on the value of the fluid density. This is clearly shown in Fig. 5.13, which contains the contour plots of the v and ρ fields. A low density value is colored to be black, an intermediate density value is colored to be gray, and a high density value is colored to be white. Similarly, a negative v value is colored black, a zero v value is colored gray, and a positive v value is colored white. Whenever there are patches of high density fluid ($\rho > \bar{\rho}$) in Fig. 5.13(b), there are corresponding patches of negative v values in Fig. 5.13(a). Alternatively, whenever there are patches of low density fluid ($\rho < \bar{\rho}$) in Fig. 5.13(b), there are corresponding patches of positive v values in Fig. 5.13(a).

5.6.3.3 Vorticity Contours

For completeness, the contours of the vorticity field are calculated also and presented in Fig. 5.14. The vorticity fields are determined according to,

$$\underline{\omega} = \nabla \times \underline{u} = \hat{i} \left(\frac{\partial w}{\partial y} - \frac{\partial v}{\partial z} \right) + \hat{j} \left(\frac{\partial u}{\partial z} - \frac{\partial w}{\partial x} \right) + \hat{k} \left(\frac{\partial v}{\partial x} - \frac{\partial u}{\partial y} \right). \tag{5.46}$$

(a) v velocity component.

(b) ρ field.
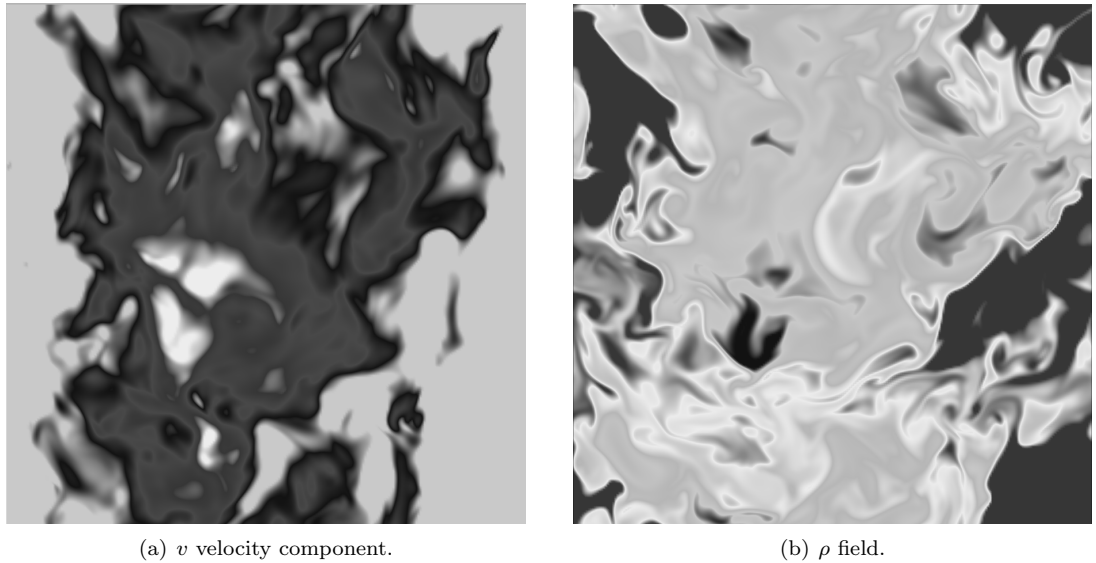
Figure 5.13: Contour plots of the v velocity component and ρ field under buoyant conditions (Table 5.5). The velocity magnitudes are colored with values between -2.5 (black), 0.00 (gray), and $+2.5$ (white). The density field values are colored by 0.8 (black), 1.0 (gray), and 1.2 (white).

The two-dimensional realizations depicted correspond to the magnitude of the vorticity field on the $x-y$ plane cut at the midplane of z. The contour plots are colored such that a low vorticity magnitude is black, an intermediate value is gray, and a high value is white. Although no conclusive inferences can be drawn from these two figures, they do suggest that the presence of buoyancy ($g \neq 0$) reduces the frequency of large magnitude vorticity occurrences relative to non-buoyant flows.

5.6.4 Summary

In summary, the analysis performed suggests that the implemented simulation framework is able to accurately reproduce key isotropic turbulent metrics. The one-dimensional and three-dimensional energy spectra under isotropic forcing conditions (case A) are found to be, indeed, isotropic. This is confirmed by agreement with Pope's model spectrum (Fig. 5.8(a)) and an approximately equal distribution of velocity variance (Fig. 5.8(c)) over all pertinent flow scales. In the other extreme, where the velocity field is fed by only buoyancy forces (case B), the deviations from isotropic behavior are both reasonable and expected. The one-dimensional energy spectra and the Taylor micro-scales indicate anisotropy, as expected since energy is provided to the velocity field by gravity, g, which is directional. Similarly, when the ratio of buoyant energy production to isotropic energy production is reduced (case C), the magnitude of the observed anisotropy correspondingly decreases. Also, gravity can be thought of as a long-wave forcing. It is, then, reasonable that, once the largest flow scales are removed (Fig 5.7(c)), the anisotropy that it induces vanishes. From these observations, it can be stated that the data predicted by the proposed methodology is both reasonable and accurate.

(a) Non-buoyant ω field.　　　　　　　　　(b) Buoyant ω field.
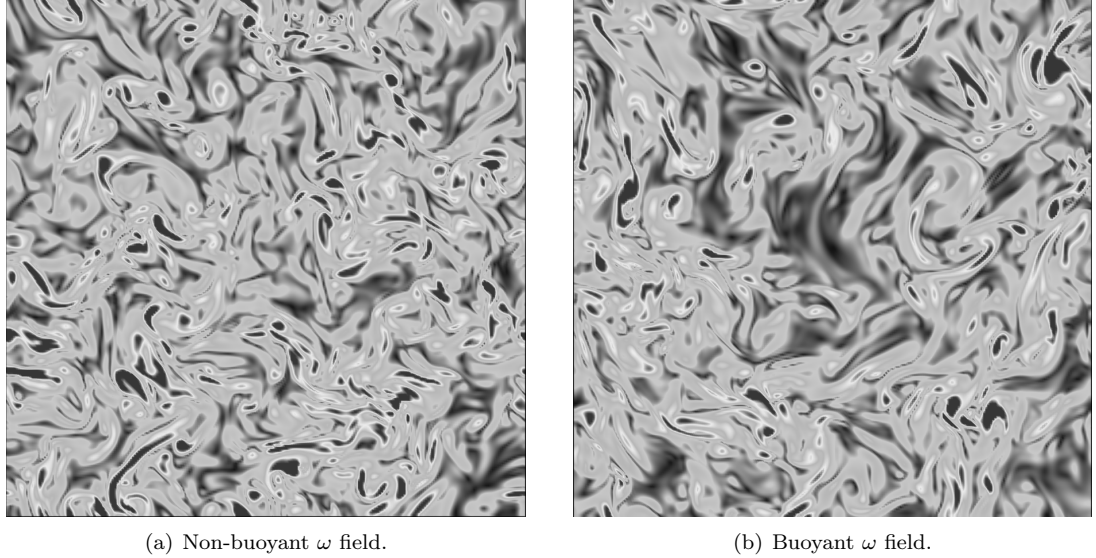
Figure 5.14: Contour plots of the vorticity field under non-buoyant and buoyant conditions (Table 5.5). The vorticity magnitudes are colored with values between 0.025 (black), 17.5 (gray), and 35 (white).

Table 5.7: Isotropically- and buoyantly-driven turbulent flows under the proposed configuration at a non-unity Schmidt number ($At = 0.13$).

No.	ϵ	ν	χ	$\mathcal{D}$	Sc	Q	$\|g\|$	N^3	$\kappa_{max}\eta$	$\kappa_{max}\eta_B$
D	2.18	0.005	1.05	3.125×10^{-4}	16	0.382	0	768^3	5.94	1.5
E	2.16	0.005	1.07	3.125×10^{-4}	16	0	12	768^3	5.96	1.5

5.7　Scalar Field Physics

The previous sections (Section 5.5 and Section 5.6) have suggested that the relevant non-dimensional parameters of importance for the velocity field, Re, Ri, and A, can be varied with respect to one another. Additionally, Section 5.5.2 showed the probability density functions (PDFs) are properly reproduced for both buoyant and non-buoyant conditions in the scalar and density fields. This section now shows that the final non-dimensional number, the Schmidt number, can be independently adjusted in the scalar field whilst holding all other parameters (A, Re, Ri) fixed. Two additional test cases are performed. The details of these two cases, one of which is subject to purely isotropic forcing in the velocity field (case D) and the other of which is subject to purely buoyant forcing in the velocity field (case E), are provided in Table 5.7. Note that these data were performed at the same Atwood number and energy dissipation rate as cases A-C ($A = 0.13$ and $\epsilon \approx 2.0$) to facilitate a comparison, and the strength of buoyant (cases B and E) and isotropic (cases A and D) forcing is the same, with $Q = 0.382$ and $g = 12$.

To prove that the $Sc = 16$ claimed in Table 5.7 is reflected indeed in the scalar field simulated,

the scalar energy spectra for cases A, B, D, and E are studied (Fig. 5.16). Note that Fig. 5.16 is normalized by the scalar dissipation rate, χ, to make the curves collapse. However, to first confirm that the velocity fields for these non-unity Schmidt number cases are equivalent to the unity Schmidt number cases, as claimed above, the energy and dissipation spectra are provided in Fig. 5.15. As is clear from Fig. 5.15, the velocity fields across the four cases are comparable. Thus, these four simulation data sets do represent two pairs of turbulent cases that have equivalent velocity fields (*i.e.*, Re, Ri, and A); only the scalar fields are subject to different conditions, *i.e.*, the Schmidt number imposed.

To determine the effective scalar diffusivity, $\mathcal{D}$, present in the scalar fields, the scalar dissipation spectra and the scalar dissipation rate, χ, are needed. Recall the definition of the scalar dissipation spectrum,

$$D_Z(\kappa) = 2\mathcal{D}\kappa^2 E_Z(\kappa), \tag{5.47}$$

that of the scalar dissipation rate,

$$\chi = \langle 2\rho\mathcal{D}|\nabla Z|^2 \rangle, \tag{5.48}$$

and the relationship between them,

$$\chi = \int_0^{\kappa=\infty} D_Z(\kappa)\, d\kappa. \tag{5.49}$$

Hence, by determining the area under the curve of the scalar dissipation spectrum and calculating the scalar dissipation rate, the (effective) value of $\mathcal{D}$ can be obtained according to,

$$\mathcal{D} = \frac{1}{2}\frac{\chi}{\int_0^{\kappa=\infty} \kappa^2 E_Z(\kappa)\, d\kappa}. \tag{5.50}$$

When this calculation is performed, the values for $\mathcal{D}$ obtained are: $\mathcal{D} = 2.94 \times 10^{-4}$ (case D) and $\mathcal{D} = 2.93 \times 10^{-4}$ (case E), which, with a kinematic viscosity of $\nu = 0.005$, give $Sc \approx 17$ for both. The Sc number calculated is not exactly the value reported in Table 5.7 ($Sc = 16$), but the difference is small, and the point is made nevertheless. The same analysis can be done for cases A and B to confirm that the Sc is different under the same Re, Ri, and A conditions. When the calculations are performed, it is found that $\mathcal{D} = 0.005$, making the $Sc = 1$, as reported in Table 5.5. This analysis confirms that the proposed configuration can be used to independently vary the Schmidt number under isotropic or buoyant conditions at a specified density ratio (Atwood number).
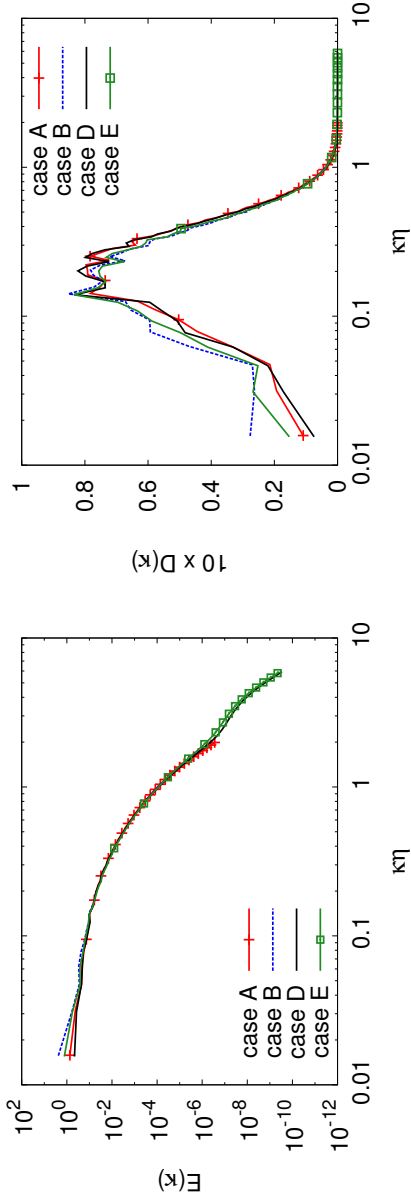
(a) Energy spectrum, $E(\kappa)$.

(b) Dissipation spectrum, $D(\kappa)$.

Figure 5.15: Energy and dissipation spectra under non-buoyant (cases A and D) and buoyant (cases B and E) conditions with an approximately constant energy dissipation rate, ϵ, and an Atwood number of 0.13.
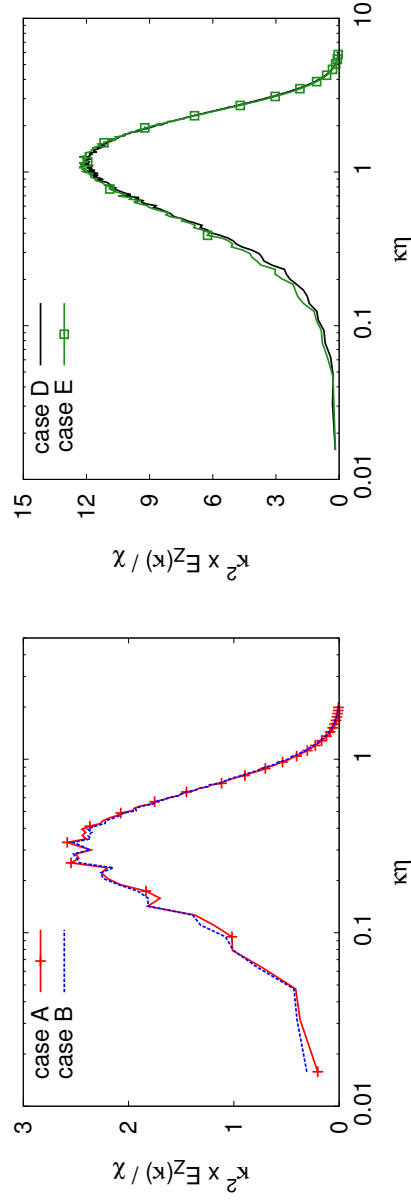
(a) Scalar dissipation spectrum, $D_Z(\kappa)/(2\mathcal{D}\chi)$, at $Sc = 1$.

(b) Scalar dissipation spectrum, $D_Z(\kappa)/(2\mathcal{D}\chi)$, at $Sc \neq 1$.

Figure 5.16: Scalar dissipation spectra for cases A, B, D, and E. These spectra result from conditions with an approximately constant energy dissipation rate, ϵ, and an Atwood number of 0.13.

5.8 Summary and Conclusions

In summary, a new computational framework for the study of turbulent buoyant flows has been presented. It enables the physics of variable density turbulent mixing to be sustained in time at a statistically stationary state, and it allows for the four important non-dimensional parameters, namely the Reynolds, Richardson, Atwood, and Schmidt numbers, to be independently varied. This simulation framework relies on the adaptation of well-known, accepted velocity and scalar field forcing methods used in numerical simulation studies of homogeneous, isotropic turbulence. The relevant governing equations have been provided, and the constraints applied to the forcing terms have been justified.

As a consequence of this forced methodology, the proposed framework is computationally efficient. The physical scenario to which it corresponds is that of the region of scalar mixing located sufficiently deep inside of a mixing layer such that the boundary conditions (or mean flow parameters) are no longer felt by (or even affect) the mixing physics. This enables the full span of turbulent buoyant flows to be systematically studied and interrogated. As a means of validation, the needed numerical operating parameters have been identified (*e.g.* grid resolution, solver order, and transport scheme quality), and canonical turbulent metrics predicted under the proposed framework have been investigated (*e.g.* single- and two-point statistics and isotropy).

Three test cases have been considered from purely isotropic to purely buoyant, and key canonical turbulent characteristics were calculated. The purely isotropically-forced case (case A) displayed isotropic Kolmogorov scales, and the velocity components were independent of the density field when conditionally-averaged, as expected. This isotropically-forced data also had almost perfectly isotropic distribution of energy content across all flow scales. The purely buoyantly-forced case (case B) displayed isotropic Kolmogorov scales, but its velocity component in the direction of the gravity vector (v) is anisotropic. This anisotropy is found to have only shallow penetration into the velocity field, and its effects are limited to only small wavenumbers ($\kappa L < 40$). The total kinetic energy is found to be anisotropically distributed; this is attributed to the single direction in which energy is injected (the non-zero direction of $\underline{g}$). Additionally, the partially buoyant case (case C) displays behaviors bounded by the purely isotropic and buoyant data, as expected.

Chapter 6

Turbulent Buoyant Flows: A Simulation Study

This chapter illustrates the application of the proposed geometry to the study of variable density, turbulent buoyant mixing. In the sections that follow, the Reynolds, Atwood, and Richardson numbers are varied whilst holding the Schmidt number fixed at $Sc = 1$. This is done, as primary focus of this final substantive chapter is on the physics present in the velocity and scalar fields when energy production is provided by non-buoyant sources, buoyant sources, or a combination of the two.

The parameter space spanned by the current study finds context in existing, published data. Beginning with scalar diffusivity, the range of Schmidt numbers examined in similar studies is a narrow one. Typically, variable density studies have been limited to low Schmidt number conditions. Commonly reported Schmidt number values include $Sc = 0.1 - 0.5$ [55, 57], 0.7 [70], and $1.0 - 2.0$ [55, 56]. The preference for low Schmidt numbers is largely due to two considerations. First, the Schmidt number of air is roughly 0.7. Second, resolution requirements limit the Schmidt number to small values when the Reynolds number is high. The $Sc = 1$ condition in this work is consistent with these ranges. The density ratios examined in the current work are also comparable to density ratios used in previous studies. A rather broad range of Atwood numbers, defined per Eq. 5.26, has been reported in the literature. Simulation and experimental studies have examined the physics of variable density mixing under $A = 0.05$ [55, 57], 0.25 [55], 0.5 [18, 70, 55, 56, 57], and 0.75 [18] conditions. It will be shown later in this chapter that the two Atwood numbers considered in this work are approximately equivalent to the $A = 0.25$ and $A = 0.5$ conditions described in previous studies.

The analysis performed and the discussions to follow are concerned with fourteen test cases. Test cases 1-6 (Table 6.1) correspond to non-buoyant turbulent fields at three Atwood numbers ($A = 0$, 0.06, and 0.12) and at two energy dissipation rates ($\epsilon = \langle 2\nu S_{ij} S_{ij} \rangle \approx 2$ and 90); the velocity field is subject to energy injection from only isotropic forcing. Test cases 7-14 (Table 6.2) are subject to buoyancy forces, and these span two Atwood number conditions at the same two dissipation rates. The data are partitioned into four groups of three, with each group of three having a fixed A, a

Table 6.1: Variable density non-buoyant cases.

Non-buoyant Case	$(Ri = 0)$ N^3	ϵ	Re_λ	Re (Eq. 5.37)	A	Sc	ν	$\kappa\eta$	$\kappa\eta_B$
1	512^3	94.6	140	1275	0	1	0.005	1.5	1.5
2	512^3	90.5	140	3443	0.06	1	0.005	1.6	1.6
3	512^3	91.0	140	2012	0.12	1	0.005	1.6	1.6
4	256^3	2.03	70	617	0	1	0.005	2.0	2.0
5	256^3	2.05	70	450	0.06	1	0.005	2.0	2.0
6	256^3	2.02	70	478	0.12	1	0.005	2.0	2.0

Table 6.2: Variable density and variable density buoyant cases.

Case	N^3	ϵ	Re	Q	Ri	At	Sc	ν	$\kappa\eta$	$\kappa\eta_B$
2	512^3	90.5	3443	1.4	0	0.06	1	0.005	1.6	1.6
7	512^3	76.6	4507	1.1	0.52	0.06	1	0.005	1.6	1.6
8	512^3	88.4	7876	0	0.55	0.06	1	0.005	1.6	1.6
3	512^3	91.0	2012	1.4	0	0.12	1	0.005	1.6	1.6
9	512^3	89.1	5230	1.05	0.53	0.12	1	0.005	1.6	1.6
10	512^3	81.7	7050	0	0.58	0.12	1	0.005	1.6	1.6
5	256^3	2.05	450	0.382	0	0.06	1	0.005	2.0	2.0
11	256^3	2.15	1516	0.287	0.50	0.06	1	0.005	2.0	2.0
12	256^3	2.05	2236	0	0.60	0.06	1	0.005	2.0	2.0
6	256^3	2.02	478	0.382	0	0.12	1	0.005	2.0	2.0
13	256^3	1.95	1188	0.287	0.50	0.12	1	0.005	2.0	2.0
14	256^3	2.03	2286	0	0.54	0.12	1	0.005	2.0	2.0

fixed ϵ, and a varied Ri. By imposing that ϵ be constant (at ≈ 2 or ≈ 90), the Kolmogorov scales, $\eta = \left(\nu^3/\epsilon\right)^{1/4}$, are held fixed across the $\epsilon \approx 90$ data sets at $\eta = 0.0060$ and across the $\epsilon \approx 2$ data sets at $\eta = 0.0156$ for all fourteen test cases. This is done to facilitate a fair comparison between the two pairs of data (at high and low ϵ conditions).

The structure of this chapter is the following. In Section 6.1, the effects of changing the Reynolds number (or, equivalently, changing the energy dissipation rate, ϵ) on the turbulent field under constant density conditions are presented. In Section 6.2, the effects that variable density have on non-buoyant turbulence are investigated. Additionally, variable density effects in the scalar field are examined. In Section 6.3, buoyancy is introduced to the variable density turbulent fields. From this, the effects that buoyant forces have on turbulence structure and statistics at two Atwood number conditions are interrogated. This discussion also investigates the impact of changing the Atwood, Richardson, and Reynolds number on the scalar field; of specific interest is the way in which the scalar field reacts to accomodate the changing nature of the velocity field. The simulation code used to perform all the simulations contained in this chapter is detailed in Appendix 8.3, Appendix 8.4, Appendix 8.5, and Appendix 8.6.

6.1   Reynolds Number Effects

To provide a baseline against which non-buoyant and buoyant variable density turbulence data can be compared, the behavior for constant density, isotropically-forced turbulence is first briefly highlighted. The analysis that follows is drawn from the data corresponding to cases 1 and 4 in Table 6.1. These two cases have different energy dissipation rates (or, equivalently, different Reynolds numbers), but all other parameters are the same between them.

Two commonly reported second-order metrics, the energy spectra, $E(\kappa) = \frac{1}{2}|\hat{u}_i|^2$, and dissipation spectra, $D(\kappa) = 2\nu\kappa^2 E(\kappa)$, are first presented. Figure 6.1 depicts these spectra. Beginning with the dissipation spectrum, recall that the area under $D(\kappa)$ is equal to the energy dissipation rate; hence, Fig. 6.1(a) confirms that these two cases have two different values of ϵ. Turning attention to the energy spectrum, a few macroscopic comments can be made. Under sufficiently high Re conditions, *i.e.* where there is meaningful scale separation, $E(\kappa)$ should display a spectral scaling of $\kappa^{-5/3}$ across an intermediate range of (inviscid) wavenumber scales. This scaling is provided in Fig. 6.1(b) along with the energy spectra for cases 1 and 4. Clearly, such a spectral scaling region is not found in either set of data; however, this is expected. Qian [79, 80] and others have suggested that such a scaling range is not to be until $Re \sim O(10^4)$. Thus, it should be expected, in all other test cases $(1-17)$ to be examined, that there are non-negligible finite Reynolds number effects, and the canonical turbulent behaviors outlined in Section 2.2 will not be realized.

As discussed in Chapter 2, the energy spectrum scaling can be explained by considering κ_{EI}, κ_{PI}, and κ_{DI}, which were initially introduced in Section 2.2. Recall that κ_{EI} is the waveshell in wavespace (starting at $\kappa = 0$) at which 90% of the total kinetic energy is obtained. Similarly, κ_{DI} characterizes the waveshell in wavespace at which 10% of the total dissipation has occurred (starting from $\kappa = 0$). Lastly, κ_{PI} indicates the waveshell in wavespace at which 90% of the energy produced has been deposited. These scales are included in Table 6.3 for cases 1 and 4. Consistent with the lack of a $\kappa^{-5/3}$ scaling range, these wavenumbers suggest that there is no scale separation at these Re_λ values. The primary point to be made is that the wavenumber at which dissipation becomes important (κ_{DI}) occurs before the energy production scales become unimportant (κ_{EI}); this constitutes overlap. It it noted that the overlap is more extensive in the lower Re_λ case $(\kappa_{EI}/\kappa_{DI} = 2.33)$ versus the higher Re_λ case $(\kappa_{EI}/\kappa_{DI} = 1.56)$, as is reasonable. The extent of scale overlap present in these flows can be quantified further using the cumulative dissipation, cumulative energy, and cumulative power
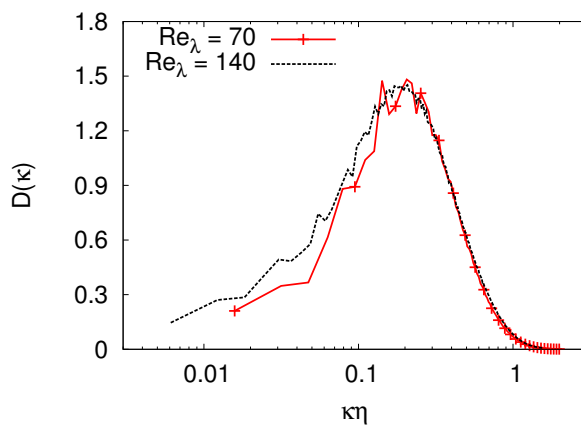
(a)   Dissipation spectrum, $D(\kappa)$.
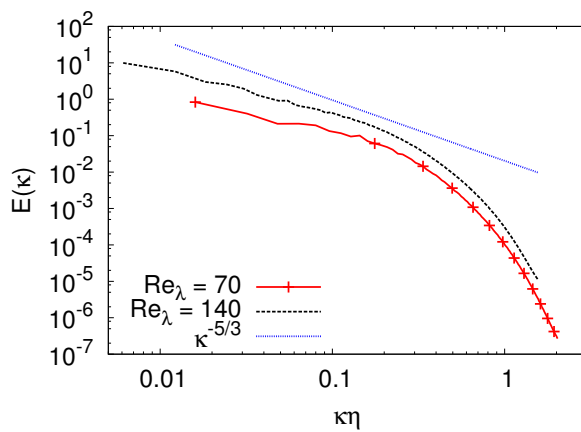
(b)   Energy spectrum, $E(\kappa)$.

Figure 6.1: Energy and dissipation spectra at different Reynolds numbers under constant density ($A = 0$) conditions (cases 1 and 4 in Table 6.1). Note the dissipation spectrum for the $Re_\lambda = 70$ case has been multiplied by 20 for purposes of plotting and comparison.

Table 6.3: Pertinent characteristic length-scales.

case ID	ϵ	κ_{DI}	κ_{EI}	κ_{PI}	κ_{EI}/κ_{DI}
case 1	90	16	25	25	1.56
case 4	2	6	14	14	2.33

spectra. These cumulative spectra are defined as,

$$D_{cum}(\kappa) = \sum_0^\kappa 2\nu\kappa^2 E(\kappa), \tag{6.1}$$

$$E_{cum}(\kappa) = \sum_0^\kappa E(\kappa), \tag{6.2}$$

$$P_{cum}(\kappa) = \sum_0^\kappa 2QE(\kappa), \tag{6.3}$$

and they are normalized by the total dissipation, energy, and power, as appropriate, when plotted in Fig. 6.2. Figure 6.2 is informative, as it shows that, although the dissipation is lagging the energy production, as it should be, the lag is not sufficient to support inviscid dynamics and the establishment of an inertial subrange. Note that the curves for $E_{cum}(\kappa)$ and $P_{cum}(\kappa)$ are coincident.

Up to this point, the discussion of cases 1 and 4 has focused on the lack of an inertial range and the associated inviscid dynamics. However, the increase in ϵ from ≈ 2 to ≈ 90 is not unimportant. To highlight the effect of the Reynolds number on the resulting turbulence, it is useful to consider the turbulent kinetic energy equation in spectral space,

$$\frac{dE(\kappa)}{dt} = T(\kappa) + P(\kappa) - D(\kappa) + R(\kappa), \tag{6.4}$$

in which there are five constituent terms. The term $\frac{dE(\kappa)}{dt}$ represents the time-rate of change of energy inside the computational domain, or the power decay rate. The transfer spectrum, $T(\kappa)$, is defined as,

$$T(\kappa) = -\hat{u}_i^* \mathscr{F}\left(u_j \frac{\partial u_i}{\partial x_j}\right), \tag{6.5}$$

where $\mathscr{F}$ denotes the Fourier transform operator, $\hat{u}$ denotes the Fourier coefficient of the velocity component u, and $(\cdot)^*$ denotes a complex conjugate. The final term, $R(\kappa)$, contains any other effects that are not included in the other four terms; this contains, for example, the effects of pressure gradients.

Of particular interest is the transfer spectrum, as it corresponds physically to the transfer of energy from the larger turbulent eddies to all turbulent eddies of a smaller size. To isolate the features of the transfer spectrum, which is plotted in Fig 6.3(a), it can be broken down into the sum
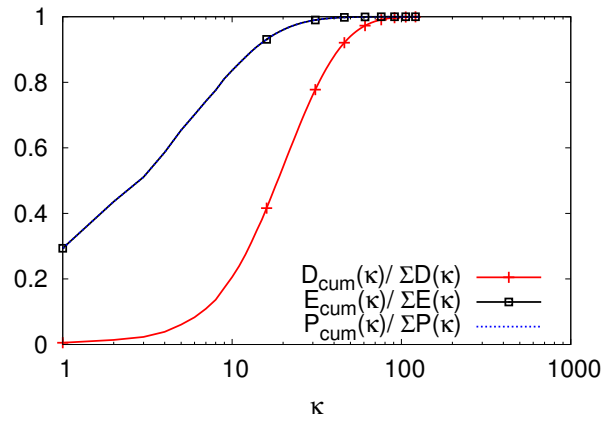
(a)   Low *Re* case ($\epsilon \approx 2$).
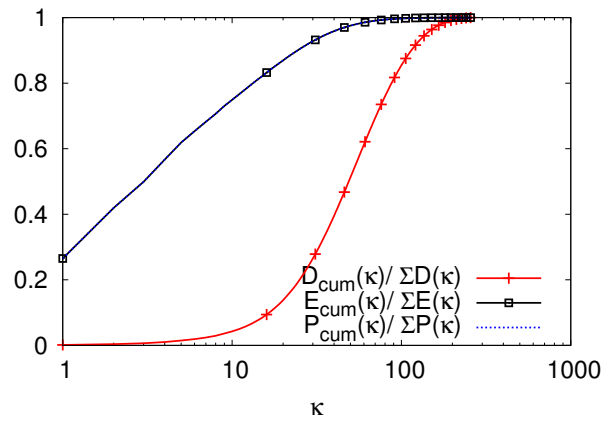
(b)   High *Re* case ($\epsilon \approx 90$).

Figure 6.2: Cumulative dissipation, energy, and power spectra under constant density conditions (cases 1 and 4 in Table 6.1).

of three contributing terms,

$$T(\kappa) = T_x + T_y + T_z. \tag{6.6}$$

These correspond to the transfer of energy along the direction of the u velocity component (T_x), the v velocity component (T_y), and the w velocity component (T_z). These three transfer spectra are defined as,

$$T_x = -\hat{u}^* \mathscr{F}\left(u\frac{\partial u}{\partial x} + v\frac{\partial u}{\partial y} + w\frac{\partial u}{\partial z}\right),$$

$$T_y = -\hat{v}^* \mathscr{F}\left(u\frac{\partial v}{\partial x} + v\frac{\partial v}{\partial y} + w\frac{\partial v}{\partial z}\right),$$

$$T_z = -\hat{w}^* \mathscr{F}\left(u\frac{\partial w}{\partial x} + v\frac{\partial w}{\partial y} + w\frac{\partial w}{\partial z}\right), \tag{6.7}$$

and they are plotted, under constant density conditions, in Fig. 6.3(b) and Fig. 6.3(c).

It was established previously that these flow fields suffer from scale overlap, and this is reflected in Fig 6.3(a), as there is no region, for either Re_λ, across which $T(\kappa)$ assumes a value of zero (a requirement for inviscid dynamics). Irrespective of that, there are qualitative differences that can be gleaned from transfer spectra. The negative regions in Fig. 6.3(a) correspond to regions over which energy is produced; the positive regions represent those over which it is dissipated. The higher Reynolds number case transitions from negative to positive (producing to dissipating) earlier in wavespace compared to the low Reynolds number case. This implies that energy production penetrates further into the smaller flow scales (larger $\kappa\eta$) when the Reynolds number is lower. Further, the three constituent transfer spectra, T_x, T_y, and T_z, indicate that the energy transfer is isotropic; at all flow scales, the three spectra are effectively equivalent.

Additionally, structure functions can be informative of Reynolds number effects. Recall the definition of the second- and third-order structure functions,

$$B_{ll}(r,t) = \langle (u_l(x + r\underline{l}, t) - u_l(x,t))^2 \rangle, \tag{6.8}$$

$$B_{lll}(r,t) = \langle (u_l(x + r\underline{l}, t) - u_l(x,t))^3 \rangle, \tag{6.9}$$

where u_l is the velocity component aligned with unit vector, $\underline{l}$, and r is the magnitude of the two-point separation between fluid points. These functions are known to display asymptotic behaviors under sufficiently high Reynolds number conditions. The third-order structure function tends towards 4/5 across an intermediate range of scales when properly normalized ($-B_{lll}/(\epsilon r) = 4/5$ [77, 58]). The second-order structure function tends towards a constant value of approximately 2.0 across such an intermediate range when suitably normalized ($B_{ll}/(\epsilon r)^{2/3} \approx 2.0$ [77, 58]). Further, it is known that these asymptotic values are slowly approached with increasing Reynolds number [59, 58].
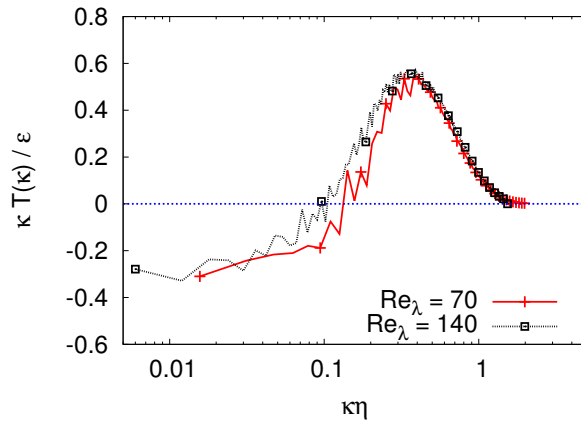
(a)   Transfer spectrum, $T(\kappa)$.
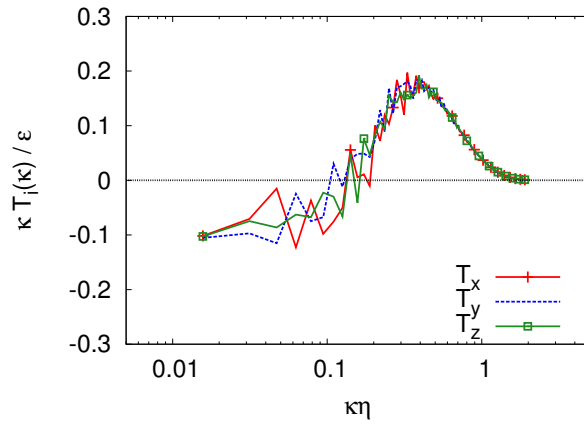
(b)   Transfer spectrum components for $Re_\lambda = 70$.
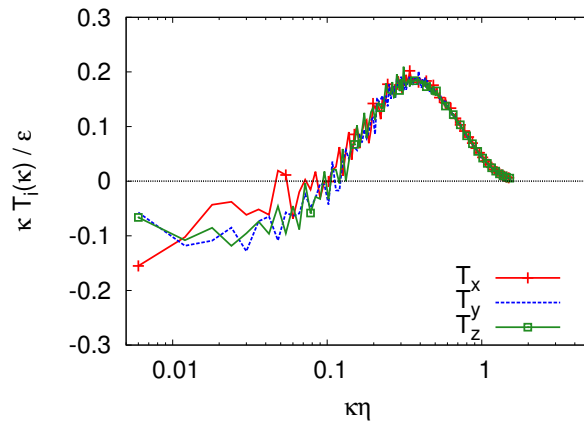
(c)   Transfer spectrum components for $Re_\lambda = 140$.

Figure 6.3: Transfer spectra at different Reynolds numbers under constant density ($A = 0$) conditions (cases 1 and 4 in Table 6.1).
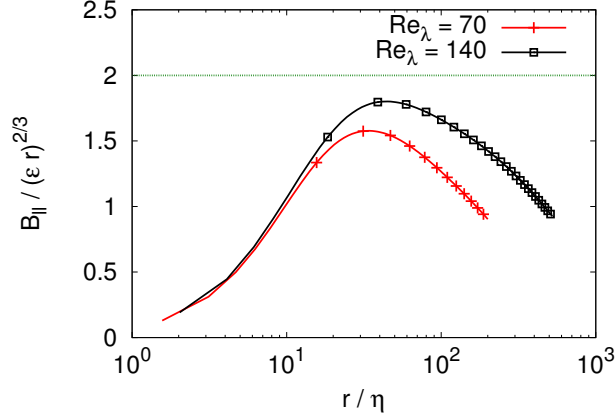
(a)   Normalized second-order structure function.
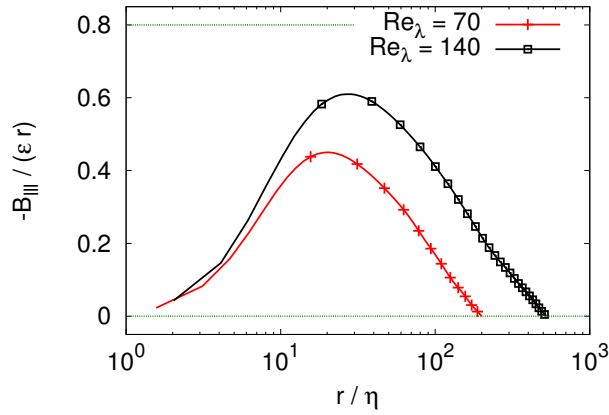
(b)   Normalized third-order structure function.

Figure 6.4: Second- and third-order longitudinal structure functions at different Reynolds numbers under constant density ($A = 0$) conditions (cases 1 and 4 in Table 6.1).

Returning to the two cases of present concern, cases 1 and 4, the second- and third-order structure functions are calculated and depicted in Fig. 6.4. Clearly in neither case are the asymptotic behaviors observed; the normalized third-order structure function is far from a constant value at 4/5 at any r separation, and the normalized second-order structure function lacks a constant region with magnitude near 2.0. What is observable, however, is the slow approach towards these asymptotic limits, with the structure function values in the $Re_\lambda = 140$ case consistently, and not insignificantly, larger in magnitude than its $Re_\lambda = 70$ counterparts.

The objective of this section was to establish the baseline behaviors of isotropic turbulence under constant density conditions at the two energy dissipation rates used in this study. Specifically, the findings are as follows. First, there is scale overlap for both the high and low ϵ cases. This precludes the presence of a $\kappa^{-5/3}$ scaling range from being obtained in the energy spectrum. Second, the transfer spectrum confirms the isotropic nature of energy transfer to the velocity fields, as

$T_x = T_y = T_z$. Third, the structure functions have compensated magnitudes that are below those obtained in an inviscid limit.

6.2 Atwood Number Effects (Variable Density)

With the nature of constant density turbulence investigated and described (Section 6.1), variable density (non-buoyant) turbulence is investigated. The analysis that follows is aimed at determining if variable density effects are significant enough to effect key turbulent metrics. The simulations of concern here are cases 1-6 in Table 6.1.

These 6 cases have Atwood numbers of 0, 0.06, and 0.12, as defined in Eq. 5.28. As the definition of Atwood number used in this work is not that which is commonly implemented in variable density turbulent studies, it is necessary to qualify how these three values stand up against the traditional measure. Recall that, traditionally, the Atwood number is defined as,

$$A_{tr} = \frac{\rho_2 - \rho_1}{\rho_2 + \rho_1},$$
(6.10)

with ρ_2 and ρ_1 representing the highest and the lowest density values. This metric is calculated normally in the context of a mixing layer or a Rayleigh-Taylor instability, where there are pure fluid reservoirs with a larger density (ρ_2) and a lower density (ρ_1). Since the framework implemented in this work does not include regions of pure fluid in the simulation geometry, a direct comparison between the reported Atwood number (A) and those values found in the literature is not possible. However, to enable an approximate comparison, the following is done. The data generated under the simulation framework presented in Chapter 5 are examined. For each discrete data file, which are separated by approximately one eddy turn-over time each, the minimum and maximum density values are found. It is assumed that these are the density values that would correspond to the pure fluid reservoirs, had they been included in the simulation geometry. Then, the traditional Atwood number definition (Eq. 6.10) is applied with $\rho_2 = \rho_{max}$ and $\rho_1 = \rho_{min}$. These discrete Atwood number values are averaged over all available data sets. Admittedly, this is not a perfect comparison, but it does provide a general idea as to the extent of density variation present in these simulations in terms of the commonly-used Atwood number definition. This process indicates that the reported $A = 0.06$ using this work's preferred definition (Eq. 5.28) corresponds to that of $A_{tr} \approx 0.25$ under Eq. 6.10. Further, $A = 0.12$, as defined in Eq. 5.28, is loosely equivalent to $A_{tr} \approx 0.5$ under Eq. 6.10. The point to be made here is simply that the simulations to be presented contain significant and strong variations in density and are well outside of the Boussinesq limit. Accordingly, any effects that a non-constant density have on the resulting turbulent fluid mechanics ought to be apparent.

To provide some context as to the physical scenario to which an $A_{tr} \approx 0.5$, $A_{tr} \approx 0.25$ or

$A_{tr} \approx 0.0$ corresponds, a few examples are provided. An $A_{tr} \approx 0.25$ represents the mixing of air ($\rho = 1.2754$ kg/m³) and ammonia (NH_3 with $\rho = 0.769$ kg/m³), helium (He with $\rho = 0.179$ kg/m³) and hydrogen (H_2 with $\rho = 0.090$ kg/m³), air and methane (CH_4 with $\rho = 0.717$ kg/m³), or air and water vapor (H_2O with $\rho = 0.804$ kg/m³), for example. All properties listed are assuming standard temperature and pressure, which is at 0 degrees Celsius and one atmosphere of pressure. An $A_{tr} \approx 0.5$ represents a mixture of methane and carbon dioxide (CO_2 with $\rho = 1.977$ kg/m³) or methane and ozone (O_3 with $\rho = 2.14$ kg/m³), where the thermodynamic properties are at standard temperature and pressure. Lastly, an $A_{tr} \approx 0$ simply describes the mixing of two fluids with approximately the same density, such as sea water ($\rho = 1025$ kg/m³) mixing with fresh water ($\rho = 998$ kg/m³). These density values assume one atmosphere of pressure at 20 degrees Celsius, and result in $A_{tr} \approx 0.01$.

6.2.1 Energy, Dissipation, and Transfer Spectra

To interrogate the effect of variations of density on turbulence, the energy and dissipation spectra are first calculated. These are depicted in Fig. 6.5 for the lower ϵ cases and Fig. 6.6 for the higher ϵ cases. It should be noted here that these spectra are defined according to,

$$E(\kappa) = \frac{1}{2}|\hat{u}_i|^2, \tag{6.11}$$

and

$$D(\kappa) = \nu\kappa^2|\hat{u}_i|^2 = 2\nu\kappa^2 E(\kappa). \tag{6.12}$$

Recall that the dynamic viscosity (μ) changes with the fluid density, but the kinematic viscosity ($\nu = \mu/\rho$) is fixed at a constant value (from Chapter 5). Although these formulations do not explicitly contain the density, the velocity field is affected by the presence of variations in density. Thus, these spectra, so defined, should indicate any impacts due to density. As is apparent in Fig. 6.5 and Fig. 6.6, there do not appear to be any differences between the two turbulent cases at the three Atwood numbers included. Note that these six test cases correspond to variable density, non-buoyant turbulent cases where isotropic forcing is applied to the velocity field.

The energy and dissipation spectra are the most commonly reported spectra in turbulence studies; the transfer spectrum is less frequently calculated. Nevertheless, the transfer spectrum is useful, as it suggests the way in which energy "cascades" into the progressively smaller scales. To determine if varying the density has any effect on this process, the transfer spectra are plotted for cases 1 through 6. The full transfer spectrum, which is defined as Eq. 6.5, and its three constituent transfer spectra, which are defined as Eq. 6.7, are plotted in Fig. 6.7 for the lower ϵ cases and in Fig. 6.8 for the

higher ϵ cases. These spectra suggest that in neither case, high nor low ϵ, are there any discernible differences in the transfer spectra despite the significant differences present in the density fields involved. Also, these spectra confirm the isotropic nature of energy transfer when subjected to the imposed isotropic velocity forcing despite the presence of density variations; $T_x = T_y = T_z$ for the two sets of data presented.

6.2.2   Scalar Field Spectra

The final spectra that will be presented for these six non-buoyant cases are the scalar energy, $E_Z(\kappa)$, and scalar dissipation, $D_Z(\kappa)$, spectra. These are defined as,

$$E_Z(\kappa) = \frac{1}{2}|\hat{Z}|^2, \tag{6.13}$$

and

$$D_Z(\kappa) = \mathcal{D}\kappa^2|\hat{Z}|^2 = 2\mathcal{D}\kappa^2 E_Z(\kappa), \tag{6.14}$$

with $\mathcal{D}$ being the diffusivity of the scalar species. These spectra are plotted in Fig. 6.9 and Fig. 6.10. The scalar dissipation spectra are normalized by the scalar dissipation rate, $\chi = \langle 2\rho\mathcal{D}|\nabla Z|^2 \rangle$, and the scalar energy spectra are normalized by the variance of the scalar field, $\sigma_Z^2 = \langle \rho Z^2 \rangle - \langle \sqrt{\rho} Z \rangle^2$, to make the curves collapse. The angled brackets, $\langle \cdot \rangle$, denote (volume) ensemble averaging. As seen with the energy and dissipation spectra in the velocity field, the effects of variable density are virtually non-existent for all six cases. Since the scalar field and the density field are coupled by the imposed equation of state Eq. 5.6, these scalar field metrics ought to show any changes induced by density variations, despite the lack of density in the formulations used (Eq. 6.13 and Eq. 6.14).

6.2.3   Alignment

With the spectra behavior of these six non-buoyant, variable density flows qualitatively examined, statistical metrics are investigated, specifically alignment characteristics. Under homogeneous, isotropic conditions for an incompressible fluid (*i.e.* constant density), the vorticity field, $\underline{\omega} = \nabla \times \underline{u}$, the gradient of the scalar field, ∇Z, and the eigenvectors ($\hat{\alpha}$, $\hat{\beta}$, and $\hat{\gamma}$) of the velocity field strain rate tensor, $S_{ij} = \frac{1}{2}\left(\frac{\partial u_i}{\partial x_j} + \frac{\partial u_j}{\partial x_i}\right)$, exhibit known and specific relative alignments [6]. In this notation, the most extensive (positive) strain-rate tensor eigenvalue is α and its associated eigenvector is $\hat{\alpha}$. The most compressive (negative) eigenvalue is γ with eigenvector $\hat{\gamma}$. The intermediate strain-rate tensor eigenvalue, β, with eigenvector $\hat{\beta}$ can be either extensive or compressive; it will assume the sense needed to satisfy continuity. In constant density flows, $\nabla \cdot u_i = 0$ implies that $\alpha + \beta + \gamma = 0$; however, when the density is variable, $\alpha + \beta + \gamma \neq 0$.

The literature and analytical studies [6] suggest the following alignments are favored in constant density, isotropic turbulent flows. The β strain-rate eigenvector, $\hat{\beta}$, tends to align with the vorticity, $\underline{\omega}$, while there is strong anti-alignment between $\underline{\omega}$ and $\hat{\gamma}$. The extensive eigenvector, $\hat{\alpha}$, is largely independent of the vorticity field, and it is equally likely to be aligned in any orientation relative to $\underline{\omega}$. Similarly, the scalar gradient vector, ∇Z, aligns preferentially with certain components of the strain-rate tensor. The scalar gradient generally aligns in the same direction as the most compressive eigenvector, $\hat{\gamma}$. Also, ∇Z tends towards anti-alignment with $\hat{\beta}$, and it has no preferential alignment with respect to $\hat{\alpha}$, as seen in the vorticity field.

Although these alignments are known under constant density conditions, it is not known if they are respected by variable density flows with or without buoyancy forces. To investigate this, the dot products of the three principle strain-rate eigenvectors and the vorticity and scalar gradient fields are taken, and the probability density functions (PDFs) are calculated. These are depicted in Fig. 6.11, Fig. 6.12, Fig. 6.13, and Fig. 6.14, for the high and low ϵ cases under constant density ($A = 0$) and variable density conditions ($A = 0.06$ and 0.12).

From Fig. 6.11 - Fig. 6.14, irrespective of the value of ϵ or A, the alignment PDFs for all six cases tell the same story. The alignments expected for incompressible flow are recovered in each instance ($A = 0$, 0.06, and 0.12) for both the vorticity and scalar fields. Figure 6.11 and Fig. 6.12 suggest that the vorticity field is insensitive to $\hat{\alpha}$, is aligned with $\hat{\beta}$, and is anti-aligned with $\hat{\gamma}$. From Fig. 6.13 and Fig. 6.14, it is clear that the scalar gradient vectors align most directly with $\hat{\gamma}$, are anti-aligned with $\hat{\beta}$, and have limited dependence on $\hat{\alpha}$. Such alignment is interesting, as the scalar, Z, is not a passive scalar; it influences the flow field through the density via the equation of state (Eq. 5.6) in these non-buoyant simulations. Thus, the analytically-derived and experimentally-measured alignment features are reproduced under variable density, turbulent conditions, with $\underline{\omega}$ preferentially orienting in the $\hat{\beta}$ direction and ∇Z aligning in the $\hat{\gamma}$ direction.

6.2.4 Structure Functions

The final metric to calculate for these non-buoyant turbulent cases are the longitudinal second- and third-order structure functions, $B_{ll}(r)$ and $B_{lll}(r)$. To determine if the variations in density are having an effect on the velocity field in some way that is not captured in the alignment PDFs or in the calculated spectra, these two structure functions are determined for the six non-buoyant data sets. The results are shown in Fig. 6.15 for the lower ϵ cases and Fig. 6.16 for the higher ϵ cases, where the curves have been properly normalized. These data suggest that the variation of density has no effect on the structure of the velocity field, as the correlation of velocity differences throughout the domain are unaffected by the strength of the Atwood number. Note that the very slight differences at large separation distances are due to the finite number of independent data files used to compute the statistically averaged quantities.

(a) Energy spectrum, $E(\kappa)$.

(b) Dissipation spectrum, $D(\kappa)$.
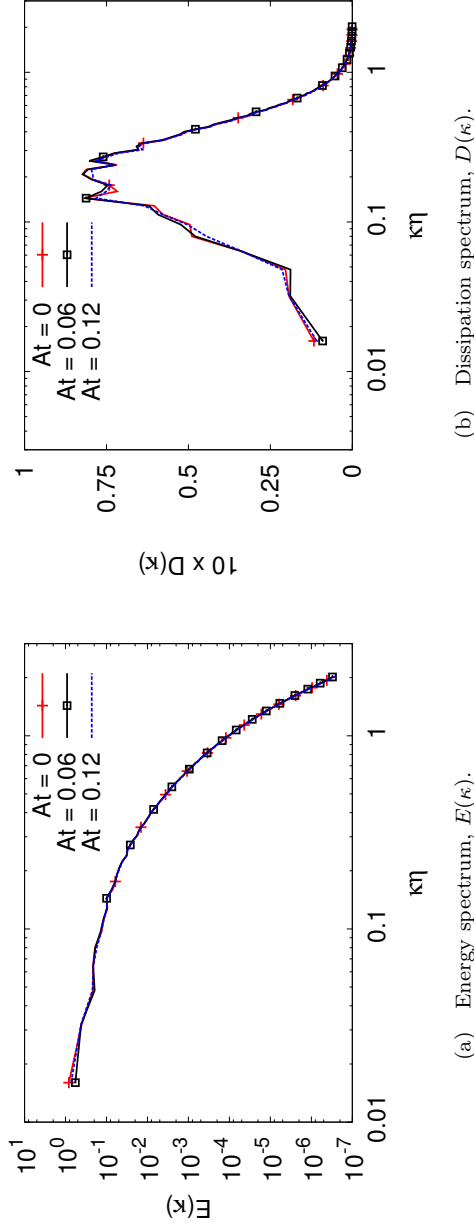
Figure 6.5: Energy and dissipation spectra at $Re_\lambda = 70$ for different Atwood numbers (cases 4, 5, and 6 in Table 6.1).

(a) Energy spectrum, $E(\kappa)$.

(b) Dissipation spectrum, $D(\kappa)$.
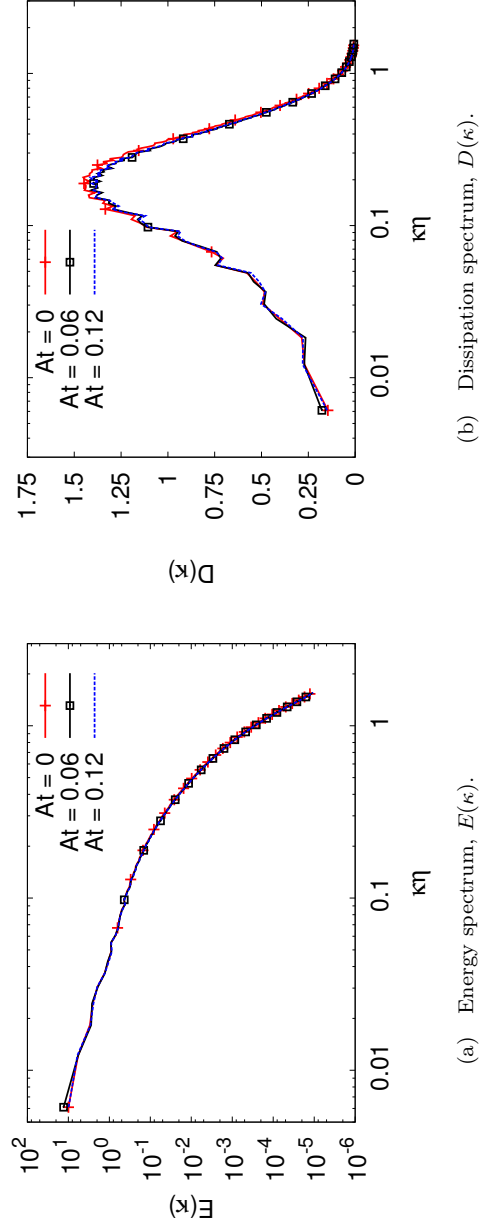
Figure 6.6: Energy and dissipation spectra at $Re_\lambda = 140$ for different Atwood numbers (cases 1, 2, and 3 in Table 6.1).

(a) $T(\kappa)$.

(b) $T_x(\kappa)$.

(c) $T_y(\kappa)$.

(d) $T_z(\kappa)$.
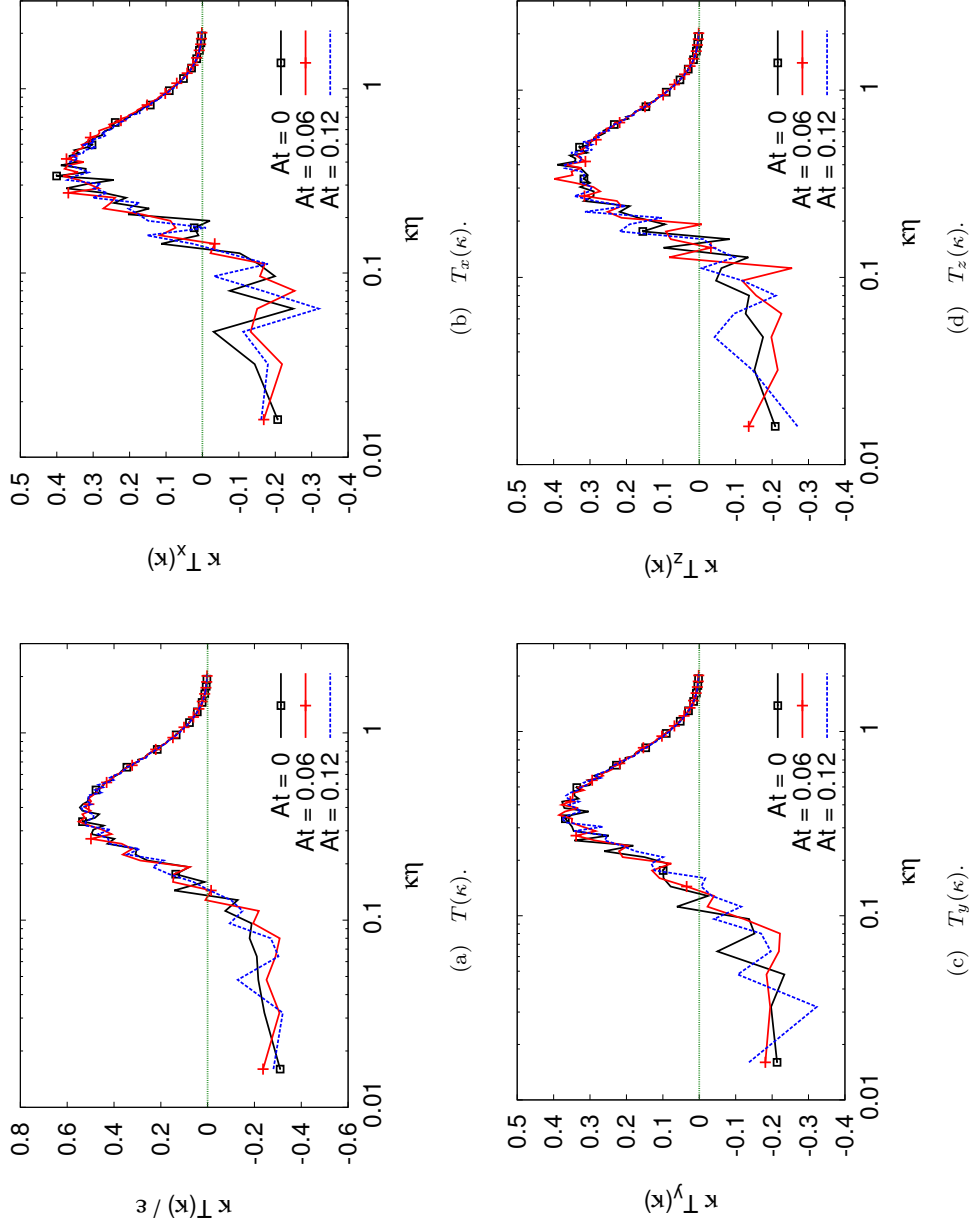
Figure 6.7: Transfer spectra for $Re_\lambda = 70$ at different Atwood numbers (cases 4, 5, and 6 in Table 6.1).
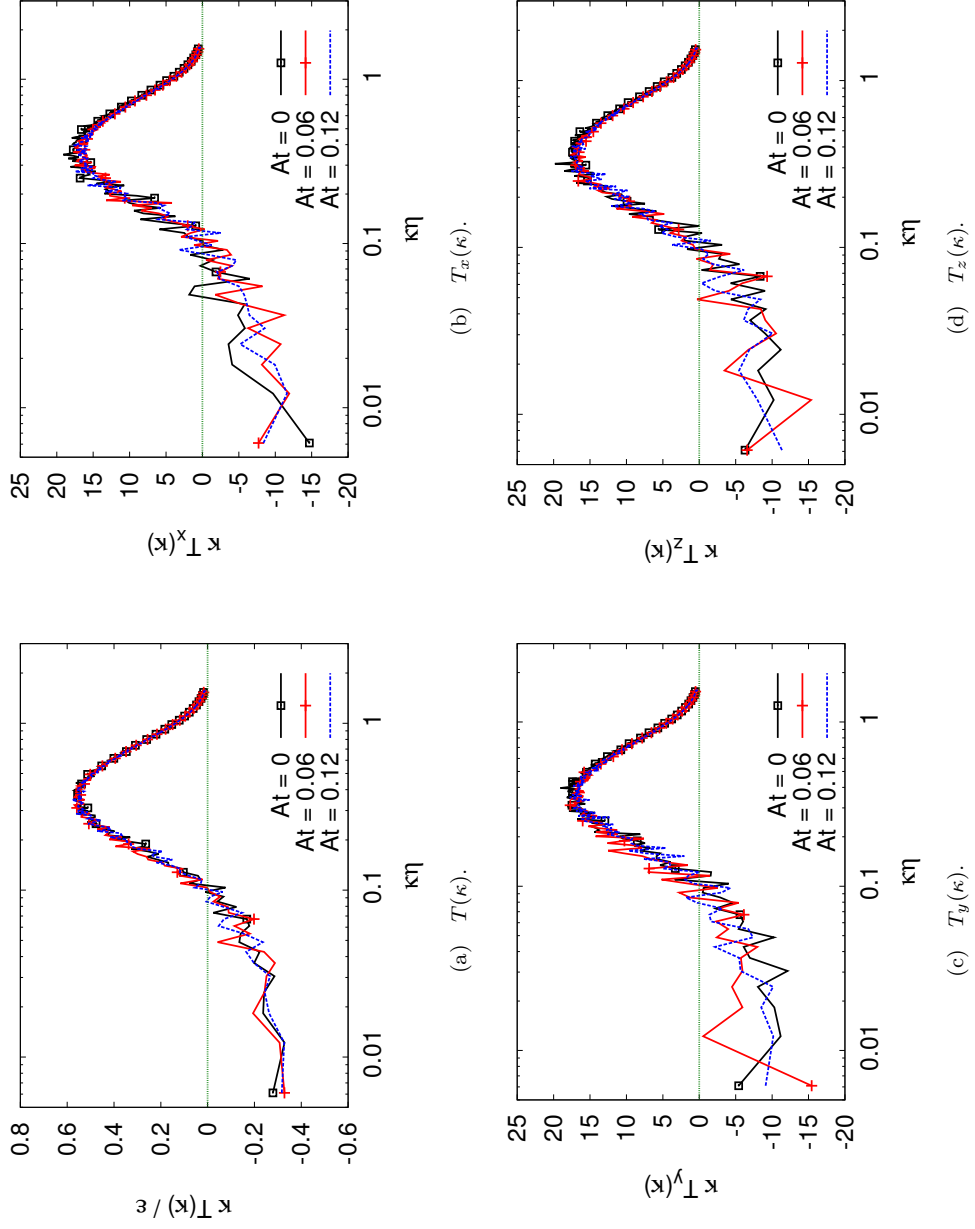
Figure 6.8: Transfer spectra for $Re_\lambda = 140$ at different Atwood numbers (cases 1, 2, and 3 in Table 6.1).
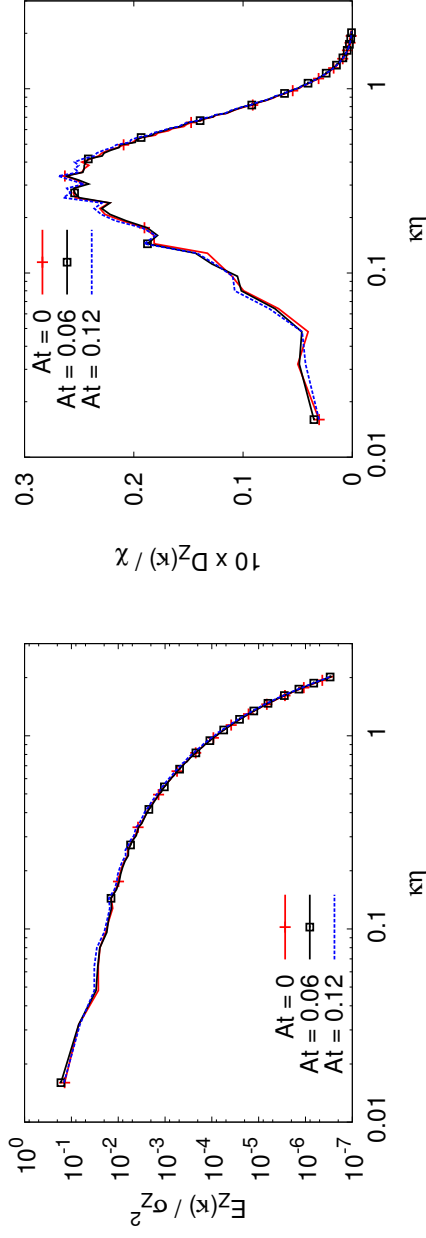
(a) Scalar energy spectrum, $E_Z(\kappa)$.

(b) Scalar dissipation spectrum, $D_Z(\kappa)$.

Figure 6.9: Scalar energy and dissipation spectra at $Re_\lambda = 70$ for different Atwood numbers (cases 4, 5, and 6 in Table 6.1).
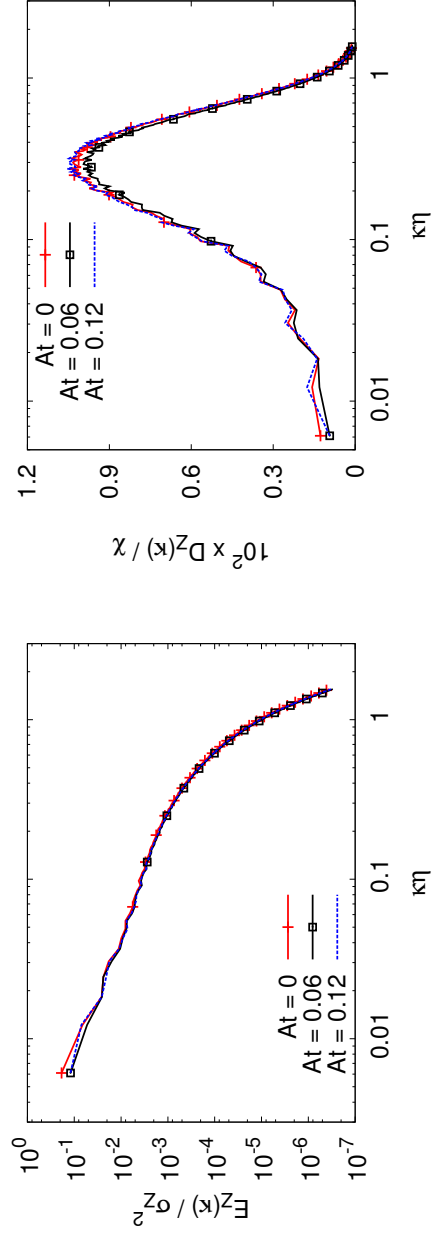
(a) Scalar energy spectrum, $E_Z(\kappa)$.

(b) Scalar dissipation spectrum, $D_Z(\kappa)$.

Figure 6.10: Scalar energy and dissipation spectra at $Re_\lambda = 140$ for different Atwood numbers (cases 1, 2, and 3 in Table 6.1).
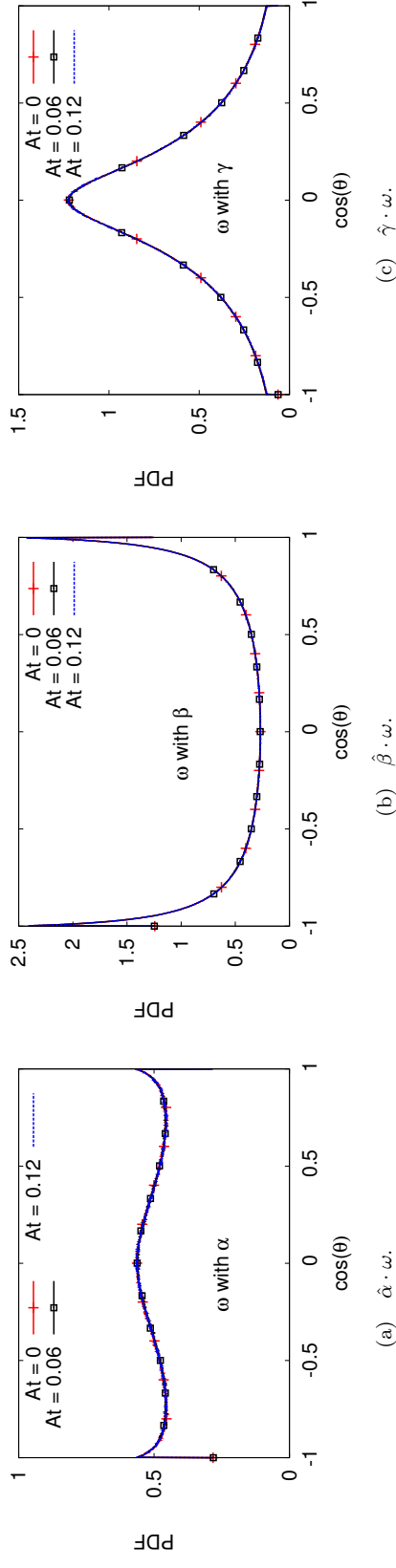
Figure 6.11: Alignment of the vorticity field, ω, with the eigenvectors of the strain-rate tensor, S_{ij}, for $Re_\lambda = 70$ at different Atwood numbers. Here, $\cos(\theta) = \pm 1$ indicates alignment (cases 4, 5, and 6 in Table 6.1).
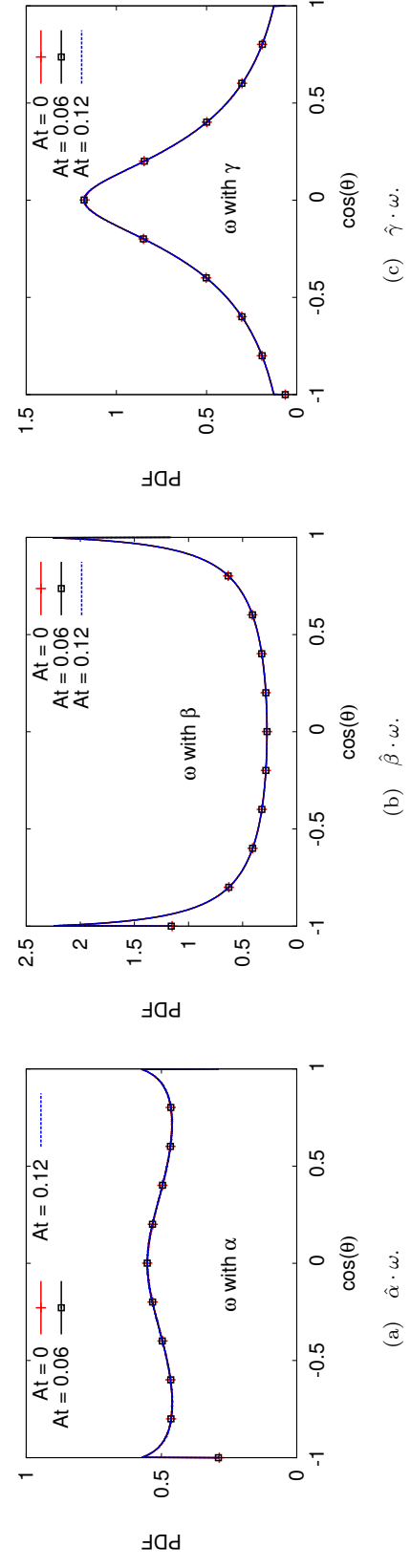
Figure 6.12: Alignment of the vorticity field, ω, with the eigenvectors of the strain-rate tensor, S_{ij}, for $Re_\lambda = 140$ at different Atwood numbers. Here, $\cos(\theta) = \pm 1$ indicates alignment (cases 1, 2, and 3 in Table 6.1).

(a) $\hat{\alpha} \cdot \nabla Z$.

(b) $\hat{\beta} \cdot \nabla Z$.

(c) $\hat{\gamma} \cdot \nabla Z$.
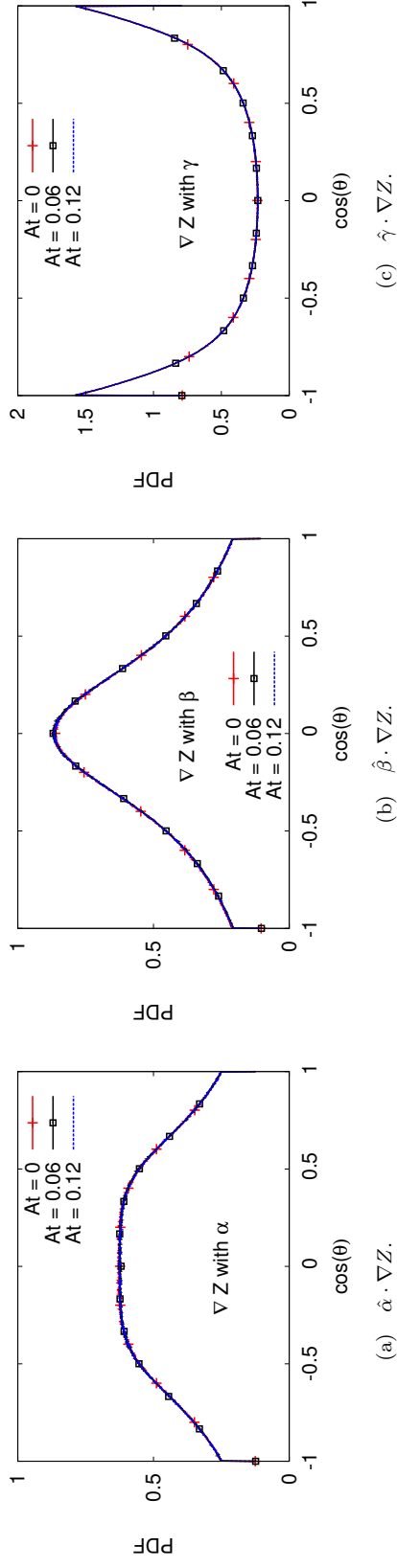
Figure 6.13: Alignment of the scalar gradient, ∇Z, with the eigenvectors of the strain-rate tensor, S_{ij}, for $Re_\lambda = 70$ at different Atwood numbers. Here, $\cos(\theta) = \pm 1$ indicates alignment (cases 4, 5, and 6 in Table 6.1).

(a) $\hat{\alpha} \cdot \nabla Z$.

(b) $\hat{\beta} \cdot \nabla Z$.

(c) $\hat{\gamma} \cdot \nabla Z$.
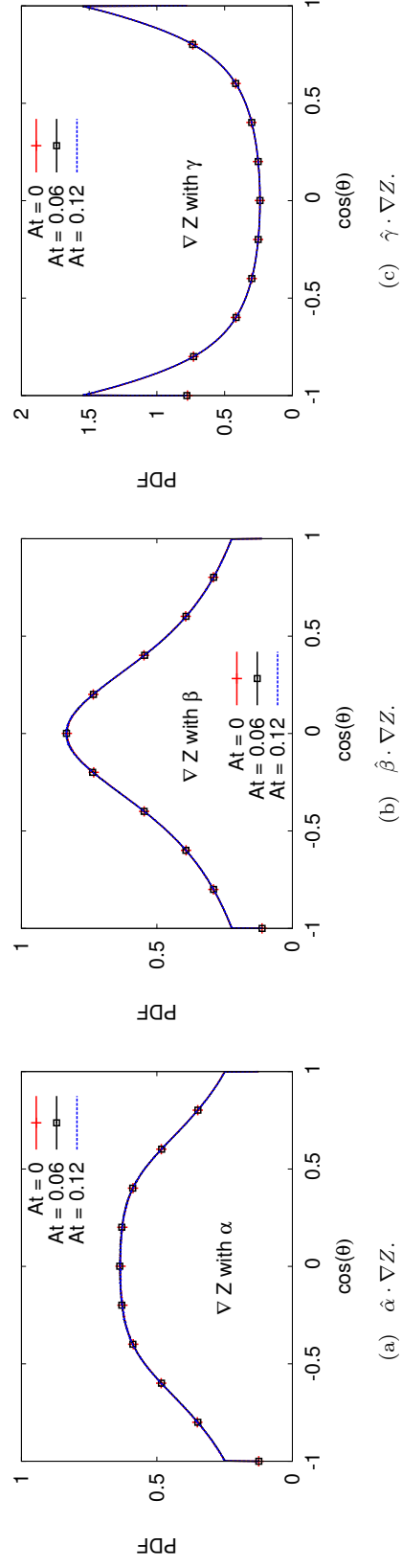
Figure 6.14: Alignment of the scalar gradient, ∇Z, with the eigenvectors of the strain-rate tensor, S_{ij}, for $Re_\lambda = 140$ at different Atwood numbers. Here, $\cos(\theta) = \pm 1$ indicates alignment (cases 1, 2, and 3 in Table 6.1).
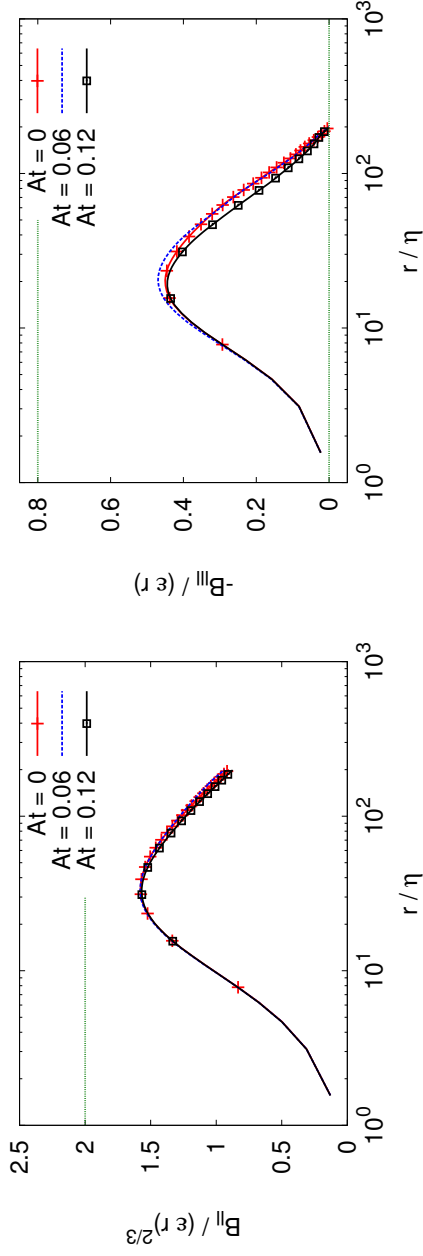
(a) Normalized second-order structure function.

(b) Normalized third-order structure function.

Figure 6.15: Second- and third-order longitudinal structure functions for $Re_\lambda = 70$ at different Atwood numbers (cases 4, 5, and 6 in Table 6.1).
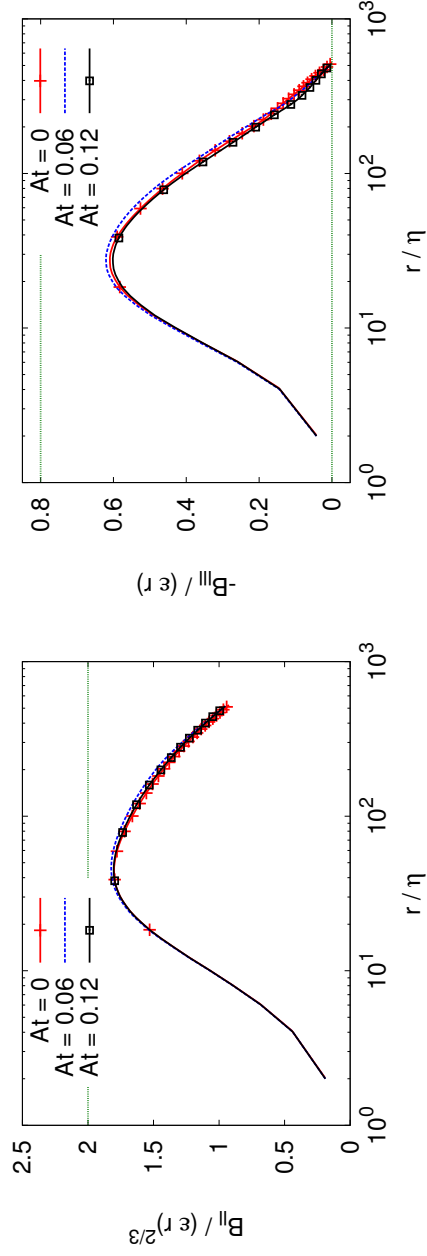
(a) Normalized second-order structure function.

(b) Normalized third-order structure function.

Figure 6.16: Second- and third-order longitudinal structure functions for $Re_\lambda = 140$ at different Atwood numbers (cases 1, 2, and 3 in Table 6.1).

6.3 Richardson Number Effects

The previous two sections have discussed the effects of Reynolds number and Atwood number on canonical metrics of non-buoyant, variable density turbulent flows. Now, it is of interest to study how the addition of buoyancy impacts turbulent structure. This is done in two parts. First, in Section 6.3.1, comparisons are done between the non-buoyant cases already presented (cases 1 and 4) and their fully buoyant counterparts (cases 8, 10, 12, and 14). Recall that these cases share the same energy dissipation rate (either $\epsilon \approx 2$ or $\epsilon \approx 90$) and all physical properties; the only difference between the cases is their source of turbulent kinetic energy. For cases 1 and 4, the source is an isotropic forcing term (Eq. 5.14); for cases 8, 10, 12, and 14, the source is gravity (with a magnitude adjusted to ensure the proper equivalent energy dissipation rate) at two different Atwood numbers. These buoyant cases have an approximately fixed Richardson number between them of $Ri \approx 0.57$. This is done, as such a comparison between the extreme cases (fully buoyant at $Ri \neq 0$ vs. non-buoyant at $Ri = 0$) should accentuate any differences between the turbulent fields. Then, in Section 6.3.2, the effect of varying the ratio of buoyant energy production to total energy production from zero to one is studied.

6.3.1 Non-buoyant vs. Fully Buoyant Conditions

6.3.1.1 Energy and Dissipation Spectra

Once again, the first metrics examined are the energy and dissipation spectra. The comparison between the non-buoyant data and fully buoyant data at $A = 0.06$ and $A = 0.12$ are shown in Fig. 6.17 and Fig. 6.18. Both pairs of spectra suggest that the differences of note are located only at the largest flow scales (small κ). The disparities at the smaller scales are negligible (large κ). This is confirmed when the buoyant velocity fields are filtered in the same way as in Section 5.6.1. The lowest wavenumber contributions to the velocity field are removed, and the spectra are calculated using these filtered velocity fields. Note that only the v velocity component is subject to filtering. The dissipation spectra of the high-pass filtered velocity field are shown in Figs. 6.17(c) and Figs. 6.18(c). From these, the deviations noted at the large scales in Fig 6.17(a), Fig. 6.17(b), Fig. 6.18(a), and Fig. 6.18(b) can be attributed to contributions from a small number of low wavenumber modes ($\kappa < 8$). When the contributions from these modes are removed, the spectrum behaviors become more consistent. It is of note that the small scale (large κ) agreement between the buoyant and non-buoyant spectra is quite robust for all Atwood numbers examined. This further confirms the discussion in Section 5.6, which stated that, once a small number of small wavenumber modes were removed from the turbulence, the non-buoyant and buoyant data became effectively equivalent.

(a) Energy spectra, $E(\kappa)$.

(b) Dissipation spectra, $D(\kappa)$.

(c) $D(\kappa)$ with $|\underline{\kappa}| < 8$ modes removed from v velocity component.
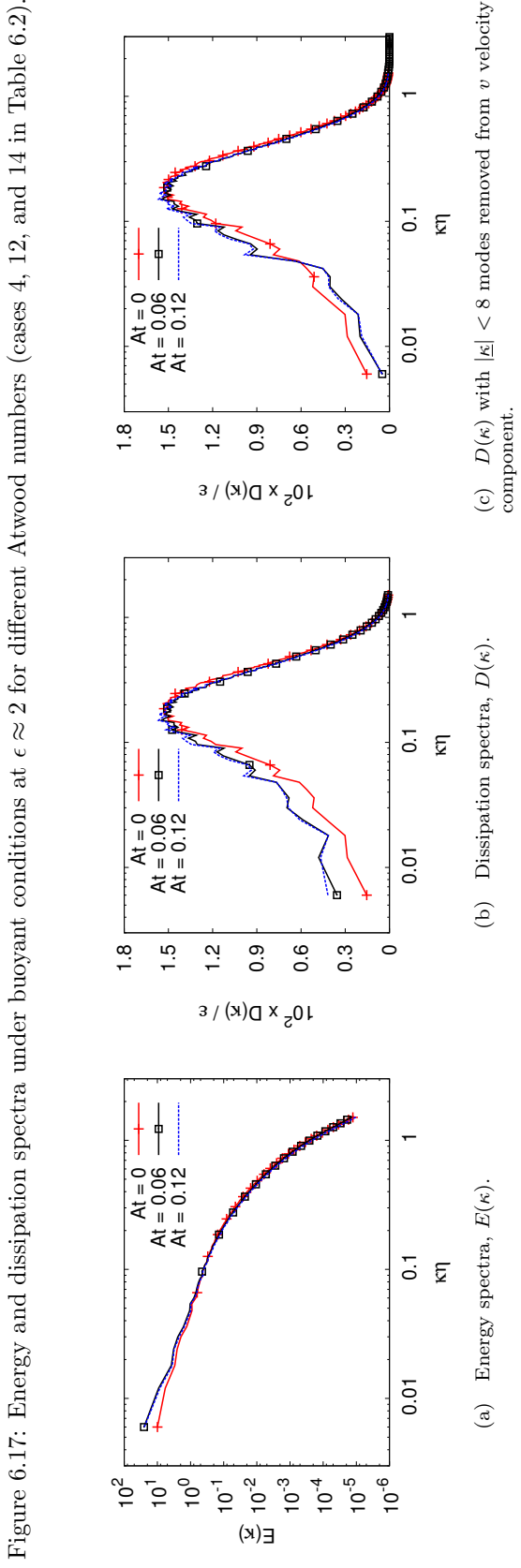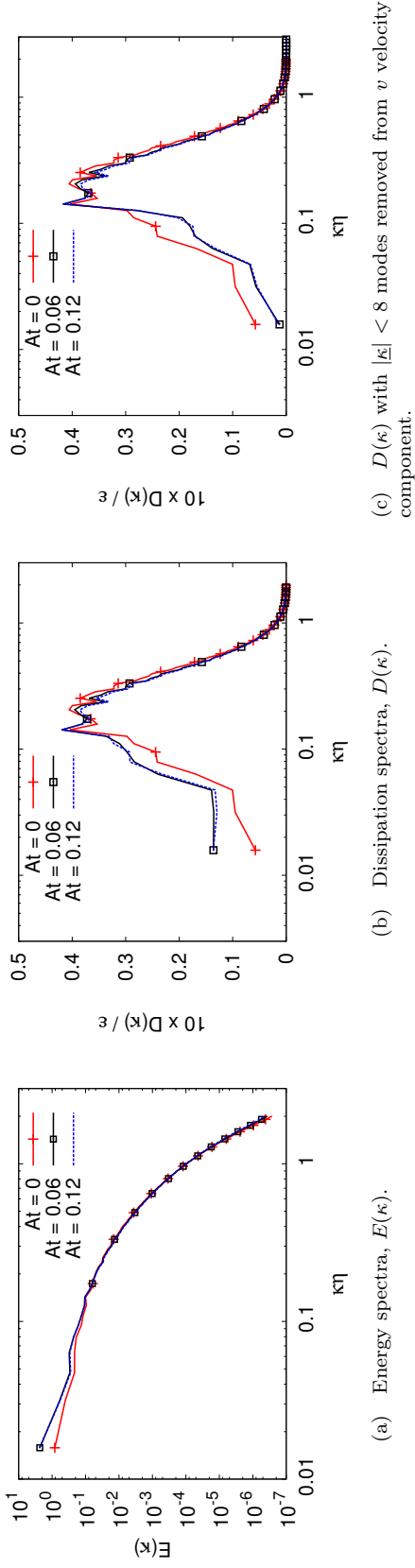
Figure 6.17: Energy and dissipation spectra under buoyant conditions at $\epsilon \approx 2$ for different Atwood numbers (cases 4, 12, and 14 in Table 6.2).

(a) Energy spectra, $E(\kappa)$.

(b) Dissipation spectra, $D(\kappa)$.

(c) $D(\kappa)$ with $|\underline{\kappa}| < 8$ modes removed from v velocity component.

Figure 6.18: Energy and dissipation spectra under buoyant conditions at $\epsilon \approx 90$ for different Atwood numbers (cases 1, 8, and 10 in Table 6.2).

6.3.1.2 Transfer Spectra

The previous discussion suggests that the distribution of energy content and energy dissipation is largely unchanged irrespective of the source of energy production (buoyant *vs.* non-buoyant isotropic). To gain a deeper understanding of this, the transfer spectra from these six cases are presented. As in Section 6.1 and Section 6.2, the transfer spectrum, $T(\kappa)$, and its three terms, T_x, T_y, and T_z, are plotted. The transfer spectra are calculated according to Eq. 6.5 and the constituents according to Eq. 6.7. These transfer spectra are depicted in Fig. 6.19 and Fig. 6.20, and they show that there is a difference in the way buoyant and non-buoyant flows transfer energy to the increasingly smaller scales. In Fig. 6.19(a) and Fig. 6.20(a), the buoyant cases clearly exhibit a different behavior than the non-buoyant, constant density data ($A = 0$). For both the high and low energy dissipation rate data, the energy transfer for the buoyant cases is of greater magnitude at smaller wavenumbers, and it has an almost linear (on the log scale x-axis) trend upwards until the peak of dissipation is reached (at approximately $\kappa\eta \approx 0.4$ for both cases). The non-buoyant, constant density data sets, however, display constant transfer until $\kappa\eta \approx 0.1$, only after which does it begin a linear climb towards the peak of the dissipation spectrum.

This can be investigated further by considering the transfer spectra in the u, v, and w component directions (Fig. 6.19 and Fig. 6.20). For both the high and low ϵ data, there are stark differences in the directional transfer spectra; T_x and T_z for the buoyant cases are effectively equivalent, in both qualitative and quantitative measures, to their non-buoyant counterparts (Fig. 6.7 and Fig. 6.8). However, T_y is larger in magnitude and has a different qualitative behavior with wavenumber. Altogether, this is not unexpected; if all energy is injected into only one direction via the v velocity component (the "y" direction), then it is reasonable that the transfer ought to be largest in this direction. The manifestation of this larger transfer magnitude is the presence of small-scale anisotropy, as energy is being removed from the "y" direction and moved into the "x" and "z" directions (see insets in Fig. 6.19 and Fig. 6.20).

6.3.1.3 Structure Functions

The longitudinal second- and third-order structure functions are now revisited for the four fully buoyant cases (8, 10, 12, and 14) listed in Table 6.2. In Section 2.3, the Karman-Howarth equation was presented and dicussed. Specifically, the relationship of structure functions to its constituent terms was developed. The third-order structure function was related to the inertial term, and, hence, is associated with the transfer of energy from large to small scales (*i.e.* $T(\kappa)$). The second-order structure function, alternatively, was related to viscous effects, associating it with the dissipation spectrum, which, in turn, is proportional to the energy content of a turbulent field (*i.e.* $E(\kappa)$). It was found in the prior section that the transfer spectra did differ under buoyant and non-buoyant

conditions. Thus, structure function data may shed light on the differences between buoyant and non-buoyant energy transfer.

The structure functions are calculated as defined in Eq. 6.8 and Eq. 6.9, and they are provided in Fig. 6.21 and Fig. 6.22. These figures suggest that the buoyant velocity fields, for the same energy dissipation rate and Richardson number, exhibit a higher effective Reynolds number than the constant density ($A = 0$) velocity data. By this, it is meant that the magnitudes of the normalized structure functions approach more closely the asymptotic limits of $B_{ll}/(\epsilon r)^{2/3} = 2.0$ and $B_{lll}(r)/(\epsilon r) = -0.8$ for the same value of ϵ.

6.3.1.4 Scalar Field Spectra

Since the energy and dissipation spectra differ under non-buoyant and fully buoyant conditions, it is of interest to determine if (and how) these differences are able to manifest in the scalar field. As the simulations of concern contain an active scalar (variable density), there is a possibility that the anisotropy found in the velocity field could penetrate into the scalar field. This is best illustrated by returning to the advection-diffusion (scalar transport) equation,

$$\frac{\partial \rho Z}{\partial t} + \frac{\partial}{\partial x_j}\left(\rho u_j Z\right) = \frac{\partial}{\partial x_j}\left(\rho \mathcal{D} \frac{\partial Z}{\partial x_j}\right) + f_Z. \tag{6.15}$$

Turbulence cannot be induced in the scalar field independent of the velocity field; the two are coupled via the scalar flux term, $\frac{\partial}{\partial x_j}\left(\rho u_j Z\right)$. It is only through the scalar flux that the scalar field can be driven to a turbulent state. Thus, if there is any anisotropy, or any statistical feature present in the velocity field, such anisotropy may penetrate into the scalar field. To investigate this briefly, key statistical metrics are calculated for both the isotropic (non-buoyant) and buoyant scalar fields. These metrics include the scalar energy spectra (Fig. 6.23(a) and Fig. 6.24(a)), the scalar dissipation spectra (Fig. 6.23(b) and Fig. 6.24(b)), and the scalar transfer spectra (Fig. 6.23(c) and Fig. 6.24(c)).

The striking feature of these resulting spectra is that there is no discernible difference between the buoyant and isotropic scalar fields; there is an almost perfect collapse of the data. From this, it appears that the scalar flux term is not able to transfer into the scalar field the significant anisotropy observed in the buoyantly-driven velocity field. Out of this it can be stated, at least for these energy dissipation rates (ϵ), anisotropy in the velocity field is unable to manifest in the scalar field, and isotropically-produced turbulent scalar fields and buoyantly-produced turbulent scalar fields are structurally similar. These results are quite remarkable, as the anisotropy in the velocity fields is due to the combined effect of gravity and a non-uniform density field, and this non-uniform density field is controlled entirely by the scalar field via the imposed equation of state (Eq. 5.6).

(a) $T(\kappa)$.

(b) $At = 0.06$.

(c) $At = 0.12$.
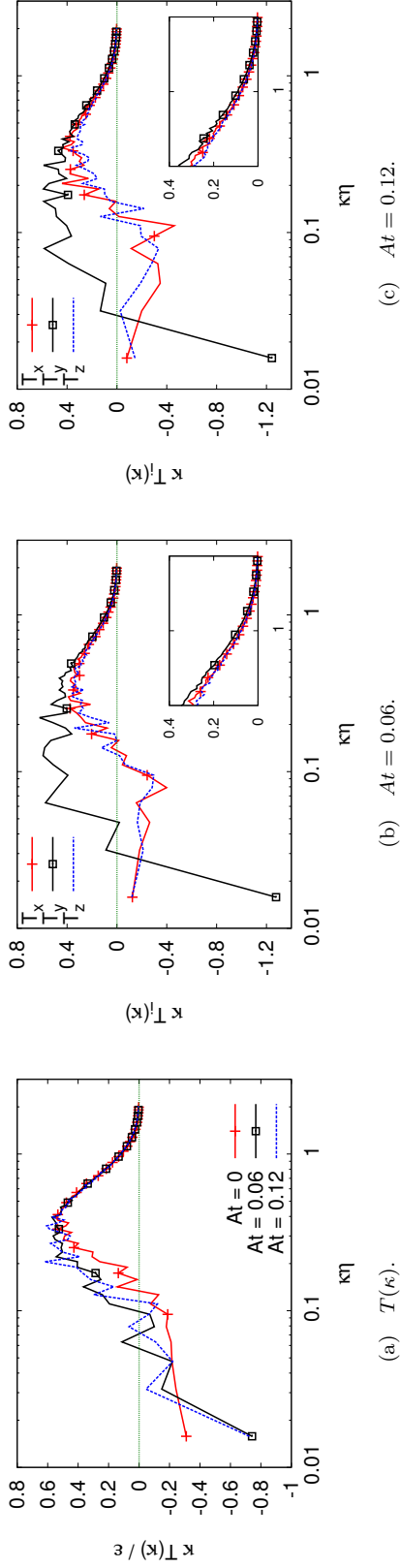
Figure 6.19: Transfer spectra under buoyant conditions at $\epsilon \approx 2$ for different Atwood numbers (cases 4, 12, and 14 in Table 6.2).

(a) $T(\kappa)$.

(b) $At = 0.06$.

(c) $At = 0.12$.
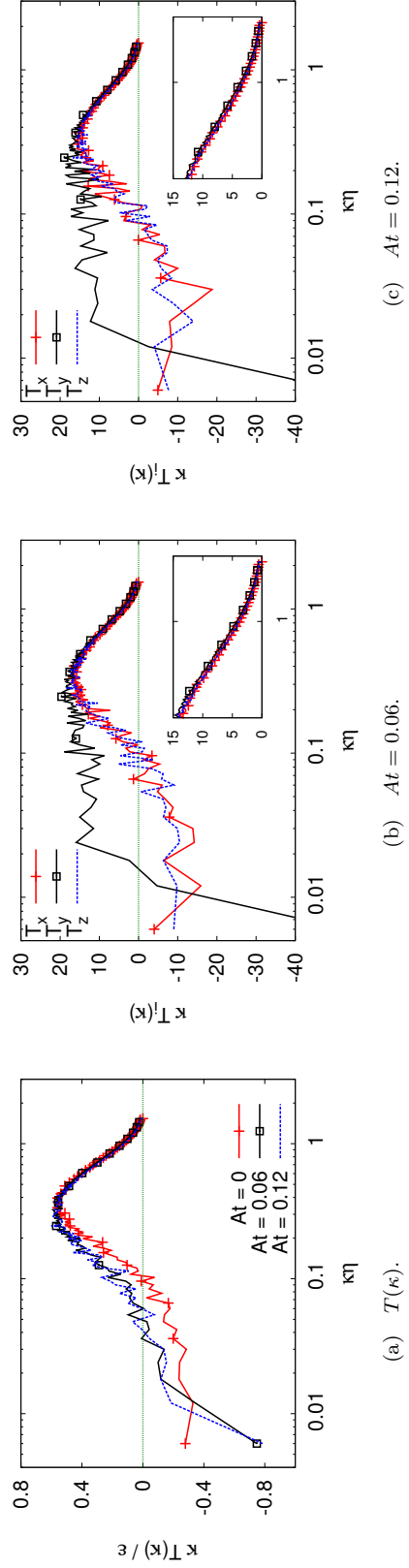
Figure 6.20: Transfer spectra under buoyant conditions at $\epsilon \approx 90$ for different Atwood numbers (cases 1, 8, and 10 in Table 6.2).
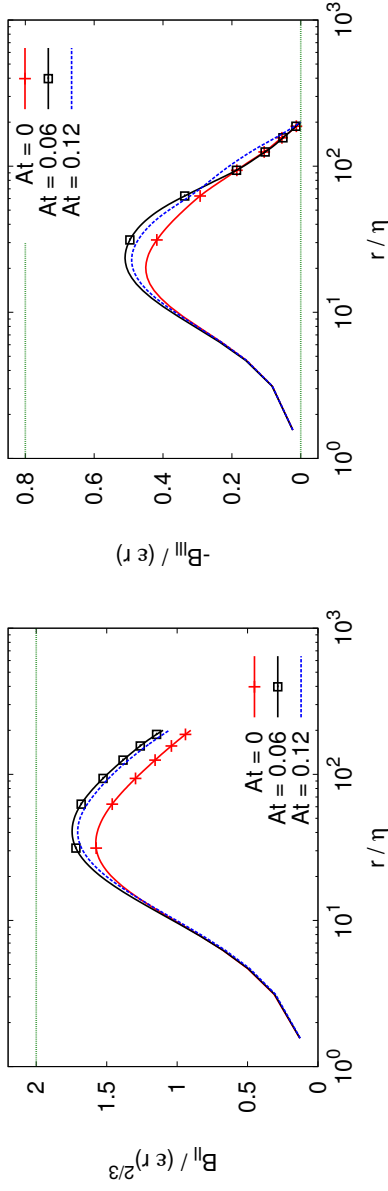
(a) Normalized second-order structure function.

(b) Normalized third-order structure function.

Figure 6.21: Second- and third-order longitudinal structure functions under buoyant conditions at $\epsilon \approx 2$ at different Atwood numbers (cases 4, 12, and 14 in Table 6.2).
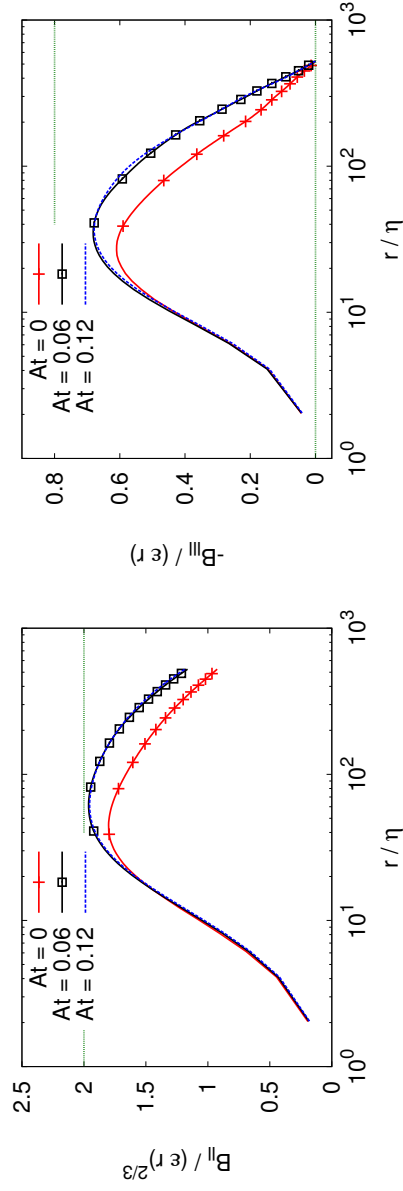
(a) Normalized second-order structure function.

(b) Normalized third-order structure function.

Figure 6.22: Second- and third-order longitudinal structure functions under buoyant conditions at $\epsilon \approx 90$ at different Atwood numbers (cases 1, 8, and 10 in Table 6.2).

(a) Scalar energy spectrum, $E_Z(\kappa)$.

(b) Scalar dissipation spectrum, $D_Z(\kappa)$.

(c) Scalar transfer spectrum, $T_Z(\kappa)$.
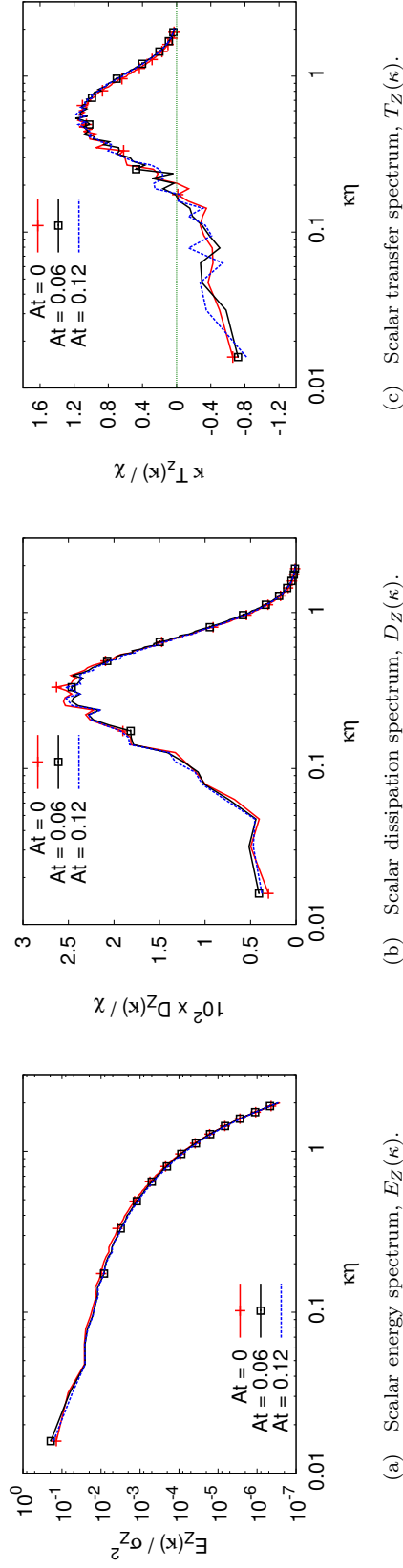
Figure 6.23: Scalar spectra under buoyant conditions at $\epsilon \approx 2$ for different Atwood numbers (cases 4, 12, and 14 in Table 6.2).

(a) Scalar energy spectrum, $E_Z(\kappa)$.

(b) Scalar dissipation spectrum, $D_Z(\kappa)$.

(c) Scalar transfer spectrum, $T_Z(\kappa)$ at $\epsilon \approx 90$.
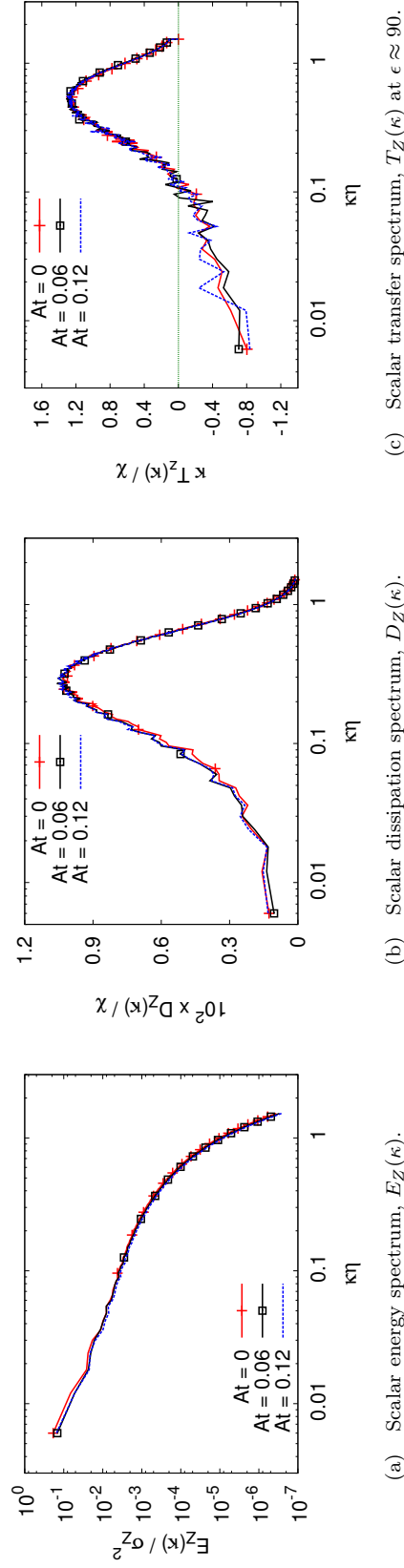
Figure 6.24: Scalar spectra under buoyant conditions at $\epsilon \approx 90$ for different Atwood numbers (cases 1, 8, and 10 in Table 6.2).

Table 6.4: Variable density turbulent cases subject to both isotropic and buoyant energy production.

Case	ϵ	A	P_{iso}	P_{buoy}	P_{total}	P_{buoy}/P_{total}	% P_{buoy}
7	76.6	0.06	50.89	38.27	89.16	0.429	43 %
9	89.1	0.12	44.26	53.96	98.22	0.549	55 %
11	2.15	0.06	0.904	1.229	2.133	0.576	58 %
13	1.95	0.12	0.904	0.984	1.888	0.521	52 %

6.3.1.5 Alignment

The discussions up to this point have found differences between the buoyant and non-buoyant turbulent fields in only four metrics: the conditional average of the v velocity component on the density field (Section 5.6.1), the energy and dissipation spectra (Section 5.6.2 and Section 6.3.1.1), the transfer spectra via T_y (Section 6.3.1.2), and the curving of structure functions (Section 6.3.1.3). It is now of interest to determine if these flows, which have significant buoyancy forces acting on them, have alignment tendencies that are changed from the purely isotropic results stated in Section 6.2.3. Recall that these results have Atwood numbers of 0.06 and 0.12, which are relatively high since they are defined based on local density values. The alignments for the four buoyant cases are provided in Fig. 6.25, Fig. 6.26, Fig. 6.27, and Fig. 6.28 along with those for the non-buoyant, constant density cases ($A = 0$). As there do not appear to be any significant differences between them for either the high or low dissipation rate groupings, this suggests that the strain-rate tensor, vorticity field, and scalar gradient assume a similar relative orientation with respect to each other irrespective of the source of the turbulent kinetic energy (*i.e.* isotropic production *vs.* buoyant production). These results were not necessarily expected, as the velocity field is not divergence free ($\partial u_i/\partial x_i \neq 0$); hence, the sum of the three eigenvalues of the strain-rate tensor is no longer zero.

6.3.2 Non-buoyant *vs.* Partially Buoyant *vs.* Fully Buoyant Conditions

It has been established that fully buoyant and non-buoyant flows do display differences in some turbulent metrics. Specifically, the structure functions and one component of the transfer spectrum behave differently. To investigate this observation, the final four simulations in Table 6.2 are examined (cases 7, 9, 11, and 13). These cases differ from the others in that they are subject to turbulent energy production from both isotropic forcing and buoyancy per Eq. 5.22. It is the objective of this discussion to comment on the extent of buoyant production necessary to trigger the behaviors noted in Fig. 6.19, Fig. 6.20, Fig. 6.21, and Fig. 6.22 versus those found in non-buoyant flows (Fig. 6.7, Fig. 6.8, Fig. 6.15, Fig. 6.16).
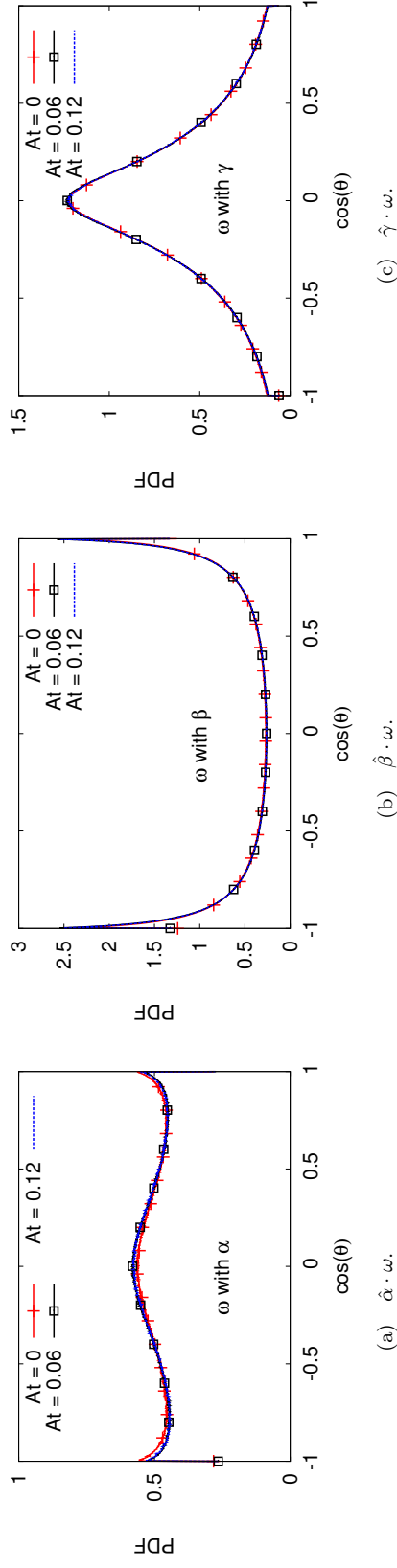
Figure 6.25: Alignment of the vorticity field, ω, with the eigenvectors of the strain-rate tensor, S_{ij}, for $\epsilon \approx 2$ at different Atwood numbers. Here, $\cos(\theta) = \pm 1$ indicates alignment (cases 4, 12, and 14 in Table 6.2).
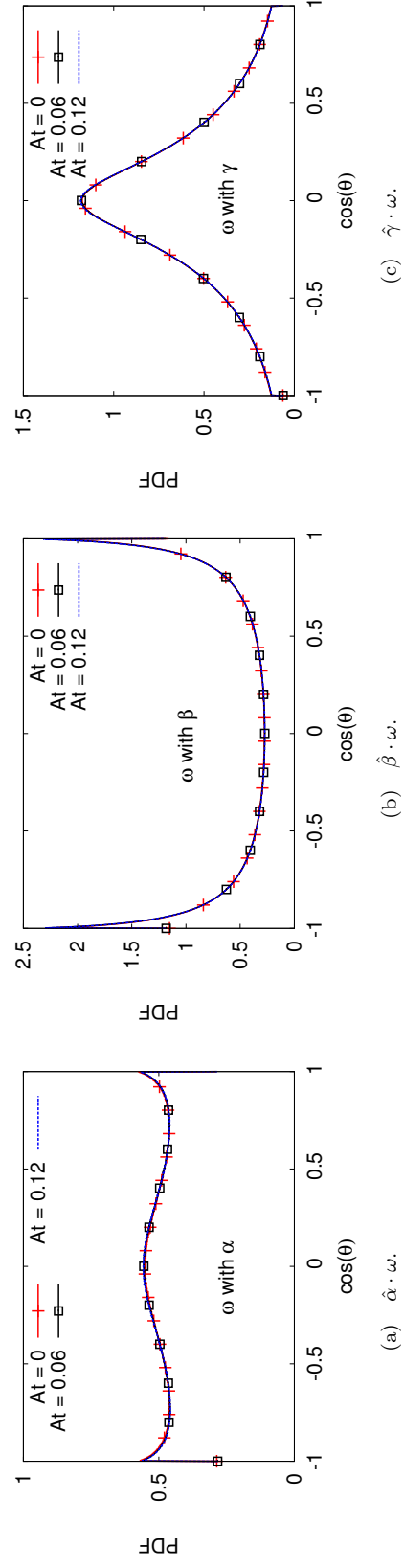
Figure 6.26: Alignment of the vorticity field, ω, with the eigenvectors of the strain-rate tensor, S_{ij}, for $\epsilon \approx 90$ at different Atwood numbers. Here, $\cos(\theta) = \pm 1$ indicates alignment (cases 1, 8, and 10 in Table 6.2).
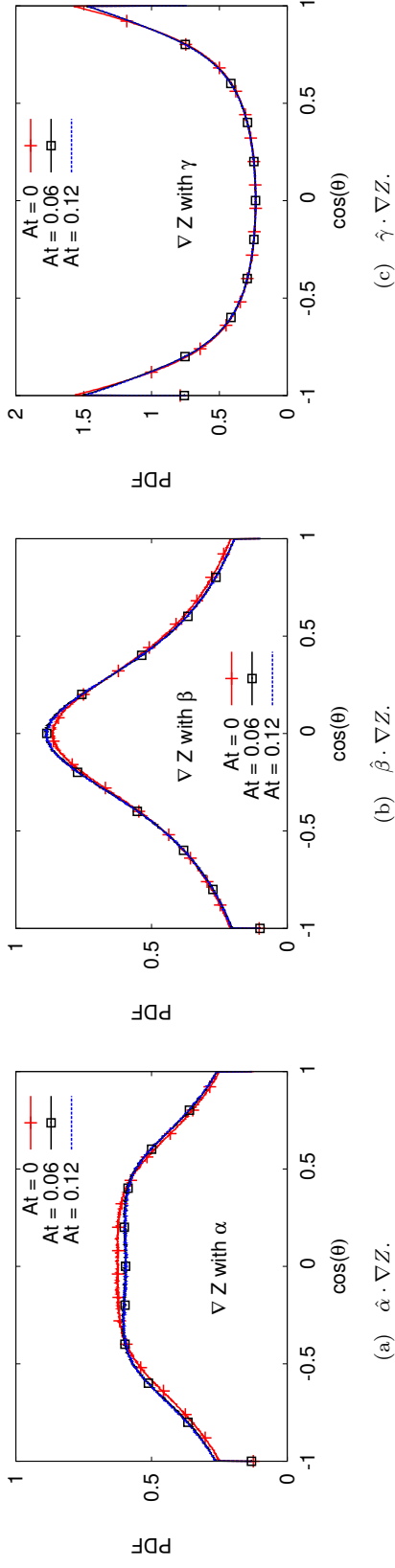
Figure 6.27: Alignment of the scalar gradient, ∇Z, with the eigenvectors of the strain-rate tensor, S_{ij}, for $\epsilon \approx 2$ at different Atwood numbers. Here, $\cos(\theta) = \pm 1$ indicates alignment (cases 4, 12, and 14 in Table 6.2).
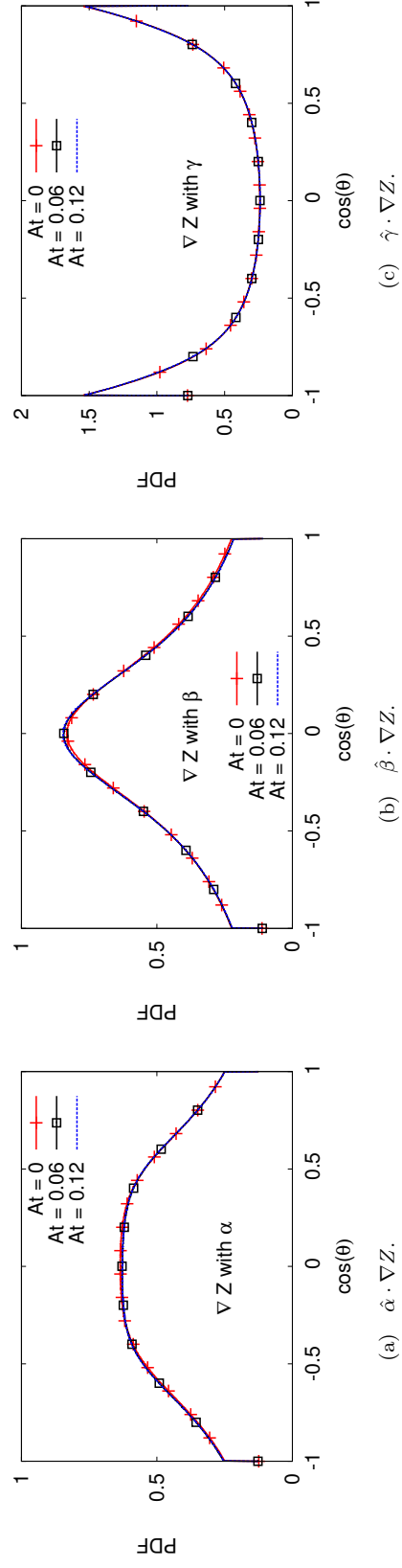
Figure 6.28: Alignment of the scalar gradient, ∇Z, with the eigenvectors of the strain-rate tensor, S_{ij}, for $\epsilon \approx 90$ at different Atwood numbers. Here, $\cos(\theta) = \pm 1$ indicates alignment (cases 1, 8, and 10 in Table 6.2).

6.3.2.1 Energy Transfer and Structure Functions

These final four simulations are defined such that approximately half of the turbulent kinetic energy provided to the velocity field comes from buoyant production and half from isotropic forcing. The power provided by each mechanism is included in Table 6.4; the right most column confirms that buoyant production accounts for approximately half of the total power necessary to maintain the turbulent fields at stationarity. Recall the energy production from these two sources can be expressed, per Eq. 3.5 and Eq. 5.22, as,

$$P_{buoy} = \langle \rho' g_i u_i \rangle, \qquad\qquad P_{iso} = 2Qk_0 = 27Q^3 l^2. \qquad\qquad (6.16)$$

The T_y component of the transfer spectrum is calculated for each of these four cases. The effect of increasing the percent of energy production from 0% (non-buoyant) to 100% (full buoyant) is easily observable in Fig. 6.29 for the lower energy dissipation rate cases and Fig. 6.30 for the higher dissipation rate cases. Clearly, even under partially buoyant conditions (cases 7, 9, 11, 13), there is persistent anisotropy in the transfer spectrum, with the magnitude of transfer in the direction of gravity greatly exceeding that in the other two directions for both Atwood numbers considered. This suggests that any buoyant energy production may have the potential to trigger the energy transfer characteristics found in fully buoyant spectral metrics.

Next, the second-order longitudinal structure functions are calculated. Note that the third-order structure function is not included, as it is related to energy transfer and contains similar information to T_y. The effects of incrementally increasing the ratio of buoyant energy production to total energy production are less clear cut than found in T_y. Figure 6.31 and Fig. 6.32 depict the second-order structure function at $P_{buoy}/P_{total} = 0, \approx 0.5$, and 1. Although at the higher Atwood conditions, shown in Fig. 6.31(b) and Fig. 6.32(b), it is suggested that a partially-buoyantly forced velocity field will tend to behave more like its fully-buoyantly forced counterpart, the lower Atwood data is more ambiguous. In fact, Fig. 6.31(a) and Fig. 6.32(a) suggest that the partially-buoyant fields behave most similarly to the non-buoyantly forced cases. This suggests that there may be a critical Atwood number at which buoyant effects become noticeably apparent in physical space metrics.

6.3.2.2 Effects on the Scalar Field

With the effect of varying P_{buoy}/P_{total} from zero to one investigated in the velocity field, the scalar field is examined. Once again it is found that, despite the presence of buoyancy in the velocity field at any relative magnitude, the scalar fields are effectively unchanged. The spectral metrics behave consistently irrespective of the mechanism of turbulent kinetic energy production, and this scalar field intransigence is shown in the calculated scalar transfer spectra (Fig. 6.33 and Fig. 6.34).
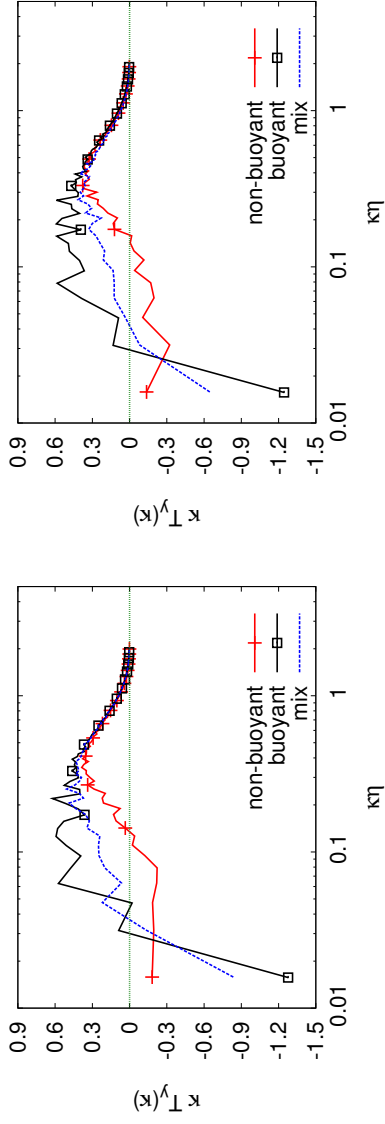
(a) $T_y(\kappa)$ with $A = 0.06$.

(b) $T_y(\kappa)$ with $A = 0.12$.

Figure 6.29: Comparison of T_y component of the transfer spectrum under non-buoyant (cases 11, 13), fully buoyant (cases 12, 14), and partially buoyant conditions (cases 11, 13).
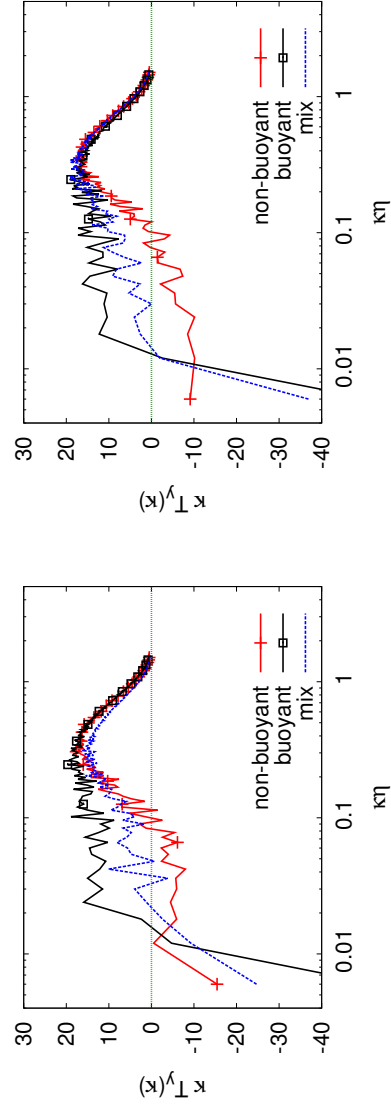
(a) $T_y(\kappa)$ with $A = 0.06$.

(b) $T_y(\kappa)$ with $A = 0.12$.

Figure 6.30: Comparison of T_y component of the transfer spectrum under non-buoyant (cases 7, 9), fully buoyant (cases 8, 10), and partially buoyant conditions (cases 7, 9).
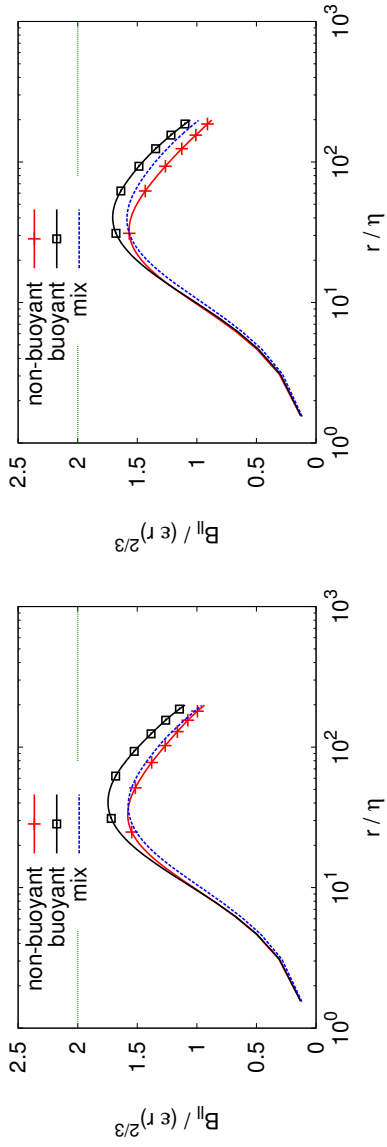
(a) Second-order structure function with $A = 0.06$.

(b) Second-order structure function with $A = 0.12$.

Figure 6.31: Comparison on second-order longitudinal structure functions under non-buoyant (cases 5, 6), fully buoyant (cases 12, 14), and partially buoyant conditions (cases 11, 13).
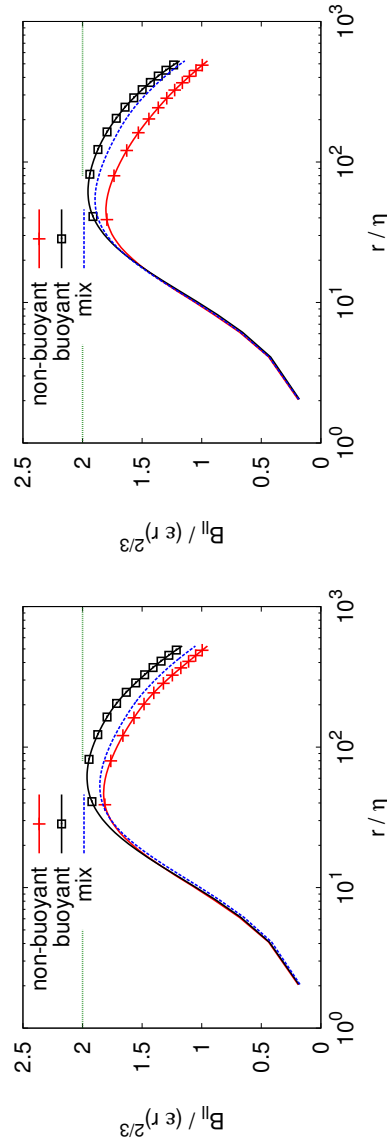
(a) Second-order structure function with $A = 0.06$.

(b) Second-order structure function with $A = 0.12$.

Figure 6.32: Comparison on second-order longitudinal structure functions under non-buoyant (cases 2, 3), fully buoyant (cases 8, 10), and partially buoyant conditions (cases 7, 9).
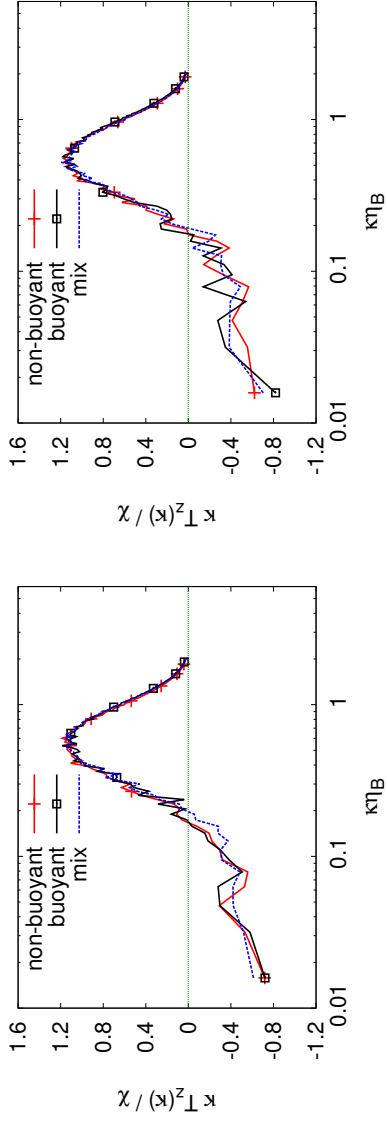
(a) $T_Z(\kappa)$ with $A = 0.06$.

(b) $T_Z(\kappa)$ with $A = 0.12$.

Figure 6.33: Comparison of scalar transfer spectra under non-buoyant (cases 5, 6), fully buoyant (cases 12, 14), and partially buoyant conditions (cases 11, 13).
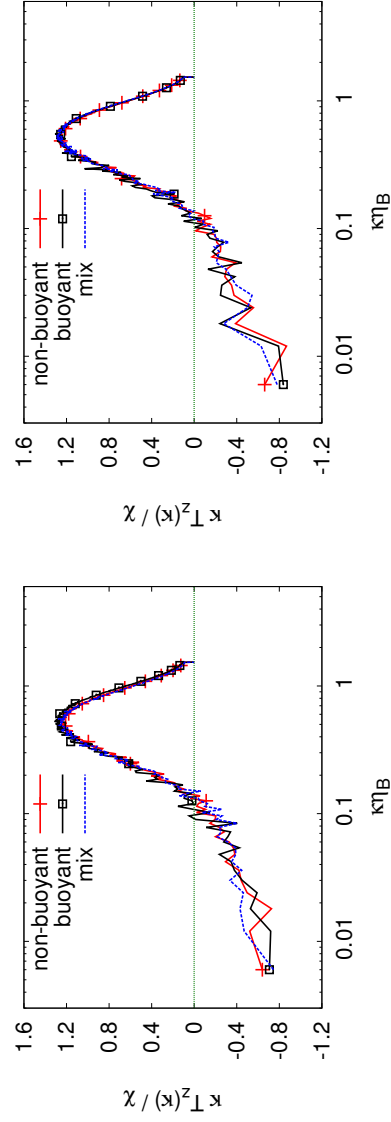
(a) $T_Z(\kappa)$ with $A = 0.06$.

(b) $T_Z(\kappa)$ with $A = 0.12$.

Figure 6.34: Comparison of scalar transfer spectra under non-buoyant (cases 2, 3), fully buoyant (cases 8, 10), and partially buoyant conditions (cases 7, 9).

6.4   Summary

In summary, the simulation framework developed has been applied to the study of the inner region of a turbulent mixing layer under purely isotropic, purely buoyant, and partially buoyant conditions. Three different Atwood numbers have been investigated, corresponding to one constant density case and two variable density cases. Two energy dissipation rates were imposed on the velocity fields, creating two sets of data, each of which had a consistent Kolmogorov scale for all simulations performed.

The baseline behaviors for constant density turbulent mixing were described for the two energy dissipation rate cases. These behaviors established that there was neither an inertial subrange nor inviscid dynamics. Further, the extent of scale overlap for both cases was explicitly quantified. Despite the lack of scale separation, the two constant density cases provided evidence of the effect of dissipation rate (or, Reynolds number) on several key turbulent metrics. First, these baseline data sets showed the slow approach of structure function data towards their analytically-derived asymptotic limits. Second, the behavior of a transfer spectrum under purely isotropic conditions was established ($T_x = T_y = T_z$). Third, the spectrum shapes for the energy and dissipation spectra were qualitatively determined.

Following this, variability in density was then added to the turbulent field to comment on the accuracy of the commonly-made assumption in modeling that density effects on the dynamics deep in a mixing layer are minimal. To qualify the magnitude of density variations present in the two non-zero Atwood number cases contained in this study, the values to which these Atwood numbers would approximately correspond under the classic definition were reported. Although this comparison is not exact, it served to confirm that these Atwood numbers represent significant variations in density such that any effects due to changes in the density field ought to be perceptible. Following the calculation of energy, dissipation, and transfer spectra, it is found that the velocity fields under constant and variable density conditions are effectively equivalent and isotropic ($T_x = T_y = T_z$). Further, the alignment of the scalar gradient and the vorticity field with the eigenvectors of the strain-rate tensor were calculated, and they were found to be consistent with their constant density versions. The effects of variations in density were also examined for the (now) active scalar field. It was found that all scalar field spectra for the variable density cases were equivalent to their constant density versions.

With the effects of density on the velocity field clarified, buoyancy was added to the simulations to determine how and if buoyancy is able to alter the structure of turbulence. For these purely buoyant cases, two Atwood numbers were considered at a single Richardson number. It was found by high-pass filtering the velocity field component aligned in the direction of gravity (the v component) that all buoyancy effects were concentrated into a small number of low wavenumber modes. When

these modes were removed, the energy and dissipation spectra approached those obtained under non-buoyant conditions. Then, to determine if buoyancy altered the way in which energy was transferred, the three components of the transfer spectrum were calculated. From these, it was found that the component of transfer in the direction of gravity was of larger magnitude than the other two components across all flow scales. Thus, the action of buoyancy introduces significant anisotropy into the velocity field, and it is reflected in the energy transfer process. Further, when the structure functions were calculated under these buoyant conditions, they suggested that buoyantly-forced data behaves as if at a higher effective Reynolds number compared to a non-buoyantly-forced equivalent case. The magnitude of the normalized structure functions, for the same energy dissipation rate, approached the asymptotic limits faster than the non-buoyant data. Despite these differences, there were no discernible disparities in the alignment tendencies of the scalar gradient, vorticity field, or strain-rate tensor eigenvectors under buoyant conditions when compared to those under non-buoyant or incompressible conditions. Also, the scalar field was unaffected by the significant anisotropy present in the velocity field, as all scalar field metrics calculated were equivalent to their non-buoyant versions.

Lastly, the point at which the behaviors associated with purely buoyant energy production began to manifest was examined. This included varying the percent of buoyant energy production in the total energy production from 0% to approximately 50% to 100%. It was found that when buoyant energy production makes up even only half of the total energy added to the turbulent field, the transfer spectra display the same significant anisotropic tendencies noted in the fully buoyant cases. This was found for both Atwood numbers. However, when physical-space metrics were considered, specifically the second-order structure functions, this became less unambiguous; the partially buoyant low Atwood number data agreed more with the non-buoyant structure function data, while the partially buoyant higher Atwood number data agreed more closely with the fully buoyant data. However, irrespective of this, the scalar field was unaffected by the presence of buoyancy in any relative amount, and all scalar field metrics indicated insensitivity to the source of turbulent kinetic energy in the velocity field.

6.5 Conclusions

Although the objectives of this work were to create a simulation method in which to study mixing under buoyant conditions and then to describe more fully the physics of buoyant mixing, there are important conclusions that can be drawn for Large-Eddy Simulation (LES) modeling. LES studies reduce the computational cost of simulations of turbulent flows by resolving only a portion of the large-scale flow physics and, then, employing models to represent the physics occurring at the smaller, dynamically important, unresolved flow scales. In an LES simulation, the momentum and

advection-diffusion equations, assumed for discussion purposes to describe an incompressible fluid and a passive scalar,

$$\frac{\partial u_i}{\partial t} + \frac{\partial u_j u_i}{\partial x_j} = -\frac{1}{\rho}\frac{\partial p}{\partial x_i} + \nu\frac{\partial}{\partial x_j}\left(\frac{\partial u_i}{\partial x_j}\right)$$
$$\frac{\partial Z}{\partial t} + \frac{\partial u_j Z}{\partial x_j} = \frac{\partial}{\partial x_j}\left(\mathcal{D}\frac{\partial Z}{\partial x_j}\right),$$
(6.17)

are filtered,

$$\frac{\partial \tilde{u}_i}{\partial t} + \frac{\partial \tilde{u}_j \tilde{u}_i}{\partial x_j} = -\frac{1}{\rho}\frac{\partial \tilde{p}}{\partial x_i} + \nu\frac{\partial}{\partial x_j}\left(\frac{\partial \tilde{u}_i}{\partial x_j}\right) - \frac{\partial \tau_{ij}^R}{\partial x_j}$$
$$\frac{\partial \tilde{Z}}{\partial t} + \frac{\partial \tilde{u}_j \tilde{Z}}{\partial x_j} = \frac{\partial}{\partial x_j}\left(\mathcal{D}\frac{\partial \tilde{Z}}{\partial x_j}\right) - \frac{\partial \tau_{Zj}}{\partial x_j}.$$
(6.18)

The LES resolves the filtered velocity field features, $\tilde{u}_i$, and the filtered scalar field features, $\tilde{Z}$, for all flow scales larger than the filter cut-off (the super-filter scales). In spectral space, this corresponds to resolving the low wavenumber flow (mixing) features. The flow features smaller than this cut-off, however, are not solved; instead, models are implemented to describe the dynamics at these sub-filter scales. These modeling terms are termed sub-filter models (or, sub-grid scale (SGS) models), and they correspond to,

$$\tau_{ij}^R = \widetilde{\tilde{u}_i \tilde{u}_j} - \tilde{u}_i \tilde{u}_j$$
$$\tau_{Zj} = \widetilde{\tilde{u}_j Z} - \tilde{u}_j \tilde{Z},$$
(6.19)

in the above filtered equations. These modeling terms are generally termed the (SGS) residual stress tensor, τ_{ij}^R, and the (SFF) sub-filter scale scalar flux vector, τ_{Zj}. Since Direct Numerical Simulation (DNS) studies of turbulent buoyant flows can become quite computationally expensive, especially under high Schmidt number and Reynolds number conditions, it is common to apply LES models to enable the simulation of these highly turbulent cases. It is currently not known whether the models that have been developed to represent Eq. 6.19 are valid for buoyant conditions. The results contained in the previous chapters of this work offer some insight into this uncertainty.

6.5.1   SGS Modeling in the Velocity Field

It is general LES practice to place the filter width at the waveshell in wavespace such that 80% of the turbulent kinetic energy is resolved (located in the inertial subrange) [77]. The smaller scales are represented by various SGS models, the primary function of which is to provide a means by which the sub-grid scales can dissipate the energy from the super-grid scales. For example, the Smagorinsky model imposes a residual viscosity on the small scales, ν_r, to ensure that they dissipate

turbulent kinetic energy. The published SGS models for $\tau_{ij}^R = \widetilde{\tilde{u}_i \tilde{u}_j} - \tilde{u}_i \tilde{u}_j$ are derived, in most cases, under an assumption of isotropy at these dissipative scales. It is of interest here to comment on the validity of using these existing models when doing LES studies of buoyant flows. Note that this work does not endorse any particular SGS model.

From this work, specifically the results from Section 5.6.1 and the current chapter, it seems that the application of SGS models in their current form to turbulent buoyant flows should be valid. This statement is based on the following findings. In Section 5.6.1, it was shown (and depicted in Fig. 5.7) that all the anisotropy introduced by buoyancy is confined to only a few low wavenumber modes. This work finds that once contributions from $\kappa L < 40$ are removed from the v component of the velocity field (which corresponds to the eight lowest wavenumbers, $\kappa < 8$), the differences between the filtered, buoyant field and an isotropic, variable density velocity field become negligible. Further, it is identified that these modes that are filtered out are responsible for 85% of the total turbulent kinetic energy present in the domain, comparable to what current LES practice suggests is necessary to accurately reproduce large scale flow features; below this point, all physics are found to be isotropic, allowing for the use of existing SGS models in their modeling.

This is further supported by the dissipation spectra calculated under buoyant conditions and then compared to non-buoyant conditions. In all instances, the small scales were coincident. Thus, the energy dissipation, ϵ, at these small scales is the same between buoyant and non-buoyant conditions. Therefore, the same methodologies used presently to impose an energy dissipation at the sub-grid scales can be used. The dissipation argument speaks to the magnitude of energy that must be dissipated, but there are also directionality concerns that must be addressed (recall τ_{ij}^R is a tensor). However, the analysis in the second half of the current chapter suggests that buoyant flows and non-buoyant flows will display the same alignment tendencies. For all physical fields calculated, including the vorticity field, scalar gradient field, and eigenvectors of the strain field, the alignment characteristics were unchanged under buoyant conditions. Thus, as written and currently used, SGS modeling approaches, which are designed to capture isotropic small-scale physics, may be applied to buoyant LES studies.

6.5.2 SFF Modeling in the Scalar Field

With modeling in the velocity field addressed, modeling in the scalar field is now discussed. The SFF vector, $\tau_{Zj} = \widetilde{\tilde{u}_j Z} - \tilde{u}_j \tilde{Z}$, captures the effects of non-linear interactions between the resolved (super-filter) and the unresolved (sub-filter) scales. SFF models currently published in the literature were derived for application to isotropic turbulence. It is the conclusion of this chapter's work that these modeling terms can be used, as they were originally written, for the study of scalar mixing under buoyant conditions. This is justified by the following arguments.

As it is a vector, the SFF term can be fully described by a magnitude and a direction. Beginning

with the directional component in the description of τ_{Zj}, the alignment PDFs presented in the current chapter show that, independent of the source of turbulent kinetic energy (buoyant energy production or isotropic energy production), the alignment of the scalar gradient vector with the strain-rate eigenframe is the same. This held under constant density conditions, variable density non-buoyant conditions, and fully buoyant conditions. Hence, the alignment in the scalar field is insensitive to the source of energy production. Thus, the directional traits imposed by SFF terms used in the study of isotropic turbulence are also appropriate for buoyant scalar mixing. The next component is the magnitude of the SFF vector. The magnitude of the SFF is important, as it determines the amount of scalar dissipation that occurs at the sub-filter scales, χ_τ. This sub-filter dissipation is defined as,

$$\chi_\tau = -\tau_{Zj}\frac{\partial Z}{\partial x_j}.$$

The buoyant scalar energy spectra, scalar dissipation spectra, and scalar transport spectra were identical between the non-buoyant and buoyant cases. Since the scalar energy dissipation rate, χ, is related to the integral of the scalar energy dissipation spectrum, then, following the results of this work, the dissipation that must be provided by the SFF term is the same between the buoyant and non-buoyant (isotopic) cases. Hence, the magnitude of the SFF vector ought to be the same for buoyant scalar mixing as it is for isotropic scalar mixing. This implies that, as originally written, published SFF vector modeling approaches can be used in LES studies of buoyant flows.

Chapter 7

Comprehensive Summary and Conclusions

In summary, this thesis work contained five pieces. The first three parts were concerned with creating and validating the necessary numerical tools for the velocity and scalar fields such that the physics deep inside a turbulent mixing layer under buoyant and non-buoyant conditions could be accurately and reliably predicted. Fourth, following the development of these tools, the velocity and scalar field methods were integrated into one simulation methodology optimized for the study of buoyant and non-buoyant turbulent mixing. Then, lastly, the fifth piece constituted the application of the previously validated simulation framework to the study of turbulent buoyant flows.

In the initial piece (Chapter 2), the two classes of velocity field forcing methods were presented and described. These included the many published spectral-space methods and a singular published physical-space method. To determine the accuracy of the turbulence predicted under their action, one representative method from each of the two classes was selected. These representative methods were Alvelius' stochastic spectral method and Lundgren's linear method. The source terms that these two methods appended to the governing momentum equations were discussed and the corresponding source terms they appended to the Karman-Howarth equation were thoroughly analyzed. It was found that these two methods, and, hence, all methods since these are representative, produce similar turbulent physics for the small, dissipative scales. Outside of this range, however, the physics that they predict vary non-negligibly. The cause for these differences outside of the small-scale region was identified as being caused directly by the behaviors of their method-specific, imposed Karman-Howarth source terms.

The major findings of Chapter 2 were threefold. First, at the small-scales ($r/\eta < 10$), the dominance of viscosity renders the specifics of any forcing method irrelevant, and the correct turbulent behaviors will be captured irrespective of the velocity field forcing method used. Second, across an intermediate range of scales, $10 < r/\eta < 0.5l_0/\eta$, the differences in the predicted turbulent physics can be directly attributed to the nature of the imposed Karman-Howarth source term. The Karman-Howarth source term governs the behavior of the second- and third-order longitudinal structure function via the viscous and inertial terms in the forced Karman-Howarth equation.

For Alvelius' case, this results in structure functions which are suggestive of inviscid dynamics at Reynolds numbers that are significantly too low. Thus, the behaviors obtained under this forcing method across these intermediate scales are more reflective of a numerical artifact than of actual physically relevant dynamics. Lundgren's linear forcing does not suffer from this feature. Third, the importance of the energy production spectrum is reaffirmed. If a method imposes an artificial separation between the energy-producing and energy-containing scales, then there is a risk that unphysical behaviors may occur. This is one of the primary shortcomings of Alvelius' forcing scheme, and, to some extent, of all other spectral forcing schemes.

Following this analysis, Lundgren's linear velocity field forcing method was judged as being the more physically based, and it was used in all subsequent simulations conducted. However, this method was known to create turbulent velocity fields with long-time turbulent statistics that could be subject to significant oscillation. This resulted in the need for longer simulation run times to attain time-invariant conditions (*i.e.* statistical stationarity) in relevant statistics. To address this, a pratical modification was made to this forcing method, and it was presented and discussed in Chapter 3. The modification was shown to reduce significantly oscillations in key turbulent quantities, which allows for more efficient simulations without sacrificing accuracy or altering the underlying turbulent physics.

With the needed velocity field forcing methods understood and validated, the scalar field was next addressed in Chapter 4. This piece addressed the need for an isotropic scalar field forcing method such that forced buoyant mixing could be studied more efficiently. Available scalar field forcing methods in the literature were either anisotropic in nature or were appropriate for a different class of scalar field physics (continuous scalar variance injection), or both. Thus, a new, isotropic scalar field forcing method was developed specifically to represent one-time scalar variance injection, which was more physically consistent with the class of scalar field mixing encountered in buoyantly-driven turbulent mixing deep inside of a mixing layer (self-similar decay). This forcing technique was termed linear scalar forcing, and it was validated based on its ability to predict the needed scalar field mixing physics.

With the velocity and scalar field forcing methods assessed and fully understood, the numerical framework to study turbulence under buoyant and isotropic (non-buoyant) conditions was integrated, and the relevant equations and forcing method constraints were presented (Chapter 5). The chief advantages of this framework were twofold. First, by focusing on a region of turbulent mixing deep inside of a mixing layer, the effect that buoyancy had on the small-scale structure of turbulence could be probed in a computationally efficient way. Second, the four important non-dimensional parameters, including the Reynolds, Schmidt, Richardson, and Atwood numbers, could be independently varied. Other available frameworks cannot do this. This feature allows for the effects that each of the four parameters have on the mixing process to be isolated and probed under the developed

simulation methodology.

The framework was validated by considering three test cases corresponding to fully isotropic, fully buoyant, and partially buoyant energy production, and reproducing key turbulent characteristics obtained from other simulations of buoyant flows in the published literature. It was found that the smallest flow scales, the Kolmogorov scales, were isotropic with and without the presence of gravity. The fully buoyant case suggested that, although buoyancy did introduce significant anisotropy into the velocity field, this anisotropy had only shallow penetration. When the lowest wavenumber modes (largest length scales) were filtered out of the velocity field, the effects of buoyancy virtually vanished, leaving velocity fields that resembled quite closely their non-buoyant, isotropically-forced counterparts.

Following the validation of this new framework in which to study forced, variable density turbulent mixing inside of a mixing layer, a simulation study was performed in Chapter 6. This numerical framework was used to investigate buoyant and isotropic turbulent mixing over a range of Richardson, Reynolds, and Atwood numbers. The nature of turbulent structure was interrogated under both conditions, and the associated energy spectra, transfer spectra, dissipation spectra, relevant velocity and scalar field structure functions, and alignment characteristics of pertinent parameters (*e.g.*, strain rate, scalar gradient, vorticity) were calculated. From these results, further insight was gained into the differences and similarities in buoyantly and isotropically-driven turbulent mixing in both the velocity and scalar fields.

Specifically, it was found that buoyant effects are found primarily in the velocity field's transfer spectra, energy spectra, and second- and third-order longitudinal structure functions; the other metrics are largely unimpacted. Beginning with buoyancy effects on energy transfer, the transfer spectrum was decomposed into three terms, one associated with energy transfer in the same direction as one of the three velocity field components. Under non-buoyant and constant density conditions, these three transfer spectra are isotropic. Under buoyant conditions, however, it was found that the transfer spectrum in the direction of gravity is of significantly larger magnitude than the other two spectra. This was attributed to the single direction through which energy is provided to the velocity field under buoyant conditions. Further, this is a robust feature; for all Atwood numbers examined and, even when only half of the total supplied turbulent kinetic energy came from buoyancy, the energy transfer spectrum aligned in the direction of the gravity vector displayed pronounced anisotropy. As noted in Chapter 5, however, these anisotropic effects were significantly mitigated in the energy and dissipation spectra following the application of a low wavenumber filter to the v component of the velocity field (the component in the direction of gravity). This supports the work from the previous Chapter 5, which claimed that the penetration of the buoyantly-produced anisotropy in the energy spectrum is not significantly deep. Lastly, the structure function data provided an interesting find when comparing the buoyant and non-buoyant turbulent fields. For the same energy dissipation

rate, the buoyant structure functions appeared as if they had a higher effective Reynolds number compared to their equivalent non-buoyant versions. The buoyant structure function data produced (properly normalized) structure functions that more rapidly approached their inviscid asymptotic limits for the same energy dissipation rate.

The alignment characteristics between the vorticity field, scalar gradient, and eigenvectors of the strain-rate tensor were found to be insensitive to variations in density or the action of buoyancy; for all test cases included in this study, the alignment PDFs between these three parameters were unchanged from the incompressible, constant density findings. Further, the scalar field dynamics were found to be quite intransigent to changes in the velocity field; the scalar energy spectra, scalar dissipation spectra, and scalar transfer spectra were equivalent under constant density, non-buoyant variable density, and buoyant conditions. Thus, it was concluded that the turbulent structure in the velocity field is indeed dependent on the mechanism of turbulent kinetic energy production, but the scalar field structure shares no such dependency.

In conclusion, following from this research, there are four key findings. First, a more thorough understanding of how velocity field forcing methods work is gained. The effects that a forcing method-imposed source term have on the generated turbulent fields are explained and connected to the implicit and explicit assumptions of the implemented velocity field forcing method. Second, a possible explanation for the differences noted between experimental results of homogeneous grid turbulence and forced box turbulence is provided. This explanation comes from the effect that the momentum source term has on the Karman-Howarth equation and the distinction between energy-containing and energy-producing scales (*i.e.* the energy production spectrum). Third, a possible explanation for the differences noted between theoretical scaling arguments, data from decaying grid turbulence experiments, and forced high Schmidt number simulation studies in the viscous-convective subrange of the scalar energy spectrum is offered. This explanation is the distinction between continuous scalar variance injection, which was implicitly assumed by both Batchelor [7] and Kraichnan [49] via their assumption of a reservoir of infinite scalar variance, and one-time scalar variance injection. The two most commonly-implemented scalar field forcing methods, mean scalar gradient and low waveband spectral forcing, both assume an infinite reservoir of variance, and, consequently, both agree with Batchelor's theoretical scaling argument. Conversely, linear scalar-forced simulation data and data from decaying grid turbulence experiments tend to agree, both of which are subject to one-time variance injection. Fourth, an improved understanding of the differences and similarities in buoyantly- and (non-buoyant) isotropically-driven turbulent mixing in the velocity and scalar fields is gained. Also, the way in which these differences and similarities change with varying Atwood, Richardson, and Reynolds numbers is clarified.

Chapter 8

Appendices

8.1 Appendix I: Isotropic Turbulent Physics: Expected Theoretical Scaling Laws

Second-Order Structure Function

Per Kolmogorov's first similarity hypothesis [77], at the small scales, the dissipation rate, ϵ, and the kinematic viscosity, ν, are sufficient to describe $B_{ll}(r)$ (Eq. 2.9), and the group $(\epsilon r)^{2/3}$ can be used to non-dimensionalize it. Accordingly, within the dissipation range, it can be written,

$$B_{ll}(r) = (\epsilon r)^{2/3}\, \hat{B}_{ll}(r/\eta), \tag{8.1}$$

where $\hat{B}_{ll}$ is a dimensionless function and $\eta = \left(\frac{\nu^3}{\epsilon}\right)^{1/4}$ is the Kolmogorov length-scale. In the inertial subrange, the physics must become inviscid (Kolmogorov's second similarity hypothesis [77]), implying that $\hat{B}_{ll}(r/\eta)$ must assume a constant value, such that,

$$B_{ll}(r) = C_K \left(\epsilon r\right)^{2/3}. \tag{8.2}$$

This scaling behavior was derived also by Lundgren via a matched asymptotic-based analysis of the Karman-Howarth equation [59].

Third-Order Structure Function

A similar scaling can be obtained for the third-order longitudinal structure function (Eq. 2.9). $B_{lll}(r)$ can be non-dimensionalized by the dimensional group, ϵr, and written in terms of a non-dimensional function, $\hat{B}_{lll}$, according to,

$$B_{lll}(r) = (\epsilon r)\, \hat{B}_{lll}(r/\eta). \tag{8.3}$$

Within the inertial subrange, $\hat{B}_{lll}(r/\eta)$ must tend to a constant value. From the original KH equation (Eq. 2.12), Kolmogorov proved this constant to be $\hat{B}_{lll}(r/\eta) = -4/5$. He obtained this "4/5-law" by arguing that, in locally isotropic turbulence, the time derivative term of $B_{ll}(r)$ is negligible and the viscous term is inactive [77]. Solving Eq. 2.12 subject to these simplifications yields,

$$B_{lll}(r) = -\frac{4}{5}\epsilon r. \tag{8.4}$$

Energy Spectrum

Additionally, with a sufficiently high Re_λ, it is expected that the energy spectrum exhibits a power-law dependence on wavenumber, $E(\kappa) \propto \kappa^{-5/3}$, across the inertial range of scales. The scaling coefficient, $n = -5/3$, assumes the presence of inviscid dynamics and the theoretical scaling for $B_{ll}(r)$ given in Eq. 8.2.

The justification for the $-5/3$ power-law comes from analysis of the velocity-spectrum tensor ($\Phi_{ij}(\underline{\kappa})$), the two-point velocity correlation tensor ($R_{ij}(\underline{r})$), and the second-order longitudinal structure function ($B_{ll}(\underline{r})$). The energy spectrum is a scalar function derived from the velocity spectrum tensor [77] as,

$$E(\kappa) = \oint \frac{1}{2}\Phi_{ii}(\underline{\kappa}) \, dS(\kappa) = 2\pi\kappa^2\Phi_{ii}(\kappa), \tag{8.5}$$

where the integration is over a sphere of radius κ. The velocity-spectrum tensor,

$$\Phi_{ij}(\underline{\kappa}) = \frac{1}{(2\pi)^3} \iiint R_{ij}(\underline{r}) \exp\left(-i\underline{\kappa}\cdot\underline{r}\right) \, d\underline{r}, \tag{8.6}$$

indicates the contribution from each Fourier mode, $\exp\left(i\underline{\kappa}\cdot\underline{r}\right)$, to the Reynolds stress, $\langle u_i u_j \rangle$. Under the condition of homogeneity, $R_{ij}(\underline{r}) = \langle u_i u_j' \rangle$ and $\Phi_{ij}(\underline{\kappa})$ form a Fourier-transform pair [77]. Writing R_{ii} in terms of B_{ll} results in,

$$\Phi_{ii}(\underline{\kappa}) = \frac{1}{(2\pi)^3} \iiint \left(3\langle u^2 \rangle - \frac{1}{2r^2}\frac{\partial}{\partial r}\left(r^3 B_{ll}\right)\right) \exp\left(-i\underline{\kappa}\cdot\underline{r}\right) d\underline{r}, \tag{8.7}$$

which can be integrated over a spherical volume, with application of $\underline{\kappa}\cdot\underline{r} = |\kappa||r|\cos(\theta)$ and use of an integration by parts procedure, to yield,

$$\Phi_{ii}(\kappa) = \frac{1}{(2\pi)^2} \int_0^\infty \left(r^2 B_{ll}(r)\cos(\kappa r) - \left(\frac{r}{\kappa}\right)B_{ll}(r)\sin(\kappa r)\right) \, dr. \tag{8.8}$$

The energy spectrum and velocity-spectrum tensor are connected via $E(\kappa) = 2\pi\kappa^2\Phi_{ii}(\kappa)$, admitting

an equation for the energy spectrum,

$$E(\kappa) = \frac{1}{2\pi} \int_0^\infty \left(\kappa^2 r^2 B_{ll}(r) \cos(\kappa r) - \kappa r B_{ll}(r) \sin(\kappa r) \right) \, dr. \tag{8.9}$$

Introducing a change of variables, $\alpha = \kappa r$, and using B_{ll} (and its non-dimensional counterpart, $\hat{B}_{ll}$, from Eq. 8.1), an expression for $E(\kappa)$ emerges as,

$$E(\kappa) = \frac{1}{2\pi} \epsilon^{2/3} \kappa^{-5/3} \int_0^\infty \hat{B}_{ll}\left(\frac{\alpha}{\kappa\eta}\right) \left(\alpha^{8/3} \cos(\alpha) - \alpha^{5/3} \sin(\alpha) \right) \, d\alpha. \tag{8.10}$$

In the inertial subrange, $\hat{B}_{ll}(r/\eta)$ should be constant. If it is, the energy spectrum will scale as $E(\kappa) \propto \kappa^{-5/3}$. However, if $\hat{B}_{ll}(r/\eta)$ is not constant, this term, which has wavenumber dependence, will contribute to the energy spectrum calculation, modifying the power-law dependence of $E(\kappa)$.

Finite Reynolds Number (Re_λ) Effect

The finite-Re_λ effect describes the situation when there is insufficient separation between the integral and viscous scales, resulting in the permeation of large-scale anisotropy into the intermediate and small, viscous scales [79]. How quickly the effects of finite-Re_λ vanish as the Re_λ is increased is not precisely known, but it has been suggested that the effects may decay slowly [80]. For instance, it has been argued that finite-Re_λ effects cannot be neglected truly until $Re_\lambda = O(10^4)$ [79].

8.2 Appendix II: The (Unforced) Karman-Howarth Equation

The Karman-Howarth equation describes the decay of an isotropic turbulent field. It is derived from the momentum and continuity equations using assumptions of incompressibility, isotropy, and homogeneity. The derivation procedure, which will be briefly summarized here, begins with the Navier-Stokes equations (Eqs. 8.11 and 8.12) written at two different points separated by a vector distance $\underline{r}$,

$$\frac{\partial u_i}{\partial t} + u_j \frac{\partial u_i}{\partial x_j} = -\frac{1}{\rho} \frac{\partial p}{\partial x_i} + \nu \frac{\partial}{\partial x_j} \left(\frac{\partial u_i}{\partial x_j} \right), \tag{8.11}$$

$$\frac{\partial u_k'}{\partial t} + u_j' \frac{\partial u_k'}{\partial x_j'} = -\frac{1}{\rho} \frac{\partial p'}{\partial x_k'} + \nu \frac{\partial}{\partial x_j'} \left(\frac{\partial u_k'}{\partial x_j'} \right). \tag{8.12}$$

The two points are related through $\underline{x}' = \underline{x} + \underline{r}$ and $\underline{u}(\underline{x} + \underline{r}, t) = \underline{u}'(\underline{x}', t)$. By multiplying Eq. 8.11 by u_k', multiplying Eq. 8.12 by u_i, adding the resulting two expressions, and then ensemble averaging (denoted by $\langle \cdot \rangle$), an equation for $R_{ik}(\underline{r}, t)$, the two-point velocity correlation tensor, is obtained,

$$\frac{\partial R_{ik}(\underline{r}, t)}{\partial t} = \frac{\partial}{\partial r_j} \left(\langle u_i u_j u_k' \rangle - \langle u_i u_k' u_j' \rangle \right) + 2\nu \frac{\partial}{\partial r_j} \left(\frac{\partial R_{ik}(\underline{r}, t)}{\partial r_j} \right). \tag{8.13}$$

Note that the two-point velocity correlation tensor is defined as $R_{ik}(\underline{r}, t) = \langle u_i(\underline{x}, t) u_k'(\underline{x}', t) \rangle$, and the pressure gradients vanish under the conditions of homogeneity and isotropy when averaged.

A consequence of the assumption of statistical isotropy is that $R_{ik}(\underline{r}, t)$ must be isotropic also. Therefore, it can be expressed in terms of two scalar functions, $f(r)$ and $g(r)$, which depend only on the separation distance, $r = |\underline{r}|$, according to,

$$R_{ik}(\underline{r}, t) = \langle u^2 \rangle(t) \left(g(r, t)\delta_{ik} + (f(r, t) - g(r, t)) \frac{r_i r_k}{r^2} \right). \tag{8.14}$$

These two functions are the longitudinal and transverse velocity correlation functions, respectively. Using continuity $(\partial R_{ik}(\underline{r}, t)/\partial r_k = 0)$, a relation between these two scalar functions is found,

$$g(r, t) = f(r, t) + \frac{1}{2} r \frac{\partial f(r, t)}{\partial r}, \tag{8.15}$$

which enables the definition of $R_{ik}(\underline{r}, t)$ with the longitudinal correlation function,

$$R_{ik}(\underline{r}, t) = \langle u^2 \rangle(t) \left(f(r, t)\delta_{ik} + \frac{1}{2} \frac{\partial f}{\partial r} \left(r\delta_{ik} - \frac{r_i r_k}{r} \right) \right). \tag{8.16}$$

Similarly, the triple velocity correlation functions $(S_{ijk} = \langle u_i u_j u_k' \rangle, \; S_{kji} = -\langle u_i u_k' u_j' \rangle)$, can be expressed in terms of three scalar functions, $A(r, t)$, $B(r, t)$, and $C(r, t)$,

$$(\langle u^2 \rangle(t))^{-3/2} S_{ijk}(\underline{r}, t) = A(r, t) \frac{r_i r_j r_k}{r^3} + B(r, t) \frac{\delta_{ij} r_k}{r} + C(r, t) \left(\frac{\delta_{jk} r_i}{r} + \frac{\delta_{ki} r_j}{r} \right). \tag{8.17}$$

It is convenient to express the longitudinal triple correlation function as,

$$S_{111} = \langle u_1^2(\underline{x}, t) u_1(\underline{x} + \underline{e}_1 r, t) \rangle = \langle u^3 \rangle(t) h(r, t), \tag{8.18}$$

where $h(r, t)$ is a scalar function of r. After the application of continuity $(\partial S_{ijk}/\partial r_k = 0)$ and considerable algebra, the triple velocity correlation function, $S_{ijk}(\underline{r}, t)$, can be expressed in terms of only $h(r, t)$,

$$2\langle u^2 \rangle^{-3/2} S_{ijk}(\underline{r}, t) = \frac{r_i r_j r_k}{r^3} \left(h - r \frac{\partial h}{\partial r} \right) - h\delta_{ij} \frac{r_k}{r} + \left(h + \frac{1}{2} r \frac{\partial h}{\partial r} \right) \left(\delta_{jk} \frac{r_i}{r} + \delta_{ki} \frac{r_j}{r} \right). \tag{8.19}$$

Upon substitution of Eq. 8.19 and Eq. 8.16 into Eq. 8.13, separating terms into δ_{ik} and $r_i r_k / r^2$ components, the original Karman-Howarth equation [25], is obtained,

$$\frac{\partial \left(\langle u^2 \rangle f \right)}{\partial t} = \langle u^2 \rangle^{3/2} \left(\frac{\partial h}{\partial r} + \frac{4}{r} h \right) + 2\nu \langle u^2 \rangle \left(\frac{\partial^2 f}{\partial r^2} + \frac{4}{r} \frac{\partial f}{\partial r} \right). \tag{8.20}$$

This equation describes mathematically the decay of an isotropic turbulent field. Although this is a deterministic equation, its dependency on two unknown functions, $f(r,t)$, and $h(r,t)$, makes it an unclosed evolution equation. It cannot be solved analytically without knowing *a priori* either $f(r,t)$ or $h(r,t)$.

8.3 Appendix III: Description of Simulation Code (NGA)

NGA is an extension of the high order conservative finite difference scheme initially developed by Morinishi *et al* [64]. It allows for three-dimensional, variable density turbulent flows to be simulated in complex geometries, which can be either cylindrical or cartesian, on uniform or non-uniform meshes [26]. It is discretely conservative of mass, momentum, and kinetic energy, and it can provide an arbitrarily high order of accuracy. NGA makes use of staggered variables to improve its performance. All scalar quantities, such as the density (ρ) and the scalar (Z), are stored at the cell (volume) centers; the velocity components (u, v, and w) are stored at the faces of the cell volumes. In all simulation data presented in the main body of this thesis document, the meshes were strictly uniform. An overview of NGA, including the governing equations being solved and the schemes by which they are solved, is here provided in support of the simulation data presented in this thesis.

8.3.1 Governing Equations

NGA solves the variable density, low Mach number Navier-Stokes equations [26]. These include expressions of mass conservation,

$$\frac{\partial \rho}{\partial t} + \frac{\partial}{\partial x_j} \left(\rho u_j \right) = 0, \tag{8.21}$$

and momentum conservation,

$$\frac{\partial \rho u_i}{\partial t} + \frac{\partial}{\partial x_j} \left(\rho u_i u_j \right) = -\frac{\partial p}{\partial x_i} + \frac{\partial \sigma_{ij}}{\partial x_j}. \tag{8.22}$$

Here, p is the pressure, u_i is one of the three-components of the velocity field, ρ is the density, and σ_{ij} is the deviatoric stress tensor. The deviatoric stress tensor is defined as,

$$\sigma_{ij} = \mu \left(\frac{\partial u_i}{\partial x_j} + \frac{\partial u_j}{\partial x_i} \right) - \frac{2}{3} \mu \frac{\partial u_k}{\partial x_k} \delta_{ij}, \tag{8.23}$$

where δ_{ij} is the Kronecker delta and μ is the dynamic viscosity. It is common to obtain the density through an imposed model equation [9]. In the simulations contained in this work, the density is written as a function of the conserved scalar quantity, Z, per Eq. 5.6, and this approach is used to represent the mixing process. The conserved scalar quantity is calculated from the transport equation,

$$\frac{\partial \rho Z}{\partial t} + \frac{\partial}{\partial x_j} (\rho u_j Z) = \frac{\partial}{\partial x_j} \left(\rho \mathcal{D} \frac{\partial Z}{\partial x_j} \right), \tag{8.24}$$

where $\mathcal{D}$ is the scalar diffusivity. In this appendix, the density field will be related to the scalar field via the generic model equation $\rho = \hat{\rho}(Z)$.

It is here noted that the boundary conditions for all equations under the simulation configuration implemented in this work are triply periodic. The iterative procedure to solve this equation system is described with the implemented second-order semi-implicit Crank-Nicolson (a time-advancement) scheme in Appendix 8.4, which is both stable and accurate [26, 76, 86].

It should be noted that these equations (Eq. 8.22 and Eq. 8.24) are unforced; they do not include momentum or scalar field source terms. The equations implemented in the main body of this thesis document are subject to numerical forcing from both buoyant and isotropic sources in the case of the momentum equation and from isotropic sources in the case of the scalar equation. However, the forced equations (Eq. 5.4 and Eq. 5.5) are solved in the same fashion as these unforced versions.

8.3.2 Variable-density Conservative Finite Difference Scheme

The coordinate system with which the current work is concerned is a standard cartesian one. Accordingly, physical space can be represented as $\underline{x} = (x, y, z)$. In NGA, physical space is mapped to a uniform computational grid of unity spacing. The grid spacing is written as $\underline{\xi} = (\xi_1, \xi_2, \xi_3)$. Here, ξ_1 is the spacing increment in the x-direction, ξ_2 is the spacing increment in the y-direction, and ξ_3 is the spacing increment in the z-direction. After applying this mapping, scaling factors associated with this transformation from a physical space representation to a computational space representation can be expressed as,

$$h_1 = \frac{dx}{d\xi_1} \qquad h_2 = \frac{dy}{d\xi_2} \qquad h_3 = \frac{dz}{d\xi_3}. \tag{8.25}$$

The Jacobian of this transformation can be written, correspondingly, as

$$J = h_1 h_2 h_3. \tag{8.26}$$

8.3.2.1 Convective Treatment

With the coordinate system defined, (discrete) operators representative of those implemented in the code can be introduced. A second-order interpolation operator of stencil size n in the ξ_i direction acting on variable ϕ is expressed as $\bar{\phi}^{n,\xi_i}(\underline{\xi})$. The interpolation operator in the ξ_1 direction,

$$\bar{\phi}^{n,\xi_1}(\xi_1, \xi_2, \xi_3) = \frac{\phi(\xi_1 + n/2, \xi_2, \xi_3) + \phi(\xi_1 - n/2, \xi_2, \xi_3)}{2}, \tag{8.27}$$

is provided as an example. Operators in the ξ_2 and ξ_3 directions are analogous. A second-order (discrete) differentiation operator of stencil size n in the ξ_i direction acting on variable ϕ is represented as $\frac{\delta_n \phi}{\delta_n \xi_i}(\underline{\xi})$. As an example, the differentiation operator in the ξ_1 direction is written as,

$$\frac{\delta_n \phi}{\delta_n \xi_1}(\xi_1, \xi_2, \xi_3) = \frac{\phi(\xi_1 + n/2, \xi_2, \xi_3) - \phi(\xi_1 - n/2, \xi_2, \xi_3)}{n}. \tag{8.28}$$

Differentiation operators in the ξ_2 and ξ_3 directions are analogous. NGA is capable of providing an arbitrarily high order of accuracy, and, therefore, employs discrete operators of arbitrarily high order. To construct n^{th} order accurate discrete operators, interpolation weights, α_l, are first calculated via,

$$\sum_{l=1}^{n/2} (2l-1)^{2(i-1)} \alpha_l = \delta_{il} \qquad \text{for } i \in [1, n/2]. \tag{8.29}$$

Following this, the nth order interpolation operator in the ξ_i direction can be expressed as,

$$\bar{\phi}^{nth,\xi_i} = \sum_{l=1}^{n/2} \alpha_l \bar{\phi}^{(2l-1)\xi_i}, \tag{8.30}$$

and the nth order differentiation operator in the ξ_i direction can be expressed as,

$$\frac{\delta_{nth} \phi}{\delta_{nth} \xi_i} = \sum_{l=1}^{n/2} \alpha_l \frac{\delta_{2l-1} \phi}{\delta_{2l-1} \xi_i}. \tag{8.31}$$

By using these staggered operators, superior effective wavenumber behavior is attained. Further, by increasing the order of the operators, this behavior improves [26]. Additionally, by using centered or staggered operators, the effect of dissipative errors is reduced [26].

Using the defined operators, the governing equations can be discretized. In the momentum

equation, Eq. 8.22, the divergence terms are represented by,

$$\frac{\partial}{\partial x}\left(\rho u_i u\right) \longrightarrow \sum_{i=1}^{3}\left\{\frac{1}{\bar{J}^{1,\xi_1}}\sum_{l=1}^{n/2}\alpha_l\frac{\delta_{2l-1}}{\delta_{2l-1}\xi_i}\left(\overline{\frac{J\rho u_i}{h_i}}\right)^{nth,\xi_1}\bar{u}^{(2l-1),\xi_i}\right\}, \qquad (8.32)$$

$$\frac{\partial}{\partial y}\left(\rho u_i v\right) \longrightarrow \sum_{i=1}^{3}\left\{\frac{1}{\bar{J}^{1,\xi_2}}\sum_{l=1}^{n/2}\alpha_l\frac{\delta_{2l-1}}{\delta_{2l-1}\xi_i}\left(\overline{\frac{J\rho u_i}{h_i}}\right)^{nth,\xi_2}\bar{v}^{(2l-1),\xi_i}\right\}, \qquad (8.33)$$

$$\frac{\partial}{\partial z}\left(\rho u_i w\right) \longrightarrow \sum_{i=1}^{3}\left\{\frac{1}{\bar{J}^{1,\xi_3}}\sum_{l=1}^{n/2}\alpha_l\frac{\delta_{2l-1}}{\delta_{2l-1}\xi_i}\left(\overline{\frac{J\rho u_i}{h_i}}\right)^{nth,\xi_3}\bar{w}^{(2l-1),\xi_i}\right\}, \qquad (8.34)$$

where the appropriate operators have been applied. The pressure gradient term is also expressed according to,

$$\frac{\partial p}{\partial x_i} \longrightarrow \frac{J}{\bar{J}^{1,\xi_i}}\frac{1}{h_i}\left(\frac{\delta_{nth}p}{\delta_{nth}\xi_i}\right). \qquad (8.35)$$

In the mass conservation equation, Eq. 8.21, the divergence term is written as,

$$\frac{\partial}{\partial x_j}\left(\rho u_j\right) \longrightarrow \sum_{i=1}^{3}\left\{\frac{1}{J}\frac{\delta_{nth}}{\delta_{nth}\xi_i}\left(\frac{J\rho u_i}{h_i}\right)\right\}. \qquad (8.36)$$

The inverse of the Jacobian in the previous relations, $1/\bar{J}^{1,\xi_i}$, is expressed via second-order interpolation, as initially suggested by Morinishi *et al* [64]. The scalar transport equation, Eq. 8.24, is treated by implementing one of two transport schemes. These are the HOUC and QUICK schemes that are discussed in Appendix 8.5.

A comment needs to be made here about the relationship between the three components of the velocity field, u_i, and the momentum vector, $g_i = \rho u_i$. As NGA staggers the variables in space, the velocity components are located at a different position as the density values. To account for this, the ith component of the momentum vector is expressed as,

$$g_i = \bar{\rho}^{2nd,x_i}u_i, \qquad (8.37)$$

where the operator acting on the density field is a second-order interpolation operator in physical space. The density field is limited to second-order interpolation such that it is total variation diminishing (TVD). Imposing a state of TVD prevents the density field from becoming unbounded, and ensures the simulations remain realizable. It should be stated that the density interpolation is limited to second-order irrespective of the order of the rest of the scheme. It was found that such a limitation had little effect on the quality of the results obtained [26].

8.3.2.2 The Pressure Field

In a low Mach number formulation of the Navier-Stokes equations, the pressure field, p, is solved for via a Poisson equation. To ensure that the Poisson equation solved for p (analytically expressed as $\nabla^2 p = 0$) has a solution, mass must be conserved in a global sense such that,

$$\Delta\left(\delta p\right) = \frac{1}{\Delta t}\left(\sum_{i=1}^{3} \frac{1}{J}\frac{\delta_{nth}}{\delta_{nth}\xi_i}\left(\frac{Jg_i}{h_i}\right)\right) = 0. \tag{8.38}$$

Here, the middle term represents continuity and the left most term represents the discrete version of the Poisson equation for pressure. Therefore, the following must be satisfied,

$$\sum_{x,y,z} J \sum_{i=1}^{3} \frac{1}{J}\frac{\delta_{nth}}{\delta_{nth}\xi_i}\left(\frac{Jg_i}{h_i}\right) = 0. \tag{8.39}$$

As long as Eq. 8.39 is satisfied, then the pressure field can be obtained from Eq. 8.38.

8.3.2.3 Viscous Treatment

As viscous terms are dissipative by nature, they are inherently more stable than the convective terms that were addressed previously. The operators that are necessary to discretize the viscous terms are different than those presented for the discretization of the convective terms, and these new operators are based on a local Lagrange polynomial representation of the quantity to which they are applied.

To develop an nth order accurate interpolation and differentiation operator for a quantity ϕ at a location x in the direction of x_i, an $(n-1)^{th}$ order Lagrange polynomial is needed. This $(n-1)^{th}$ order Lagrange polynomial is fit through the n data points that are present in the stencil. As this fitting operation is centered about the point being evaluated, the interpolation or differentiation of the quantity ϕ is calculated from an equal number of points on either side of the point being evaluated. The new interpolation operator can be written as,

$$\bar{\phi}^{nth,x_i} = P(x), \tag{8.40}$$

while the new differentiation operator can be written as,

$$\frac{\delta_{nth}\phi}{\delta_{nth}x_i} = P'(x), \tag{8.41}$$

where $P(x)$ and $P'(x)$ are the Lagrange polynomial expression and the derivative of the Lagrange polynomial expression. Using this approach, the viscous terms in the Navier-Stokes equations can be written in terms of these viscous operators. First, the divergence of the velocity field vector

becomes,

$$\frac{\partial u_i}{\partial x_i} \longrightarrow \frac{\delta_{nth}u}{\delta_{nth}x} + \frac{\delta_{nth}v}{\delta_{nth}y} + \frac{\delta_{nth}w}{\delta_{nth}z}, \tag{8.42}$$

which is termed A_{div} in the deviatoric stress tensor relations to follow. The deviatoric stress tensor is expressed as,

$$\frac{\partial \sigma_{i1}}{\partial x} \longrightarrow \frac{\delta_{nth}}{\delta_{nth}x} \left\{ 2\mu \left(\frac{\delta_{nth}u}{\delta_{nth}x} - \frac{1}{3}A_{div} \right) \right\} + \frac{\delta_{nth}}{\delta_{nth}y} \left\{ \overline{\mu^{2nd,x}}^{2nd,y} \left(\frac{\delta_{nth}u}{\delta_{nth}y} + \frac{\delta_{nth}v}{\delta_{nth}x} \right) \right\}$$
$$+ \frac{\delta_{nth}}{\delta_{nth}z} \left\{ \overline{\mu^{2nd,x}}^{2nd,z} \left(\frac{\delta_{nth}u}{\delta_{nth}z} + \frac{\delta_{nth}w}{\delta_{nth}x} \right) \right\}, \tag{8.43}$$

$$\frac{\partial \sigma_{i2}}{\partial y} \longrightarrow \frac{\delta_{nth}}{\delta_{nth}x} \left\{ \overline{\mu^{2nd,x}}^{2nd,y} \left(\frac{\delta_{nth}v}{\delta_{nth}x} + \frac{\delta_{nth}u}{\delta_{nth}y} \right) \right\} + \frac{\delta_{nth}}{\delta_{nth}y} \left\{ 2\mu \left(\frac{\delta_{nth}v}{\delta_{nth}y} - \frac{1}{3}A_{div} \right) \right\}$$
$$+ \frac{\delta_{nth}}{\delta_{nth}z} \left\{ \overline{\mu^{2nd,y}}^{2nd,z} \left(\frac{\delta_{nth}v}{\delta_{nth}z} + \frac{\delta_{nth}w}{\delta_{nth}y} \right) \right\}, \tag{8.44}$$

and

$$\frac{\partial \sigma_{i3}}{\partial z} \longrightarrow \frac{\delta_{nth}}{\delta_{nth}x} \left\{ \overline{\mu^{2nd,x}}^{2nd,z} \left(\frac{\delta_{nth}w}{\delta_{nth}x} + \frac{\delta_{nth}u}{\delta_{nth}z} \right) \right\}$$
$$+ \frac{\delta_{nth}}{\delta_{nth}y} \left\{ \overline{\mu^{2nd,y}}^{2nd,z} \left(\frac{\delta_{nth}w}{\delta_{nth}y} + \frac{\delta_{nth}v}{\delta_{nth}z} \right) \right\} + \frac{\delta_{nth}}{\delta_{nth}z} \left\{ 2\mu \left(\frac{\delta_{nth}w}{\delta_{nth}z} - \frac{1}{3}A_{div} \right) \right\}. \tag{8.45}$$

8.3.2.4 Scalar Treatment

Similar to the momentum equation (Eq. 8.22), differential operators for the terms in the scalar transport equation (Eq. 8.24) can be obtained. The differential operator for the advection term is defined to be,

$$\frac{\partial}{\partial x_j} \left(\rho u_j Z \right) \longrightarrow \sum_{i=1}^{3} \left\{ \frac{1}{J} \frac{\delta_{nth}}{\delta_{nth}\xi_i} \left(\frac{J}{h_i} \rho u_i \overline{\overline{Z}}^{\xi_i} \right) \right\}. \tag{8.46}$$

Here, $\overline{\overline{Z}}^{\xi_i}$ represents the interpolation of a scalar quantity, Z, from its position of storage at the cell center to the cell face in the ξ_i direction. The diffusion term can be discretized similarly according to,

$$\frac{\partial}{\partial x_j} \left(\rho \mathcal{D} \frac{\partial Z}{\partial x_i} \right) \longrightarrow \sum_{i=1}^{3} \left\{ \frac{1}{J} \frac{\delta_{nth}}{\delta_{nth}\xi_i} \left(\frac{J}{h_i} \overline{\rho}^{\xi_i} \overline{\mathcal{D}}^{\xi_i} Z' \right) \right\}, \tag{8.47}$$

where the primed variable, Z', denotes the gradient of the scalar quantity, Z, at the cell face, and $\overline{\rho}^{\xi_i}$ and $\overline{\mathcal{D}}^{\xi_i}$ denote the interpolation of the density and scalar diffusivity to the cell faces. The means by

which these quantities are interpolated to the cell face depends on the transport scheme employed. The operator varies with the method implemented. The specific form that this interpolation operator takes is described in Appendix 8.5 for the two scalar transport schemes used in this thesis work, namely the QUICK scheme [52] and the HOUC5 scheme [68].

8.4   Appendix IV: Time Integration

Lastly, with the convective and viscous operators expressed, the time integration can be performed. The Navier-Stokes equations are time-advanced via a second-order, semi-implicit Crank-Nicolson method [76]. This method makes use of a fractional step approach [47], and it uses staggering in time between the momentum, scalar, and density fields. The scalar field is first solved. Then, the density field is updated through the imposed model relation ($\rho = \hat{\rho}(Z)$). After this, the momentum equations are advanced in time. Finally, the pressure field is addressed by solving a Poisson equation for the pressure to enforce continuity, as previously discussed [26]. This six-part iterative, time integration process is described below, where a uniform time step, Δt, is employed. There are a total of M sub-iterations assumed. The scalar quantities are first adressed in the algorithm; the density, scalar, and pressure fields are advanced from time $t^{n+1/2}$ to time $t^{n+3/2}$. Then, the velocity field is advanced from time t^n to time t^{n+1}.

First, assuming the previous time step has converged, these converged solutions are $\rho^{n+1/2}$ for the density field, $p^{n+1/2}$ for the pressure field, $\underline{u}^n$ for the velocity component fields, and $Z^{n+1/2}$ for the scalar fields. These values are used as the initial values in the iterative steps to come,

$$\rho_0^{n+3/2} = \rho^{n+1/2} \qquad p_0^{n+3/2} = p^{n+1/2} \qquad \underline{u}_0^{n+1} = \underline{u}^n \qquad Z_0^{n+3/2} = Z^{n+1/2}, \tag{8.48}$$

where the superscript denotes the time and the subscript denotes the sub-iteration level, $k \in [0, M]$. Second, the scalar field is treated. When the semi-implicit Crank-Nicolson scheme is applied to the scalar transport equation (Eq. 8.24), it is obtained,

$$Z_k^* = \frac{Z^{n+1/2} + Z_{k-1}^{n+3/2}}{2},$$

$$\rho_{k-1}^{n+3/2} Z_k^{n+3/2} = \rho^{n+1/2} Z^{n+1/2} + \Delta t \cdot \left([C_k^{n+1} + D_k^{n+1}] \cdot Z_k^* \right) +$$
$$\frac{\Delta t}{2} \left(\frac{\partial C}{\partial Z} + \frac{\partial D}{\partial Z} \right)_k^{n+1} \cdot \left(Z_k^{n+3/2} - Z_{k-1}^{n+3/2} \right). \tag{8.49}$$

In this notation, and for compactness, the differentiation/interpolation operators in the convective and diffusive terms are denoted $\partial C/\partial Z$ and $\partial D/\partial Z$. Third, the density field is advanced from the

imposed equation of state,

$$\rho_k^{n+3/2} = \frac{1}{aZ_k^{n+3/2} + b}. \tag{8.50}$$

Fourth, the momentum equation is advanced according to,

$$\underline{u}_k^* = \frac{\underline{u}^n + \underline{u}_{k-1}^{n+1}}{2}, \tag{8.51}$$

$$\frac{\rho^{n+1/2} + \rho_k^{n+3/2}}{2}\underline{u}_k^\dagger = \frac{\rho^{n-1/2} + \rho^{n+1/2}}{2}\underline{u}^n + \Delta t \cdot \left([C_k^{n+1/2} + D_k^{n+1/2}] \cdot \underline{u}_k^* + \nabla p_{k-1}^{n+3/2}\right) +$$
$$\frac{\Delta t}{2}\left(\frac{\partial C}{\partial \underline{u}} + \frac{\partial D}{\partial \underline{u}}\right)_k^{n+1/2} \cdot \left(\underline{u}_k^\dagger - \underline{u}_{k-1}^{n+1}\right), \quad (8.52)$$

where $\underline{u}_k^\dagger$ is an intermediate velocity that is the solution to the above momentum equation. Again, for compactness, the differentiation/interpolation operators in the convective and diffusive terms are denoted $\partial C/\partial \underline{u}$ and $\partial D/\partial \underline{u}$. Fifth, the Poisson equation for the pressure field is solved. This calculates the hydrodynamic pressure to be,

$$\nabla^2\left(\delta p_k^{n+3/2}\right) = \frac{1}{\Delta t}\left(\nabla \cdot \left\{\frac{\rho^{n+1/2} + \rho_k^{n+3/2}}{2}\underline{u}_k^\dagger\right\} + \frac{\rho_k^{n+3/2} - \rho^{n+1/2}}{\Delta t}\right). \tag{8.53}$$

The velocity field is then updated accordingly by projecting it onto a divergence free grid,

$$\underline{u}_k^{n+1} = \underline{u}_k^\dagger - \frac{2\Delta t}{\rho^{n+1/2} + \rho_k^{n+3/2}} \cdot \nabla\left(\delta p_k^{n+3/2}\right). \tag{8.54}$$

A converged solution is obtained following M sub-iterations. Once the sub-iterations are converged, then, lastly, the calculated (time-advanced) field values are updated and stored,

$$\rho^{n+3/2} = \rho_M^{n+3/2} \qquad p^{n+3/2} = p_M^{n+3/2} \qquad \underline{u}^{n+1} = \underline{u}_M^{n+1} \qquad Z^{n+3/2} = Z_M^{n+3/2}. \tag{8.55}$$

Following this process, the next time step is addressed, and the process begins again.

8.5   Appendix V: Description of Scalar Transport Schemes

For illustrative purposes, the two scalar transport schemes to be presented are applied in only one dimension (the x-direction). Here, the subscripts denote the scalar field variable value to the right $(i + 1)$ or to the left $(i - 1)$ of the central node. The central node has index i. Recall that the grid is staggered, so the momentum fluxes, ρu, are stored at the cell faces; the cell faces have indices

$i + 1/2$ and $i - 1/2$. From this it follows that the finite-volume algorithm implemented by NGA can be written as,

$$\frac{\partial \left(\rho Z\right)_{i,j,k}}{\partial t} + \frac{(\rho u Z)_{i+1/2,j,k} - (\rho u Z)_{i-1/2,j,k}}{\Delta x} = \frac{\left(\rho \mathcal{D} \frac{\partial Z}{\partial x}\right)_{i+1/2,j,k} - \left(\rho \mathcal{D} \frac{\partial Z}{\partial x}\right)_{i-1/2,j,k}}{\Delta x}. \quad (8.56)$$

The values of the momentum fluxes at the cell faces are known ($(\rho u)_{i+1/2}$ and $(\rho u)_{i-1/2}$), but the scalar field values are known only at the cell centers. To determine the value of the scalar at the cell face, the cell-centered value is interpolated from its storage position at i, $i + 1$, or $i - 1$ to the cell wall at $i + 1/2$ or $i - 1/2$,

$$(\rho u Z)_{i-1/2,j,k} = (\rho u)_{i-1/2,j,k} \, \overline{\overline{Z}}_{i-1/2,j,k}$$
$$(\rho u Z)_{i+1/2,j,k} = (\rho u)_{i+1/2,j,k} \, \overline{\overline{Z}}_{i+1/2,j,k}, \quad (8.57)$$

where the operation $\overline{\overline{Z}}_{i+1/2,j,k}$ determines the value of the scalar at the cell face from the value at the cell center by use of polynomial fitting. The form of this interpolation operation (polynomial expression) is specific to the scalar transport scheme. The two used in this work are presented in the next sub-sections.

8.5.1 Quadratic Upstream Interpolation for Convective Kinematics (QUICK) Scheme

The QUICK scheme was developed to provide a means by which the accuracy offered by central differencing convective schemes and the stability offered by upstream differencing convective schemes could be combined. It makes use of an asymmetrically placed interpolation scheme, as this allows for upstream shifting [52]. Its development is based on a conservative control-volume approach.

It writes the values of computational cell walls as a quadratic interpolation. In each coordinate direction and for each computational node, this interpolation uses the two adjacent nodes and the next upstream node. The ultimate result of this is a convective differencing scheme that has better accuracy than central differencing schemes on their own, while also obtaining the stable convective nature of upstream-weighted schemes [52]. The QUICK scheme is third-order accurate (with respect to spatial grid size, $O(\Delta x^3)$) and offers superior stability characteristics owing to its hybrid approach.

The QUICK scheme imposes the following interpolation polynomial to the cell-centered scalar values,

$$\overline{\overline{Z}}_{i-1/2,j,k} = -\frac{1}{6} Z_{i-2} + \frac{5}{6} Z_{i-1} + \frac{1}{3} Z_i$$
$$\overline{\overline{Z}}_{i+1/2,j,k} = \frac{1}{3} Z_{i-1} + \frac{5}{6} Z_i - \frac{1}{6} Z_{i+1}, \quad (8.58)$$

which allows for the flux terms,

$$(\rho u Z)_{i-1/2,j,k} = (\rho u)_{i-1/2,j,k} \, \overline{\overline{Z}}_{i-1/2,j,k}$$

$$(\rho u Z)_{i+1/2,j,k} = (\rho u)_{i+1/2,j,k} \, \overline{\overline{Z}}_{i+1/2,j,k}, \tag{8.59}$$

to be calculated.

The diffusion terms are treated similarly, although the scalar gradient term is evaluated at the cell face according to,

$$\left(\frac{\partial Z}{\partial z}\right)_{i+1/2,j,k} = \frac{Z_{i+1,j,k} - Z_{i,j,k}}{\Delta x}$$

$$\left(\frac{\partial Z}{\partial z}\right)_{i-1/2,j,k} = \frac{Z_{i,j,k} - Z_{i-1,j,k}}{\Delta x}. \tag{8.60}$$

The interpolation polynomials are also used to calculate the density, ρ, and the scalar diffusivity, $\mathcal{D}$, at the cell face (recall these scalar field variables are stored at the cell centers). This (QUICK) interpolation can be written as,

$$\overline{\overline{\rho}}_{i-1/2,j,k} = -\frac{1}{6}\rho_{i-2} + \frac{5}{6}\rho_{i-1} + \frac{1}{3}\rho_i$$

$$\overline{\overline{\rho}}_{i+1/2,j,k} = \frac{1}{3}\rho_{i-1} + \frac{5}{6}\rho_i - \frac{1}{6}\rho_{i+1}, \tag{8.61}$$

and

$$\overline{\overline{\mathcal{D}}}_{i-1/2,j,k} = -\frac{1}{6}\mathcal{D}_{i-2} + \frac{5}{6}\mathcal{D}_{i-1} + \frac{1}{3}\mathcal{D}_i$$

$$\overline{\overline{\mathcal{D}}}_{i+1/2,j,k} = \frac{1}{3}\mathcal{D}_{i-1} + \frac{5}{6}\mathcal{D}_i - \frac{1}{6}\mathcal{D}_{i+1}. \tag{8.62}$$

Once the relevant components of the diffusive term have been calculated at the cell faces, then the scalar equation (Eq. 8.56) can be time advanced.

8.5.2   High-Order Upstream Central (HOUC) Schemes

HOUC schemes are an extension of QUICK schemes, and they are commonly implemented to advect scalar species. They are subject to extremely low numerical dissipation [26], and they can be made to be of very high order in terms of accuracy [68]. (QUICK schemes are at best third-order accurate.) Further, they are known to capture sharp gradients and other fine scalar field features [68].

Focusing on the HOUC5 scheme used for the current work, the needed interpolation polynomials

are specified as,

$$\overline{\overline{Z}}_{i+1/2,j,k} = -\frac{6}{120}Z_{i-1,j,k} + \frac{54}{120}Z_{i,j,k} + \frac{94}{120}Z_{i+1,j,k} - \frac{26}{120}Z_{i+2,j,k} + \frac{4}{120}Z_{i+3,j,k}$$

$$\overline{\overline{Z}}_{i-1/2,j,k} = -\frac{6}{120}Z_{i-2,j,k} + \frac{54}{120}Z_{i-1,j,k} + \frac{94}{120}Z_{i,j,k} - \frac{26}{120}Z_{i+1,j,k} + \frac{4}{120}Z_{i+2,j,k}. \qquad (8.63)$$

Note that these polynomial coefficients assume a uniform grid mesh.

To transport the scalar quantity, Z, according to this HOUC scheme, the same process as described for the QUICK scheme is performed. The scalar quantity is interpolated from the cell centers to the cell faces such that the scalar flux term can be calculated from Eq. 8.63,

$$(\rho u Z)_{i-1/2,j,k} = (\rho u)_{i-1/2,j,k} \overline{\overline{Z}}_{i-1/2,j,k}$$

$$(\rho u Z)_{i+1/2,j,k} = (\rho u)_{i+1/2,j,k} \overline{\overline{Z}}_{i+1/2,j,k}, \qquad (8.64)$$

The scalar gradient is calculated using two adjacent scalar values at cell centers according to,

$$\left(\frac{\partial Z}{\partial z}\right)_{i+1/2,j,k} = \frac{Z_{i+1,j,k} - Z_{i,j,k}}{\Delta x}$$

$$\left(\frac{\partial Z}{\partial z}\right)_{i-1/2,j,k} = \frac{Z_{i,j,k} - Z_{i-1,j,k}}{\Delta x}. \qquad (8.65)$$

Lastly, the density and scalar diffusivity are interpolated to the cell faces, which results in,

$$\overline{\overline{\rho}}_{i+1/2,j,k} = -\frac{6}{120}\rho_{i-1,j,k} + \frac{54}{120}\rho_{i,j,k} + \frac{94}{120}\rho_{i+1,j,k} - \frac{26}{120}\rho_{i+2,j,k} + \frac{4}{120}\rho_{i+3,j,k}$$

$$\overline{\overline{\rho}}_{i-1/2,j,k} = -\frac{6}{120}\rho_{i-2,j,k} + \frac{54}{120}\rho_{i-1,j,k} + \frac{94}{120}\rho_{i,j,k} - \frac{26}{120}\rho_{i+1,j,k} + \frac{4}{120}\rho_{i+2,j,k}. \qquad (8.66)$$

and

$$\overline{\overline{\mathcal{D}}}_{i+1/2,j,k} = -\frac{6}{120}\mathcal{D}_{i-1,j,k} + \frac{54}{120}\mathcal{D}_{i,j,k} + \frac{94}{120}\mathcal{D}_{i+1,j,k} - \frac{26}{120}\mathcal{D}_{i+2,j,k} + \frac{4}{120}\mathcal{D}_{i+3,j,k}$$

$$\overline{\overline{\mathcal{D}}}_{i-1/2,j,k} = -\frac{6}{120}\mathcal{D}_{i-2,j,k} + \frac{54}{120}\mathcal{D}_{i-1,j,k} + \frac{94}{120}\mathcal{D}_{i,j,k} - \frac{26}{120}\mathcal{D}_{i+1,j,k} + \frac{4}{120}\mathcal{D}_{i+2,j,k}. \qquad (8.67)$$

Once this is done, the solution can be time advanced.

8.6 Appendix VI: Initialization Procedure

The simulation data presented in this thesis contained six field variables, including the three components of the velocity field, one scalar field quantity, the density field, and the pressure field. The initialization procedures for each of these field variables involved in the scalar mixing process are described here.

8.6.1 Velocity Field

The velocity field is initialized in a method that follows Eswaran and Pope [33]. This method imposes on the velocity field an initial energy distribution as developed by Passot and Pouquet [75]. The Passot-Pouquet energy spectrum is defined as,

$$E(\kappa) = A \left(\frac{\kappa}{\kappa_e} \right)^4 \exp \left(-2 \left(\frac{\kappa}{\kappa_e} \right)^2 \right),$$ (8.68)

where A is the amplitude of the energy spectrum, κ is the wavenumber of a given wavevector, $\underline{\kappa}$, and κ_e is the wavenumber about which the energy is initially clustered. Generally, and in the current work, $\kappa_e = 2$. This is done such that the energy content is concentrated primarily in the largest scale flow features, with limited energy content at the smaller, viscous scales [75]. The energy spectrum amplitude, A, is defined to be,

$$A = 16 \frac{u_t^2}{\kappa_e} \sqrt{\frac{2}{\pi}},$$ (8.69)

where u_t is the user-specified magnitude of turbulent fluctuations. In the current work, $u_t = 0.1$.

Following the application of the user-specified turbulent conditions (u_t, κ_e), the spectral distribution of energy content at each wavevector, $\underline{\kappa} = [\kappa_x, \kappa_y, \kappa_z]$, in the domain is calculated. κ_x, κ_y, and κ_z are the wavevector components in the x, y, and z ordinate directions, respectively. This defines the energy content at each grid point. First, the wavevector to which each grid point corresponds is calculated. Then, the energy spectrum at that wavevector is calculated according to Eq. 8.68. With the energy spectrum known at each grid point, the Fourier coefficients for the velocity field can be calculated. There are two coefficients that are needed, and they are obtained via,

$$a(\underline{\kappa})_{i,j,k} = \left(\sqrt{2\pi/L} \right)^3 \sqrt{\frac{E(\underline{\kappa})_{i,j,k}}{2\pi \kappa_{i,j,k}^2}} \exp \left(\mathcal{I} \, \theta_1 \right) \cos \left(\psi \right),$$

$$b(\underline{\kappa})_{i,j,k} = \left(\sqrt{2\pi/L} \right)^3 \sqrt{\frac{E(\underline{\kappa})_{i,j,k}}{2\pi \kappa_{i,j,k}^2}} \exp \left(\mathcal{I} \, \theta_2 \right) \sin \left(\psi \right),$$ (8.70)

where $\mathcal{I} = \sqrt{-1}$. The extent of the (periodic) computational box is represented by L. In all simulations performed in this work, $L = 2\pi$. The variables θ_1, θ_2, ψ represent random numbers bounded between $-\pi$ and π $(\theta_1, \theta_2, \psi \in [-\pi, \pi])$. The use of random numbers promotes isotropy in the velocity field imposed.

With the two coefficients at all points in the simulation domain, the three-dimensional velocity field can be computed from the Fourier coefficients. The velocity field components are orthogonal

to one another, and, accordingly, they are obtained from a and b as written,

$$\hat{u}(\underline{\kappa})_{i,j,k} = \frac{a(\underline{\kappa})_{i,j,k}\,(\kappa_{i,j,k})\,(\kappa_y)_{i,j,k} + b(\underline{\kappa})_{i,j,k}\,(\kappa_x)_{i,j,k}\,(\kappa_z)_{i,j,k}}{(\kappa_{i,j,k})\,\sqrt{\left(\kappa_x^2 + \kappa_y^2\right)_{i,j,k}}}, \tag{8.71}$$

$$\hat{v}(\underline{\kappa})_{i,j,k} = \frac{b(\underline{\kappa})_{i,j,k}\,(\kappa_y)_{i,j,k}\,(\kappa_z)_{i,j,k} - a(\underline{\kappa})_{i,j,k}\,(\kappa_x)_{i,j,k}\,(\kappa_{i,j,k})}{(\kappa_{i,j,k})\,\sqrt{\left(\kappa_x^2 + \kappa_y^2\right)_{i,j,k}}}, \tag{8.72}$$

$$\hat{w}(\underline{\kappa})_{i,j,k} = \frac{-b(\underline{\kappa})_{i,j,k}\sqrt{\left(\kappa_x^2 + \kappa_y^2\right)_{i,j,k}}}{\kappa_{i,j,k}}. \tag{8.73}$$

These expressions define the Fourier coefficients at all points in the domain, but, owing to the fact that the velocity components must be real quantities, a few modifications still need to be made. These components of $\hat{u}(\underline{\kappa})$, $\hat{v}(\underline{\kappa})$, and $\hat{w}(\underline{\kappa})$ are defined as,

$$\hat{u}(1,j,k) = \hat{u}^*(1, N+2-j, N+2-k) \qquad \text{for } k \in [2, N],\ j \in [N/2+1, N], \tag{8.74}$$

$$\hat{u}(1,1,k) = \hat{u}^*(1, 1, N+2-k) \qquad\qquad \text{for } k \in [N/2+1, N]. \tag{8.75}$$

Note that N is the number of grid points in one direction along the grid. In these expressions, $(^*)$ denotes the complex conjugation of the variable specified and j and k correspond to indices in the three-dimensional computational domain. Although only the $\hat{u}$ component is depicted here, the same operations are needed for the $\hat{v}$ and $\hat{w}$ components. Once this is done, to obtain the initial velocity field components in physical space, all that is required is to take the inverse Fourier transform of the spectral terms $\hat{u}(\underline{\kappa})$, $\hat{v}(\underline{\kappa})$, and $\hat{w}(\underline{\kappa})$ to express $u(\underline{x})$, $v(\underline{x})$, and $w(\underline{x})$,

$$u(\underline{x}, t=0) = \sum_{\underline{\kappa}} \hat{u}(\underline{\kappa}) \exp\left(\mathcal{I}\,\underline{\kappa}\cdot\underline{x}\right),$$
$$v(\underline{x}, t=0) = \sum_{\underline{\kappa}} \hat{v}(\underline{\kappa}) \exp\left(\mathcal{I}\,\underline{\kappa}\cdot\underline{x}\right),$$
$$w(\underline{x}, t=0) = \sum_{\underline{\kappa}} \hat{w}(\underline{\kappa}) \exp\left(\mathcal{I}\,\underline{\kappa}\cdot\underline{x}\right). \tag{8.76}$$

8.6.2   Scalar Field

The scalar field is initialized in a similar fashion as the velocity field; by this, it is meant that a scalar energy spectrum is imposed via a defined distribution and then the physical space scalar field values are obtained from the defined spectral form. The details of this scalar field initialization are described below. The process implemented is based on that developed by Eswaran and Pope [32]. The Fourier coefficients of the scalar field, $\hat{Z}$, are obtained from the imposed distribution,

$$\hat{Z}(\underline{\kappa}) = \sqrt{\frac{f_\phi(\kappa)}{4\pi\kappa^2}} \exp\left(2\pi\mathcal{I}\,\theta(\underline{\kappa})\right). \tag{8.77}$$

In this distribution, $\theta(\underline{\kappa})$ is a random number bounded between zero and one and f_ϕ is a top hat function defined according to,

$$f_\phi(\underline{\kappa}) = \begin{cases} 1 & \text{if } \kappa_s - 1/2 < \kappa \ \& \ \kappa < \kappa_s + 1/2, \\ 0 & \text{otherwise.} \end{cases} \qquad (8.78)$$

Here, $\kappa = \sqrt{\kappa_x^2 + \kappa_y^2 + \kappa_z^2}$ and, for the simulations contained in this work, $\kappa_s = 1$. As with the velocity field, the scalar field quantities must be real. To ensure this, it is applied,

$$\hat{Z}(1, j, k) = \hat{Z}^*(1, N+2-j, N+2-k) \qquad \text{for } k \in [2, N], \ j \in [N/2+1, N], \qquad (8.79)$$

$$\hat{Z}(1, 1, k) = \hat{Z}^*(1, 1, N+2-k) \qquad \text{for } k \in [N/2+1, N], \qquad (8.80)$$

where $\hat{Z}^*$ denotes complex conjugation, N is the number of grid points in one direction along the computational domain, and $N/2+1$ is the maximum possible wavenumber supported by such a grid size. The scalar field is then inverse Fourier-transformed, bringing it into physical space coordinates. Then, a double-delta function distribution is applied to scalar field by imposing,

$$Z(\underline{x}) = \begin{cases} 1 & \text{if } Z(\underline{x}) > 0, \\ 0 & \text{if } Z(\underline{x}) \le 0. \end{cases} \qquad (8.81)$$

Imposing such a double-delta function on the scalar field introduces significant grid point-to-grid point variation in scalar field value. This can result in the high wavenumber scalar field components being poorly resolved. To address this, a smoothing function is applied to the scalar field. To perform the smoothing step, the scalar field is Fourier-transformed back into spectral space. In spectral space, the Fourier amplitudes, $\hat{Z}(\underline{\kappa})$, are multiplied by a filtering function, $F(\underline{\kappa})$, which is defined as,

$$F(\underline{\kappa}) = \begin{cases} 1 & \text{if } \kappa \le \kappa_c, \\ (\kappa_c/\kappa)^2 & \text{if } \kappa > \kappa_c. \end{cases} \qquad (8.82)$$

Here, κ_c denotes the filter cut-off wavenumber; in all simulation performed, $\kappa_c = 2$. Recall that κ is the magnitude (wavenumber) of wavevector $\underline{\kappa}$. Implementing this filter function removes a significant portion of the poorly resolved, high wavenumber features of the scalar field. Following this, Eq. 8.79 and Eq. 8.80 are again applied, and then the scalar field is inverse Fourier-transformed back into the physical space,

$$Z(\underline{x}, t = 0) = \sum_{\underline{\kappa}} \hat{Z}(\underline{\kappa}) \exp\left(\mathcal{I} \, \underline{\kappa} \cdot \underline{x}\right). \qquad (8.83)$$

This is the initial scalar field used to seed all performed simulations contained in this work, unless otherwise stated.

8.6.3   Density and Pressure Fields

The density field was initialized in the same way as the scalar field [32]. The pressure field, owing to its treatment described in Appendix 8.3, is initialized as having everywhere in the domain a constant value. As only the pressure gradient is of consequence, the constant value can be set to any value. In this case, and for simplicity, it is set to an initial value of zero. As the time integration scheme advances, the needed pressure field value to satisfy mass conservation at every discrete time step is determined.

Bibliography

[1] K. Alvelius. Random forcing of three-dimensional homogeneous turbulence. *Physics of Fluids*, 11(7):1880, 1999.

[2] R. A. Antonia and P. Burattini. Approach to the 4/5 law in homogeneous isotropic turbulence. *Journal of Fluid Mechanics*, 550:175, 2006.

[3] R.A. Antonia and P. Orlandi. Effect of Schmidt number on small-scale passive scalar turbulence. *Applied Mechanics Reviews*, 56(6):615, 2003.

[4] R.A. Antonia, M. Ould-Rouis, F. Anselmet, and Y. Zhu. Analogy between predictions of Kolmogorov and Yaglom. *Journal of Fluid Mechanics*, 332:395–409, 1997.

[5] R.A. Antonia, R.J. Smalley, T. Zhou, F. Anselmet, and L. Danaila. Similarity solution of temperature structure functions in decaying homogeneous isotropic turbulence. *Physical Review E*, 69(1):016305, 2004.

[6] W.T. Ashurst, A.R. Kerstein, R.M. Kerr, and C.H. Gibson. Alignment of vorticity and scalar gradient with strain rate in simulated Navier–Stokes turbulence. *Physics of Fluids*, 30(8):2343, 1987.

[7] G.K. Batchelor. Small-scale variation of convected quantities like temperature in turbulent fluid. *Journal of Fluid Mechanics*, 5:113–133, 1958.

[8] F.P. Bertolotti, T. Herbert, and P.R. Spalart. Linear and nonlinear stability of the Blasius boundary layer. *Journal of Fluid Mechanics*, 242:441–474, 1992.

[9] R.W. Bilger. *Turbulent flows with nonpremixed reactants*. in P.A. Libby, F.A. Williams (Eds.), Turbulent Reacting Flows, Springer-Verlag, Berlin, 1980.

[10] G. Brethouwer, P. Billant, E. Lindborg, and J.-M. Chomaz. Scaling analysis and simulation of strongly stratified turbulent flows. *Journal of Fluid Mechanics*, 585:343–368, 2007.

[11] W.H. Cabot and A.W. Cook. Reynolds number effects on Rayleigh–Taylor instability with possible implications for type Ia supernovae. *Nature Physics*, 2(8):562–568, 2006.

[12] P.L. Carroll and G. Blanquart. A proposed modification to Lundgren's physical space velocity forcing method for isotropic turbulence. *Physics of Fluids*, 25(10):105114, 2013.

[13] P.L. Carroll and G. Blanquart. The effect of velocity field forcing techniques on the Karman-Howarth equation. *Journal of Turbulence*, 15(7):429–448, 2014.

[14] P.L. Carroll, S. Verma, and G. Blanquart. A novel forcing technique to simulate turbulent mixing in a decaying scalar field. *Physics of Fluids*, 25(9):095102, 2013.

[15] C.P. Caulfield and W.R. Peltier. The anatomy of the mixing transition in homogeneous and stratified free shear layers. *Journal of Fluid Mechanics*, 413:1–47, 2000.

[16] S. Chen and N. Cao. Anomalous scaling and structure instability in three-dimensional passive scalar turbulence. *Physical Review Letters*, 78(18):3459–3462, 1997.

[17] S. Chen, G.D. Doolen, R.H. Kraichnan, and Z. She. On statistical correlations between velocity increments and locally averaged dissipation in homogeneous turbulence. *Physics of Fluids A: Fluid Dynamics*, 5(2):458–463, 1993.

[18] D. Chung and D. I. Pullin. Direct numerical simulation and large–eddy simulation of stationary buoyancy–driven turbulence. *Journal of Fluid Mechanics*, 643:279, 2010.

[19] A.W. Cook, W. Cabot, and P.L. Miller. The mixing transition in Rayleigh–Taylor instability. *Journal of Fluid Mechanics*, 511:333–362, 2004.

[20] S. Corrsin. Heat transfer in isotropic turbulence. *Journal of Applied Physics*, 23(1):113, 1951.

[21] S. Corrsin. On the spectrum of isotropic temperature fluctuations in an isotropic turbulence. *Journal of Applied Physics*, 22(4):469, 1951.

[22] L. Danaila, F. Anselmet, T. Zhou, and R.A. Antonia. A generalization of Yaglom's equation which accounts for the large-scale forcing in heated decaying turbulence. *Journal of Fluid Mechanics*, 391(1999):359–372, 1999.

[23] L. Danaila and L. Mydlarski. Effect of gradient production on scalar fluctuations in decaying grid turbulence. *Physical Review E*, 64(1):016316, 2001.

[24] L. Danaila, T. Zhou, F. Anselmet, and R.A. Antonia. Calibration of a temperature dissipation probe in decaying grid turbulence. *Experiments in Fluids*, 28(1):45–50, 2000.

[25] T. de Karman and L. Howarth. On the statistical theory of isotropic turbulence. *Proceedings of the Royal Society of London. Series A, Mathematical and Physical Sciences*, 164(917):192–215, 1938.

[26] O. Desjardins, G. Blanquart, G. Balarac, and H. Pitsch. High order conservative finite difference scheme for variable density low Mach number turbulent flows. *Journal of Computational Physics*, 227(15):7125–7159, 2008.

[27] T. M. Dillon. Vertical overturns: A comparison of Thorpe and Ozmidov length scales. *Journal of Geophysical Research*, 87(C12):9601–9613, 1982.

[28] G. Dimonte and M. Schneider. Density ratio dependence of Rayleigh–Taylor mixing for sustained and impulsive acceleration histories. *Physics of Fluids*, 12(2):304, 2000.

[29] D.A. Donzis, K.R. Sreenivasan, and P.K. Yeung. Scalar dissipation rate and dissipative anomaly in isotropic turbulence. *Journal of Fluid Mechanics*, 532:199–216, 2005.

[30] D.A. Donzis, K.R. Sreenivasan, and P.K. Yeung. The Batchelor spectrum for mixing of passive scalars in isotropic turbulence. *Flow, Turbulence and Combustion*, 85(3-4):549–566, 2010.

[31] H.W. Emmons, C.T. Chang, and B.C. Watson. Taylor instability of finite surface waves. *Journal of Fluid Mechanics*, 7:177–193, 1959.

[32] V. Eswaran and S. B. Pope. Direct numerical simulations of the turbulent mixing of a passive scalar. *Physics of Fluids*, 31(3):506, 1988.

[33] V. Eswaran and S.B. Pope. An examination of forcing in direct numerical simulations of turbulence. *Computers & Fluids*, 16(3):257–278, 1988.

[34] H.J.S. Fernando. Turbulent mixing in stratified fluids. *Annual Review of Fluid Mechanics*, 23:455–493, 1991.

[35] D. Fukayama, T. Oyamada, T. Nakano, T. Gotoh, and K. Yamamoto. Longitudinal structure functions in decaying and forced turbulence. *Journal of the Physical Society of Japan*, 69(3):701–715, 2000.

[36] Y. Gagne, B. Castaing, C. Baudet, and Y. Malecot. Reynolds dependence of third-order velocity structure functions. *Physics of Fluids*, 16(2):482, 2004.

[37] A. E. Gargett. Evolution of scalar spectra with the decay of turbulence in a stratified fluid. *Journal of Fluid Mechanics*, 159:379–407, 1985.

[38] A.E. Gargett. Evolution of scalar spectra with the decay of turbulence in a stratified fluid. *Journal of Fluid Mechanics*, 159:379, 2006.

[39] C.H. Gibson. Fine structure of scalar fields mixed by turbulence. 2. Spectral theory. *Physics of Fluids*, 11:2316–2327, 1968.

[40] C.H. Gibson and W.H. Schwarz. The universal equilibrium spectra of turbulent velocity and scalar fields. *Journal of Fluid Mechanics*, 16(03):365–384, 1963.

[41] T. Gotoh and T. Watanabe. Scalar flux in a uniform mean scalar gradient in homogeneous isotropic steady turbulence. *Physica D: Nonlinear Phenomena*, 241(3):141–148, 2012.

[42] T. Gotoh and P.K. Yeung. Passive scalar transport in turbulence: A computational perspective. In P.A. Davidson, Y. Kaneda, and K.R. Sreenivasan, editors, *Ten chapters in turbulence.* Cambridge University Press, 2014.

[43] H. L. Grant, B. A. Hughes, W. M. Vogel, and A. Moilliet. The spectrum of temperature fluctuations in turbulent flow. *Journal of Fluid Mechanics*, 34(03):424–442, 1968.

[44] Jayesh, C. Tong, and Z. Warhaft. On temperature spectra in grid turbulence. *Physics of Fluids*, 6(1):306–312, 1994.

[45] W.S. Jevons. On the cirrous form of cloud. *London, Edinburgh, and Dublin Philosophical Magazine and Journal of Science*, pages 22–35, 1857.

[46] R.M. Kerr. Higher-order derivative correlations and the alignment of small-scale structures in isotropic numerical turbulence. *Journal of Fluid Mechanics*, 153:31–58, 1985.

[47] J. Kim and P. Moin. Application of a fractional-step method to incompressible Navier-Stokes equations. *Journal of Computational Physics*, 59:308–323, 1985.

[48] S. Komori, T. Kanzaki, Y. Murakami, and H. Ueda. Simultaneous measurements of instantaneous concentrations of two species being mixed in a turbulent flow by using a combined laser-induced fluorescence and laser-scattering technique. *Physics of Fluids A: Fluid Dynamics*, 1(2):349, 1989.

[49] R.H. Kraichnan. Small-scale structure of a scalar field convected by turbulence. *Physics of Fluids*, 11(5):945, 1968.

[50] B.E. Launder and B.I. Sharma. Application of the energy dissipation model of turbulence to the calculation of flow near a spinning disk. *Letters in Heat and Mass Transfer*, 1, 1974.

[51] J.W. Lavelle. Buoyancy-driven plumes in rotating, stratified cross flows: Plume dependence on rotation, turbulent mixing, and cross-flow strength. *Journal of Geophysical Research*, 102:3405–3420, 1997.

[52] B.P. Leonard. A stable and accurate convective modelling procedure based on quadratic upstream interpolation. *Computer Methods in Applied Mechanics and Engineering*, 19:59–98, 1979.

[53] X. Liu, S. Osher, and T. Chan. Weighted essentially non-oscillatory schemes. *Journal of Computational Physics*, 115:200–212, 1994.

[54] D. Livescu and J.R. Ristorcelli. Buoyancy-driven variable-density turbulence. *Journal of Fluid Mechanics*, 591:43–71, 2007.

[55] D. Livescu and J.R. Ristorcelli. Variable-density mixing in buoyancy-driven turbulence. *Journal of Fluid Mechanics*, 605:145–180, 2008.

[56] D. Livescu, J.R. Ristorcelli, R.A. Gore, S.H. Dean, W.H. Cabot, and A.W. Cook. High-Reynolds number RayleighTaylor turbulence. *Journal of Turbulence*, 10:1–32, 2009.

[57] D. Livescu, J.R. Ristorcelli, M.R. Petersen, and R.A. Gore. New phenomena in variable–density Rayleigh–Taylor turbulence. *Physica Scripta*, T142:014015, 2010.

[58] T S Lundgren. Linearly forced isotropic turbulence. *Center for Turbulence Research*, (2):461–473, 2003.

[59] T.S. Lundgren. Kolmogorov two-thirds law by matched asymptotic expansion. *Physics of Fluids*, 14(2):638, 2002.

[60] P.L. Miller and P.E. Dimotakis. Stochastic geometric properties of scalar interfaces in turbulent jets. *Physics of Fluids A: Fluid Dynamics*, 3(1):168, 1991.

[61] P.L. Miller and P.E. Dimotakis. Measurements of scalar power spectra in high Schmidt number turbulent jets. *Journal of Fluid Mechanics*, 308:129, 1996.

[62] F. Moisy, P. Tabeling, and H. Willaime. Kolmogorov equation in a fully developed turbulence experiment. *Physical Review Letters*, 82(20):3994–3997, 1999.

[63] A.S. Monin and A.M. Yaglom. *Statistical fluid mechanics: Mechanics of turbulence*. The MIT Press, Cambridge, 1975.

[64] Y. Morinishi, O.V. Vasilyev, and T. Ogi. Fully conservative finite difference scheme in cylindrical coordinates for incompressible flow simulations. *Journal of Computational Physics*, 197(2):686–710, 2004.

[65] L. Mydlarski and Z. Warhaft. On the onset of high-Reynolds-number grid-generated wind tunnel turbulence. *Journal of Fluid Mechanics*, 320:331, 1996.

[66] L. Mydlarski and Z. Warhaft. Passive scalar statistics in high-Peclet-number grid turbulence. *Journal of Fluid Mechanics*, 358:135–175, 1998.

[67] J. Nordstrom, N. Nordin, and D. Henningson. The fringe region technique and the Fourier method used in the direct numerical simulation of spatially evolving viscous flows. *SIAM Journal on Scientific Computing*, 20(4):1365–1393, 1999.

[68] R.R. Nourgaliev and T.G. Theofanous. High-fidelity interface tracking in compressible flows: Unlimited anchored adaptive level set. *Journal of Computational Physics*, 224(2):836–866, 2007.

[69] A.M. Obukhov. Structure of the temperature field in a turbulent flow. *Izv Akad Nauk SSSR Geographical and Geophysical Ser*, 13:58–69, 1949.

[70] B.J. Olson, J. Larsson, S.K. Lele, and A.W. Cook. Nonlinear effects in the combined Rayleigh-Taylor/Kelvin-Helmholtz instability. *Physics of Fluids*, 23(11):114107, 2011.

[71] E.S. Oran. Astrophysical combustion. *Proceedings of the Combustion Institute*, 2004.

[72] P. Orlandi and R. A. Antonia. Dependence of the non-stationary form of Yaglom's equation on the Schmidt number. *Journal of Fluid Mechanics*, 451:99, 2002.

[73] M.R. Overholt and S.B. Pope. Direct numerical simulation of a passive scalar with imposed mean gradient in isotropic turbulence. *Physics of Fluids*, 8(11):3128, 1996.

[74] M.R. Overholt and S.B. Pope. A deterministic forcing scheme for direct numerical simulations of turbulence. *Computers & Fluids*, 27, 1998.

[75] T. Passot and A. Pouquet. Numerical simulation of compressible homogeneous flows in the turbulent regime. *Journal of Fluid Mechanics*, 181:441–466, 1987.

[76] C.D. Pierce and P. Moin. Progress-variable approach for large eddy simulation of turbulent combustion. *Ph.D. Thesis, Rep. TF80, Flow Physics and Computation Division, Dept. Mech. Eng., Stanford Univ.*, 2001.

[77] S.B. Pope. *Turbulent flows*. Cambridge University Press, Cambridge, 1st edition, 2000.

[78] J. Qian. Viscous range of turbulent scalar of large Prandtl number. *Fluid Dynamics Research*, 15(2):103–112, 1995.

[79] J. Qian. Inertial range and the finite Reynolds number effect of turbulence. *Physical Review E*, 55(1):337–342, 1997.

[80] J. Qian. Slow decay of the finite Reynolds number effect of turbulence. *Physical Review E*, 60(3):3409–12, 1999.

[81] C. Rosales and C. Meneveau. Linear forcing in numerical simulations of isotropic turbulence: Physical space implementations and convergence properties. *Physics of Fluids*, 17(9):095106, 2005.

[82] S.G. Saddoughi and S.V. Veeravalli. Local isotropy in turbulent boundary layers at high Reynolds number. *Journal of Fluid Mechanics*, 268:333–372, 1994.

[83] D.L. Sandoval. The dynamics of variable-density turbulence. *PhD thesis, University of Washington, Seattle*, 1995.

[84] D.H. Sharp. An overview of Rayleigh–Taylor instability. *Physica D: Nonlinear Phenomena*, 12:3–18, 1984.

[85] E. J. Shaughnessy and J. B. Morton. Laser light-scattering measurements of particle concentration in a turbulent jet. *Journal of Fluid Mechanics*, 80(01):129–148, 1977.

[86] L. Shunn, F. Ham, and P. Moin. Verification of variable-density flow solvers using manufactured solutions. *Journal of Computational Physics*, 231(9):3801–3827, 2012.

[87] E.D. Siggia and G. S. Patterson. Intermittency effects in a numerical simulation of stationary three-dimensional turbulence. *Journal of Fluid Mechanics*, 86(03):567–592, 1978.

[88] J.W. (Lord Rayleigh) Strutt. Investigation of the character of the equilibrium of an incompressible heavy fluid of variable density. *Proc. London Math. Soc.*, 14:170–177, 1883.

[89] N.P. Sullivan, S. Mahalingam, and R.M. Kerr. Deterministic forcing of homogeneous, isotropic turbulence. *Physics of Fluids*, 6(4):1612, 1994.

[90] G.I. Taylor. The instability of liquid surfaces when accelerated in a direction perpendicular to their planes. I. *Proceedings of the Royal Society A: Mathematical, Physical and Engineering Sciences*, 201(1065):192–196, 1950.

[91] H. Tennekes and J.L. Lumley. *A first course in turbulence*. The MIT Press, Cambridge, 1972.

[92] S.R. Tieszien. On the fluid mechanics of fires. *Annual Review of Fluid Mechanics*, 33:67–92, 2001.

[93] M.L. Waite. Stratified turbulence at the buoyancy scale. *Physics of Fluids*, 23(6):066602, 2011.

[94] Z. Warhaft. Passive scalars in turbulent flows. *Annual Review of Fluid Mechanics*, 32(1):203–240, 2000.

[95] Z. Warhaft and J. L. Lumley. An experimental study of the decay of temperature fluctuations in grid-generated turbulence. *Journal of Fluid Mechanics*, 88:659–684, 1978.

[96] T. Watanabe and T. Gotoh. Statistics of a passive scalar in homogeneous turbulence. *New Journal of Physics*, 6:40–40, 2004.

[97] T. Watanabe and T. Gotoh. Intermittency in passive scalar turbulence under the uniform mean scalar gradient. *Physics of Fluids*, 18(5):058105, 2006.

[98] T. Watanabe and T. Gotoh. Scalar flux spectrum in isotropic steady turbulence with a uniform mean gradient. *Physics of Fluids*, 19(12):121701, 2007.

[99] D.C Wilcox. *Turbulence modeling for CFD*. DCW Industries, Inc., La Canada, 2nd edition, 2000.

[100] R.M. Williams and C.A. Paulson. Microscale temperature and velocity spectra in the atmospheric boundary layer. *Journal of Fluid Mechanics*, 83:547–567, 1977.

[101] A.M. Yaglom. On the local structure of a temperature field in a turbulent flow. *Dokl. Akad. Nauk SSSR*, 69:743, 1949.

[102] V. Yakhot and S.A. Orszag. Renormalization group analysis of turbulence: 1. Basic theory. *Journal of Scientific Computing*, 1, 1986.

[103] P. K. Yeung. Lagrangian characteristics of turbulence and scalar transport in direct numerical simulations. *Journal of Fluid Mechanics*, 427:241–274, 2001.

[104] P.K. Yeung, S. Xu, D.A. Donzis, and K.R. Sreenivasan. Simulations of three-dimensional turbulent mixing for Schmidt numbers of the order 1000. *Flow, Turbulence and Combustion formerly 'Applied Scientific Research'*, 72(2-4):333–347, 2004.

[105] P.K. Yeung, S. Xu, and K.R. Sreenivasan. Schmidt number effects on turbulent transport with uniform mean scalar gradient. *Physics of Fluids*, 14(12):4178, 2002.

[106] D.L. Youngs. Numerical simulation of turbulent mixing by Rayleigh–Taylor instability. *Physica D: Nonlinear Phenomena*, 12(1-3):32–44, 1984.

[107] T. Zhou, R.A. Antonia, L. Danaila, and F. Anselmet. Transport equations for the mean energy and temperature dissipation rates in grid turbulence. *Experiments in Fluids*, 28(2):143–151, 2000.

[108] Y. Zhou. Degrees of locality of energy transfer in the inertial range. *Physics of Fluids A: Fluid Dynamics*, 5(5):1092, 1993.